

# Galaxies, Black Holes and Star Power

W. Horton

February 22, 2020

# Chapter 1

## Star Power from Nuclear Ion

### 1.1 Our Sun is a typical main sequence G–type star

The first black hole was observed by a large coordinated international science team with different instruments from 2017 to 2018 and published in a series of six articles in the Astrophysical Journal Letters 875:L1–L6 in April 2019. This was the first measurements of the properties of the massive black hole M87 shown in Fig. 1.1. The concept of Black Holes was first published by Rip Thorn in 1994 and with their discovery was awarded the Nobel Prize.

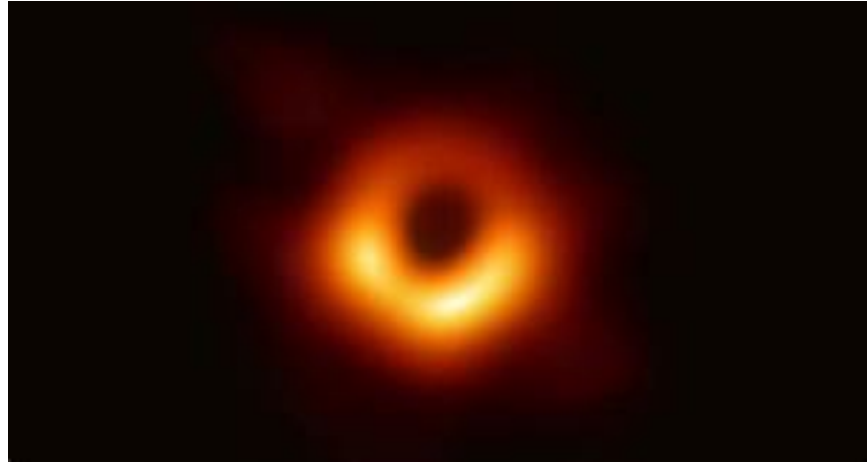


Figure 1.1: One of numerous images of the black hole M87. This image was taken at 1.3 mm wavelengths in April 2017. The diameter of the ring is  $40\mu$  as measured with instruments at different several wavelengths used to observe M87 by four independent teams with an array of different optical instruments.

The object was first noted in 1918 in a giant elliptical galaxy named Virgo. Optical and infrared data in 1997 gave estimates of mass  $\text{MBH} = 3 - 6 \times 10^9 M_\bullet$  solar masses at a distance of

17 Mpc. This object was the second largest visible black hole after that in Sagittarius named Sgr  $A^*$ . The M87 has a powerful kpc long bright plasma jet observed in both the radio and optical frequency emissions and in the X-ray bands. Plasma material moves down the jet approaching the black hole at the speed of light.

The bright edges of the jet VLBI data are launched in the central  $100\mu\text{As}$ . The high mass and proximity of M87 gives the clear images of the black hole and its jet. The launching on the horizon is explained by Generalized Relativistic MHD (GRMHD).

The spin distribution of the plasma in the Massive Black Holes (MBHs) contains rich information on the MBH growth and history. The spin evolution of MBHs shows that each MBH experiences two phases of accretion. An initial phase of coherent accretion following either the standard thin disk accretion or the super-Eddington disk. The second phase is a chaotic-accretion phase composed of many episodes with different disk orientations. When the chaotic-accretion phase is significant to the growth of an MBH, the MBH spin quickly reaches the maximum value because of the initial coherent accretion, then changes to a quasi-equilibrium state fluctuates in the chaotic-accretion episodes around a value determined by the mean ratio of the disk to the MBH mass ( $M_\bullet$ ) . The fluctuation decline in the late chaotic accretion if  $M_\bullet \gtrsim (1 - 3) \times 10^8 M_\odot$ .

The turning point to this decline is determined by the equality of the disk radius and disk size. By matching the currently available spin measurements with samples generated from the two-phase models on the spin-mass plane, we find that MBHs must experience significant chaotic-accretion phase with many episodes and that the mass accreted in each episode is roughly 1-2% of  $M_\bullet$ . MBHs with  $M_\bullet \gtrsim 10^8 M_\odot$  appear to have intermediate-to-high spins ( $\sim 0.5-1$ ) . The best matches also infer that (1) the radiative efficiencies ( $\eta$ ) of the active MBHs, the correlation between  $\eta$  and  $M_\bullet$  is weak; (2) the mean radiative efficiency of active MBHs in the range  $\langle\eta\rangle \sim 0.09-0.15$ , consistent with the global constraints [*Zhang and Lu (2019)*].

- 1.2 G-stars burn hydrogen in their core for billions of years**
- 1.3 Stars explosively expand as the hydrogen and then helium burn-up forming red giants — Aldebaran and Alpha Centauri — or grow into Black Holes**
- 1.3.1 Red Giants**
- 1.4 The Sun formed an accretion disk 4.5 billion years ago**

The Sun formed an accretion disk 4.5 billion years ago leaving residual plasma that collapsed into the planets during formation of our solar system.

- 1.5 Planet Earth is an optimal distance from the Sun**
- Planet Earth is an optimal distance from the Sun allowing life to form as recorded from the fossils. The fossils on Earth show the evolution of the planet from the Cambrian to the recent Cenozoic fossils.
- 1.6 Mars shows forms of life but hotter Venus shows no evidence of life**
- 1.6.1 G-type stars burn hydrogen in their core**

G-type stars burn hydrogen in their core for 10 billion years and then expand to become red giants like Aldebaran or Alpha Centauri.

# Bibliography

- [1] Zhang, X. and Lu, Y. (2019). On constraining the growth history of massive Black Holes via their distribution on the spin–mass plane, *Astrophys. J.* **873**, p. 101, <https://doi.org/10.3847/1538-4357/ab06c6>.

# Chapter 2

## Explosive hydrogen fusion reactions

### 2.1 Core solar plasma is burning hydrogen to helium exhaust

Core solar plasma is burning hydrogen to form helium exhaust plasma through reactions of the hydrogen isotopes — deuterium and tritium.

**2.2. UNDERSTANDING OF FUSION REACTIONS LED TO DEVELOPMENT OF THE FUSION BOMB**

**2.2 Understanding of fusion reactions led to development of the fusion bomb “Mike” after World War II**

**2.2.1 History of the hydrogen bomb**

**2.3 History of the hydrogen bomb** in *Dark Sun* by R. Rhodes (2005) records the history and controversies of developing the fusion bomb from 1955–1973.

**2.4 Cold War and the proliferation of the hydrogen bomb research, development and deployment**

**2.5 Declassification of the thermonuclear reaction through Vienna IAEA Treaty 19XX**

**2.6 Comparison of the inventions in the Soviet Union**

Comparison of the inventions in the Soviet Union, the United States at both Princeton under the Sherwood Project, Los Alamos Nuclear Laboratory and the Lawrence Livermore Laboratory.

**2.7 International Treaty bans further atmospheric H–bomb testing**

International Treaty bans further atmospheric H–bomb testing leads first to underground testing and then forbidden testing.

**2.8 Light–weight H–bombs**

Continued secret development of light–weight J–bombs and the Strategic Defense Initiative.

# Bibliography

- [1] Rhodes, R. (2005). *Dark Sun*, ISBN:978-0-684-82414-7.
- [2] Rice, J. E., Greenwald, M. J., Podpaly, Y. A., Reinke, M. L., Diamond, P. H., Hughes, W., Howard, N. T., Ma, Y., Cziegler, I., Duval, B. P., Ennever, P. C., Ernst, D., Fiore, C. L., Gao, C., Irby, J. H., Marmar, E. S., Porkolab, M., Tsujii, N. and Wolfe, S. M. (2012). Ohmic energy confinement saturation and core toroidal rotation reversal in Alcator C-Mod plasmas, *Phys. Plasmas* **19**, p. 056106, <http://dx.doi.org/10.1063/1.3695213> (copyright 2013, American Institute of Physics).

# **Chapter 3**

## **Soviet Union Development of the TOKAMAK Toroidal Fusion Plasma Confinement Vessel**

### **3.1 Declassification Laws Following the 1967 Geneva Conference**

Declassification laws following the 1967 Geneva Conference allows international sharing progress for fusion power.

### **3.2 British Team Uses New LASER Technology**

British Team uses new LASER technology to verify Soviet claim of high plasma temperature and fusion power from T-3 tokamak at the Kurchatov Nuclear Laboratory in Moscow.

### **3.3 USA drops their Stellarator project**

USA drops their Stellarator project and reproduces the Soviet results in large toroidal plasma machine using Neutral Beam Injectors (NBI) and high-power RF heating that increased plasmas temperature to fusion power levels.

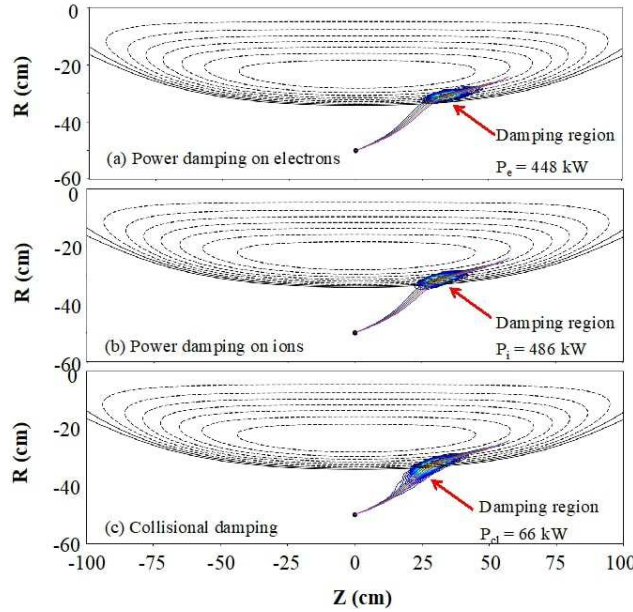


Figure 3.1: Wave propagation distance (cm). 5 rays with different initial  $n_{\parallel}$  between 4 (blue) and 6 (purple); each ray has 200 KW power at launching point. The region of significant power damping is between 30 cm and 50 cm.

Radio Frequency methods for heating the electron component of the magnetically-confined plasma becomes the internationally-accepted method for producing fusion-grade plasmas. Japan, Europe and the US produce several magnetic-confinement machines with KeV electron temperatures.

### 3.4 Radio frequency heating in FRC plasmas

High-electron temperatures  $T_e$  reduce charge exchange losses and increase fast particle-slaving down time, thereby enhancing the efficiency of plasma heating and current drive. The role of RF electron heating is critical in the Field-Reversed Configuration (FRC) plasma, as described in this chapter.

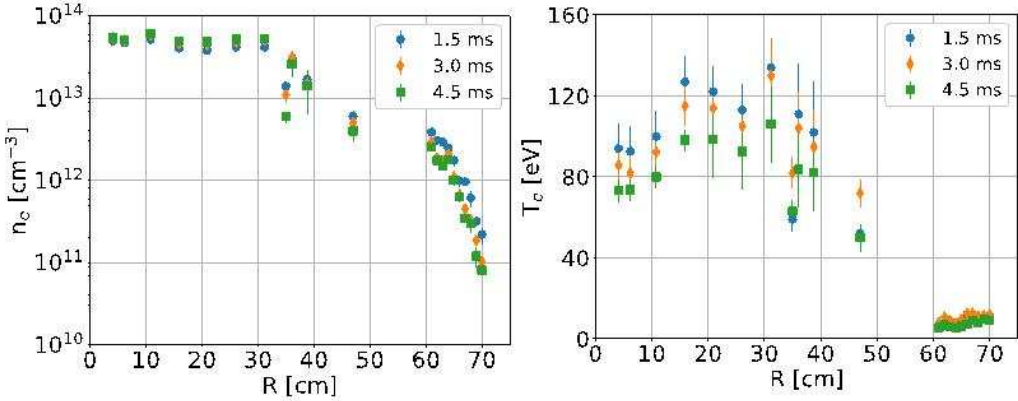


Figure 3.2: The electron density and temperature profiles measured in “Norman” in 2018.

High  $T_e$  improves FRC plasma confinement and performance. The RF study produces new insights into the physics underlying effects of unique FRC magnetic configuration on traditional RF heating regimes. Plasma is over-dense ( $\omega_{pe} > 30\omega_{ce}$ ).

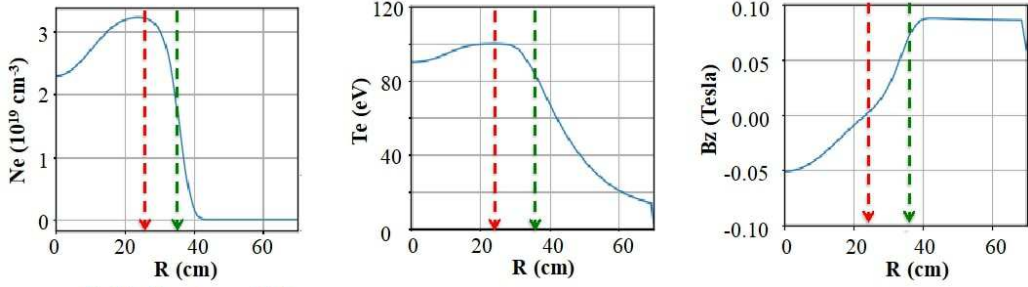


Figure 3.3: High  $T_e$  reduces charge exchange losses and increases fast particle slowing down time, thereby enhancing the efficiency of NB heating and NBCD. High  $T_e$  improves FRC plasma confinement and performance. Produces new insights into the physics underlying important effects of unique FRC magnetic configuration on traditional RF heating regimes.

- EBW (2.45 GHz, 5 GHz, 8 GHz, 18 GHz, and 28 GHz)
- Upper-hybrid resonant frequency (50 GHz, 55 GHz)
- Whistler wave frequency (0.5-1.0 GHz).
  - Landau damping — the force acting on electrons is  $F_{LD} = eE_{||}$
  - Transit-Time Magnetic Pumping (TTMP or MP), in which the force is  $F_{MP} = -\nabla_{||}(\mu B_{||})$

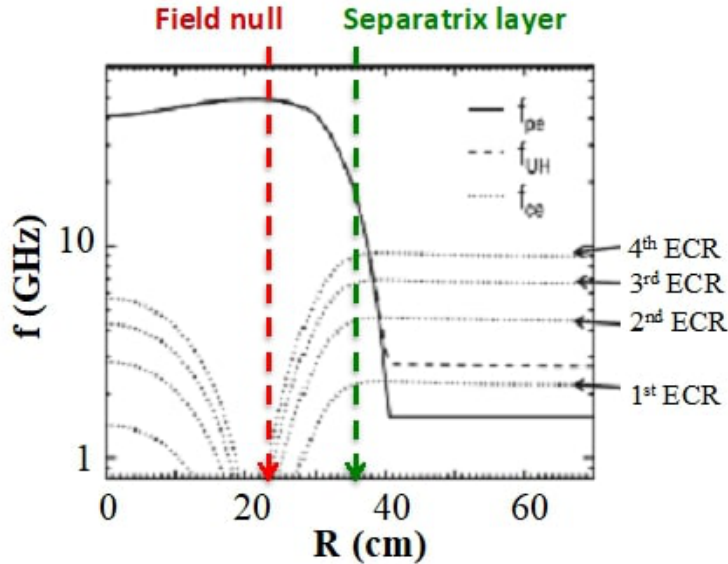


Figure 3.4: Plasma is over-dense ( $\omega_{pe} > 30\omega_{ce}$ ) plasma. The magnetic field  $B$  drops quickly to 0 within 12 cm radial distance. In this case, the ECR harmonic resonant layers are compacted into a narrow radial region and the microwaves propagate radially only for a short distance.

Table 3.1: Parameters achieve in C-2W *Norman* (2018)

Parameter	Value
$B_{ext}$	$\sim 1$ KG
$r_s$	$\sim 36$ cm
$L$	2-3 m
$N_e$	$\sim 3 \times 10^{13}$ cm $^{-3}$
$T_i$	1000-2000 eV
$T_e$	300 eV
$W = 4$ kJ	
$P_{NB}$	800-1000 MW

Here  $e$  and  $\mu$  are the charge and the magnetic moment of an electron  $E_{||}$  and  $B_{||}$  are the parallel components of the fast wave electric and magnetic field.

Inside the separatrix where  $K_{\perp\rho\text{Larmor}} \gg 1$ , at magnetic field null in mid-plane ( $z = 0$ ). This leads to thermal ions heating from the HHFW damping on the thermal ions.

The data shows good wave penetration into the plasma core with strong ion heating and with high electron absorption efficiency away from the mid-plane.

The parameters that have effects on this balance are

- Initial ratio of  $\omega/\omega_{ci[D]}$ ;
- Initial value of  $n_{\parallel}$ ;
- Antenna radial and axial location;

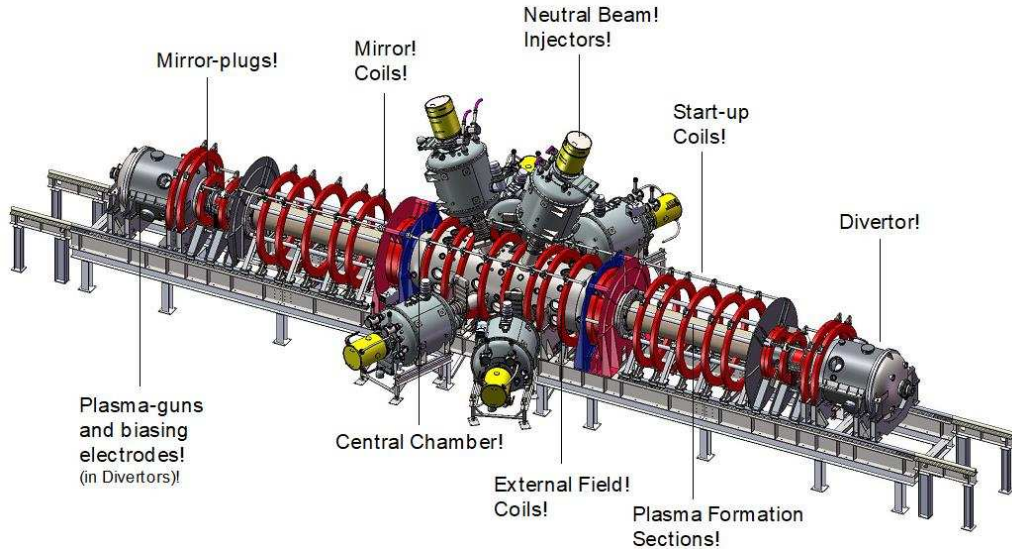


Figure 3.5:

- Density profile

Absorption, harmonics number  $n = (11 - 20)$

Conditions for significant power damping on ions  $K_{\perp} \times \rho_{\text{Larmor}} \gg 1$  and  $\omega/k_{\perp}, 2V_{Ti}$

The radial profiles of the HHFW heating in the C-2 FRC plasmas are shown in Fig. 3a for fire frequencies.

100% single pass power absorption;

TTMP is the dominated power absorption mechanism for core electron heating;

Maximum power damping on electrons occurs when wave parallel phase velocity  $V_{ph\parallel} = \omega/k_{\parallel} < V_{Te}$ ;

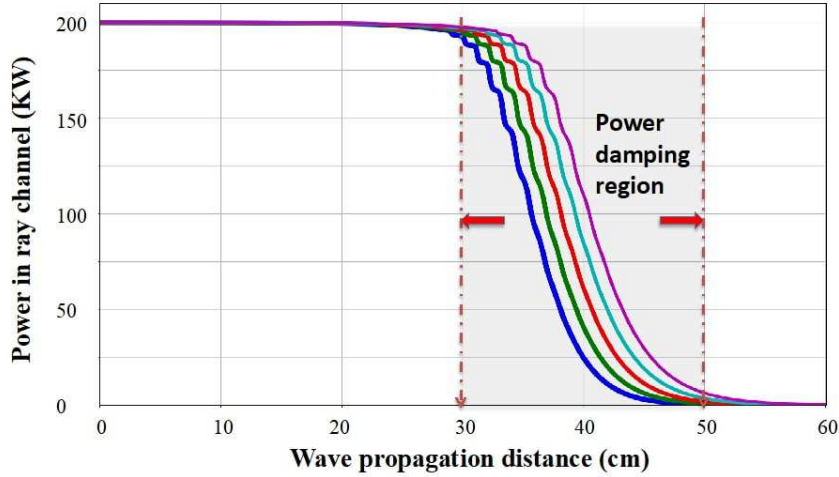


Figure 3.6: Wave propagation distance (cm)

Significant power absorption by thermal ions occurs where the conditions of  $k \perp \rho_{\text{Larmor}} \gg 1$  and  $\omega/k \perp < 2y_{Ti}$ ;

There is a trade-off between good wave penetration and favorable power partition between electrons and ions.

### 3.4.1 Radio Frequency RF Plasma Control

The RF control of the plasma is a key tool for maintaining the steady-state fusion power for all types of magnetic confinement geometries. RF plasma control encompasses a wide range of activity from theoretical and design work on antennas, to wave propagation and absorption research requiring numerical simulation and experiments. The experimental work includes both high-temperature RF plasma heating and control in tokamaks, stellarators, and advanced concepts such as the linear reversed-field confinement machine.

Scattering of Lower Hybrid (LH) RF waves by turbulence in WEST and EAST tokamaks yields key information on the core current drive [Horton. et al. (2017), Horton (2018)]. Anomalous ECH current drive from six gyrotrons in DIII-D shows the RF wave refraction and scattering from the electron density fluctuations from the drift wave turbulence [Brookman (2017)].

Drift-kinetic equations and anisotropic FLR-MHD models predict the intermittent blob emission and transport [Zheng, et al. (2016, 2017), Hatch, et al. (2017)] measured in the outer regions of the toroidal plasmas.

### 3.4.2 Filaments in the edge–confinement region of TJ-II Stellarator

Floating potential measurements from two remote reciprocating probes in the plasma edge region of the TJ-II stellarator [*van Milligen, et al.* (2017)] are analyzed using the transfer entropy, revealing the spatial dimensions and propagation properties of the lamentary wave structures. The results were verified by performing simulations with a resistive MHD model and analyzing data from synthetic diagnostics. The transfer entropy captures the rotation of the plasma elements and allows the calculating of their rotation velocity. The deduced velocity was compared to the poloidal velocity of the plasma and showed agreement [*Milligen, et al.* (2018)].

### 3.4.3 D-<sup>3</sup>He Fueled FRC Power Plant for the 21st Century

The principle advantage of D-<sup>3</sup>He fueled fusion is the mitigation of the engineering problems produced by the 14 MeV neutrons. *Momota and Tomita* (1992) describe the requirements needed to construct an attractive D-<sup>3</sup>He fusion reactor. The intrinsic characteristics of a field-reversed magnetic confinement is to provide a high plasma-pressure confinement machine configuration.

Potential and critical issues are the basis of a comprehensive D-<sup>3</sup>He fueled FRC reactor design called “ARTEMIS”, which offers an attractive prospect of fusion power development for the 21st century. The ARTEMIS fusion reactor is inherently safe and environmentally acceptable in view of the low radioactivity and fuel resources. Furthermore, the estimated cost of electricity is relatively low compared to a light water reactor. An experimental research program needed to develop the D-<sup>3</sup>He fueled FRC fusion reactors is discussed by *Momota and Tomita* (1992). Magnetic reconnection is a common mechanism or phenomena in space plasmas, such as coronal mass ejections and magnetospheric substorms and also a mechanism of confinement degradation due to violation of magnetic surfaces in magnetically-confined plasmas [*Biskamp* (2000), *Drake* (2001), *Yamada, et al.* (2010)].

### 3.4.4 Driven magnetic reconnection

The concept of driven magnetic reconnection is explained in the framework of theory [*Horton and Tajima* (1988)]. An imposed small-amplitude Magnetohydrodynamics (MHD) plasma flow velocity is specified at a finite distance from the magnetic neutral line in a plasma current sheet. The critical condition for driven reconnection is shown to be a function of the wavelength of the imposed flow compared with its distance from the neutral line as well as the orientation of the incoming plasma flow. Two-dimensional, incompressible extended MHD is used to develop the theory for a simple model of the collisionless magnetic reconnection problem. The linear, driven reconnection growth rate is analyzed. The theoretical model gives the time scale of the delay of the substorm energization of the order of a half an hour.

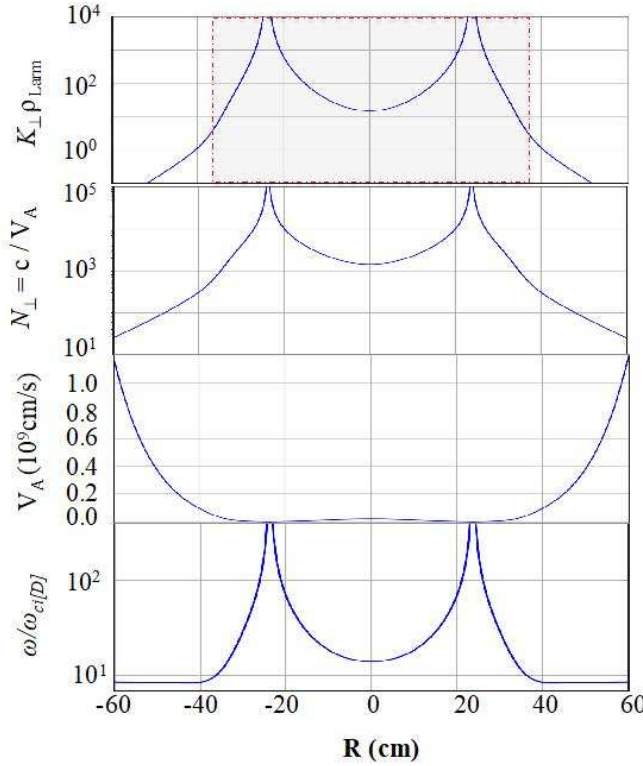


Figure 3.7: The RF wave parameters as a function of plasma radius  $R$  for the waves shown in Fig. 3.7.

### 3.4.5 Super-saturation mechanism of tokamak sawtooth relaxation

Theoretical and computational analysis using the full 3D magnetohydrodynamic equations was carried out [Sato, *et al.* (1989)]. The plasma data and simulations showed that while a slow super-saturation mechanism is continuing between a slow current peaking and a slow  $m = 1$  kink mode growth, a sudden crash occurs when an  $m = 1$  large-scale nonlinear unstable kink instability takes place, overcoming a nonlinear crescent magnetic structure which protects the flood of the super-saturation mechanism.

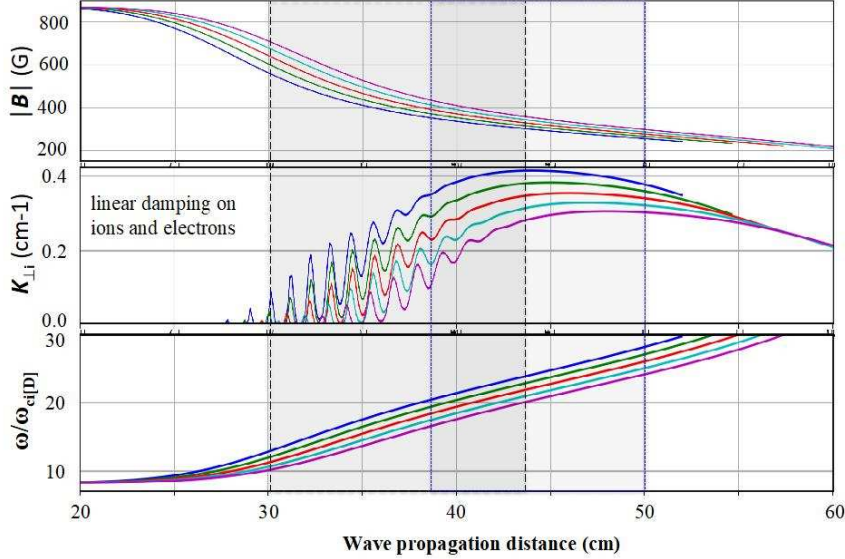


Figure 3.8: Wave propagation distance (cm)

### 3.4.6 Measurements of electron thermal transport due to electron temperature gradient modes in basic plasma experiments

The first experimental scaling of the thermal conductivity  $\chi_e(r)$  versus the amplitude of the electron temperature gradient fluctuation  $\tilde{T}_e(r, t)$  was measured versus the electron temperature profile. Production and identification of Electron Temperature Gradient (ETG) modes in a steady-state cylinder with hydrogen plasma was reported in the CLM by Wei, *et al.* (2010). A measurement of electron thermal conductivity  $\chi_e(r)$  was carried out using a high-frequency triple probe giving a value of  $\chi_{\perp e}$  ranging between  $2\text{-}10 \text{ m}^2/\text{s}$ , which is of the order of a several times the gyroBohm diffusion coefficient. The experimental result agreed with the value of nonlocal thermal conductivity obtained from theoretical calculations and are consistent with gyrokinetic simulation results and were reported in the Columbia Linear Machine (CLM). The ETG turbulence is of key importance for fusion plasmas.

For the tokamak plasma inside a single null magnetic separatrix, Zheng, *et al.* (2016) and Miura, *et al.* (2018) show how the drift-kinetic equations and anisotropic FLR-MHD model explored with theory and simulations explain the strength of the intermittent plasma blob emissions and transport across the magnetic separatrix in the Scrape-Off Layer (SOL). The complex structures propagating in SOL plasma have mixed ballooning-interchange and tearing mode features [Miura, *et al.* (2017)].

Impurity and dust transport across the Last Closed Flux Surface (LCFS) into the core plasma

is described by drift–wave turbulence that becomes strong in the Scrape–Off Layer (SOL) driven fluxes. Controlling the plasma crossing the SOL requires advanced uses of Radio Frequency RF plasma heating and current drive.

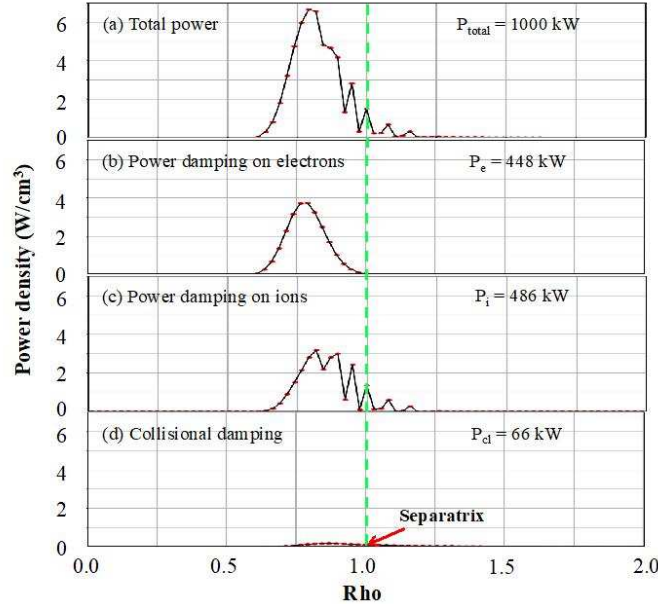


Figure 3.9: Wave propagation distance (cm)

Research centers on the impact of scattering of RF waves by plasma turbulence where RF waves are an irreplaceable tool for current drive and for control of plasma instabilities. LH waves drive currents as shown in several machines including Tore Supra, WEST and EAST. WEST research shows that the deposition profile EC waves drive current and suppress magnetic islands and our DIII–D research identifies why the RF deposition region is larger than previously predicted. Inductive start–up produces runaway electrons that accelerate without limit. RF external controls are needed to control the driving toroidal current without runaways.

### 3.4.7 Comparative calculations of the intrinsic stochasticity of tokamak divertor configurations

Poloidal divertors are the prime technique for controlling impurities, Hall–MHD stability of high performance modes of operation in tokamaks. The complex mixture of magnetic islands and stochastic magnetic field lines across the lower single divertor is shown in detail showing the genesis of the magnetic transport developing from a last closed magnetic surface at  $q = 0.7$  and on the outboard mid-plane at  $R = 0.73 \text{ m}$  tokamak. A complex region of magnetic island and

chaotic field lines is shown in the region of  $0.4\text{ m} \times 0.4\text{ m}$  surrounding the lower X-point of lower single null divertor.

*Caldas, et al.* (2006) develop the plasma turbulence developed from the drive waves in these plasmas and compare with experimental data from the TBR and TCABR tokamaks in Brazil. The conclusion is that low dimensional drift wave turbulence describe the measured turbulence and transport including the measured intermittency, temporarily and space scales of the turbulence. Overview of the turbulence measured in the TCABR tokamak is given by *Bellintani, et al.* (2006) with 4.0 to 4.5 MHz Alfvén waves driven plasmas that develop transport barriers with the LH transitions. Runaway plasmas with 33 GHz electron plasma and electron cyclotron frequency waves are measured and modeled showing the locale Alfvén waves resonances measured with reflectometers and confirming the Alfvén wave resonance model predictions.

High-power electron cyclotron waves ECH propagating perpendicular to the magnetic field produce ponderomotive forces and are used to create poloidal forces and flows which in turn produce radial forces on the plasma. This is used in J. J. Martinelli CP875, Plasma Fusion Science, to drive plasma spin-up in a poloidal direction along with an associate driving of the toroidal plasma current. The radial ponderomotive force produces the poloidal rotation driving the *Biglari, et al.* (1990) transition to an improved plasma confinement state. Martinelli calculates with numerical simulations that a  $5\text{ kW/cm}^2$  produces the radial ponderomotive force that leads to the transition in the to the H-mode plasma confinement. Both the X-mode and O-modes forced from the EC waves are analyzed and used to drive a steady-state plasma toroidal plasma current in the tokamak models.

Spin-offs from control of the outer layers of plasma transport and heating work provide the opportunity for improved descriptions and predictions of first wall erosion created by the escaping plasma and by thermal plasma bursts.

The disruption-induced forces on the tokamak wall are evaluated analytically within the standard large-aspect-ratio model with axisymmetry, circular plasmas in the absence of halo currents. Additionally, the ideal wall reaction is assumed. The plasma disruptions are modeled as rapid changes in the plasma pressure Thermal Quench (TQ) and net Current Quench (CQ). The disruption force distribution over the poloidal angle is derived as a function of these inputs. The derived formulas allow comparison of the TQ- and CQ-produced forces calculated with and without the poloidal current induced in the confinement-vessel wall. The latter variant without the walls represents the inherent property of the codes treating the wall as a set of toroidal filaments. Such a simplification leads to unacceptably large errors in the simulated forces for both thermal quench and current-quench dynamics. The TQ part of the force must prevail over that due to CQ in the high- $\beta$  scenarios developed for JT-60SA and ITER [*Pustovitov and Kiramov* (2018)].

- 3.5 Soviet Union and China build toroidal fusion power machines
- 3.6 First Deuterium–Tritium Tokamak Fusion Test Reactor (TFTR) at Princeton Plasma Physics Laboratory produces significant fusion power approaching break-even called  $Q_{DT} = 1$
- 3.7 France and MIT sets records developing high- $B$  fueled smaller tokamak fusion machines facilities with special heating methods
- 3.8 Germany develops an independent approach with the Stellarator confinement vessel at Wendelstein and the Heisenberg and Stuttgart laboratories
- 3.9 International agreement in European Union is to build a large volume-shaped toroidal D–T fusion machine, named the Joint European Torus (JET) and achieve a record for D–T fusion burning plasma power

# Bibliography

- [1] Biskamp, D. (2000). *Magnetic Reconnection in Plasmas* (Cambridge University Press), <http://adsabs.harvard.edu/abs/2000mrp..book....B>.
- [2] Bellintani Jr., V., Elfimov, A. G., Elizondo, J. I., Fagundes, A. N., Fonseca, A. M. M., Galvão, R. M. O., Guidolin, L., Kuznetsov, Yu. K., Lerche, E. A., Machida, M., Mariz, C., Nascimento, I. C., Ribeiro, C., Ruchko, L. F., de Sá, W. P., Sanada, E. K., Severo, J. H. F., da Silva, R. P., Tsypin, V., Usuriaga, O. C. and Vannucci, A. (2006). Overview of Recent Results of TCABR, *AIP Conf. Proceed.* **875**, p. 350, <https://doi.org/10.1063/1.2405964>.
- [3] Biglari, H., Diamond, P. H., and Terry, P. W. (1990). Influence of sheared poloidal rotation on edge turbulence, *Phys. Fluids B* **2**, pp. 1–4, <https://doi.org/10.1063/1.859529>.
- [4] Brookman, W. M., Austin, M. E., Gentle, K. W., Petty, C. C., Ernst, D. E., Peysson, Y., Decker, J. and Barada, K. (2017). Experimental measurement of ECH deposition broadening: Beyond anomalous transport, *EPJ Web of Conferences* **147**, p. 03001, <https://doi.org/10.1051/epjconf/201714703001>.
- [5] Caldas, I. L., Marcus, F. A., Batista, A. M., Viana, R. L., Lopes, S. R., Heller, M. V. A. P., Guimarães–Filho, Morrison, P. J. and Horton, W. (2006). Turbulence–induced transport in tokamaks, *AIP Conf. Proceed.* **875**, p. 341, <https://doi.org/10.1063/1.2405962>.
- [6] Drake, J. F. (2001). Magnetic explosions in space, *Nature* **410**, pp. 525–526, <https://doi.org/10.1038/35069160>.
- [7] Hatch, S. M., LaBelle, J., Lotko, W., Chaston, C. C. and Zhang, B. (2017). IMF control of Alfvénic energy transport and deposition at high latitudes, *JGR Space Physics* **122**, pp. 189–12,211, <https://doi.org/10.1002/2017JA024175>.
- [8] Horton, W. and Tajima, T. (1988). Linear theory of driven reconnection, *J. Geophys. Res.* **93**, pp. 2741–2748, <http://dx.doi.org/10.1029/JA093iA04p02741>.
- [9] Horton, W., Brookman, M., Goniche, M., Peysson, Y. and Ekedahl, A. (2017). RF Heating Technology Workshop and US/JAPAN Workshop on RF Physics, “High–frequency RF waves in lower–hybrid current drive”, Santa Monica, California, USA, Sept. 5–8, 2017.
- [10] Horton, W. (2018). *Turbulent Transport in Magnetized Plasmas*, 2nd Edition (World Scientific, 2018), ISBN:978–981–3225–86–6.

- [11] Miura, H., Zheng, L. and Horton, W. (2017). Numerical simulations of interchange/tearing instabilities in 2D slab with numerical model for edge plasma, *Phys. Plasmas* **24**, p. 092111, <http://dx.doi.org/10.1063/1.4993962>.
- [12] Miura, H., Miyazaki, J., Ide, M., Miyagi, D., Tsuda, M. and Yokoyama, S. (2018). Estimation method of optimal amount of overshooting current for temporal uniform magnetic field in conduction-cooled HTS coils, *IEEE Trans. Appl. Superconductivity* **28**, <https://doi.org/10.1109/TASC.2018.2805688>.
- [13] Momota, H. and Tomita, Y. (1992). D-<sup>3</sup>He Fueled FRC Power Plant for the 21st Century, *Plasma Phys. Fusion Tech.* **67**, pp. 539–549, <https://doi.org/10.1585/jspf1958.67.539>.
- [14] Pustovitov, V. D. and Kiramov, D. I. (2018). Local and integral disruption forces on the tokamak wall, *Plasma Phys. Control. Fusion* **60**, p. 045011, <https://doi.org/10.1088/1361--6587/aab056>.
- [15] Sato, T., Nakayama, Y., Hayashi, T., Watanabe, K. and Horiuchi, R. (1989). Super-saturation and nonlinear crash of tokamak sawtooth oscillations, *Phys. Rev. Lett.* **63**, p. 528, <https://doi.org/10.1103/PhysRevLett.63.528>.
- [16] van Milligen, B. Ph., Nicolau J. H., Garcia, L., Carreras, B. A., Hidalgo, C. and the TJ-II Team. (2017). The impact of rational surfaces on radial heat transport in TJ-II, *Nucl. Fusion* **57**, p. 056028, <https://doi.org/10.1088/1741-4326/aa611f>.
- [17] van Milligen, B. Ph., Hidalgo, C. and The TJ-II Team (2018). Filaments in the edge-confinement region of TJ-II, *Nucl. Fusion* **58**, p. 026030, <https://doi.org/10.1088/1741-4326/aa9db6>.
- [18] Wei, X., Sokolov, V. and Sen, A. K. (2010). Experimental production and identification of electron temperature gradient modes, *Phys. Plasmas* **17**, p. 042108, <https://doi.org/10.1063/1.3381070>.
- [19] Yamada, M., Kulsrud, R. and Ji, H. (2010). Magnetic reconnection, *Rev. Mod. Phys.* **82**, p. 603, <https://doi.org/10.1103/RevModPhys.82.603>.
- [20] Zheng, L., Horton, W., Miura, H., Shi, T. H. and Wang, H. Q. (2016). Nonneutralized charge effects on tokamak edge magnetohydrodynamic stability, *Phys. Lett. A* **380**, pp. 2654–2657, <http://dx.doi.org/10.1016/j.physleta.2016.06.027>.

# Chapter 4

## Alternative Confinement Vessels for Fusion Power

### 4.1 Stellarator machines eliminate the Mega–Amperes of plasma currents by nonsymmetric Magnetic Field Configurations

Max-Planck Institute for Plasma Physics first in Garching and now in Greifswald, Germany

### 4.2 Large Helical Device (LHD) produces fusion power developed in Japan

#### 4.2.1 Dense core plasmas in LHD and Internal Transport Barriers

The Large Helical Device (LHD) [*Nakamura, et al.* (2014, 2017), *Yoshinuma, et al.* (2010)] has achieved high-density plasmas with Internal Transport Barriers (ITB) also called Internal Diffusion Barriers in the LHD research program at the National Institute of Fusion Science (NIFS). The core plasma density and pressure exceeded  $10^{21}\text{m}^{-3}$  and 150 kPa in 1989 with an internal transport barrier. The foot point of the Internal Diffusion Barrier extends to the last closed magnetic surface at  $k_{\max n_e} = 3.9$  to 4.0 m.

- 4.3 Linear machines designed by Norman Rostoker produce record mirror-confined plasmas — the planetary magnetospheres of Earth, Jupiter and Saturn**

# Bibliography

to be added later....

# Chapter 5

## Plasma Confinement with Superconducting Magnetic Fields

### 5.1 C–Mod machine at MIT uses superconducting coils to produce record plasma confinement

In tokamaks a technique to accurately measure the electron temperature gradient scale length  $L_{T_e} = -T_e/\nabla T_e$  was developed. The technique is to vary the toroidal magnetic field  $B_T$  by 1 to a few 2% to slew the ECE channels [Houshmandyar, et al. (2016)]. The measurements are in agreement with the calculation of the gradient scale length  $L_{T_e}$  from the temperature profile. The method captures the fine structures in the  $T_e$  profiles that are missed in the common fitting techniques [Houshmandyar, et al. (2018)]. The  $T_e(r, t)$  measurements using this technique have limited time resolution since rapid modulation of  $B_T$  is not possible. Additionally, the  $B_T$  variation is not practical for tokamaks that employ superconducting magnets. Still the method of slewing the ECE channels to measure  $\nabla T_e$  and  $L_{T_e}$  works for the plasma dynamics in plasmas with superconducting toroidal machines.

- 5.2 A new version of the C-Mod machine is being developed at MIT with super conducting coils in a private sector company**
- 5.3 Mirror confinement with large expansion grids biased to reflect the escaping electrons operate at Novosibirsk Budker Institute and at the Tri Alpha Laboratory in Irvine California**
- 5.4 Private sector companies are pursuing their special approaches to affordable fusion power**

# Bibliography

- [1] Houshmandyar, S., Yang, Z. J., Phillips, P. E., Rowan, W., Hubbard, A. E., Rice, J. E., Hughes, J. W. and Wolfe, S. M. (2016). Temperature gradient scale length measurement: A high accuracy application of electron cyclotron emission without calibration, *Rev. Sci. Instrum.* **87**, p. 11E101, <https://doi.org/10.1063/1.4955297>.
- [2] Houshmandyar, S., Yang, Z. J., Liao, K. T., Zhao, B., Phillips, P. E., Rowan, W. L., Cao, N., Ernst, D. R. and Rice, J. E. (2017). Electron profile stiffness and critical gradient length studies in the Alcator C–Mod Tokamak, *Division of Plasma Physics Meeting JP11.00092*, <http://meetings.aps.org/link/BAPS.2017.DPP.JP11.92>.



## Chapter 6

# International Treaty Agreement to Build D-T Fusion Power Producing Tokamak Fusion Reactor with Output Power 10X the injected heating power

- 6.1 Recognition of the Cost and Technical Design Effort to Build a Power-producing Plasma — Like a star — in the Laboratory Led to the ITER Treaty
- 6.2 The Greifswald Stellarator machine W7X makes a breakthrough with 10 KeV hydrogen plasma driven by high-power RF heating avoiding the Mega-Amperes of plasma currents
- 6.3 Helical Magnetic Confinement System Invented in Japan — the Large Helical Device (LHD) Produces Fusion Power Deuterium Plasma for 30-minute Steady States
  - 6.3.1 Steady-state lower-hybrid RF current drive produces steady-state plasmas eliminating runaway electrons

To maintain steady-state or long-pulse, fusion plasmas, one must use high-power RF driven waves launched from antennas along the vessel walls. The first successful steady-state toroidal

plasmas were demonstrated in Tore Supra using Lower Hybrid Current Drive (LHCD). The steady-state experiments are described and reviewed in Chapter 13 of *Turbulent Transport in Magnetized Plasmas*, 2nd Ed., *Horton* (2018) ISBN:978-981-3225-86-6.

Long-pulse tokamak operation requires the change from the inductive transformer-driven toroidal electric field driven by the transformer coils to steady-state plasmas with radio frequency RF antennas that drive the plasma current. The most effective RF current driver is the Lower Hybrid Current Drive (LHCD) (for the development of a fusion power reactor).

The first phase of plasma formation with inductive start-up electric fields from the tokamak transformer shows the development of electron distribution functions with parallel momentum electron groups that are continuously accelerated by the inductive electric fields. The energy gain of these runaway electrons must be terminated or controlled by RF waves tuned to push the relativistic electrons to the radial edge of the trapped plasma through the magnetic separatrix [*Fontanilla and Breizman* (2017), *Breizman and Aleynikov* (2017)]. Without control of the runaway electrons, severe damage to the metal vessel wall occurs.

The RF current drive works from wall-mounted antennas with phased arrays of TE<sub>1,0</sub> wave guides that launch focused quasi-electrostatic 3-5 GHz lower hybrid plasma waves at about one-half the speed of light in the direction opposite to the toroidal plasma current. Modeling of the LHCD with the Tore Supra group [*Horton, et al.* (2013)] and continuing this work for the WEST and EAST tokamaks [*Horton, et al.* (2017)], *Santa Monica RF Conference* explains the measured toroidal plasma currents.

Work continues on understanding the LHCH experiments with a magnetic separatrix that isolates the wall plasma from the hot core plasma. The WEST machine is a modification of Tore Supra with tungsten walls inserted to model the walls needed for a reactor at a small scale. New issues arose in attempting to reproduce the results from Tore Supra with circular flux surfaces. WEST has a lower single-null tungsten divertor which makes the modeling and dynamics more complex. Simulation codes take into account the wall shape and the X-point on the separatrix [*Horton, et al.*, *Santa Monica Proceedings of RF Conference* (2017) and *Horton, et al.*], Aix-en Provence, June (2017) to model WEST and EAST [*Goniche, et al.* (2019), *Decker, et al.* (2011), *Peysson, et al.* (2011, 2016), *Goniche, et al.* (2019), *Hoang, et al.* (2003), *Horton, et al.* (2013a,b, 2017)].

For steady-state or long-pulse tokamak operation LHCD is required and the extended, asymmetric electron distribution  $f_e(p_{\parallel}, p_{\perp}, r, t)$  changes the stability of the ETG turbulence driven by fast electrons. This interaction modifies both electron current-carrying distribution function and the state of the ETG plasma turbulence. The ETG turbulence also scatters the RF waves used in diagnostics systems essential to measuring and controlling the tokamak plasma.

Wall erosion for multi-KeV electron plasmas driven for minutes by the Klystrons is observed and requires further investigation. Full wave codes and RF ray simulation codes are used to test the theoretical formulas derived for steady-state RF operation. Modeling includes the angle scattering of the RF rays from the low-frequency drift wave turbulence that is modified by the anisotropic electron momentum distributions that extend from 3-4v<sub>e</sub> up to the antenna-launched RF phase velocity at approximately one-half the speed of light.

Density fluctuations from the Electron Temperature Gradient (ETG) driven drift waves scat-

ter the gigaHertz RF waves from the slow wave polarization (quasi-electrostatic lower hybrid wave) into the fast wave — or whistler — RF wave polarization. The density fluctuation scattering and the coupling of the slow to the fast RF waves is computed and gives RF spectra closer to those measured in WEST and EAST than calculations without the RF scattering.

Secondly, the importance of including the scattering of the launched RF waves into the longer wavelength fast waves is that the scattering gives more RF current drive in the core plasma. The core current drive is missed by models that only follow the launched slow RF waves. Both simulations and data for the WEST and EAST current drive experiments need the fast RF waves to explain the observed electron X-ray spectrum. (EAST launches 3 GHz and Tore Supra/WEST launches 5 GHz LHCD waves). The RF wave scattering broadens the fast electron distributions producing the observed X-ray spectrum and giving the larger core toroidal currents than those derived from the electrostatic LHCD RF codes [Horton, et al. (2017)] without the coupling to the fast wave (DIII-D).

### **6.3.2 Electron Cyclotron Heating (ECH) for control of 3/2 and 2/1 magnetic islands and steady-state tokamak plasmas in DIII-D, EAST and KSTAR**

DIII-D demonstrated the use of RF Doppler Backscattering (DBS) experiments for measuring the radial distribution of the resonant ECH driven electron heating and the associated modification or control of the toroidal plasma current [Brookman, et al. (2017)]. The ECH theory and modeling are essential for developing real-time control of the growth of magnetic islands at the  $q(r) = 3/2$  and  $2/1$  rational surfaces. Theoretical analysis of the RF code data from LUKE/C3P0 and GENRAY simulations for the experiments with six 110 GHz gyrotrons producing the Doppler Backscattering (DBS) database. With modeling of the “ $B_t$ -jog” diagnostic technique [Houshmandyar, et al. (2017)], one is able to interpret the interplay of the ECH RF waves with the ETG turbulence.

Both DIII-D data and earlier data from TFTR is analyzed to determine the required focusing and to estimate the total RF gyrotron powers needed to stop, or control, the growth of the magnetic islands. Without the RF control the island growth leads to plasma disruptions and events that lower the plasma  $Q_{DT}$  by significant factors. Near real-time RF-ECH control is now understood to be essential for steady tokamak operation.

### **6.3.3 Direct $\nabla T_e$ measurements with high spatial resolution of $T_e$ -profiles using electron cyclotron emission**

Electron Cyclotron Emission (ECE) diagnostics use Yttrium-Iron-Garnet (YIG) bandpass filters to measure with precision of electron temperature  $T_e(r, t)$  profiles and fluctuations  $\delta T_e$ . These variable frequency filters were compared with fixed frequency filters and gave higher resolution

electron temperature measurements. *Houshmandyar, et al.* (2018) present proof-of-principle for high temporal resolution measurements of the electron temperature gradient, via real-time slewing with a YIG filter for measuring the location of an ECE channel during a long pulse. The key instrument is the application of YIG tunable filters with their narrow bandwidths and capability for a high slew rate of their center frequency. This instrument permits fast relocation of the ECE channels for direct measurement of the gradients with close spacing of channels to study the magnetic island's dynamics.

Electron Cyclotron Emission (ECE) diagnostics are essential to tokamaks and all fusion machines. Employing narrow bandwidth bandpass filters in the Intermediate Frequency (IF) section of a radiometer ECE diagnostic increases the spatial resolution of  $T_e$ -profile [*Troung, et al.* (2014)] and sensitivity for  $T_e$ -fluctuation ( $\delta T_e$ ) [*Fontana, et al.* (2017)] measurements. Utilizing Yttrium–Iron–Garnet (YIG) bandpass filters reduces the threshold for the  $\delta T_e$  measurements. These instruments are critical to correlational ECE measurements for turbulent transport studies [*Fontana, et al.* (2018)]. The tunable feature of the YIG filters yields the flexibility for moving the ECE channels to different spatial regions during a single discharge. This is important in plasma control during the fast rearranging of the ECE channels to rational surfaces that generates enough information for the actuators to control the Neoclassical Tearing Modes (NTM).

### 6.3.4 Impurity ion injection and transport dynamics in tokamak plasmas

The JET ITER-Like Wall (JET-ILW) experiments showed that predicting and controlling of wall erosion and inward transport of high- $Z$  ions from the W wall coatings is critical for maintaining steady fusion power plasmas.

Both the early intro-ELM and inter-ELM periods produce inputs of tungsten and beryllium ions into the core plasma under a variety of conditions. Theoretical modeling and comparisons with data from the fusion tokamaks WEST, EAST, KSTAR, JET and DIII-D show that the inward fluxes of impurity ions and their accumulation conditions are critical issues for ITER. *Michoski, et al.* (2017) and *Michoski and Horton* (2019) used theoretical models and simulations for the vessel-wall emission problem combined with drift wave impurity transport formulas. The models interpret the spectroscopic emission data taken from the impurity ions and dust particles crossing the magnetic separatrix to enter the core plasma in tokamaks and in the Large Helical Device. The research produces models for the rate of accumulations of Be and W ions during an ELM event and during minor disruptions. A set of impurity transport equations is solved using formulas for impurity fluxes driven by drift waves with ion particles and hydrogen isotopes. The spectral emission work extends the earlier models from the Alcator C-MOD impurity transport research [*Rowan, et al.* (2008)] and recent applications to DIII-D impurity injection transport experiments [*Houshmandyar, et al.* (2016, 2018), *Michoski, et al.* (2017), *Michoski and Horton* (2019)].

In order to obtain a better understanding of tungsten (W) transport processes, we are devel-

oping the Monte Carlo W transport code IMPGYRO. The code has the following characteristics which are important for calculating W transport: (1) the exact Larmor motion of W ions is computed so that the effects of drifts are automatically taken into account; (2) Coulomb collisions between W impurities and background plasma ions are modeled using the Binary Collision Model which provides more precise kinetic calculations of the friction and thermal forces. By using the IMPGYRO code, the W production/transport in the ITER geometry has been calculated under two different divertor operation modes (Case A: partially detached state and Case B: high-recycling state) obtained from the SOLPS-ITER code suite calculation without the effect of drifts. The results of the W-density in the upstream Scrape-off Layer (SOL) strongly depend on the divertor operation mode. From the comparison of the W impurity transport between Case A and Case B, obtaining a partially-detached state is shown to be effective to reduce W-impurities in the upstream SOL. The limitations of the employed model and the validity of the above results are discussed and future problems are summarized for further applications of IMPGYRO code to ITER plasmas [*Yamoto, et al. (2017)*].

### 6.3.5 RF wave control of tokamak

RF waves are an irreplaceable tool for plasma current-drive and for controlling plasma instabilities. RF research quantitatively predicts how the SOL turbulence and core turbulence scatter the RF waves leading to deposition profiles that strongly modify currents given by neoclassical and collisional transport models. This RF power leads to and couples directly to the wall erosion mechanisms through the development of plasma wall dust and impurity transport from the SOL through the magnetic separatrix into the core plasma. Elucidation of these critical processes brings the tokamak fusion program closer to the predictive capability that will be needed for interpreting the ITER plasma data. The new impurity models and software are essential for the design of a future tokamak fusion reactor.

### 6.3.6 Impurity transport from Tracer-Encapsulated Solid Pellets (TESPEL) experiment in LHD with impurity diagnostics

Experiments with additional strong auxiliary RF heating (ICH/ECH) have demonstrated the suppression and mitigation of the core impurity accumulation. The data is from the TESPEL experiments [*Sudo, et al. (2012)*] on the LHD and the impurity control experiments on the W7-AS Stellarator [*Burhenn, et al. (2009)*] and on KSTAR [*Hong, et al. (2015)*].

The TESPEL experiments on the LHD use tracer encapsulated balls of polystyrene with Mn, Co, V impurities in balls of 0.1 mm size that are injected into the plasma. Measuring with spectrometers the emitted radiation lines gives level and spatial distribution of impurities. Other machines with impurity control experiments are the W7-AS Stellarator [*Burhenn, et al. (2009)*] and the KSTAR [*Hong, et al. (2015)*].

In the KSTAR experiments [*Hong, et al.* (2015)] the addition of electron cyclotron RF heating (ECH) of 1.5 MW 154 GHz ECH suppresses the impurity emission from the highly-ionized V tracer atoms. The LHD experiments show that high-power (1.5 MW) 154 GHz ECH can reduce the accumulation of the impurities. Optimum ECH conditions (Power, Absorbed Position and Duration) are used to control the impurity accumulation.

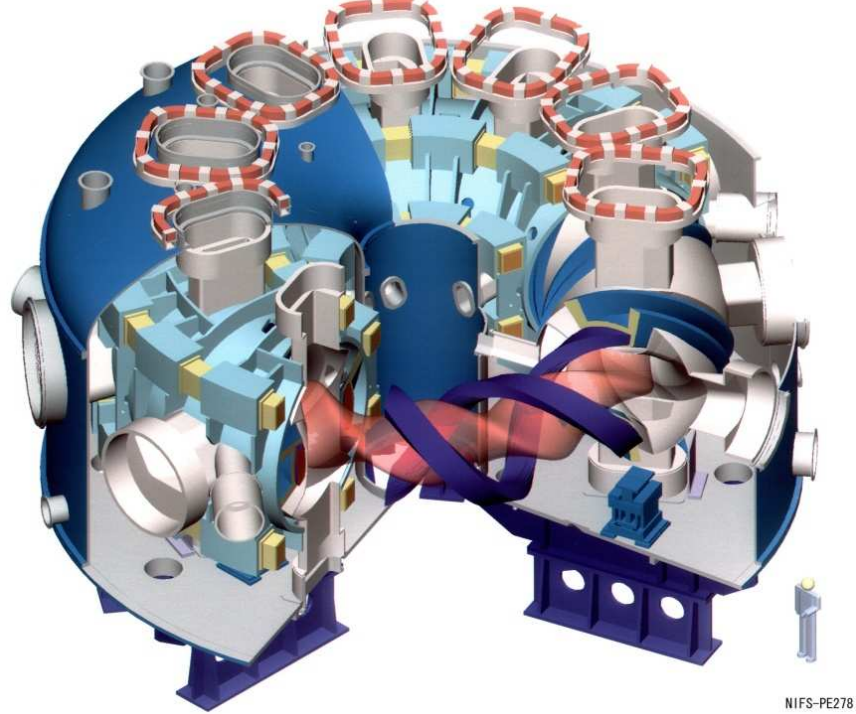


Figure 6.1: The Large Helical Device with the helical coils in black surrounding the helical plasma in gray. There are fourteen injection chambers around the top and around the outside of the torus.

Experiments on DIII-D traced the anomalous radial distribution of the ECH power deposition by the RF scattering from the ambient plasma turbulence. Modeling for WEST steady-state RF operation yields contributions to the core current drive that were previously missed in modeling without the plasma turbulence. The critical steps include pitch-angle scattering of the RF rays from the drift wave density turbulence as modified by the anisotropic electron momentum distributions produced from the antenna-launched RF waves phase velocities ranging from  $4v_e$  to one-half the speed of light. The modeling shows how the density fluctuations from the electron temperature gradient turbulence scatter the RF waves from the slow-wave polarization (quasi-electrostatic lower hybrid waves) into the fast wave or whistler RF waves [*Horton, et al.* (2017)]. This turbulence scattering is necessary to explain the measured core electron X-ray emissions. Extending the LHCD research for WEST [*Horton, et al.* (2017)] is reported in the RF Heating Conference Proceedings Aix en Provence, June 2017.

The plasma turbulence, due to the steep gradients across the Last Closed Flux Surface (LCFS), is critical in scattering the RF waves. The wave-scattering calculations show how these pressure gradients drive FLR-balloonning interchange instabilities producing pulses of vortices into the SOL edge plasma [*Miura, et al.* (2017, 2018)]. The anisotropies created in the ion velocity distributions span from inside the last closed flux surfaces into the Scrape-Off Layer (SOL) creating (i) the inward radial electric fields, (ii) the ion pressure anisotropy ( $p_{\parallel}, p_{\perp}$ ) and (iii) the sheared  $E_r$  fields that control the Hall-MHD turbulence and the creation of vortex structures or plasma “blobs”.

Research on the turbulence inside and outside the last closed flux surface is a focus in future research for ITER. Work on the RF-driven plasma structures will expand in the coming years with high priority.

### 6.3.7 Reduction of edge plasma turbulence via cross-phase decrease by zonal fields

Transport of the near-adiabatic plasma is simulated numerically. The Zonal Flow (ZF) along the poloidal direction is found to emerge self-consistently from the nonzonal turbulence. Zonal fields are found to feed back to turbulence by reducing the cross phase. As a result, the turbulence is localized with depressed peaks. Turbulence is very low and the cross phase  $\delta$  is negative near  $V = 0$ , where the gradient  $V'$  (vorticity) of ZF along the radial direction is large. The fluctuations are almost localized where the zonal-density gradient  $\bar{n}'$  is a positive peak and  $V$  is locally large. Positive  $\bar{n}'$  or positive  $V'S$  is shown to reduce the cross phase between the electric potential and the density fluctuation [*Kim, et al.* (2019)].

## Action principles for extended magnetohydrodynamic models

The general, nondissipative, two-fluid model in plasma physics is Hamiltonian, but this property is sometimes lost or obscured in the process of deriving simplified (or reduced) two-fluid or one-fluid models from the two-fluid equations of motion. To ensure that the reduced models have a Hamiltonian structure, *Charidakos, et al.* (2014) start with the general two-fluid action functional, and make all the approximations, changes of variables, and expansions directly within the action variables context. The resulting equations are then mapped to the Eulerian fluid variables using a novel nonlocal Lagrange-Euler map. Using this method, the *Lüst* (1960) general two-fluid model, the extended Magnetohydrodynamic (MHD), the Hall-MHD, and the electron MHD model are all derived from a unified framework. The variational formulation allows the application of the Noether’s theorem to derive conserved quantities for each action symmetry of the plasma.

A hollow cathode is the electronic source and neutralizer of the Hall thruster and an ion thruster. When the orbit of an all-electric propulsion satellite changes from 100 km to 36000 km, the back-pressure changes by two to three orders of magnitude. In this paper, the influence

of the back-pressure on the discharge characteristics of the hollow cathode has been studied experimentally in the so-called diode configuration. With the increase in the back pressure, the anode voltage decreases gradually, and the amplitude of the current oscillation decreases significantly. Additionally, the plasma is relatively stable, the most probable ion energy and the width of the ion energy distribution reduces, and the electron distribution function inclines toward the Maxwell distribution under high back pressure. The analysis results show that the back pressure affects the gas ionization and the ionic acoustic turbulence, which also affects the discharge characteristics of the hollow cathode [*Ning, et al. (2018)*].

### 6.3.8 Creation of plasma “blobs” outside the magnetic separatrix

Theory for the formation and dynamics of the plasma “blobs” opens up the possibility that the SOL profiles can be predicted with greater accuracy. Research on the smaller lab machines, including the Helimak and LAPD, indicates that blob filaments contribute to and possibly dominate the plasma profiles. Erosion at the vessel walls competes with emission at the divertor wall in determining the impurity contamination in the plasmas. The SOL plasma plays an important role in impurity erosion and thus the total impurity content of the core plasma. The *Breizman, et al. (2018)* work shows that during an inductive start-up, there develops a nonmonotonic distribution function in parallel momentum for a group of electrons that are continuously accelerated. The energy gain of these runaway electrons is limited by a combined effect of pitch-angle scattering and synchrotron radiation. The result is a radial transport with high-energy electrons through the magnetic separatrix. This scenario is qualitatively confirmed by the ohmic plasma data in both JET and Tore Supra [*Fontanilla and Breizman (2017)*, *Breizman and Aleynikov (2017)*].

### 6.3.9 Convective transport by intermittent blob–filaments

A blob–filament (or simply a “blob”) is a localized magnetic field-aligned plasma vortex structure that is considerably denser than the surrounding background plasma and localized in the directions perpendicular to the equilibrium magnetic field  $B$ . In experiments and simulations, these intermittent filaments are often formed near the boundary between open and closed field lines, and seem to arise in theory from the saturation process for the turbulence edge instabilities. Blobs become charge-polarized under the action of an external force which causes unequal drifts on ions and electrons; the resulting polarization-induced  $\mathbf{E} \times \mathbf{B}$  drifts that move vortices radially outwards across magnetic separatrix into the Scrape-Off Layer (SOL) plasma of toroidal and in mirror machines (CLM).

The blob transport is a general phenomenon occurring in nearly all plasmas outside the closed magnetic flux surfaces. *D’Ippolito, et al. (2011)* review the relationship between the experimental and theoretical results on blob formation, dynamics and transport and assesses the degree to

which blob theory and simulations can be compared and validated against experiments. There are numerous publications on the dynamics of the vortices and blobs in the SOL plasma.

A profile for the critical temperature gradient scale length [ $L_{T_e}^{-1} = -\nabla T_e/T_e$ ] was extensively measured in L-mode discharges in the Alcator C-Mod tokamak, where electrons were heated by ICRF waves through the minority heating method that produces changes by simultaneously varying heat fluxes and the local temperature gradients. The electron temperature gradient scale length profile was measured via the  $B_T$ -jog technique [Houshmandyar, et al. (2016)] and compared with electron heat flux from power balance analysis using TRANSP. The  $T_e$  profiles were shown to be stiff and already at the critical gradient values. The measured  $L_{T_e,\text{crit}}$  profile is in agreement with ETG turbulence models which predict the dependence of  $q/L_{\text{crit}}$  on the local  $Z_{\text{eff}}, T_e/T_i$ , and the ratio of the magnetic shear to the safety factor  $s/q$ . The GENE gyrokinetic simulations confirm that the ETG is the dominant mode of turbulence in the electron scale ( $k_{\perp}\rho_s \gg 1$ ). The gradient-turbulence data results agree with results first shown for LHCD driven  $T_e(r, t)$  profiles in Tore Supra in Horton, et al. (2000) and Hoang, et al. (2003). The results for WEST were subsequently developed in Horton, et al. (2017).

A profile carried out analysis of the L-mode plasmas near the critical electron temperature gradient scale length ( $L_c$ ) in the Alcator C-Mod tokamak [Housman, et al. (2018)], where the electrons were heated by an ion cyclotron range of frequency through a minority-heating method. The analysis was simultaneously varying the heat flux and that continuously changed the local temperature profiles and their gradient scale lengths. The electron temperature gradient scale length ( $L_{T_e}^{1/4}jr T_{ej}/T_e$ ) profile was measured via a  $B_T$ -jog technique [Houshmandyar, et al. (2016)] and was compared with electron heat flux measured  $T_e$  profiles with a power balance (TRANSP) analysis. The  $T_e$  profiles were shown to be very stiff and already above the critical values. The profile stiffness was found to be reduced near the  $q = 1/4$  and  $3/2$  surface. The measured critical scale length  $L_c$  from the  $T_e(r)$  profile is shown to be in agreement with Electron Temperature Gradient (ETG) model which predict the dependence of  $L_c^1$  critical scale length on the dependent on the local  $Z_{\text{eff}}, T_e/T_i$ , and the ratio of the magnetic shear to the safety factor. The results from linear GENE gyrokinetic simulations suggest ETG to be the dominant mode of turbulence in the electron scale ( $k_{qs} > 1$ ), and ion temperature gradient/trapped electron mode modes in the ion scale ( $k_{qs} < 1$ ). The measured  $L_c$  profile is in agreement with the profile of ETG critical gradients deduced from GENE simulations. Published by AIP Publishing (<https://doi.org/10.1063/1.5022180>).

### 6.3.10 Enhanced confinement properties in H-mode and Super-H shots

Fusion power requires one to maintain the burning plasmas with confinement properties significantly improved over those observed in auxiliary-heated L-mode tokamak discharges in order to achieve the key objectives of fusion plasmas. Thus, we understand the important of the physics responsible for the favorable trends exhibited, for example, by (supershot discharges in TFTR and by the H-mode-type divertor-controlled plasmas. In addressing this general issue, Tang, et al. (1989) reports results of theoretical investigations dealing with: the onset conditions of

the microinstabilities most strongly influencing the plasma confinement behavior with gyrokinetic particle simulations interpreted with analytic models for the saturation and transport properties of the persistent forms of these instabilities. Comparisons of experimental results with predictions from turbulent transport codes using microinstability-based theoretical formulas for particle, momentum, and energy fluxes must agree with the plasma data.

The theoretical and numerical studies on kinetic microinstabilities, including Ion Temperature Gradient (ITG) driven modes, Trapped Electron Modes (TEMs) in the presence of impurity ions as well as impurity modes (IMs), induced by impurity density gradient alone, in toroidal magnetized plasmas, such as tokamak and Reversed-Field Pinch (RFP) are reviewed briefly. The basic theory for IMs, the electrostatic instabilities in tokamak and RFP plasmas, are discussed. The observations of hybrid and coexistence of the instabilities are categorized systematically. The effects of impurity ions on electromagnetic instabilities such as ITG modes, the Kinetic Ballooning Modes (KBMs) and kinetic shear Alfvén modes induced by impurity ions in tokamak plasmas of finite- $\beta$  (= plasma pressure/magnetic pressure) are analyzed.

Microinstabilities, such as Ion Temperature Gradient (ITG) driven modes and Trapped Electron Modes (TEMs), are widely accepted to be responsible for the anomaly of cross field particle, momentum and energy transports, observed experimentally in magnetic confinement fusion plasmas, and have been under intensive investigation in recent decades [Horton (1999), Tang (1978), Liewer (1985), Doyle (2007)]. On the other hand, it is well recognized that (nonhydrogenic) impurity ions are inevitable in toroidal fusion plasmas, owing to unavoidable interactions between plasma and plasma-facing materials such as vacuum vessel and divertor plates. It is well recognized that impurity ions have significant effects on plasma confinement via radiation loss of energy and dilution of main ion density. In addition, impurity transport, induced by neoclassical mechanism and turbulence, is an important subject in fusion studies. In particular, turbulent impurity transport, induced by ITG and TEM instabilities, has been studied theoretically and experimentally, and significant progress has been achieved [Moradi, et al. (2011, 2012), Angioni and Peeters (2006), Angioni, et al. (2017a,b), Fülöp and Nordman (2009), Wade, et al. (2000), Sertoli, et al. (2011, 2015), Futatani, et al. (2010)]. The isotope effects of the instabilities and transport in the presence of impurity ions have also been investigated by Dong, et al. (1994), Shen, et al. (2016a,b), Guo, et al. (2016). Impurity effects on residual zonal flow in deuterium-tritium plasmas has been studied [Guo, et al. (2017)].

Isotope effects on instabilities driven by Ion Temperature Gradient (ITG) and impurities in tokamak plasmas in the presence of tungsten ions are numerically studied [Shen, et al. (2018)]. It is revealed that the tungsten ions significantly modify the isotope scaling of the maximum growth rates of the instabilities with respect to the main or effective ion mass number  $M_i$  or  $M_{\text{eff}} [= (1 - f_z)M_i + f_z M_z]$  with  $f_z (= Zn_z/n_e)$  being impurity charge concentration. The most reasonable scaling is deduced as  $\gamma_{\max} = M_{\text{eff}}^{-15 \pm \beta}$  with  $\beta \sim 0.8$ , for ITG-driven modes, while  $\gamma_{\max} = M_i^{-0.4 \pm \beta_1} Z_{\text{eff}}^{12 \pm \beta_2}$  holds with  $\beta_1 \sim 0.2$ ,  $\beta_2 \sim 0.4$  for tungsten impurity modes, in significant contrast with the case of light or intermediate impurities where the scaling is  $\gamma_{\max} = M_{\text{eff}}^{-0.5}$  and  $\gamma_{\max} = M_i^{-0.5} Z_{\text{eff}}^{1.5}$  for ITG and impurity modes, respectively. These results suggest that existence of tungsten impurity would enhance (weaken) the isotope effect of instability driven by ITG (tungsten impurity ions), which is beneficial (harmful) for improvement of confinement when

hydrogen isotopes are used in plasmas. The results might also provide hints on studies of particle and energy transports and discharge performance, particularly, in ITER-like wall machines.

The analysis of the influx of impurities from the confinement vessel walls called the “plasma-facing components” is described in detail by *Casson, et al.* (2015).

Research extending the earlier development of models for inward turbulent transport of impurities from the first wall and the divertor walls [*Don, et al.* (1999), *Futatani, et al.* (2010)] is carried out with experiments in WEST with tungsten divertor walls. Large Helical Device (LHD) data with hydrogen plasmas shows the inward transport of plasma dust particles from 100 nm to micro-sized dust particles. The physics of these large negatively-charged dust grains is similar to that of dust transport in deserts of West Texas is closely related to the charged  $\text{SiO}_2$  dust that rises from solar heating in Dust Devils. The dust devil models and the codes [*Onishchenko, et al.* (2014)] are generalized to the plasma dust transport problem.

The LHD plasmas provide a data set for comparison with simulations. Studies called TESPEL for dust transport in the WEST and EAST deuterium plasmas. The TESPEL data from *Nakamura, et al.* (2017) in the Large Helical Device (LHD) injects micro-sized plastic balls containing the elements with neighboring atomic numbers to the iron and chromium atoms in the vessel walls — namely the three tracer elements  $V(Z = 23)$ ,  $Mn(Z = 25)$  and  $Co(Z = 27)$  described in *Nakamura, et al.* (2014).

The WEST and the EAST tokamaks create quasi-steady-state high-temperature plasmas that have plasma dust particles from their beryllium, molybdenum and tungsten wall components simulations of the dust transport of these elements explains the observed light emission data. There are experiments in the Magnetized Dusty Plasma Experiments (MDPX) at Auburn University that may provide a test bed for dust formulation and transport theory and simulations. The transport of impurities into fusion-grade plasmas with numerous earlier publications on impurity ion transport starting with the TEXT transport experiments [*Horton and Rowan* (1994)] and continuing with electrical engineering scientists and their graduate students.

### 6.3.11 Dust particles in edge plasmas

Dust particles emitted from the plasma-wall interactions modify the drift waves in the plasma scrape-off layer which causes some dust particles to again sufficient energy to be injected through the magnetic separatrix into the core plasma. The plasma in contact to the vessel walls produces evaporation and the ejection of ions from the wall into the scrape-off layer plasma. The ions ejected from the walls are often in clumps of about 500 nm to 1 micron in size and are called plasma dust particles. These dust particles gain charge become negatively charged and gain energy from the electric fields in the edge or Scrape-Off Layer (SOL) plasma. Some of the dust particles are accelerated to high energies and cross the magnetic separatrix into the core plasma.

The dust particles are continuously undergoing a change in their charge  $Z_{de}$  due to the interaction with the ionized plasma. The dust particles become highly charged with  $Z_d = 10^3$  to  $10^4$  with a radius  $a$  of the space dust particle  $a$  much less than the Debye length. The radius  $a$  of the dust particles range from of order 10 nm to 1 micron (= 1000 microns). The charging rate is

$dZ_d/dt$  is a function of the electron and ion thermal velocities and the parameter

$$Z = \frac{Z_d e^2}{a T_e}. \quad (6.1)$$

With the balance for steady state occurring when  $Z(t)$  reaches the value

$$\frac{\omega_{pe}^2}{v_{Te}} = \frac{\omega_{pi}^2}{v_{Ti}} \frac{T_i}{T_e + Z}. \quad (6.2)$$

For  $m_i/m_e = 1836$  and  $T_e = T_i$ , the charge balance occurs with  $Z = 2.5$  [Benkadda, et al. (1995)]. When the charging rate reaches steady state  $dI(Z_d)/dt = 0$ . The charging rate is approximately deviation given by

$$\frac{d\delta Z_d}{dt} = -\iota/\chi\delta Z_d \quad (6.3)$$

where the rate is given by

$$\nu\chi = \omega_{pi}^2 d \frac{(1 + \tau + Z)}{\sqrt{(2\pi v_i)}}. \quad (6.4)$$

## Advances in modeling of plasma pedestal behavior and ELM control in ITER reference plasma scenarios

Progress in the modeling of the edge–pedestal plasma behavior in ITER plasmas including linear and nonlinear MHD stability analysis, ELM triggering by pellet injection and vertical plasma oscillations and ELM control by the application of 3D fields is described. These activities are implemented under the framework of ITER Scientist Fellow Network Pedestal Group to improve the understanding of the physics processes that dominate ITER pedestal plasmas thus providing a firmer physics base to evaluate the edge plasma properties in ITER H-mode plasmas and for the physics-based extrapolation of results obtained in present experiments to ITER [Loarte, et al. (2018)].

ELMy H-mode experiments at JET in 2000/mid–2002 have focused on discharges with normalized parameters for plasma density, energy confinement and beta similar to those of the ITER  $Q_{DT} = 10$  reference regime ( $n/n_{GW} \sim 0.85$ ,  $H_{98(y,2)} \sim 1$ ,  $\beta_N \sim 1.8$ ). ELMy H-mode plasmas have been realized reaching or even exceeding those parameters in steady-state conditions (up to  $\sim 5$ , s or  $12\tau_E$ ) in a reproducible way and only limited by the duration of the additional heating phase. These results have been obtained (a) in highly–triangular plasmas, by increasing the average triangularity  $\delta$  towards the ITER reference value ( $d \sim 0.5$ ), and (b) in plasmas at low triangularity ( $d \sim 0.2$ ) by seeding of Ar and placing the X-point of the plasma on the top of the septum. Pellet injection from the high-field side is a third method yielding high density and high confinement, albeit not yet under steady-state conditions. In highly–triangular plasmas the influence of input power, plasma triangularity and impurity seeding with noble gases has been studied. Density

profile peaking at high densities has been obtained in (a) impurity–seeded low–triangularity discharges, (b) ELMy H–modes with low levels of input power and (c) discharges fueled with pellet injection from the high field side. New ELM behavior has been observed in high–triangularity discharges at high density, opening a possible route to ELM heat–load mitigation, which can be further amplified by Ar impurity seeding. Current extrapolations of the ELM heat load to ITER show possibly a window for Type I ELM operation. Confinement scaling studies indicate an increase in confinement with triangularity and density peaking, and a decrease in confinement with the Greenwald number. In addition, experiments in H isotope and He indicate  $\tau_E \propto M^{0.19} Z^{-0.59}$ . The threshold power for the LH transition in He plasmas shows the same parametric dependence as in D plasmas, but with a 50% higher absolute value.

The experimental campaigns of the last three years on JET have resulted in a simultaneous extension of density and confinement in ELMy H–mode plasmas using various methods. By further increasing the average triangularity of the plasma, discharges have now been realized with values for  $H_{98(y,2)} \geq 1$  and  $n/n_{GW} \sim 1.1$ , which exceeds what is required for the ITER  $Q = 10$  standard scenario. The flat–top duration of these discharges is about 5 s and is only limited by technical constraints on JET. These high–density, high–confinement discharges exhibit energy losses by other mechanisms than pure ELM activity, and this points to a possible way of ELM mitigation. High density in high– $\delta$  discharges leads to a reduction in ELM frequency, which is in contrast to the usual relation between ELM frequency and ELM size. Detailed analysis of the ELM behavior and additional thermographic measurements on the divertor targets indicate that there is a possible window for operation for Type I ELM discharges in ITER. Impurity seeding is an additional tool to mitigate ELMs in discharges with high and low triangularity and has no detrimental effect on energy confinement or neutron production. Pellet injection from the high–field side with a tailored injection rate has also resulted in discharges with high density and high confinement, but more work is needed to optimize the stationarity. Discharges with strong density peaking ( $n(0)/n_{ped} \sim 2$ ) have also been obtained without pellet injection, by careful gas dosing over long time intervals. Density peaking and high– $\beta$  values both favor the destabilization of NTMs due to the associated increased bootstrap current fraction. This can be a limiting factor for the confinement properties of such plasmas, unless care is taken to avoid the creation of large seed islands, induced by, e.g., large first ELMs or sawteeth, or by varying the ICRH phasing. Confinement studies show an increase of energy confinement with density peaking and triangularity, but still a degradation of confinement with increasing Greenwald factor. Density peaking and plasma shaping have a beneficial influence on confinement. Confinement scaling studies with data from He discharges confirmed the mass dependence of the IPB98(y, 2) scaling, and combined with previous T and H studies, suggest  $\tau_E \propto M^{0.19} Z^{-0.59}$ . Threshold power studies in He show the same dependence on magnetic field, density and mass as for deuterium, but the absolute value is about 50% higher in He. Extensions of the results presented in this paper to higher currents, fields and heating powers and towards longer flat–top durations on JET are prepared, in view of continued preparation for ITER. New plasma configurations at high average triangularity have been developed, reducing the disruptive forces of the ITER–like configuration, allowing plasma operation at JET up to 4 MA/4 T, in order to study the performance at higher absolute densities and to operate closer to  $\rho_*^{ITER}$ . Such plasmas will require at least 25 MW of additional heating power to reach the H–mode and this level of

power should become available during 2003 on JET. Various diagnostics have been and are being enhanced to increase the diagnostic capabilities of JET. A new inboard pellet track aiming more centrally and allowing higher pellet speeds has been installed to further optimize plasma fueling by high-field side pellet injection. Very long pulse scenarios have been prepared with a divertor phase of over 50 s and with potential for further extensions well over 1 min, presenting a new and interesting tool for studies on the stationarity of various plasma parameters and of recycling during very long time intervals.

With its divertor configuration, plasma size, heating, current drive and diagnostic systems, tritium, beryllium and remote-handling capabilities, the JET device accesses a wide range of operating regimes in experimental conditions very close to those of a burning plasma experiment. Prior to and during the design phase of ITER, JET produced major contributions to the ITER physics basis [*ITER Physics Basis* (1999)] used to extrapolate plasma performance to ITER. The JET research program has focused on issues critical to finalizing the details of the ITER design and preparing its operation.

In the 2004 shutdown, a new in-port ICRF antenna was installed. The aim was to validate key elements of the ITER-ICRF design (such as ELM tolerant operation at a high-power density) and to deliver an additional 7 MW of heating power, allowing higher performance operation closer to ITER plasma parameters. Diagnostic upgrades include CXRS core and edge, magnetics, bolometry, neutron spectrometry, microwave waveguides and divertor diagnostics. New diagnostics installed include a high-resolution TS system, TAE active antenna system, wide-angle infrared view, halo sensors, lost  $\alpha$  detectors and a comprehensive system of erosion/re-deposition diagnostics.

JET continues to provide vital contributions to our understanding of tokamak physics, scaling predictions for ITER, further development of ITER operating scenarios and testing of ITER relevant systems such as heating and current drive, diagnostics and tritium technologies.

The impact of an initial random magnetic field on the temporal evolution of a two-dimensional incompressible turbulent shearless mixing layer is investigated using direct numerical simulation. Different intensities of the initial random magnetic field are imposed with uniform probability distribution on an identical flow field. The initial flow-field condition is the turbulent shearless mixing layer with different kinetic energy ratio ( $E_H/E_L = 6.7$ ) and identical integral length scale. Simulations are carried out in a moderate magnetic Reynolds number, which causes a two-way interaction between the velocity and magnetic fields. In order to analyze the effect of the initial random magnetic field on the mixing characteristics, the intermittency inside the mixing layer and the mixing evolution parameters are investigated. It is found that with small initial magnetic field intensity, the intermittency in both large and small scales are larger than those values in hydrodynamic flow. However, increasing the intensity of the initial magnetic field reduces the intermittency in the mixing region to lower values compared to the hydrodynamic flow. The mixing layer growth rate and the mixing efficiency both show reduction by increasing the initial magnetic field intensity, which is attributed to the reduction of the averaged Reynolds number of both homogeneous isotropic turbulent regions due to the suppressing effect of the Lorentz force on the velocity fields of these regions.

Plasma response to three-dimensional Resonant Magnetic Perturbations (RMP), applied for

the purpose of controlling type-I Edge Localized Modes (ELMs) in ITER with the baseline ELM control coils, is computed using a toroidal, resistive, full magnetohydrodynamic model. Considered are five representative ITER plasmas, designed for different phases of the ITER exploration. The plasma response, measured by the plasma boundary corrugation, is found to be similar for the two DT scenarios at full plasma current (15 MA) and full toroidal field (5.3 T) but different fusion gain factors ( $Q = 5$  versus  $Q = 10$ ), indicating similar ELM control performance with the same RMP coil current configuration. The other plasma scenarios, with proportionally scaled down plasma current and toroidal field, can have different plasma boundary corrugation. The key plasma parameter affecting the response is the plasma toroidal flow near the pedestal region, which significantly varies depending on the transport model assumption for the toroidal momentum. Lower pedestal flow leads to a stronger edge peeling response from the plasma and thus probably a better ELM control. The optimal coil configuration for controlling type-I ELMs is similar for all four ITER plasmas with similar safety factor but different current levels, but is significantly different for the case at half plasma current (7.5 MA) and full field (5.3 T). On the other hand, for the purpose of controlling the radial profile of the plasma toroidal rotation in ITER using 3D fields, the relative amplitude of the toroidal torque density, between the plasma core and edge region, is optimized. Generally, a strong coupling between the core and edge torques is observed, largely due to the middle row ELM control coils. The best decoupling scheme of the core–edge torque distribution thus de-emphasizes the role of the middle row coils. Optimal coil current configurations are found for the ITER 15 MA/5.3  $Q = 10$  plasma, that synergistically maximize the plasma edge-peeling response (indication for good ELM control) and the toroidal torque near the plasma edge (good for RMP field penetration through pedestal) [Li, et al. (2019)].

The effect of Resonant Magnetic Perturbation (RMP) on boundary turbulence and transport in J–TEXT plasma is experimentally investigated. Edge plasma fluctuations in discharges with and without the ( $m/n = 3/1$ ) RMP currents are diagnosed by using Langmuir probe arrays. It was found that fluctuations in the edge and Scrape–Off Layer (SOL) regions decrease with the application of a 6 kA RMP. The broadband turbulence at the radial location of  $\rho \sim 0.9$  which has a characteristic frequency of 40–150 kHz was strongly suppressed when applying RMP, as was the radial turbulent particle flux and blob transport in the near–SOL region. These experimental findings make RMP a promising method of suppressing and controlling turbulence and particle transport in a plasma boundary [Wu, et al. (2019)].

Significant progress in understanding of the physics processes that determine pedestal plasma behavior in ITER plasmas, their MHD stability and instability leading to ELMs as well as of ELM control has taken place by the modeling activities implemented under the ITER Scientist Fellow Network Pedestal Group. New nonlinear MHD simulations show that ITER pedestal plasmas have the required characteristics to access the QH–mode regime without ELMs by destabilization and saturation of low– $n$  kink–peeling modes, although it is not yet clear if the rotational shear required to stabilize higher– $n$  ballooning modes can be provided by the joint application of the NBI torque and the breaking torque provided by 3D fields from the in–vessel ELM control coils. Controlled ELM triggering has been further assessed for two schemes: pellet injection and vertical plasma position oscillations. For pellet triggering, it has been found that the proximity of the pedestal pressure to MHD stability limits plays a very important role in determining the pellet size

required to trigger an ELM (which is favorable regarding the optimization of plasma performance and minimizing fuel throughput for ELM control).

The required pellet sizes to trigger ELMs at lower plasma currents are much lower than for 15 MA plasmas, particularly at high  $q_{95}$ . This ensures that this scheme can be explored in the initial H-mode operational phases of the ITER Research Plan at lower plasma currents so that a decision can be taken regarding its applicability for high  $Q/I_p$  operation in ITER, which may require an upgrade of the pellet injection system from 4 to 6 injectors. Regarding vertical plasma oscillations, the nonlinear MHD simulations have given the physics basis to evaluate this scheme for ELM control in ITER and confirmed that pellet injection (tungsten ion W) can be used for currents up to 7.5 MA as backup when the other ITER ELM control schemes are being developed/tested (ELM control by 3D fields and by pellet pacing).

## 6.4 High Magnetic Field Toroidal Fusion Machines

The IGNITOR Program maintains the objective of approaching D-T ignition conditions by incorporating systematically advances in relevant high magnetic field technology and in experiments on high density well confined plasmas. Another objective is to chart the development of the high field line of experiments. Considering that a detailed machine design has been carried out [*Coppi, et al. (2013)*], the advances made in different areas of the physics and technology that are relevant to the IGNITOR project are reported. These are included within the following sections of this paper: Main Components Issues, Assembly and Welding Procedures; Robotics Criteria; Nonlinear Feedback Control Simulations with 3D Structures and Disruption Studies; ICRH and Dedicated Diagnostics Systems; Anomalous Transport Processes Including Self-organization for Fusion Burning Regimes and Zero-Dimensional Model; Tri-dimensional Structures of the Thermonuclear Instability and Control by ICRH Heating; Superconducting Components of the Machine; Envisioned High-Field Superconducting Experiments.

The main objective of the IGNITOR Program is to explore the ignition conditions of magnetically confined D-T plasmas while producing significant amounts of fusion power (up to about 100 MW). For this, a (necessarily) compact, high-field device has been designed that advances the line of high-field experiments which began with the Alcator program at MIT and was later also developed in Italy with the FT program. A relatively short but complete description and analysis of the machine core (see Fig. 6.10) has been given in *Coppi, et al. (2013)*.

**Vertical cross-section of the IGNITOR machine as presently designed.**

**Sketch of the vertical cross section of the IGNITOR machine where the main components are indicated.**

A detailed design of all the main machine components has been carried out and its results and drawings are now ready to be transferred to the industrial groups that have been identified

as capable of constructing all the components of the machine core. The IGNITOR facility is expected to be operated at the Troitsk site of Rosatom and managed by the IGNIR collaboration between Italy and Russia. At this time the IGNITOR Program is the only one that has retained the objective of investigating the approach and the access to ignition conditions thanks to the regular updates of the machine design that have followed relevant advances in physics, technology and materials. The main machine parameters are included in Table 6.1 [Coppi, et al. (2013)].

Table 6.1: Example of Plasma Parameters [Coppi, et al. (2013)] for an 11 MA Operational Scenario (JETTO Code)

Toroidal plasma current $I_p$ (MA)	11
Toroidal field $B_T$ (T)	13
Major radius $R_0$ (m)	1.32
Minor radius $a \times b$ (m) <sup>2</sup> )	$0.47 \times 0.86$
Elongation $k$	1.83
Triangularity $\delta$	0.4
Plasma volume $V_9$ (m <sup>3</sup> )	10
Central electron temperature $T_{e0}$ (KeV)	11.5
Central ion temperature $T_{i0}$ (KeV)	10.5
Central electron density $n_{e0}$ (m <sup>-3</sup> )	$9.5 \times 10^{20}$
Average electron density $\langle n_e \rangle$ (m <sup>-3</sup> )	$4.8 \times 10^{20}$
Central plasma pressure $p_0$ (MPa)	3.3
Alpha density parameter $n_\alpha^*$ (m <sup>-3</sup> )	$1.2 \times 10^{18}$
Average alpha density $\langle n_\alpha \rangle$ (m <sup>-3</sup> )	$1.1 \times 10^{17}$
Fusion alpha power $P_\alpha$ (MW)	19.2
Plasma stored energy $W$ (MJ)	11.9
OH power $P_{OH}$ (MW)	11.2
ICRF power $P_{ICRH}$ (MW)	0
Bremsstrahlung power loss $P_{brem}$ (MW)	3.9
Poloidal beta $\langle \beta_p \rangle$	0.20
Toroidal beta $\langle \beta_T \rangle$ (%)	1.2
Edge safety factor $q\psi = q\psi(a)$	3.5
Bootstrap current $I_{bs}$ (MA)	0.86
Poloidal plasma current (MA)	$\cong 8.4$
Energy confinement time $\tau_{\alpha, sd}$ (S)	0.05

A major effort in the machine design has been that of producing a plasma column in which a high mean poloidal field  $\overline{B}_p \simeq \sqrt{10}$  T can be reached together with plasma currents  $I_p \simeq 10$ -11 MA while maintaining reasonable safety factors against the onset of macroscopic instabilities (i.e.  $q(\psi_a) \simeq 3.6$ ). The rough arguments for this choice of objectives are as follows: High values of the confinement parameter  $n\tau_E$ ,  $n$  being the particle density and  $\tau_E$  the energy replacement time,

should be reached considering that the maximum particle density should be related to the average current density  $\langle J_{\parallel} \rangle \sim \overline{B}_p/\overline{a}$ , where  $\overline{a}$  is the mean plasma minor radius, and that the confinement time should have a significant dependence on  $I_p$ . Then the maximum values of  $n\tau_E$  should be related to  $\overline{B}_p^2$  as  $I_p \simeq 5\overline{a}\overline{B}_p$ . Moreover, if we consider the mean plasma pressure to be limited by the magnetic pressure  $\overline{B}_p^2/(2\mu_0)$ , the plasma reactivity represented by  $n^2\langle\sigma_f v\rangle \propto n^2T^2$  can be expected to be related to  $\overline{B}_p^4$ . These considerations have in fact been supported by sophisticated numerical simulations that have been carried out by 1+1/2D transport codes [*Coppi, et al.* (2010, 2013), *Airoldi and Cenacchi* (1997)]. In this connection we observe that well-confined plasmas with maximum densities close to  $10^{21} \text{ m}^{-3}$  have been obtained repeatedly by the Alcator line of experiments and, with lower temperatures, by the Large Helical Device machine. To facilitate the attainment of these densities, the adoption, as in the case of the Alcator C experiments, of a pellet injector is planned. In the case of IGNITOR, however, the required pellet speeds are considerably higher and further advances (expected to be possible) in the technology of these injectors are needed.

An important additional criterion that has driven the IGNITOR design process is that of having a strong Ohmic heating that would persist up to temperatures where  $\alpha$ -particle heating can take over. Thus the need for an auxiliary heating system (ICRH is the only feasible option) is minimized together with the deterioration of the energy confinement time that has to be dealt with when Ohmic heating ceases to be significant. Assuming that the loop voltage is about constant, as has been observed experimentally until now, the best criterion to be followed in order to have a strong Ohmic heating rate is to have a major radius with the lowest possible values. An essential requirement to achieve ignition condition is the degree of plasma purity that has to be high as discussed in *Coppi, et al.* (2013). This restricts the spectrum of plasma regimes with which IGNITOR has to operate in order to fulfill its main objectives. Therefore while following the progress made in analyzing various transport regimes the main attention remains devoted to the very high density L-regime discovered originally by Alcator that can be reliably obtained and to the I-regime that continues to be the subject of a series of investigations whose results are promising. In both regimes the observed degrees of purity are well within the limits required for ignition.

#### 6.4.1 Main Components Issues, Assembly and Welding Procedures

A key structural solution that has made the present design of the IGNITOR machine possible, that combines a remarkably low major radius and the ability to produce plasma currents up to 10-11 MA with realistic degrees of stability, is the mechanical collaboration between the central solenoid and the toroidal magnet. This is the so-called “bucking and wedging” of the toroidal magnet coils for their inner vertical legs that are subjected to a radial electromagnetic force toward the (vertical) axis of symmetry. Considering a cross-section on the equatorial plane, with the bucking (against the central solenoid) and wedging solution the coils are subjected to compressional forces both in the radial and tangential directions (see Fig. 6.4).

**“Bucking and Wedging” solution.** The objective is to minimize the unbalance between the principal stress components.

The toroidal magnet system is subdivided into 12 sectors (Fig. 6.4). Each sector contains 20 coils. The outer supporting structure consists of the so-called C-clamps surrounding the toroidal coils with exception of their vertical leg. The total current in the toroidal magnet is 87.12 MA  $\pm$  turn and corresponds to a current of 363 kA in each turn.

The plasma chamber (Fig. 6.2) is a particularly difficult system to design as it has multiple functions, has to operate under different and extreme conditions and most important has to withstand the forces associated with macroscopic disruptions of the plasma column. In fact, the

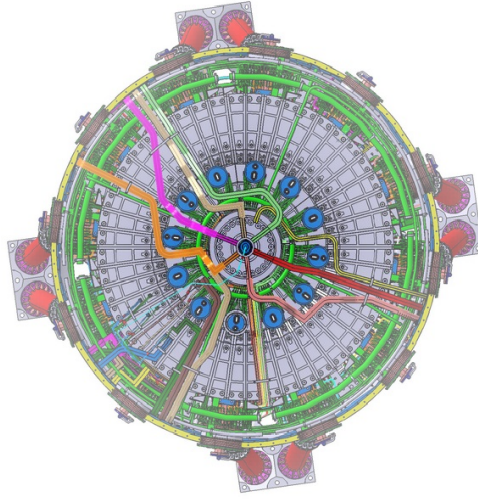


Figure 6.2: View from above the core of the IGNITOR machine. The subdivision of it into 12 modules is evident.

evaluation of both these forces and of the number of the disruptions that can take place during the expected lifetime of the machine is subject to relatively large uncertainties. The thick plasma chamber as designed (with a varying mantle thickness from 2.6 to 5.2 cm) can withstand a limited number of large disruptions that, taking into account the success achieved (in particular by the DIII-D machine) in preventing the development of disruptions at their onset by appropriate feedback systems, can be considered as realistic. The plasma chamber is mechanically supported by the C-clamps and provides the mechanical support for the Molybdenum tiles (actually, a variety of relevant materials is being constantly examined for these) that are in contact with the plasma. As indicated later, the replacement of the tiles during the operating phase of the machine is carried out by a dedicated robotic system.

#### Plasma chamber with access ports.

Given the importance of avoiding stress concentrations and considering other adopted machine design criteria, a great deal of attention has been devoted to preparing a detailed procedure for the various phases of assembly of the machine and for the welding of the plasma chamber. Two important phases are: i) the joining of 30° adjacent sectors, whose main components are a sector of the plasma chamber and the corresponding toroidal field coils and C-clamps package, until a 180° “super sector” is completed. This phase is to be carried out in a specifically equipped site away from the site in which the machine has to be operated; ii) the joining the two 180° super sectors that involves carrying out the final two weldings of the plasma chamber remotely by an appropriate robotic system. Following this joining, the high precision mechanical coupling process of the toroidal magnet with the central solenoid can be undertaken. We note also that the equipment for the assembly of the machine in its different phases has been designed adopting solutions that permit the handling of the very heavy machine components with relative ease [Fig. 6.7]. TIG welding with and without filler material is envisioned to join adjacent sectors of the plasma chamber and to be carried out from the outside.

**Example of equipment designed for the machine assembly.**

### 6.4.2 Robotics Criteria

Robotics is a fundamental element in the construction and operation of the machine: it plays a key role in two phases of the machine life: during its construction, for the closing of the plasma chamber, and during the phase in which experiments are carried out for maintenance operations. Given the different functions and constraints in either case robotics system with different characteristics of operation will be adopted.

During the final machine assembly the closing of the plasma chamber can be performed only using a robot capable of operating through a narrow vertical opening (a diagnostics port) and of performing the delicate welding of the two 180° sectors of the machine. The robot will have to be sufficiently rigid to support the welding equipment and will have to be coupled to sensors and instruments in order to follow the welding path with great accuracy. This is an absolute necessity in order to guarantee the correct positioning of the welding structure and the execution of a weld of the highest quality.

During the operation of IGNITOR a robot with many degrees of freedom will ensure all forms of ordinary and out of the ordinary maintenance, allowing the substitution of damaged antennae and tiles. The robot will have to be able to operate within the plasma chamber through a relatively narrow access port and its path will have to extend through the entire plasma chamber. The robot will carry a “wrist” with 3 degrees of freedom at the least and one or more dedicated grippers that would allow it to perform a sensored and adaptive grip. This is needed in order to secure and unsecure critical elements of the machine structure.

### 6.4.3 Nonlinear Feedback Control Simulations with 3D Structures and Disruption Studies

The nonlinear plasma evolution in presence of conductors is a complex event, which requires in principle extremely detailed models to be developed. Presently, several modeling approaches are available for the analysis of the electromagnetic interaction between the plasma and the conductors [Albanese and Villone (1998), Portone, et al. (2008), Czarny and Huijsmans (2008), Villone, et al. (2010)]. However, none of them can be applied to all cases of interest, due to specific limitations and ranges of applicability. In particular, codes solving linearized plasma equations are conveniently used in the feedback controller design. However, they cannot analyze a nonlinear plasma evolution characterized by large displacements and/or a wide excursion of the relevant plasma parameters. To this purpose, a new computational tool has been developed (CarMaONL [Czarny and Huijsmans (2008)]), that can describe the nonlinear evolution of axisymmetric plasmas through equilibrium points, in the presence of three-dimensional conducting structures. This allows an electromagnetically self-consistent treatment of plasma evolution during all the events for which the usual linearized approximation may be no longer valid. The formulation is in the stream of the CarMa code [Czarny and Huijsmans (2008)], using a coupling surface to describe the electromagnetic interaction between the plasma and the conductors. The mathematical model and the numerical formulation is presented in Villone, et al. (2013). In particular, the 3D passive structures are efficiently modeled by the integral formulation of Villone, et al. (2013). The results of the analysis made for IGNITOR by means of a dedicated upgrade of CarMaONL are presented, including the position-shape current-integrated feedback controller inside the code [Albanese and Rubinacci (1988)].

As a first case, we consider the reference 11 MA scenario, for which a centroid vertical displacement of 3 cm is required, assuming ideal power supplies (no delay, no saturation).

This equilibrium configuration is characterized by a plasma current  $I_p = 11$  MA, poloidal beta  $\beta_p = 0.203$ , internal inductance  $l_i = 0.818$ , radial position of the current centroid  $R_C = 1.299$  m. The plasma region is discretized with a 2D triangular mesh made of 5704 nodes, which coincides with the number of nonlinear equations solved at each time step; the trace of the coupling surface  $\partial\Omega$  is a line made of a set of 309 edges of such triangles, just inside the vacuum chamber.

**Plasma configurations and current densities in 3D structures for the simulation of the control action after imposing an initial centroid vertical displacement of 3 cm at 2.2 ms (top) and at 32.2 ms (bottom).**

In Fig. 6.8, the plasma configurations and current densities in 3D structures at two instants of the simulation of the control action are reported. In Fig. 6.9a we show the vertical position of the plasma current centroid as a function of time, assuming both an axisymmetric plasma linearized model (green) and a nonlinear three-dimensional model, without ports (blue) and with ports (red). These three traces are almost indistinguishable. This result shows that the vertical stabilization controller is resilient to both nonlinear and 3D effects, as any controller tends to

“hide” the differences in open-loop models. Therefore, we can conclude that the vertical position response is not much influenced by nonlinear and 3D effects. As shown in Fig. 6.9b some differences are instead present on the evolution of the radial position that call for a future analysis on the whole plasma shape control. These are small effects anyway, since the vertical controller action has a small undesired influence on radial position, thanks to a good decoupling design.

**Time evolution of the plasma current centroid, assuming an axisymmetric linearized model (green) and a nonlinear three-dimensional model, without ports (blue) and with ports (red): (a) vertical position; (b) radial position.**

The prediction of the plasma disruption features and the evaluation of the EM loads associated with these events, have played a key role in the design of the plasma chamber in the formulation of the machine operation scenarios and the design of in-vessel components as the EM loads produced by these events are by far the largest among those that in-vessel components must withstand. On the basis of experimental data from existing machines, the range of expected variation of the main parameters characterizing disruptions is estimated. That is, the thermal and current quench time, the evolution of plasma current ( $\hat{A}$  and  $l_i$ ), the safety factor limits, the halo current fraction and the radiated heat fraction. The MAXFEA axisymmetric 2D MHD code has been used to evaluate the effects, on the induced currents and the EM loads, of variations of the disruption parameters.

#### 6.4.4 Anomalous transport processes including self-organization for fusion burning regimes in IGNITOR

The most advanced scenario of operation for the IGNITOR experiment refers to a toroidal field on axis  $B_T \approx 13$  T and  $I_p \approx 11$  MA [see *Coppi, et al.* (2013)]. A special version of the JETTO equilibrium transport code [*Airoldi and Cenacchi* (1997)] was developed for the analysis of the plasma regimes to be produced by IGNITOR and employed by considering thermal transport coefficients that include (“profile consistency” [*Coppi* (1980)] criteria and constraints. Then the results (in particular, density and temperature profiles) obtained by applying different models of the electron thermal diffusion have been compared with each other. In these models the ion thermal diffusion is assumed to be represented by a collisional (neoclassical) coefficient, increased by a fraction of the electron diffusion. The first considered model assumes the *Coppi–Mazzucato* (1979) diffusion coefficient to which an appropriate fraction of a coefficient associated with the excitation of the ubiquitous modes [*Coppi, et al.* (1992)] is added.

By operating at optimized plasma parameters ( $\langle n_e \rangle \approx 4.7 \times 10^{20} \text{ m}^{-3}$ ,  $\langle Z_{\text{eff}} \rangle \approx 1.2$ ) ignition is achieved shortly after the end of the current ramp (at  $t = 4.75$  s, where the end of current ramp occurs at  $t = 4$  s). Similar optimized plasma parameters, by using a mixed Bohm–gyroBohm model, lead to obtain a delay of ignition by  $\approx 1.2$  s. The poloidal beta is  $\beta_p \approx 0.2$  in both cases.

More recently the so-called “Coppi–Tang” model, used to predict plasma profiles and parameters for the ITER experiment [*Casper, et al.* (2010)] was applied. In this case ignition is achieved

at  $t = 4.5$  s and the “safety factor”  $q(\psi)$  remains well over unity in the central part of the plasma column. In the following Fig. 6.10 the obtained energy confinement times are compared to the ITER97L scaling.

**Evolution of the energy confinement time evaluated by the JETTO code  $t_E = W_{\text{tot}}/P_{\text{tot}}^*$ , compared to those given by the scalings ITER97L and IPB98, where  $P_{\text{tot}}^* = P_W + P_a + P_{\text{aux}} - dW_{\text{tot}}/dt$ . The adopted thermal energy transport models involve respectively, the so-called Coppi–Mazzucato, Bohm–gyroBohm, and Coppi–Tang transport coefficients.**

#### 6.4.5 Tri-dimensional Structures of the Thermonuclear Instability and Control by ICRH

A surprising result of the most recent theory [Coppi (2014)] of the thermonuclear instability that can take place in D–T plasmas close to ignition is that this develops with tri-dimensional structures emerging from an axisymmetric toroidal confinement configurations. These are helical filaments that are localized radially around a given rational magnetic surface [Coppi (2014)]. Until now well known analyses of the fusion burning process of magnetically confined plasmas have been carried out by  $1 + \frac{1}{2}D$  transport codes. Therefore new analyses, drastically different from the one performed as a first approach to the problem and described in the following, will have to be developed.

The ICRH system is to be used as an independent means to control the plasma temperature, to accelerate the achievement of ignition in the extended first wall configuration with  $B_T = 13$  T/ $I_p = 10 - 11$  MA, and to facilitate the transition to the I-regime in the double X-point plasma configuration ( $B_T = 9 - 13$  T,  $I_p = 6 - 10$  MA). The thermonuclear instability develops at ignition with high-peak densities ( $n_0 \cong 10^{21}$  m $^{-3}$ ), and relatively low temperatures when the complete self-heating of the plasma by the fusion-produced  $\alpha$ -particles takes over. This can lead to an increase of its plasma pressure. Then, internal plasma modes may be excited and saturate the thermonuclear instability at acceptable levels without external intervention.

In the case where an internal process may not be effective, a scenario is considered whereby IGNITOR is led to operate in a slightly subcritical regime, i.e. the plasma parameters are so chosen that the thermonuclear heating power is slightly less than the power lost, and a small fraction of  $^3\text{He}$  is added to the optimal Deuterium–Tritium mixture. The difference between power lost and heating is compensated by additional ICR heating that should be able to energize the minority species (minority ion heating scheme) directly, which can transfer the power to the main plasma species by collisions.

### 6.4.6 H–Regime with Reduced Machine Parameters: Zero–Dimensional Model Analysis

While making extensive use of the JETTO code, we have developed an improved zero–dimensional code solving the relevant thermal energy balance equations, and used it at first for the analysis of operation scenarios in the H–regime at reduced parameters ( $B_T = 8\text{ T}$ ,  $I_p = 5\text{ MA}$ ) referring to a double–null configuration (geometry of the last closed magnetic surface with X–points) and plasma profiles with pedestals at the edge. Access to the H–regime requires an input power  $P_{in} = P_{ohm} + P_{ICRF} + P_\alpha$  higher than a threshold value  $P_{thr}$  for which the expression given by the latest multi–machine ITPA scaling law,  $P_{thr,08}$  [Martin, et al. (2008)], is employed. This condition sets a lower limit in terms of input power on the operating window available. An upper limit is set by the maximum power that the ICRF system can deliver, which is about  $P_{ICRF} \approx 10\text{ MW}$  at the reduced resonant frequency for operation at  $B_T = 8\text{ T}$ . We then find that a somehow limited operating window exists for values of the fusion gain parameter up to  $Q \approx 1$ ; typical values for the central electron density and temperature are  $n_{e0} \approx 3.4 \times 10^{20}\text{ m}^{-3}$  and  $T_{e0} \approx 10.7\text{ KeV}$  respectively. A wider window of operation is obtained if the threshold power for accessing the H–regime is lower than that predicted by  $P_{thr,08}$ . Recent experiments on JET [Maggi, et al. (2014)] with a new metallic beryllium/tungsten) wall have shown a significant reduction of  $P_{thr}$  and how this effect is correlated with low values of  $Z_{eff}$ . A reduction of  $P_{eff}$  may then be expected also for IGNITOR, as is designed to operate at low values of  $Z_{eff}$ .

### 6.4.7 ICRH and Dedicated Diagnostics Systems

ICRH system injecting power in the frequency range  $80 \div 115\text{ MHZ}$  is designed to accelerate the plasma ignition and facilitate the access to high confinement regimes such as the H and I regimes. The reference plant configuration of the system is shown in Fig. 6.11 and the following operation scenarios have been considered: a)  $115\text{ MHz}$ :  $13\text{ T}$ ,  $11\text{ MA}$  full performance scenario; b)  $80\text{ MHz}$ ,  $9\text{ T}$ ,  $6\text{--}7\text{ MA}$  reduced performance scenario.

In order to have high flexibility of operation and to optimize the launch of the RF power into the plasma, the RF system has been conceived with a modular configuration, with each module based on 4 RF generators capable to operate in the frequency range indicated above.

Note that: i) the  $80\text{ MHz}$ ; is the central frequency of the selected generators and around this value the max power obtained by each unit is  $2\text{ MW}$ ; ii) the  $115\text{ MHz}$ ; this frequency is located at the upper side of the generators bandwidth and, consequently, the generated power drops down to  $1\text{ MW}$  per unit.

The ICRH System is based on 2 modules with the following main characteristics:  $N^\circ$  of Generators 8;  $N^\circ$  of Antennas 4; Frequency Range (MHz):  $80 \div 115$ ; Generated RF Power (MW):  $16 \div 8$ ; RF Power at the Plasma  $12.8 \div 6.4$ ; Pulse Length (sec) : 4; Duty Factor:  $1/200$ ; Type of Generators: Cavity Coupled RF Tetrode; Type of Antenna: 4 Current Strap.

One of the most critical issue of the system is the safe transfer of the power to the plasma in presence of vacuum and high VSWR. For this reason the max electrical field in the vacuum region of the transmission line and straps has been limited at 5 kV/cm with the consequent limitation of the power per strap at 400 kW. This value nicely fits the RF generated power in the full performance regime (13 T, 11 MA, 115 MHz, 8 MW at the generators); In the reduced performance regime (9 T, 6-7 MA, 80 MHz, 16 MW at the generators) the availability of the generated power will allow an increase the power per strap up to 800 kW through proper RF conditioning in the critical regions. A full size prototype of the Vacuum Transmission Line (VTL), placed between the port flange and antenna straps, has been manufactured and electrically tested; high voltage tests, at different vacuum and voltage conditions, have been carried out to check the electrical capability of the system with respect to the high voltage (12 kV) and electric field (5 kV/cm), associated with the RF Power and the strong VSWR of the plasma. A precise guiding system of the rigid coaxial cables and an innovative quick latching system have been verified and a perfect fitting with the BeCu spring electrical contacts has been obtained.

**Electrical configuration of the system: the indicator scheme is relevant to 1 module and sketches the main components of the plant and their connections.**

## Dedicated Diagnostics Systems

The Second Harmonic Interferometer (SHI) [*Brandi and Giannanco (2007)*] is adopted for the interferometric measurements of the plasma density as is scarcely sensible to vibrations and mechanical noise. The SHI has been used in the past in various experiments, and is composed of two optical units externally connected through optical fibers and the laser, the detectors and all the electronics can be placed in a separated, shielded room. The positioning of the different harmonic chords is essential so as to ensure that the whole machine is monitored. The SHI includes a section for the measurement of the Faraday rotation along the same path of the integrated electron density measurement.

The plasma ion temperature can be evaluated through high-resolution spectroscopy, by measuring the Doppler broadening of the impurities atomic lines (usually O-IV or O-V). The low concentration of impurities expected in the machine does not represent an insurmountable problem for the current diagnostics technology.

## 6.5 Superconducting Components of the Machine

Intermediate temperature superconducting cables have been adopted for the largest poloidal field coils of IGNITOR. The MgB<sub>2</sub> strands by Columbus Superconductors [*Coppi, et al. (2013)*] can achieve the target specifications for the considered vertical coils, with about 5 meters of outer

diameter and maximum field on the conductor  $< 5 \text{ T}$ . The cable design includes about 300 MgB2 multifilamentary strands of 1 mm in diameter and a copper tube for the He–gas flow in the center. Significant improvements in the design and electrical properties allow higher critical current densities and better current sharing properties between the different strands than previously reported.

## 6.6 The Dynamics of Geomagnetic Storms and Substorms with the WINDMI Model

### OUTLINE

- Brief Description of the WINDMI Model.
- Substorm trigger in the model.
- Periodic Substorms (Sawtooth Events) — Model behavior.
- Isolated Substorms — Parameter values on substorm trigger.

#### WINDMI Model

- An 8-dimensional state space model of the nightside Magnetosphere–Ionosphere
- Nonlinear ODE’s result from the application of conservation laws to global energy components of the system.
- Lumped nonlinear representation of magnetosphere.
- Kinetic effects are included in a simplified manner.

#### WINDMI Model

WINDMI Model The largest energy reservoirs in the magnetosphere–ionosphere system are:

- Plasma ring current energy  $W_{rc}$ .
- Geotail lobe magnetic energy  $W_m$ .
- The R1 FAC associated with the westward auroral electrojet.
- The FAC at the lower latitude closing on the partial ring current.
- Kinetic energy proportional to  $\mathbf{E} \times \mathbf{B}$  perpendicular plasma flows.
- Kinetic energy  $K_{\parallel}$  due to mass flows along magnetic field lines.
- Plasma Sheet thermal energy component  $p_{cps}$ .

WINDMI Model input is  $V_{\text{sw}}$  and Model outputs are  $I_1$  and  $W_{\text{rc}}$

$$L \frac{dI}{dt} = V_{\text{sw}}(t) - V + M \frac{dI_1}{dt} \quad (6.5)$$

$$C \frac{dV}{dt} = I - I_1 - I_{\text{ps}} - \Sigma V \quad (6.6)$$

$$\frac{3}{2} \frac{dp}{dt} = \frac{\Sigma V^2}{\Omega_{\text{cps}}} - u_0 p K_{\parallel}^{1/2} \Theta(u) - \frac{p V A_{\text{eff}}}{\Omega_{\text{cps}} B_{\text{tr}} L_y} - \frac{3p}{2\tau_E} \quad (6.7)$$

$$\frac{dK_{\parallel}}{dt} = I_{\text{ps}} V - \frac{K_{\parallel}}{\tau_{\parallel}} \quad (6.8)$$

$$L_I \frac{dI_1}{dt} = V - V_I + M \frac{dI}{dt} \quad (6.9)$$

$$C_I \frac{dV_I}{dt} = I_1 - I_2 - \Sigma_I V_I \quad (6.10)$$

$$L_2 \frac{dI_2}{dt} = V_I - (R_{\text{prc}} + R_{A2}) I_2 \quad (6.11)$$

$$\frac{dW_{\text{rc}}}{dt} = R_{\text{prc}} I_2^2 + \frac{p V A_{\text{eff}}}{B_{\text{tr}} L_y} - \frac{W_{\text{rc}}}{\tau_{\text{rc}}} \quad (6.12)$$

### WINDMI Physical Parameters

Table 6.2: WINDMI Nominal Parameters, estimated by physical considerations of the state and geometry of the nightside magnetosphere. See Table 6.3 for more parameters.

$L$	90 H	Inductance of the lobe cavity surrounded by the geotail current $I(t)$ . The nominal value is $L = \mu_0 A_\ell / L_x^{\text{eff}}$ in Henries where $A_\ell$ is the lobe area and $L_x^{\text{eff}}$ the effective length of the geotail solenoid.
$M$	1 H	The mutual inductance between the nightside region 1 current loop $I_1$ and the geotail current loop $I$ .
$C$	50000 F	Capacitance of the central plasma sheet in Farads. The nominal value is $C = \rho_m L_x L_z / (B^2 L_y)$ where $\rho_m$ is the mass density in kg/m <sup>3</sup> , $L_x L_z$ is the meridional area of the plasma sheet, $L_y$ the dawn-to-dusk width of the central plasma sheet and $B$ the magnetic field on the equatorial plane. Computations of $C$ are given in <i>Horton (1996)</i> .
$\Sigma$	8 S	Large gyroradius $\rho_i$ plasma sheet conductance from the quasineutral layer of height $(L_z \rho_i)^{1/2}$ about the equatorial sheet. The nominal value is $\Sigma = 0.1(n_e/B_n)(\rho_i/L_z)^{1/2}$ . Computation of $\Sigma$ is given in <i>Horton and Tajima</i> .
$\Omega_{\text{cps}}$	$2.6 \times 10^{24} \text{ m}^3$	Volume of the central plasma sheet that supports mean pressure $p(t)$ , initial estimate is $10^4 R_E^3$ .
$u_0$	$4e - 9 \text{ m}^{-1} \text{ kg}^{-1/2}$	Heat flux limit parameter for parallel thermal flux on open magnetic field lines $q_{\parallel} = \text{const} \times v_{\parallel} p = u_0 (K_{\parallel})^{1/2} p$ . The mean parallel flow velocity is $(K_{\parallel}/(\rho_m \Omega_{\text{cps}}))^{1/2}$ .
$I_c$	$1.78 \times 10^7 \text{ A}$	The critical current above which unloading occurs.
$\alpha$	$8 \times 10^{11}$	The geotail current driven by the plasma pressure $p$ confined in the central plasma sheet. Pressure balance between the lobe and the central plasma sheet gives $B_{\ell}^2 / 2\mu_0 = p$ with $2L_x B_{\ell} = \mu_0 I_{\text{ps}}$ . This defines the coefficient $\alpha$ in $I_{\text{ps}} = \alpha p^{1/2}$ to be approximately $\alpha = 2.8 L_x / \mu_0^{1/2}$ .

### Model Input I

- Measured Solar Wind parameters from ACE.
- Two functions have been found to be most useful and reliable:
- Input Coupling Function 1 (Rectified vBs (kV)):

$$V_{\text{sw}}^{\text{Bs}} = V_0 + v_{\text{sw}} B_s^{\text{IMF}} L_y^{\text{eff}}$$

- Input Coupling Function 2 (in kV)(Newell 2007):

$$\begin{aligned} V_{\text{sw}}^{\text{N}} &= V_0 + \nu_n v_{\text{sw}}^{4/3} B_T^{2/3} \sin^{8/3}(\theta_c/2) \\ V_{\text{sw}}^{\text{NP}} &= V_0 + \nu_{\text{np}} p^{1/2} v_{\text{sw}}^{4/3} B_T^{2/3} \sin^{8/3}(\theta_c/2) \end{aligned}$$

### Model Outputs of the WINDMI model

- The outputs are the AL and  $Dst$  indices, which are compared to ground measurements.
- The AL index from the model is obtained from the region 1 current  $I_1$
- The  $D_{\text{st}}$  signal from the model is partly given by ring current energy  $W_{\text{rc}}$  through the Dessler–Parker–Sckopke relation:

$$Dst_{W_{\text{rc}}} = -\frac{\mu_0}{2\pi} \frac{W_{\text{rc}}(t)}{B_E R_E^3}$$

- The geotail current is compared to the Magnetotail Index (MT Index)(Asikainen JGR 2010) via  $Dst$

### Substorm Mechanism and Control in WINDMI Model

- The trigger function controls when the substorm is initiated:

$$\Theta(u) = \frac{1}{2} \left[ 1 + \tanh \left( \frac{I - I_c}{\Delta I} \right) \right] \quad (6.13)$$

- The character (growth, expansion, recovery phases) is strongly controlled by the first three equations of the model:

$$L \frac{dI}{dt} = V_{\text{sw}}(t) - V + M \frac{dI_1}{dt} \quad (6.14)$$

$$C \frac{dV}{dt} = I - I_1 - I_{\text{ps}} - \Sigma V \quad (6.15)$$

$$\frac{3}{2} \frac{dp}{dt} = \frac{\Sigma V^2}{\Omega_{\text{cps}}} - u_0 p K_{\parallel}^{1/2} \Theta(u) - \frac{p V A_{\text{eff}}}{\Omega_{\text{cps}} B_{\text{tr}} L_y} - \frac{3p}{2\tau_E} \quad (6.16)$$

Table 6.3: WINDMI Nominal Parameters, estimated by physical considerations of the state and geometry of the nightside magnetosphere using the Tsyganenko magnetic field model. See Table 6.2 for other parameters.

$\tau_{\parallel}$	10 min	Confinement time for the parallel flow kinetic energy $K_{\parallel}$ in the central plasma sheet.
$\tau_E$	30 min	Characteristic time of thermal energy loss through earthward and tailward boundary of plasma sheet.
$L_1$	20 H	The self-inductance of the wedge current or the nightside region 1 current loop $I_1(t)$
$C_I$	800 F	The capacitance of the nightside region 1 plasma current loop.
$\Sigma_I$	3 mho	The ionospheric Pedersen conductance of the westward electrojet current closing the $I_1$ current loop in the auroral (altitude $\sim 100$ km, $68^\circ$ ) zone ionosphere.
$R_{\text{prc}}$	0.1 ohm	The resistance of the partial ring current.
$\tau_{\text{rc}}$	12 hrs	The decay time for the ring current energy.
$L_2$	8 H	The inductance of the region 2 current.
$R_{A2}$	0.3 ohm	Resistance of the region 2 footprint in the Auroral Region.
$B_{\text{tr}}$	$5 \times 10^{-9}$ T	The magnetic field in the transition region.
$A_{\text{eff}}$	$8.14 \times 10^{13}$ m <sup>2</sup>	The average effective area presented to the geotail plasma for plasma entry into the inner magnetosphere, estimated to be $2R_E^2$ .
$L_y$	$3.2 \times 10^7$ m	The effective width of the Alfvén layer aperture, estimated to be $5R_E$ .
$\Delta I$	$1.25 \times 10^5$ A	The rate of turn-on of the unloading function.

- Parameters in red are tuned manually in this study.

October 4 2000 Sawteeth Event I

ACE data between 3–7 October 2000

October 4 2000 Sawteeth Event II

See *Spencer et. al.* (2007, 2009) for details. Here  $I_c = 10.5$  MA,  $C = 105000$  F. Using oxygen O2+ with number density 20e6 per cubic meter and magnetic field 18nT gives 107000 F.

Substorm And Pseudo-Breakup Data Set

- *Kalmoni et. al.* (2015) JA021470 use a set of Substorm and Pseudo-Breakup events to study how the growth rate of auroral beads are related to possible instability mechanisms in the near-earth plasma sheet.
- We used the same set of events but studied the substorm energy and triggering conditions using solar wind and IMF as drivers.
- 17 events. Good solar wind data for 13 events. 9 events where triggering with the model is possible.
- Compared model substorm trigger time against auroral observations (Dotted vertical red lines in all figures).
- $\Omega = 10000R_E^3$  ( $100 \times 20 \times 5$ ) for all the results.

28 November 2005 10:08 am

02 October 2008 04:29 am

15 March 2009 04:28 am

07 March 2010 05:15 am

Model Performance On Substorm Data

Table 6.4: WINDMI Model Triggering Conditions And Associated Parameters

Date	Onset (Mdl. Onset) ( $\Delta t$ )	$\Sigma$ [S]	$I_c$ [MA]	$C$ [F]
28/03/2008	05:36 (05:32) (-4)	10	3.7	8000
28/11/2005	10:08 (10:08) (0)	10	4.4	10000
22/02/2006	06:26 (06:36) (+10)	10	3.7	5000
07/03/2007	05:50 (05:47) (-3)	10	3.4	5000
02/10/2008	04:29 (04:23) (-6)	10	4.9	10000
03/01/2009	04:36 (04:24) (-12)	5	3.5	7000
24/02/2009	07:32 (07:26) (-5)	5	2.5	8000
15/03/2009	04:28 (04:24) (-4)	10	3.7	5000
07/03/2010	05:15 (05:25) (+10)	10	3.7	5000

Parameter And Variable Values — Possible Physics

- Fixing the average  $B_z$  in the central plasma sheet, the effective width  $L_y$ , and  $\Omega$ , we can estimate the mass density present in the central plasma sheet from the capacitance values needed to trigger a substorm.
- The perpendicular  $v_E = E \times B$  flow velocity with  $B = B_z = 10\text{ nT}$  goes as  $100\text{ km/s}$  per  $1\text{ mV/m}$  electric field. Need to find consistent satellite data for the average  $E_y$  or  $v_E$ .
- From the geotail current we can track how the curvature  $d\hat{\mathbf{b}}/ds$  changes during the substorm development, which is a condition for ballooning instability.
- We can use the critical current parameter  $I_c$  to estimate the conditions when current driven instabilities may be triggered.
- The pressure gradient current  $I_{ps}$  in the model is an estimate of  $dp/dx$ , which is also related to conditions for ballooning instability.
- Need to track  $\beta = 2\mu_0 nkT/B^2$ .

#### Summary

- Model is able to capture substorms. We can study onset time, possible state of magnetosphere when onset occurs.
- It may be possible to infer triggering  $B_z$  condition if ACE to Earth advance is known more precisely.
- We can track intermediate variables in the model and use them as a proxy to compare to satellite data.
- Previously we used the AL index to train the model. This resulted in the parameters fluctuating somewhat unpredictably.
- Here we used the onset time as identified from auroral observations to constrain the trigger mechanism in the model, and obtained better results.
- Parameter and state variable values in the model could be used to establish bounds for instabilities that trigger substorm onset.

## 6.7 Envisioned High–Field Superconducting Experiments

An important incentive to undertake the analysis of high field superconducting experiments is the recent realization that “hybrid” high–field magnets can be fabricated using two superconducting components: MgB<sub>2</sub> for the “low” field ( $\gtrsim 10\text{ T}$ ) outer part and a high temperature superconductor for the high–field inner part. An evident advantage of an entirely superconducting machine relative

to one like IGNITOR, whose high-field components involve copper magnets, is that the length of the pulse and the duty cycle are not limited by the heating of the coils. For the inner part of the toroidal magnet a helical configuration of the type proposed originally in *Coppi et al.* (1987) can be envisioned. The main function of this is to contribute to magnetic flux variation needed to induce the high toroidal currents ( $I_p \gtrsim 15$  MA) that the considered compact experiments should be able to produce.

The structural analysis of the IGNITOR machine load assembly has been performed taking into account the friction coefficients at the interfaces between the significant components. The finite element ANSYS model was used to analyze the nonlinear mechanical behavior of the structure. The calculation shows stresses within the allowable limits at the operating temperature. Interlaminar shear stresses values on TFC insulation have been validated by the results of test performed by Ansaldo. Two full size IGNITOR TFC turns have been manufactured by Kabel Metal to qualify the fabrication process and the hardening of the material OFHC. Several samples of the cooling channel were machined to validate the Electron Beam (EB) welding process.

IGNITOR structural analysis show that the structural stability of the Load Assembly is assured also during the worst plasma disruptions. The production of the new turn prototypes has allowed to validate the new design concept and to optimize the process in view of the plate series production. This prototype production has been accomplished under a strict quality assurance in order to identify and record any production aspect that may affect cost and quality.

A qualitative model which includes three loops of zonal flow vs. turbulence and turbulence vs pressure gradient is proposed for the experimentally-observed two types of limit Cycle Oscillations (LCOs) and low-intermediate-high (L-I-H) confinement transitions. The experimental evidences supporting the model and revealing the roles of turbulence and pressure-gradient-induced flows in triggering the H-mode at marginal heating power in tokamak plasmas are presented. The dominant role played by pressure-gradient-induced flows in I-phase of type-J LCO as well as I-H transition is demonstrated, along with that done by the turbulent-Reynolds stress-driven zonal flows in the L-I transition as well as I-phase of type-Y LCO. The trigger and conditions for the I-H transition are identified from the experimental observations.

High-confinement mode is essential for realization of magnetic-confinement nuclear-fusion energy application and study of nonlinear transitions among multi-equilibrium states of complex systems, such as tokamak plasmas [*Wagner, et al.* (1982)]. However, the physics mechanism for low-to-high (L-H) confinement transition has not been fairly understood and is still a challenge facing the plasma physics and fusion community.

Two kinds of LCOs have been observed on the HL-2A tokamak when the plasma approaches the H-mode. The first one is a correlation between zonal flow and turbulence. The turbulence firstly drives zonal flow, and then the enhanced zonal flow suppresses the turbulence, which is characterized by the clockwise LCO (Y-LCO) with turbulence leading the zonal flow. The second correlation is between turbulence and the shear flow dominated by pressure gradient. The shear flow firstly enhances and then the turbulence is suppressed, which is characterized by the counter-clockwise LCO (Y-LCO) with the shear flow prior to turbulence. The suppressed turbulence can further make edge pressure gradient steeper and then enhance the poloidal flow. This is a positive feedback, which is necessary for triggering the L-I-H transition.

An important issue has been resolved regarding the potential of ELM control for W exhaust in ITER by modeling the effect on W transport of the nonlinear MHD growth during ELMs. The results have confirmed the initial conjecture that ELMs do not contribute to W exhaust, but rather the opposite, for conditions in which W neoclassical temperature screening dominates at the pedestal between the ELMs. This puts into question the viability of the controlled ELM triggering approach to provide W exhaust over a wide range of ITER H-mode plasmas, particularly those at high  $Q/I_p$  for which the separatrix density needs to be high to provide radiative divertor cooling leading to good W screening in the pedestal.

## 6.8 Linear Mirror Machines and the Field-Reversed Confinement Machines

Linear Mirror Machines developed at the Lawrence Livermore Laboratory in California and in the Budker Institute in Novosibirsk, have unique properties that are complementary to those of the toroidal plasmas.

### 6.8.1 Global simulations of the FRC fusion plasmas

Global Particle-In-Cell (PIC) code, called ANC, with electrostatic drift waves is used in simulations of the electron drift wave turbulence in C-2/C-2U plasmas [Lau, *et al.* (2017)]. The simulations show that turbulence grows up in the SOL and then spreads into the core field-reversed region in the nonlinear steady state through an inverse cascade from  $k_\phi \rho_s$  from the maximum linear growth rates with toroidal mode numbers of 70 to 75 corresponding to  $k_\phi \rho_s \sim 15$  to 20. The turbulence saturates with  $k_\phi \rho_s \sim 5$ -10 in the SOL. In the core the spectrum peaks at  $k_\phi \rho_s \sim 10$  from nonlinear coupling driven by the high level of turbulence in the scrape-off layer. In the saturated state the turbulence peak shifts from the mid-plane to the mirror regions near  $z = +, -2$  m in the SOL. New simulations with nonadiabatic electron dynamics and the Alfvén waves active remain to be performed. The electrostatic drift wave turbulence is consistent with the Doppler Backscatter (DBS) density fluctuation data reported by Schmitz, *et al.* (2016). The fluctuation backscatter diagnostic instrument used to measure the density fluctuations is described in Schmitz *et al.* (2014). The properties of the electrostatic drift waves in the beam driven Field-Reversed Configuration (FRC) are unstable producing a turbulent ion thermal flux. The unstable axial eigenmodes are commute for toroidal mode number  $n = 20$  axial for four machine lengths ranging from  $27R_0$  to  $42R_0$  where  $R_0 = 26.8$  cm is the radius of the central confinement chamber. The  $k_\perp \rho_i = 2.0$  is fixed and the growth rate frequency normalized to  $v_{th,i}/L$  with  $L = 0.4R_0$ . The growth rates range from  $0.0022\Omega_{cp}$  to  $0.0037\Omega_{cp}$  with even and odd mode symmetries about the center of the mirror chamber. There are flute-like modes with even parity and an odd parity modes with respect to the  $z \rightarrow -z$  axial reflection symmetry about  $z \rightarrow -z$ . The maximum mode amplitudes occur well

outside the SOL separatrix and maximum in mirror region beyond the  $B_{\max}$  at  $Z/R = \pm 10$ .

Typical frequency and growth rates are  $\omega = -6v_{thi}/L_s$  and  $\gamma = 1.0$  to  $1.2 v_{vth,i}/L_s$  where  $L_s = 20R_0$  the length of the field line for a typical mode with  $n = 20$  corresponding to  $k_s\rho_i = 0.36$  and  $n = 20$  and  $k_r\rho_i = 0.6$ .

In the closed magnetic field region the magnetic gradient drift is opposite to the diamagnetic drift direction. Outside the magnetic curvature drift is in the same direction as the diamagnetic drift in the outer mid-plane and opposite the diamagnetic drive in the mirror throats. Contour plots of the eigenmode structures are shown in *Bao, et al.* (2019). The maximum amplitude of the axial wave functions is in the “bad” magnetic curvature region in the formation section at  $|z|/R_0 \gtrsim 15$  to  $20$ . The maximum of the wave function is in the two-end formation sections of the long central cell. The formation section is past the end-region mirrors cells and before the divertor end-cell region. The unstable drift waves are only strong in the SOL outside the closed FRC separatrix. The global particle-in-cell code GTC-X with the Alfvén wave coupling gives the details of the plasma waves and transport. The ITG mode is stable inside the magnetic separatrix. The linear electrostatic eigenmode calculations show that the turbulent ion thermal transport is outside the field reversal region.

The impurity effects on Ion Temperature Gradient (ITG) driven instability in Transport Barriers (TBs) are numerically investigated with the gyrokinetic integral eigenmode equations in tokamak plasmas. In particular, the effects of temperature and density gradients of the main ions ( $\varepsilon_{Ti}$  and  $\varepsilon_{ni}$ ) are analyzed independently to understand the physical mechanisms better, instead of keeping their ratio  $\eta_i = \varepsilon_{ni}/\varepsilon_{Ti} = \text{const}$  as carried out in previous works, when the parameters of impurity ions vary. It is found that the effect of impurity ions with outwardly peaked density profiles on ITG modes depends on the competition between the destabilizing effect of the impurity density gradient  $L_{ez}$  and the stabilizing effect induced by the dilution of main ions from impurity ions when  $\varepsilon_{Ti}$  is fixed, which is in significant contrast with the results for a fixed  $\eta_i$ . The destabilizing effects include enhancement of ITG modes and coupling to the Impurity Mode (IM) in weak ITGs (big  $\varepsilon_{Ti}$ ) and strong impurity density gradient regimes. In addition, the stability boundaries for ITG modes, including high-order modes, are discussed in detail, and compared with previous works [*Fröjdahl, et al.* (1992)]. Furthermore, the impurity ions with either inwardly or slightly outwardly peaked density profiles have weaker and stronger stabilizing effects on small and big poloidal wave vector  $k_\theta\rho_s$  modes, respectively. However, the impurity ions with steeper outwardly peaked density profiles have stronger stabilizing effects on big  $k_\theta\rho_s$  modes. Moreover, the inwardly-peaked impurity ion density profiles are beneficial for main ion confinement and impurity decumulation, due to the main (impurity) ions flowing inwardly (outwardly). Finally, analyses of eigenmode structure and the quasilinear particle flux are performed in detail. The results show that impurity ions have non-negligible effects, especially on higher order ITG modes.

### 6.8.2 High pressure-relaxed plasma confinement

High-pressure plasmas with reversed magnetic fields and nonuniform rotational flows are ubiquitous in nature and are produced in Field-Reversed Confinement (FRC) laboratory plasmas

[*Schmitz, et al.* (2016)]. A large toroidal plasma current driven by neutral beam injection and external magnetic field driven by poloidal field coils produce the confinement geometry. The Grad–Shafranov equilibria [*Copenhaver* (1983), *Cerfon and Freidberg* (2010)] describe cylindrical magnetic fields from external field coils and toroidal plasma currents [*Schmitz, et al.* (2014, 2016)]. We describe the ion and electron orbits in the geometry of the Norman FRC machine with 12 external coils and the plasma current. Ions are launched from 8 NBI injectors at 35 KeV for 100 msec producing a  $T_i \sim 2\text{--}3\text{ KeV}$  and  $T_e \sim 500\text{ eV}$  plasma. There is sheared  $\mathbf{E} \times \mathbf{B}$  flow across the outer closed magnetic field lines. The ion orbits become chaotic in the mirroring region where radius of curvature is comparable to ion gyroradius. There are ion orbits called the “butterfly pitch angle” distributions measured in the magnetosphere and chaotic orbits [*Shibahara, et al.* (2010)]. These orbits affect the drift waves and the Alfvén wave stabilization. Analytic theory and 3D computer simulations are used to interpret the results of the measured plasma. A strong radial electric field  $E_r(r, t)$  develops  $\mathbf{E} \times \mathbf{B}$  sheared rotation suppresses the core turbulence.

Turbulence in the scrape-off layer plasma is modified by the nonlinear transverse cascade. The  $p \sim B^2/2\mu_0$  plasma is in a relaxed self-organized state. The turbulence is compared with the density fluctuations measured from X- and O-mode RF wave field scattering data [*Schmitz, et al.* (2016)].

In space physics the generation mechanism of a butterfly Pitch–Angle Distribution (PAD) of energetic ions is demonstrated by test particle simulations in the stretched magnetic field [*Shibahara, et al.* (2010)]. Polar satellites detect some events of the butterfly PADs of the energetic protons  $\gtrsim 80\text{ KeV}$  in the outer ring current region around midnight near the equatorial plane. They were observed at a relatively disturbed time in the inner magnetosphere and the ring current appeared to be developed; that is, magnitude of the magnetic field at the Polar satellite was highly depressed and the adiabaticity of the protons were expected to be violated. To reproduce the butterfly pitch–angle distribution, a test particle simulation in which the first adiabatic invariant  $\mu$  can be monitored are performed. When the radius of the field line becomes comparable to the Larmor radius of a proton, the protons have significant scattering of pitch angle ( $\alpha$ ) due to change of  $\mu$ . This  $\mu$ –scattering process reforms the PADs. Owing to cumulative  $\mu$ –scattering, the flux of the protons ends to have a peak at  $\alpha \sim 40^\circ$  (or  $140^\circ$ ) and collapses at  $\alpha \sim 0^\circ$  (or  $180^\circ$ ) and  $90^\circ$ , which produces butterfly PAD distribution. The computed PAD resembles the butterfly PADs observed by the Polar satellite [*Shibahara, et al.* (2010)]. The nonadiabatic effect is important for not only the generation mechanisms of the butterfly PAD but also the development of the storm–time ring current.

### 6.8.3 Voyager 1 and Voyager 2 Explore the Solar System Over 45 years from 1975 to 2020

The solar wind plasma increases from the sun in the heliosphere plasma is approximately an isothermal expansion due to the rapid electron thermal transport. The speed and Mach numbers are roughly (i) at the Earth 400 km/s with  $M_s = 4$ , and (ii) at Jupiter 800 km/s with  $M_s = 8$ .

Jupiter's magnetic moment  $M_J = 2 \times 10^4$  ME and radius where  $R_J = 7.1 \times 10^4$  km. Jupiter's magnetopause radius is  $R_{mp} \simeq 45 R_J = 3 \times 10^6$  km where  $R_J = 7.1 \times 10^4$  km. The Earth's magnetic moment is  $M_E = 8 \times 10^{15}$  T.m<sup>3</sup>. Jupiter has a high level of relativistic electrons (flux  $> 10^6$  cm<sup>-2</sup>s<sup>-1</sup>) up to 20 MeV in energy. There is strong decimeter wavelength synchrotron radiation from the relativistic electrons in the magnetosphere of Jupiter [Dessler (1983)].

Voyager I and II are now in the vicinity of the heliopause and are searching for the termination shock. At the time of writing in 2005, these spacecraft had not crossed the termination shock at the heliopause separating the interstellar medium from the solar system plasma. Voyager I crossed the magnetopause 2012 and Voyager II crossed the magnetopause in 2018.

Mildly supersonic  $M_s = u/c_s \sim 1.4\text{--}5$  plasma winds are common place in astrophysics and space physics. The winds may be associated with accretion to a central star. Winds occur in the precursor phase to the Type Ia supernova (SNIa) where plasma is pulled into the magnetic white dwarf (WD) from the companion star. Plasma winds are intercepted by neutron stars (NS). After stars are ignited, the stellar wind outflow creates bow shocks at the magnetic planets and at the termination of the stellar outflow where the thermal pressure jumps to match that of the interstellar gas. In the 1990s the heliopause was estimated to be at 110–180 AU and Voyager 1 was expected to be able to observe the accelerated particles when passing through the associated shock.

### 6.8.4 Exploring the Solar System with Voyager 1 and Voyager 2

Voyager 2 did not cross into interstellar space until 2018. Subsequently, five teams of astronomers analyzed the data returned from Voyager 1 and 2 to reconstruct a picture of this boundary in the outer solar system shown in Fig. 6.3.

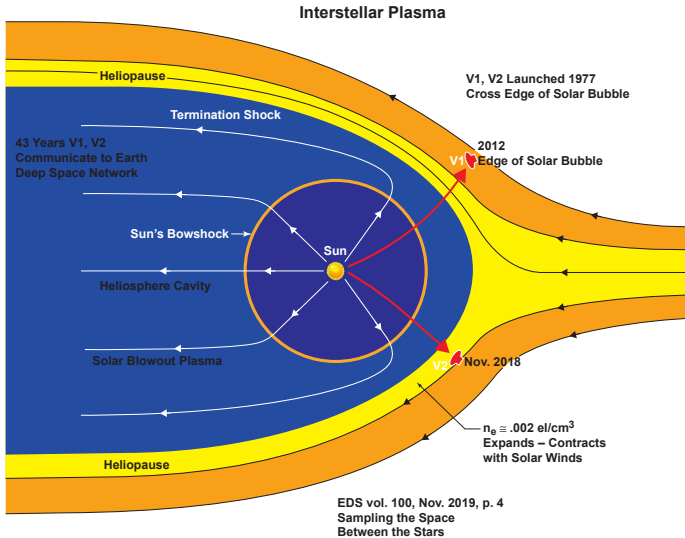


Figure 6.3: This illustration shows the position of NASA's Voyager 1 and Voyager 2 probes outside of the heliosphere. Voyager 1 crossed the heliopause, or the edge of the heliosphere, in August 2012. Heading in a different direction, Voyager 2 crossed another part of the heliopause in November 2018. The lines mark the direction of plasma flow both inside and outside the heliopause. Solar plasma flows in a different direction than the interstellar plasma (NASA/JPL-Caltech).

Four decades after its launch into the outer solar system, Voyager 2 crossed the boundary that separates the Sun's domain from the stuff that floats between the stars. Its crossing on November 5, 2018 happened six years after that of the speedier Voyager 1.

Voyager 1 returned a surprisingly messy view of this outer boundary. In fact, astronomers had a hard time figuring out when the spacecraft had actually made the crossing. Now, Voyager 2 promises a point of comparison. In a dedicated issue of *Nature Astronomy*, astronomers analyze its report from the frontier.

### Far from the Sun

One could argue that neither Voyager has really left the solar system. For example, the Sun's gravity holds the hypothesized shell of icy objects known as the Oort Cloud in orbit at a distance of some 100,000 astronomical units (a.u., the average distance between Earth and the Sun) — far beyond the Voyagers. What the two spacecraft have left behind, however, is the heliosphere, the cavity around the Sun blown out by the solar wind.

Even though the Sun is pouring out charged particles into this bubble, the density of those particles decreases as the square of their distance from the Sun. By the edge of the heliosphere, matter has become incredibly sparse, a mere 0.002 electrons per cubic centimeter, as Donald Gurnett and William Kurth [Gurnett and Kurth (2019)] (both at University of Iowa) report in their study of Voyager 2 data. These particles haven't lost their energy, though, and they remain very hot.

The gas and dust between the stars, on the other hand, is cold and dense. The particles of the interstellar medium, and the magnetic fields they carry, sweep around the heliosphere like ocean waves around a boat. The boundary between the two, known as the heliopause, is by its nature unstable. It “breathes,” expanding when the Sun is more magnetically active and shrinking when the Sun goes quiet.

Wherever the boundary is, scientists expect it to be marked by the same changes: a jump in particle density and a drop in temperature. That is what they were looking for as the Voyagers traveled farther and farther from the Sun.

### A Journey Outward



Figure 6.4: Interactive 3D Spacecraft Model. The identical Voyager spacecraft are three-axis stabilized systems that use celestial or gyro referenced attitude control to maintain pointing of the high-gain antennas toward Earth. The prime mission science payload consisted of 10 instruments (11 investigations including radio science) (NASA/JPL-Caltech).

The Voyagers launched a few weeks apart in 1977 for a grand tour of the outer solar system. Traveling faster, Voyager 1 reached the heliopause first, speeding through the boundary in the northern hemisphere. However, some of its plasma instruments failed in 1980, so scientists had to analyze data from its other working instruments to get readings on what particles in its vicinity were doing. While Voyager 1 reached the edge of the solar bubble on August 25, 2012, scientists didn't fully realize this until a year later.

What made the matter more confusing was that scientists had expected the direction of the magnetic field to change abruptly as Voyager 1 traversed from one particle bath to another. But Voyager 1 saw no change. Was it simply a coincidence that the magnetic field from inside the bubble, which comes from the Sun, had lined up just right with the one from outside the bubble, which comes from the stars?

### Voyager 2’s View of the Heliopause

Like Voyager 1, Voyager 2 crossed the “nose” of the heliosphere — that is, into the flow of interstellar plasma, though Voyager 2 passed through the southern hemisphere. But unlike

Voyager 1, Voyager 2 has five working instruments, including the plasma instrument that failed on Voyager 1. This instrument's reading of a 20-fold jump in density is what confirmed that Voyager 2 had gone beyond the heliopause. The change occurred over only 0.005 a.u.

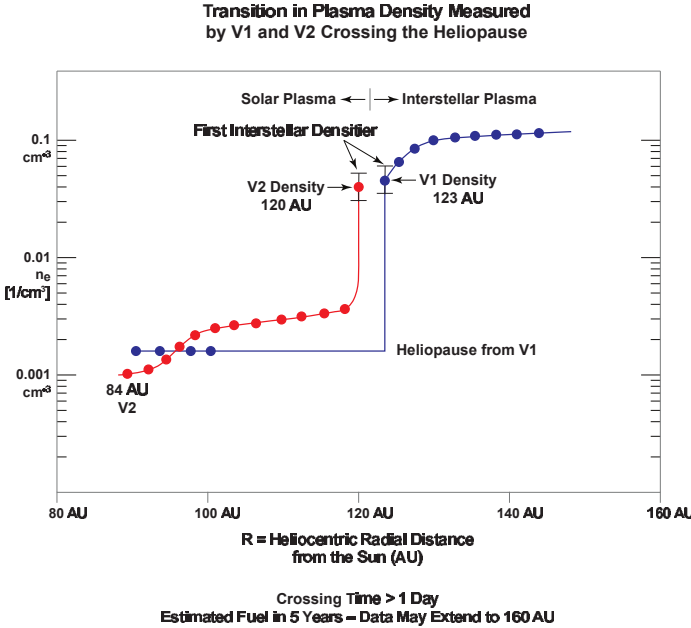


Figure 6.5: Data from Voyager 1 and Voyager 2 during their crossing from the boundary from the magnetosphere called the heliopause into the interstellar plasma. The boundary during the crossing of Voyager 1 — back dashed lines — was more complex at  $\sim 123$  AU and distorted by the solar activity compared than the boundary during the crossing by Voyager 2 — red dots at 120 AU. The overall increase in the plasma density was approximately 100 for both crossings.

Particle number densities versus radial distance from the Sun in astronomical units (AU) is shown in Fig. 6.5. The black dots and lines are from Voyager 1 (V1) and red dots and lines are from Voyager 2 (V2). Densities from plasma oscillations are electron densities from the plasma wave instrument (PWS). Densities in black data are from V1 with the PLS (plasma) instrument are proton densities which are almost the same as the electron densities [Gurnett and Kurth (2019)].

Another marker of the heliopause is a sudden change in the distributions of the energetic particles. The energies of solar wind particles are low compared those beyond the boundary in the galaxy at large. As Voyager 2 crossed through the heliopause, the low-energy ions from the solar wind drop away and were replaced by high energy ions in the galactic cosmic rays. The high-energy ions come from distant supernova explosions.

In contrast to Voyager 1 the Voyager 2 data shows no sudden shift in magnetic field accompanying the changes in particle density. Studies by Leonard Burlaga [Burlaga, et al. (2019)] (NASA Goddard) asserts this there must be some physical process that this is due to the change in the magnetic field across this region that needs further study.

What is interesting is that both spacecraft had crossed the heliopause at roughly the same distance from the Sun: 121.6 and 119 a.u., respectively. Voyager 1 made its crossing when the Sun was nearing a peak in activity, sending out regular “explosions” of plasma and energy from coronal mass ejections. By the time Voyager 2 went across the heliopause the Sun had quieted down. While the heliopause should have “breathed in” during this time, both spacecraft went over the boundary at roughly the same distance from the Sun.

Density measurements show that both spacecraft crossed the heliopause in under a day, yet neither one saw a whole boundary. Voyager 1 saw the outside leaking in [Stone, *et al.* (2019)]. Between the V1 and V2 crossings there were periods when the interstellar plasma had penetrated the heliopause propagating into the heliosphere.

For Voyager 2 the situation was reversed. After its heliopause crossing, the spacecraft V2 was still detecting particles originating in the solar wind showing that magnetospheric plasma was leaking out. Observations from the V1 and V2 crossings show the complexity of the heliopause. Voyager 1 saw a “stagnation region” before the heliopause where ion velocities dropped near zero. In contrast the Voyager 2 data showed multiple boundary layers inside the heliopause. Both spacecraft saw a boundary layer extending at least 10 a.u. past the heliopause — a boundary layer region that is analogous to the boundary layer in the air that forms over an airplane wing or around a ship in a lake or ocean.

Bow plasma waves forming in the heliosphere will travel through the interstellar medium similar to those of from in the atmosphere and lakes. Depending on how fast the solar system travels through the higher density inter stellar plasma this wave would form a be a shock as is the case for the bow shock in front of fighter jets. As the Voyagers continue to zip along at 3 a.u. per year they are expected to reach this shock boundary with working instruments. The estimates are that the Voyagers have another five years of power left. There is time, however, to measure the interstellar medium that is undisturbed by the Sun. Thus one is expecting unique new data on the heliosphere plasma from V1 and V2 for a few more years

Voyager 1 and Voyager 2 were launched by NASA in 1997 to explore our solar system and after 43 years of first exploring the planets from Mercury to Jupiter and Saturn (1980) and then celestial orbiters, especially Jupiter, headed to find the limiting boundaries of the solar system. In the past few years, 2017–2019, the Voyager spacecrafts have been sending data on the plasma in the boundary of our star — the sun–solar system. In 2019 they passed through the solar plasma’s boundary into the interstellar plasma. The plasma measured in crossing the boundary was complex for Voyager 1 and simple for Voyager 2. This boundary was measured to be at a 22 billion km or at 147 AU from Earth on 4 November 2019. Voyager 1 crossed the heliopause in 2012 entering the interstellar plasma.

The path of Voyager spacecraft measured properties of Jupiter, Saturn, Uranus and then a very distant planet-like object named Pluto. Due to the nature of Pluto’s orbit and its unique low-temperature partially-ionized atmosphere, the earlier classification of Pluto as the most distant planet was changed in 2006 to that of a Dwarf Planet. Voyager 1 reported the weather of Pluto and the pair of mobleons that circle Pluto.

Voyager 2 studied Jupiter, Saturn, Uranus and Neptune — the first spacecraft to study these two giant ice planets, and crossed the outer boundary of the Solar System plasma in November

2019.

Jupiter's moon Europa was found to have complex structure by Voyager 2. Europa has a thin ice water crust floating on deep ocean. Three new small satellites were found orbiting Jupiter near the large moon Europa.

Galileo found the four large moons of Jupiter in 1610 with his invention of the telescope and they are named Io, Europa, Ganymede and Callisto. Io has a volcano emission that is of great interest and use for understanding the differential rotation of the plasma surrounding Jupiter. Measurements of the plasma emitted from the Io give an understanding of the plasma rotational velocity and large plasma surrounding and merging with the plasma emitted by the sun. Callisto is the second largest of the moons of Jupiter with Ganymede the largest moon. The largest moon orbiting Saturn is named Titan. Callisto is locked to the rotation of Jupiter with the same side always facing Jupiter and has density just above that of water at  $18\text{ g/cm}^3$ .

## View of the Solar System from Voyager 2

Voyager 2 left the heliosphere on November 5, 2018. While Voyager 2 left the heliosphere six years earlier, the signals from its crossing were complex and difficult to interpret. In contrast, the signals from Voyager 2 were simple and showed monotonic increase in the plasma density from  $0.002\text{ ions/cm}^3$  in the heliosphere to  $0.5\text{ ions/cm}^3$  to, in a period less than one hour, crossing the heliopause to interstellar plasma [Nature Astronomy November 2019.] This shows clearly, as expected, that the plasma between the stars is higher density and colder than inside the heliosphere. The more complex data from the earlier Voyager 1 crossing are now interpreted as there was bulge or plume of interstellar plasma penetrated into the heliosphere plasma on the other side of the path, drawn between the widely-separated exiting points of the two Voyager spacecrafts. The two spacecrafts have several years of travel time in the interstellar plasma on opposite sides of the heliopause [Sky and Telescope, p. 10, February, 2020 and <https://is.gd/voyager2>.

For our Milky Way galaxy the Large Magellanic Cloud is the largest neighboring galaxy and has a large number of hot stars emitting X-rays in a star-forming region of that Galaxy. A new X-ray telescope, EROSITA, is mapping out the locations of the X-ray stars. The expectation is that EROSITA may find thousands of X-ray sources. EROSITA is an X-ray instrument built by the Max Planck Institute for Extraterrestrial Physics in Germany as part of the Russian-German Spektr-RG space observatory, which also carries the Russian telescope ART-XC. It was launched by Roscosmos on 13 July 2019 from Baikonur and deployed in a six-month halo orbit around the second Lagrange point.

### Summary Notes on the Voyager 1 and 2 plasma data

The Voyager encounters with Saturn occurred nine months apart in November 1980 and August 1981. While Voyager 1 was leaving the solar system Voyager 2 completed its encounter with Uranus in January 1986 and with Neptune in August 1989.

The heliosphere may be viewed as a "protective bubble" of particles and magnetic fields

created by the Sun. Voyager 1 crossed this boundary in 2012 while Voyager 2 carries more sophisticated instrumentation that will provide more detailed data on the interstellar space plasma.

Comparing data from different instruments aboard the two spacecraft shows how the plasma moves and changes at the heliopause. Voyager 2 is more than 20 billion kilometers from Earth and it takes about 17 hours for the data to travel from the spacecraft to Earth compared to light traveling from the Sun takes about eight minutes to reach Earth.

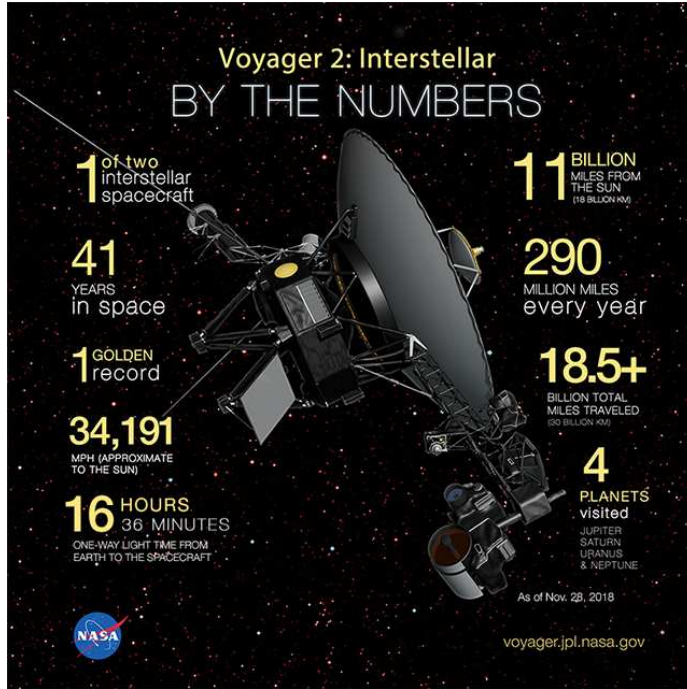


Figure 6.6: An artist's concept of the Voyager 2 spacecraft, with a look at the remarkable numbers from its mission.

In addition to the plasma data, the Voyagers data has given data on the cosmic ray subsystem, the low-energy charged-particle instrument and the magnetometer. Together, the two Voyagers provides new data on how heliosphere interacts with the constant interstellar plasma wind. NASA also is preparing a new upcoming mission called the Interstellar Mapping and Acceleration Probe (IMAP) expected to be launched in 2024. Voyager 1 and Voyager 2 have not yet left the solar system. The boundary of the solar system is considered to be beyond the outer edge of the Oort Cloud, a collection of small objects that are still under the influence of the Sun's gravity. The width of the Oort Cloud is not known precisely, but it is estimated to begin at about 1,000 astronomical units (AU) from the Sun and to extend to about 100,000 AU. One AU is the distance from the Sun to Earth. It would take approximately 300 years for Voyager 2 to reach the inner edge of the Oort Cloud.

The Voyager probes are powered using heat from the decay of radioactive material, contained

in a device called a Radioisotope Thermal Generator (RTG). The power output of the RTGs diminishes by about four watts per year, which means that various parts of the Voyagers, including the cameras on both spacecraft, have been turned off over time to manage power.

Voyager 2 launched in 1977, 16 days before Voyager 1, and both have traveled well beyond their original destinations. The spacecraft were built to last five years and conduct close-up studies of Jupiter and Saturn. Their five-year lifespans have stretched to 41 years. As the spacecraft flew across the solar system, remote-control reprogramming was used to endow the Voyagers with greater capabilities than they possessed when they left Earth.

Voyager's mission controllers communicate with the probes using NASA's Deep Space Network (DSN), a global system for communicating with interplanetary spacecraft. The DSN consists of three clusters of antennas in Goldstone, California; Madrid, Spain; and Canberra, Australia.

The Voyager Interstellar Mission is a part of NASA's Heliophysics System Observatory, sponsored by the Heliophysics Division of NASA's Science Mission Directorate in Washington. JPL built and operates the twin Voyager spacecraft. NASA's DSN, managed by JPL, is an international network of antennas that supports interplanetary spacecraft missions and radio and radar astronomy observations for the exploration of the solar system and the universe. The network also supports selected Earth-orbiting missions. The Commonwealth Scientific and Industrial Research Organization, Australia's national science agency, operate both the Canberra Deep Space Communication Complex, part of the DSN, and the Parkes Observatory, which NASA is using to downlink data from Voyager 2.

### 6.8.5 Analysis of the bimodal nature of solar wind — magnetosphere coupling

Early analysis of auroral substorm and storm data was based on the linear prediction filter relating the solar wind electric field and the geomagnetic activity defined by the AL index. The data was both bimodal and dependent on the level of the magnetosphere activity. Early studies truncated the prediction filter to a five-parameter model containing two low-pass-filtered delta functions of arbitrary amplitude and delay time. Subsequent analysis by *Smith and Horton* (1998) on the nature of the bimodal response developed the five-parameter model to quantify the effects of the level of geomagnetic activity on each of the modes of the filter. All levels of activity, the second mode, occurring at  $\sim 1$  hour, is relatively unchanged. The first mode, however, has a one-parameter dependence on the level of activity in the magnetosphere. The amplitude of the first mode was shown to increase with respect to activity, and this dependence is sufficient to characterize the changing properties of the magnetosphere with respect to the level of the solar wind activity.

### 6.8.6 Real-time predictions of geomagnetic storms and substorms: Use of the Solar Wind Magnetosphere–Ionosphere System model

A low-dimensional plasma physics nonlinear dynamical model of the coupled magnetosphere–ionosphere system, called the Real-Time Solar Wind Magnetosphere–Ionosphere System (WINDMI), is able to predict AL and Dst values approximately one hour before geomagnetic substorm and storm events. Subsequently, the 10-min ground-based measurements compiled by World Data Center, Kyoto, are compared with model predictions (<http://orion.ph.utexas.edu/~windmi/realtim/>). WINDMI model runs are also available at the Community Coordinated Modeling Center (<http://ccmc.gsfc.nasa.gov>). The performance of the Real-Time WINDMI model is quantitatively evaluated for 22 storm/substorm event predictions from February 2006 to August 2008. Three possible input solar wind–magnetosphere coupling functions are used in WINDMI: (i) the standard rectified coupling function, (ii) a function due to Siscoe, and (iii) a function due to Newell. Model AL and Dst predictions are validated using the Average Relative Variance (ARV), Correlation Coefficient (COR), and Root Mean Squared Error (RMSE). The Newell input function yields the best model AL predictions by all three measures (mean ARV, COR, and RMSE), followed by the rectified, then Siscoe input functions. Model AL predictions correlate at least 1 standard deviation better with the AL index data than a direct correlation between the input coupling functions and the AL index. The mean Dst ARV results show better prediction performance for the rectified input than the Siscoe and Newell inputs. The mean Dst COR and RMSE measures do not clearly distinguish between the three input coupling functions.

### 6.9 Private sector company TAE in Irvine, California, linear fusion machine

Private sector company in Irvine, California, linear fusion machine *Norman* and produces record mirror-confined deuterium plasmas through planetary magnetospheres-like processes.

#### Tokamak/Stellarator vs. FRC: Transport and Other Fundamentals (Y. Kishimoto and T. Tajima)

Plasma, highly–nonlinear medium consisting of ions and electrons, exhibits prominent characteristics, self-organization and structure formation, once several conditions are fulfilled. In some cases, they are expected and useful in achieving a purpose, while in some cases, accidental and eliminated. Fusion device, one of the promising plasma applications for future energy resource, is designed so as to minimize macro and microinstabilities in achieving high stability and confinement, so that the characteristics are of specific importance [Horton (1999)]. When we design a device, we usually

reply on the linear aspect, while uncertain whether the characteristics, i.e. the self-organization and structure formation, support the approach or lead contradiction.

Tokamaks and stellarators have strong toroidal magnetic fields and additional magnetic field, i.e. poloidal magnetic field, by plasma current in tokamaks and by external coil in stellarators, so that the latter is more rigid than the former, which possess more freedom in magnetic configuration. Such magnetic structures are designed to have magnetic shear in minimizing various instabilities from the linear aspect while is found to induce the overlap of drift wave “islands” called streamers, i.e. global modes, and causes avalanche-like intermittent bursts leading to self-organized critical transport [Kishimoto, *et al.* (1996)]. This is peculiar to so called L-mode that causes anomalous ion/electron diffusion known as the Bohm transport. A recipe to prevent such anomalous diffusion is to weaken and/or eliminate the magnetic shear by the reversal of magnetic shear or by the annihilation of streamers by the additional electric field generated shear, which leads to high confinement state, e.g. internal transport barrier.

We compare and understand that the presence of null magnetic shear in stellarator enhances its confinement, much the similar way to the above tokamak’s local shearlessness contributing to the enhanced confinement [Ishizawa, *et al.* (2016)]. Namely, through the series of research on fusion devices with strong and then rigid guiding magnetic field, we found a reciprocal relation between linear stability and nonlinear turbulent transport as that the configuration with more unstable smaller magnetic shear plasma provides smaller turbulent transport nonlinearly than that with moderate shear. This suggests that softening the (“rigidness” of the system is of importance for the plasma to be self-organized in keeping higher stability and confinement.

From this viewpoint, high-energy beam assisted FRC [Binderbauer, *et al.* (2015)] is charming system. FRC is devoid of strong shell-like’ fields and thus is bound to be wobbly. First, the FRC core is devoid of magnetic shear (an agent of the radial extended transport channels). Secondly, the core is devoid of the instability driving mechanism of drift wave due to the Finite Larmor Radius (FLR), short electron connection length, and reversed  $\nabla - B$  drift. However, the beam-driven FRC has an entirely additional dimension. The beam introduces the backbone to the overall plasma that makes FRC globally stable, while enhanced FLR due to the beam further solidifies the FRC stability. The additional but not yet well-known robustness of the beam-FRC combo is the principle that the beam-induced waves with high phase velocity cannot destroy the plasma confinement, just similar to the intense wake field not destroying the plasma accelerator. We are planning to check this point by our gyrokinetic code of FRC.

### 6.9.1 Local turbulence measurements in the Large Helical Device by phase contrast imaging

Two-dimensional phase contrast imaging (2D) installed on the Large Helical Device (LHD) is a unique diagnostic for local turbulence measurements. Using a 10.6 micron infrared CO<sub>2</sub> laser and a  $6 \times 8$  channel HgCdTe 2D detector are used. The length of the scattering volume is larger than plasma size. However, the asymmetry of turbulence structure with respect to the magnetic

field and magnetic shear make local turbulence measurements possible. From a 2D image of the integrated fluctuations, the spatial cross-correlation function is estimated using time domain correlation analysis, then, the integrated 2D  $k$ -spectrum is obtained using maximum entropy method.

The 2D  $k$ -spectrum is converted from Cartesian coordinates to cylindrical coordinates. Finally, the angle in cylindrical coordinate is converted to flux surface labels. The fluctuation profile over almost the entire plasma diameter can be obtained at a single moment. The measurable  $k$ -region can be varied by adjusting the detection optics. In the LHD plasma,  $k = 1 - 10 \text{ cm}^{-1}$  fluctuations are measured which is expected region of ion temperature gradient and trapped electron turbulence in LHD. The spatial resolution is 10%–50% of the plasma minor radius [Tanaka, *et al.* (2008)].

## 6.10 Gamma 10 mirror-confined plasmas

The electric potential experiments on GAMMA-10 [Cho, *et al.* (2008)] are consistent with the potential results on the Norman (TAE-x) field-reversed plasmas. The mirror plasma-parameter improvement is essential. The Internal Transport Barrier (ITB) and H-mode pedestal in tokamaks has similar physics enhancing the plasma confinement.

In the central cell of GAMMA-10 the ECH injection raises  $T_e$  from 100 eV to 1000 eV in association with an increase in the ion temperature  $T_i$  from 500 eV to 1 KeV because of a significant reduction of electron drag from KeV electron temperature and the ICH ion heating produced by hot ions in the central cell with  $T_i \sim 1 \text{ KeV}$ . The ECH heating level was  $P_{\text{ECH}} \leq 170 \text{ kW}$  [Pratt and Horton (2006)].

The experiments showed that ECH heating with high-power gyrotrons for bulk electron heating may produce plasma with fusion-grade parameters.

Tandem mirror plasmas show that radial transport barriers can be produced by the use of off-axis ECH electron heating. This off-axis application of the ECH produces a radial electric field profile that controls the electron end losses. A cylindrical shell of high-energy electron is a layer at  $r = 4 - 7 \text{ cm}$  formed from the barrier through the central cell and into the end region. 2 KeV but with low density relative to the bulk electrons. The electron end losses from the layer result in the formation of a positive ambipolar potential and disrupts confining ions locally near  $r = 4-7 \text{ cm}$  because of loss of negatively-charged electrons.

The potential hills in turn make the change in the sign of  $E_r(r)$  at the local peak position of the potential hill near  $r = 4-7 \text{ cm}$ . The  $E_r$  reversal leads to the direction reversal of the sheared  $E_r(r) \times B(z)$  drift flow in the azimuthal (theta) direction at the potential peak radius similar to the Internal Transport Barrier (ITB) in toroidal devices. As a result, turbulence and intermittent vortex-like structures in hot-ion plasmas are suppressed near the reversal layer. Such a sheared  $E_r(r)$  formation and a separation between the internal and outward plasmas due to the layer at  $r = 4-7 \text{ cm}$  [Cho, *et al.* (2008)] results in the enhancement of temperature gradients in the layer. The thermal isolation effects make  $T_e$  and  $T_i$  increase in the internal region in the low-density

plasma layer formed by the ECH barrier.

### 6.10.1 Shearless local ITB transport barriers in tokamaks produced by control of the radial electric field

In tokamaks, internal transport barriers are observed and measured when  $q(r)$  has a minimum  $q_{\min}$ . They are produced by modifications of the toroidal plasma current profile. The internal  $q_{\min}$  surface separates the rational surfaces which reduces particle transport and improves plasma confinement [Marcus, et al. (2019)]. The triggering of the internal transport barriers and their dependence on the plasma profiles is a key nonlinear dynamics problem under current investigation. In tokamaks, internal transport barriers are produced by  $q_{\min}$  from the plasma current profile by modifications of the plasma current profile, which reduces particle transport and improves plasma confinement. Progress to understand this reduction, the triggering of internal transport barriers and its dependence with the plasma profiles is an active research area [Rowan, et al. (2008)]. The onset of shearless invariant curves inside the plasma creates  $q_{\min}$  internal transport barriers. A nonintegrable drift–kinetic model is used to describe particle transport driven by drift waves for large aspect ratio tokamaks to investigate the onset and growth of these internal transport barriers. Currently observed plasma profiles, shearless particle transport barriers can be triggered by properly modifying the  $\Delta E_r$  electric field profile and the influence of nonresonant modes in the barriers onset [Miura, et al. (2017)]. In particular, a broken barrier can be restored by enhancing nonresonant modes  $\Delta\phi_{m,n}(r)$  for  $q(r_0) \neq m/n$  or eliminating  $q = m/n$  surface.

Marcus, et al. (2019) develop the internal  $q_{\min}$  creates the onset of shearless invariant curves inside the plasma which produces an internal transport barrier. A nonintegrable drift–kinetic model is used to describe particle transport driven by drift waves and to investigate the onset of these shearless barriers in tokamaks. Shearless particle transport barriers can be triggered by properly modifying the electric field profiles and the influence of nonresonant modes in the barriers onset [Miura, et al. (2017)]. In particular, the broken barrier can be restored by enhancing the neighboring nonresonant modes, as shown in theory and simulations by Marcus, et al. (2019).

## 6.11 Mirror confinement with expansion grids

Mirror confinement with expansion grids biased to reflect the escaping electrons operates as GDT at Novosibirsk and in the Tri Alpha Company machine in Irvine, California

- 6.12 Private sector companies are pursuing special designs for more affordable fusion power magnetic confinement machines**

# Bibliography

- [1] Airoldi, A. and Cenacchi, G. (1997). Approach to ignition in the IGNITOR experiment, *Nucl. Fusion* **37**, p. 1117, <https://doi.org/10.1088/0029-5515/37/8/I0>.
- [2] Albanese, R. and Rubinacci, G. (1988). Integral formulation for 3D eddy-current computation using edge elements, *IEEE Proc. A.* **135**, pp. 457–462, <https://doi.org/10.1049/ip-a-1.1988.0072>.
- [3] Albanese, R. and Villone, F. (1998). The linearized CREATE-L plasma response model for the control of current, position and shape in tokamaks, *Nucl. Fusion* **38**, p. 723, <https://doi.org/10.1088/0029-5515/38/5/307>.
- [4] Angioni, C. and Peeters, A. G. (2006). Direction of impurity pinch and auxiliary heating in tokamak plasmas, *Phys. Rev. Lett.* **96**, p. 095003, <https://doi.org/10.1103/PhysRevLett.96.095003>.
- [5] Angioni, C., Sertoli, M., Bilato, R., Bobkoy, V., Loarte, A., Ochoukov, R., Odstrcil, T., Pütterich, T., Stober, J. and The ASDEX Upgrade Team. (2017a). A comparison of the impact of central ECRH and central ICRH on the tungsten behaviour in ASDEX Upgrade H-mode plasmas, *Nucl. Fusion* **57**, p. 056015, <https://doi.org/10.1088/1741-4326/aa6453>.
- [6] Angioni, C., Bilato, R., Casson, F. J., Fable, E., Mantica, P., Odstrcil, T., Valisa, M., ASDEX Upgrade Team and JET Contributors. (2017b). Gyrokinetic study of turbulent convection of heavy impurities in tokamak plasmas at comparable ion and electron heat fluxes, *Nucl. Fusion* **57**, p. 022009, <https://doi.org/10.1088/0029-5515/57/2/022009>.
- [7] Bao, J., Lau, C. K., Lin, Z., Wang, H. Y., Fulton, D. P., Detrick, S. and Tajima, T. (2019). Global simulation of ion temperature gradient instabilities in a field-reversed configuration, *Phys. Plasmas* **26**, p. 042506, <https://doi.org/10.1063/1.5087079>.
- [8] Benkadda, S., Verga, A., Tsytovich, V. N. (1995). Influence of dust on drift instability in edge tokamak plasma, *Comm. Plasma Phys. Control. Fusion*, **16**, pp. 321–333, ISSN 0374–2806.
- [9] Binderbauer, M. W., Tajima, T., Steinhauer, L. C., Garate, E., Tuszewski, M., Schmitz, L., Guo, H. Y., Smirnov, A., Gota, H., Barnes, D., Deng, B. H., Thompson, M. C., Trask, E., Yang, X., Putvinski, S., Rostoker, N., Andow, R., Aefsky, S., Bolte, N., Bui, D. Q.,

- Ceccherini, F., Clary, R., Cheung, A. H., Conroy, K. D., Detrick, S. A., Douglass, J. D., Feng, P., Galeotti, L., Giammanco, F., Granstedt, E., Gupta, D., Gupta, S., Ivanov, A. A., Kinley, J. S., Knapp, K., Korepanov, S., Hollins, M., Magee, R., Mendoza, R., Mok, Y., Necas, A., Primavera, S., Onofri, M., Osin, D., Rath, N., Roche, T., Romero, J., Schroeder, H., Sevier, L., Sibley, A., Song, Y., Van Drie, A. D., Walters, J. K., Waggoner, W., Yushmanov, P., Zhai, K., and the TAE Team (2015). A high-performance field-reversed configuration, *Phys. Plasmas* **22**, p. 056110, <http://dx.doi.org/10.1063/1.4920950>.
- [10] Brandi, F. and Giammanco, F. (2007). Versatile second-harmonic interferometer with high temporal resolution and high sensitivity based on a continuous-wave Nd:YAG laser, *Opt. Lett.* **32**, p. 2327, <https://doi.org/10.1364/OL.32.002327>.
- [11] Breizman, B. N. and Aleynikov, P. B. (2017). Kinetics of relativistic runaway electrons, *Nucl. Fusion* **57**, p. 125002, <https://doi.org/10.1088/1741-4326/aa8c3f>.
- [12] Breizman, B. N. Aleynikov, P. B., Fontanilla, A. K., Helander, P., Oliver, H.J. C. and Sharapov, S.E. (2018). The feeder pellets and the killer pellets in a plasma, Talk presented at Joint Varenna–Lausanne International Workshop on Theory of Fusion Plasmas. Varenna. 2018–08–27–2018–08–31.
- [13] Brookman, W. M., Austin, M. E., Gentle, K. W., Petty, C. C., Ernst, D. E., Peysson, Y., Decker, J. and Barada, K. (2017). Experimental measurement of ECH deposition broadening: Beyond anomalous transport, *EPJ Web of Conferences* **147**, p. 03001, <https://doi.org/10.1051/epjconf/201714703001>.
- [14] Burhenn, R., Feng, Y., Ida, K., Maassberg, H., McCarthy, K. J., Kalinina, D., Kobayashi, M., Morita, S., Nakamura, Y., Nozato, H., Okamura, S., Sudo, S., Suzuki, C., Tamura, N., Weller, A., Yoshinuma, M. and Zurro, B. (2009). On impurity handling in high-performance stellarator/heliotron plasmas, *Nucl. Fusion* **49**, p. 065005, <https://doi.org/10.1088/0029-5515/49/6/065005>.
- [15] Casper, T. A., Meyer, W. H., Jackson, G. L., Luce, T. C., Hyatt, A. W., Humphreys, D. A and Turco, F. (2010). Validation of the thermal transport model used for ITER startup scenario predictions with DIII-D experimental data, *Nucl. Fusion* **51**, p. 013001, <https://dx.doi.org/10.1088/0029-5515/51/1/013001>.
- [16] Casson, F. J., Angioni, C., Belli, E. A., Bilato, R., Mantica, P., Odstrelil, T., Pütterich, T., Valisa, M., Garzotti, L., Giroud, C., Hobirk, J., Maggi, C. F., Mylnar, J., Reinke, M. L., *et al.* (2015). Theoretical description of heavy impurity transport and its application to the modeling of tungsten in JET and ASDEX Upgrade, *Plasma Phys. Control. Fusion* **57**, p. 014031 <http://dx.doi.org/10.1088/0741-3335/57/1/014031>.
- [17] Cerfon, A. J. and Freidberg, J. P. (2010). “One size fits all” analytic solutions to the Grad–Shafranov equation, *Phys. Plasmas* **17**, p. 032502, <https://doi.org/10.1063/1.3328818>.

- [18] Charidakos, I., Keramidas, Lingam, M., Morrison, P. J., White, R. L. and Wurm, A. (2014). Action principles for extended magnetohydrodynamic models, *Phys. Plasmas* **21**, p. 092118, <https://doi.org/10.1063/1.4896336>.
- [19] Cho, T., Pastukhov, V. P., Horton, W., Numakura, T., Hirata, M., Kohagura, J., Chudin, N. V. and Pratt, J. (2008). Active control of internal transport barrier formation due to off-axis electron–cyclotron heating in GAMMA–10 experiments, *Phys. Plasmas* **15**, p. 056120, <http://dx.doi.org/10.1063/1.2906262>.
- [20] Copenhaver, C. (1983). Axisymmetric toroidal equilibria with plasma flow, *Phys. Fluids* **26**, p. 2635, <https://doi.org/10.1063/1.864455>.
- [21] Coppi, B. and Mazzucato, E. (1979). Transport of electron thermal energy in high temperature plasmas, *Phys. Letts. A* **71**, p. 337, [http://dx.doi.org/10.1016/0375-9601\(79\)90071-9](http://dx.doi.org/10.1016/0375-9601(79)90071-9).
- [22] Coppi, B. (1980). Nonclassical transport and the ‘principle of profile consistency’, *Comm. Plasma Phys. Control. Fusion (UK)* **5**, pp. 261–269, ISSN:0374–2806.
- [23] Coppi, B., Lanzavecchia, L. and Airoldi, A. (1987). Compact ignition experiments: physics and design issues, *Comm. Plasma Phys. Control. Fusion (UK)* **11**, pp. 47–61, ISSN:0374–2806.
- [24] Coppi, B., Nassi, M. and Sugiyama, E. (1992). Physics basis for compact ignition experiments, *Physica Scripta* **45**, p. 112, <https://dx.doi.org/10.1088/0031-8949/45/2/010>.
- [25] Coppi, B., Airoldi, A., Albanese, R., Ambrosino, G., Berta, S., Bianchi, A., Bombarda, F., Cardinali, A., Cenacchi, G., Chilton, L., Clai, G., Detragiache, P., Faelli, G., Frattolillo, A., Frosi, P., Giunchi, G., Grasso, G.; Mantovani, S., Migliori, S., Penco, R., Pierattini, S., Pironti, A., Pizzicaroli, G., Ramogida, G., Rebusco, P., Rubinacci, G., Sassi, M., Villone, F., Zhou, T.C., Zucchetti, M. (2010). *Near Term Perspectives for Fusion Research and New Contributions by the IGNITOR Program*, pp. 1–12. Proc. 23rd IAEA Fusion Energy Conf. (Daejeon, Republic of Korea) Conf. ID: 38091 (2010) (Vienna: IAEA) Overview Paper OV/P-2.
- [26] Coppi, B., Airoldi, A., Albanese, R., Ambrosino, G., Bombarda, F., Bianchi, A., Cardinali, A., Cenacchi, G., Costa, E., Detragiache, P., De Tommasi, G., DeVellis, A., Faelli, G., Ferrari, A., Frattolillo, A., Frosi, P., Giannanco, F., Grasso, G., Lazzaretti, M., Mantovani, S., Migliori, S., Pierattini, S., Pironti, A., Ramogida, G., Rubinacci, G., Sassi, M., Tayani, M., Tumino, A. and Villone, F. (2013). New developments, plasma physics regimes and issues for the IGNITOR experiment, *Nucl. Fusion* **53**, p. 104013, <https://doi.org/10.1088/0029-5515/53/10/104013>.
- [27] Coppi, B. (2014). Presentation at the Sherwood Theory Meeting, San Diego, CA, April 2014.

- [28] Czarny, O. and Huijsmans, G. (2008). Bézier surfaces and finite elements for MHD simulations, *J. Comput. Phys.* **2277**, pp. 7423–7445, <https://doi.org/10.1016/j.jcp.2008.04.001>.
- [29] D’Ippolito, D. A., Myra, J. R. and Zweben, S. J. (2011). Convective transport by intermittent blob-filaments: Comparison of theory and experiment, *Phys. Plasmas* **18**, p. 060501, <https://doi.org/10.1063/1.3594609>.
- [30] Decker, J., Peysson, Y., Hillairet, J., Artaud, J.-F., Basiuk, V., Becoulet, A., Ekedahl, A., Goniche, M., Hoang, G. T., Imbeaux, F., Ram, A. K. and Schneider, M. (2011). Calculations of lower-hybrid current drive in ITER, *Nucl. Fusion* **51**, p. 073025, <http://dx.doi.org/10.1088/0029-5515/51/7/073025>.
- [31] Decker, J., Peysson, Y. and Coda, S. (2012). Effect of density fluctuations on ECCD in ITER and TCV, *EPJ Web of Conferences* **32**, pp. 01016.1–01016.6, <http://dx.doi.org/10.1051/epjconf/20123201016>.
- [32] Decker, J., Peysson, Y., Artaud, J.-F., Nilsson, E., Ekedahl, A., Goniche, M., Hillairet, J. and Mazon, D. (2014). Damping of lower-hybrid waves in large spectral gap configurations, *Phys. Plasmas* **21**, p. 092504, <http://dx.doi.org/10.1063/1.4894749>.
- [33] Don, et al. (1999).
- [34] Dong, J.-Q., Horton, W., and Dorland, W. (1994). Isotope scaling and  $\eta_i$  mode with impurities in tokamak plasmas), *Phys. Plasmas* **1**, p. 3635, <https://doi.org/10.1063/1.870942>.
- [35] Doyle, E. J., Houlberg, W. A., Kamada, Y., Mukhovatov, V., Osborne, Polevoi, A., Bateman, G., Connor, J. W. Cordey, J. G., Fujita, T., Garbet, X., Hahm, T. S., Horton, L. D., Hubbard, A. E., Imbeaux, F., Jenko, F., Kinsey, J. E., Kishimoto, Y., Li, J., Luce, T. C., Martin, Y., Ossipenko, M., Parail, V., Peeters, A., Rhodes, T. L., Rice, J. E., Roach, C. M., Rozhansky, V., Ryter, F., Saibene, G., Sartori, R., Sips, A. C. C., Snipes, J. A., Sugihara, M., Synakowski, E. J., Takenaga, H., Takizuka, T., Thomsen, K., Wade, M. R., Wilson, H. R., ITPA Transport Physics Topical Group, ITPA Confinement Database and Modeling Topical Group, and ITPA Pedestal and Edge Topical Group. (2007). Chapter 2: Plasma confinement and transport, *Nucl. Fusion* **47**, p. 099801, <http://dx.doi.org/10.1088/0029-5515/47/6/S02>.
- [36] Fontana, M., Porte, L. and Cabrera, P. Molina (2017). Correlation electron cyclotron emission diagnostic in TCV, *Rev. Sci. Instrum.* **88**, p. 083506, <https://doi.org/10.1063/1.4997075>.
- [37] Fontana, M., Porte, L., Coda, S., Sauter, O. and The TCV Team (2018). The effect of triangularity on fluctuations in a tokamak plasma, *Nucl. Fusion* **58**, p. 024002, <https://doi.org/10.1088/1741-4326/aa98f4>.

- [38] Fontanilla, A. K. and Aleynikov, P. B. (2017). Lifetime and universal distribution of seed runaway electrons, *Phys. Plasmas* **24**, p. 112509, <https://doi.org/10.1063/1.5001931>.
- [39] Frójd़h, M., Liljestrom, M. and Nordman, H. (1992). Impurity effects on  $\eta_i$  mode stability and transport, *Nucl. Fusion* **32**, p. 419, <https://doi.org/10.1088/0029-5515/32/3/I06>.
- [40] Fülöp, T. and Nordman, H. (2009). Turbulent and neoclassical impurity transport in tokamak plasmas, *Phys. Plasmas* **16**, p. 032306, <https://doi.org/10.1063/1.3083299>.
- [41] Futatani, S., Horton, W., Benkadda, S., Bespamyatnov, I. O. and Rowan, W. L. (2010). Fluid models of impurity transport via drift wave turbulence, *Phys. Plasmas* **17**, p. 072512, <http://dx.doi.org/10.1063/1.3459062>.
- [42] Goniche, M., Artaud, J. F., Bourdelle, C., Bucalossi, J., Desgranges, C., Delpech, L., Devynck, P., Dumont, R., Ekedahl, A., Fedorczak, N., Garcia, J., Gil, C., Gunn, J., Klepper, C. C., Maget, P., Mazon, D., Meyer, O., Morales, J., Moreau, Ph., Nouilletas, R., Peysson, Y., Regal-Mezin, X., Reux, C., Saint-Laurent, F., Vezinet, D. and the WEST Team (2019). First Lower Hybrid Current Drive experiments on the WEST tokamak, preprint.
- [43] Guo, W., Wang, L. and Zhuang, G. (2017). Impact of impurities on zonal flow driven by trapped electron mode turbulence, *Nucl. Fusion* **57**, p. 126052, <https://orcid.org/0000-0002-5881-6139>.
- [44] Hoang, G. T., Horton, W., Bourdelle, C., Hu, B., Garbet, X. and Ottaviani, M. (2003). Analysis of the critical electron temperature gradient in Tore Supra, *Phys. Plasmas* **10**, pp. 405–413, <http://dx.doi.org/10.1063/1.1534113>.
- [45] Hong, S.-H. Hong, Kim, K.-M., Song, J.-H., Bang, E.-N., Kim, H.-T., Lee, K.-S., Litnovsky, A., Hellwig, M., Seo, D. C., Lee, H. H., Kang, C. S., Lee, H.-Y., Hong, J.-H., Bak, J. G., Kim, H.-S., Juhn, J.-W., Son, S.-H., Kim, H.-K., Douai, D., Grisolía, C., Wu, J., Luo, G.-N., Choe, W.-H., Komm, M., Van Den Berg, M., De Temmerman, G. and Pitts, R. (2015). Toward Tungsten Plasma-Facing Components in KSTAR: Research on Plasma-Metal Wall Interaction, *Fusion Sci. Tech.* **68**, pp. 36–43, <https://doi.org/10.13182/FST14-897>.
- [46] Horton, W. and Rowan, W. (1994). Impurity transport studies in the Texas Experimental Tokamak (TEXT), *Phys. Plasmas* **1**, p. 901, <http://dx.doi.org/10.1063/1.870749>.
- [47] Horton, W. (1999). Drift waves and transport, *Rev. Mod. Phys.* **71**, p. 735, <http://dx.doi.org/10.1103/RevModPhys.71.735>.
- [48] Horton, W., Zhu, P., Hoang, G. T., Aniel, T., Ottaviani, M. and Garbet, X. (2000). Electron transport in Tore Supra with fast wave electron heating, *Phys. Plasmas* **7**, pp. 1494–1511, <http://dx.doi.org/10.1063/1.873969>.

- [49] Horton, W., Goniche, M., Peysson, Y., Decker, J., Ekedahl, A. and Litaudon, X. (2013). Penetration of lower-hybrid current drive waves in tokamaks, *Phys. Plasmas* **20**, p. 112508, <http://dx.doi.org/10.1063/1.4831981>.
- [50] Horton, W., Brookman, M., Goniche, M., Peysson, Y. and Ekedahl, A. (2017). RF Heating Technology Workshop and US/JAPAN Workshop on RF Physics, *High-frequency RF waves in lower-hybrid current drive* Santa Monica, California, USA, Sept. 5–8, 2017.
- [51] Horton, W. (2018). *Turbulent Transport in Magnetized Plasmas*, 2nd Edition (World Scientific, 2018), ISBN:978-981-3225-86-6.
- [52] Houshmandyar, S., Yang, Z. J., Phillips, P. E., Rowan, W. Hubbard, A. E., Rice, J. E., Hughes, J. W. and Wolfe, S. M. (2016). Temperature gradient scale length measurement: A high-accuracy application of electron cyclotron emission without calibration, *Rev. Sci. Instrum.* **87**, p. 11E101, <https://doi.org/10.1063/1.4955297>.
- [53] Houshmandyar, S., Yang, Z. J., Liao, K. T., Zhao, B., Phillips, P. E., Rowan, W. L., Cao, N., Ernst, D. R. and Rice, J. E. (2017). Electron profile stiffness and critical gradient length studies in the Alcator C-Mod Tokamak, *Division of Plasma Physics Meeting JP11.00092*, <http://meetings.aps.org/link/BAPS.2017.DPP.JP11.92>.
- [54] Houshmandyar, S., Austin, M. E., Brookman, M. W., Liu, Y., Rowan, W. L. and Zhao, H. (2018). Variable location channels to improve efficiency and precision for direct  $\nabla T_e$  measurements and high spatial resolution  $T_e$ -profile measurements using electron cyclotron emission, *Rev. Sci. Instrum.* **89**, p. 10H109, <https://doi.org/10.1063/1.5035429>.
- [55] Ishizawa, A., Nakamura, Y. and Kishimoto, Y., 26th IAEA Fusion Energy Conference, IAEA CN-234, 17–22 October 2016, Kyoto International Conference Center, Takaragaike, Sakyo-ku, Kyoto 606-0001 Japan.
- [56] ITER Physics Expert Groups on Confinement and Transport and Confinement Modeling and Database, ITER Physics Basis Editors, and ITER EDA. (1999). *Nucl. Fusion* **39**, p. 2175, <http://epub.iaea.org/fusion>.
- [57] Kim, Chang-Bae, An, Chan-Yong and Byunghoon, M. (2019). Reduction of edge plasma turbulence via cross-phase decrease by zonal fields, *Plasma Phys. Control. Fusion* **61**, p. 085024, <https://doi.org/10.1088/1361-6587ab2973>.
- [58] Kishimoto, Y., Tajima, T., Horton, W., LeBrun, M. J. and Kim, J-Y. (1996). Theory of self-organized critical transport in tokamak plasmas, *Phys. Plasmas* **3**, pp. 1289–1307, <http://dx.doi.org/10.1063/1.871754>.
- [59] Lau, C. K., Fulton, D. P., Holod, I., Lin, Z., Binderbauer, M., Tajima, T. and Schmitz, L. (2017). Drift-wave stability in the field-reversed configuration, *Phys. Plasmas* **24**, p. 082512, <https://doi.org/10.1063/1.4993630>.

- [60] Li, L., Liu, Y., Loarte, A., Pinches, S., Polevoi, A. R., Liang, Y. and Zhong, F. (2019). Modeling 3D plasma boundary corrugation and tailoring toroidal torque profiles with RMP fields in ITER, *Nucl. Fusion*, Accepted manuscript, <https://doi.org/10.1088/1741-4326/ab2bca>.
- [61] Liewer, P. C. (1985). Measurements of microturbulence in tokamaks and comparisons with theories of turbulence and anomalous transport, *Nucl. Fusion* **25**, p. 543, <https://doi.org/10.1088/0029-5515/25/5/004>.
- [62] Loarte, A., Polevoi, A. R., Weyens, T., Liu, Y. Q., Li, L., Huijsmans, G. T. A., Artola, J., van Vugt, D. C., Liu, F., Sanchez, R., Reynolds-Barredo, J. M., Tribaldos, V., Medvedev, S. Y. and Futatani, S. (2018). Advances in modeling of plasma pedestal behaviour and ELM control in ITER reference plasma scenarios, Paper presented at 27th IAEA Fusion Energy Conference (FEC 2018), Gandhinger, India, <https://www.persistent-identifier.nl/urn:nbn:nl:ui:25-2eedee3e-5ff1-4be7-be96-68d8b289f567>.
- [63] Lüst, R. (1960). Magnetofluid dynamic shock waves, *Rev. Mod. Phys.* **32**, p. 706, <https://doi.org/10.1103/RevModPhys.32.706>.
- [64] Marcus, F. A., Roberto, M., Caldas, I. L., Rosalem, C. and Elskens, Y. (2019). Influence of the radial electric field on the shearless transport barriers in tokamaks, *Plasma Phys.* **26**, p. 022302, <https://doi.org/10.1063/1.5071437>.
- [65] Martin, Y. R., Takizuka, T. and the ITPA CDBM H-mode Threshold Database Working Group. (2008). Power requirement for accessing the H-mode in ITER, *J. Phys: Conference Series* **123**, p. 101033, <https://doi.org/10.1088/1742-6596/123/1/012033>.
- [66] Michoski, C., Horton, W., Tamura, N. (2017), IFS Report.
- [67] Michoski, C. and Horton, W. (2019), IFS Report.
- [68] Miura, H., Zheng, L. and Horton, W. (2017). Numerical simulations of interchange/tearing instabilities in 2D slab with numerical model for edge plasma, *Phys. Plasmas* **24**, p. 092111, <http://dx.doi.org/10.1063/1.4993962>.
- [69] Miura, H., Miyazaki, J., Ide, M., Miyagi, D., Tsuda, M. and Yokoyama, S. (2018). Estimation method of optimal amount of overshooting current for temporal uniform magnetic field in conduction-cooled HTS coils, *IEEE Trans. on Appl. Superconductivity* **28**, pp. 1–5, <https://doi.org/10.1109/TASC.2018.2805688>.
- [70] Moradi, S., Fülöp, T., Mollen, A. and Pusztai, I. (2011). A possible mechanism responsible for generating impurity outward flow under radio frequency heating, *Plasma Phys. Control. Fusion* **53**, p. 115008, <https://doi.org/10.1088/0741-3335/53/11/115008>.
- [71] Moradi, S., Pusztai, I., Mollen, A. and Fülöp T. (2012). A possible mechanism responsible for generating impurity outward flow under radio frequency heating, *Plasma Phys. Control. Fusion* **53**, p. 115008, <https://doi.org/10.1088/0741-3335/53/11/115008>.

- [72] Nakamura, Y., Kobayashi, M., Yoshimura, S., Tamura, N., Yoshinuma, M., Tanaka, K., Suzuki, C., Peterson, B. J., Sakamoto, R., Morisake, T. and the LHD Experiment Group (2014). Impurity shielding criteria for steady-state hydrogen plasmas in the LHD, a heliotron-type device, *Plasma Phys. Control. Fusion* **56**, p. 075014, <https://doi.org/10.1088/0741-3335/56/7/075014>.
- [73] Nakamura, Y., Tamura, N., Kobayashi, M., Yoshimura, S., Suzuki, C., Yoshinuma, M., Goto, M., Motojima, G., Nagaoka, K., Tanaka, K., Sakamoto, R., Peterson, B. J., Ida, K., Osakabe, M., Morisake, T. and the LHD Experiment Group (2017). A comprehensive study on impurity behavior in LHD long pulse discharges, *Nucl. Mat. Energy* **12**, pp. 124–132, <https://doi.org/10.1016/j.nme.2016.11.005>.
- [74] Ning, Z-X., Zhang, H-G., Zhu, X-Ming., Ouyang, L., Liu, X-Y., Jiang, B-H. and Yu, Da-R. (2018). 10000 Ignition-Cycle Investigation of a LaB6 Hollow Cathode for 3–5-Kilowatt Hall Thruster, *ARC* **35**, <https://doi.org/10.2514/1.B37192>.
- [75] Onishchenko, O. G., Onishchenko, O., Pokhotelov, O. A., Horton, W., Smolyakov, A., Kaladze, T., Kaladze, T. and Fedun, V. (2014). Rolls of the internal gravity waves in the Earth's atmosphere, *Annales Geophysicae* **32**, pp. 181–186, <https://doi.org/10.5194/angeo-32-181-2014>.
- [76] Peysson, Y., Decker, J., Morini, L. and Coda, S. (2011). RF current drive and plasma fluctuations, *Plasma Phys. Control. Fusion* **53**, p. 124028, <http://dx.doi.org/10.1088/0741-3335/53/12/124028>.
- [77] Peysson, Y., Decker, N. E., Atraud, J.-F., Ekedah, A., Goniche, M., Hillairet, J., Ding, B., Li, M., Bonoli, P. T., Shiraiwa, S. and Madi, M. (2016). Advances in modeling of lower-hybrid current drive, *Plasma Phys. Control. Fusion* **58**, p. 044008, <https://doi.org/10.1088/0741-3335/58/4/044008>.
- [78] Portone, A., Villone, F., Liu, Y., Albanese, R. and Rubinacci, G. (2008). Linearly perturbed MHD equilibria and 3D eddy current coupling via the control surface method, *Plasma Phys. Control. Fusion* **50**, p. 085004, <https://doi.org/10.1088/0741-3335/50/8/085004>.
- [79] Pratt, J. and Horton, W. (2006). Global energy confinement scaling predictions for the kinetically-stabilized tandem mirror, *Phys. Plasmas* **13**, p. 042513, <http://dx.doi.org/10.1063/1.2188913>.
- [80] Rowan, W. L., Bespamyatnov, Igor O. and Fiore, C. L. (2008). Light impurity transport at an internal transport barrier in Alcator C-Mod, *Nucl. Fusion* **48**, p. 105005, <https://doi.org/10.1088/0029-5515/48/10/105005>.
- [81] Schmitz, L., Ruskov, E., Deng, B. H., Gota, H., Gupta, D., Tuszewski, M., Douglass, J., Peebles, W. A., Binderbauer, M. and Tajima, T. (2014). Multi-channel Doppler backscattering measurements in the C-2 field reversed configuration, *Rev. Sci. Instr.* **85**, p. 11D840, <https://doi.org/10.1063/1.4891415>.

- [82] Schmitz, L., Ruskov, E., Deng, B. H., Binderbauer, M., Tajima, T., Gota, H., Tuszewski, M. and the TAE Team Control of ion gyroscale fluctuations via electrostatic biasing and sheared  $\mathbf{E} \times \mathbf{B}$  flow in the C-2 field-reversed configuration (2016). *AIP Conf. Proc.*, p. 1721, <http://dx.doi.org/10.1063/1.4944018>.
- [83] Sertoli, M., Angioni, C., Dux, R., Neu, R., Pütterich, Igochine, V. and the ASDEX Upgrade Team. (2011). Local effects of ECRH on argon transport in L-mode discharges at ASDEX Upgrade, *Plasma Phys. Control. Fusion* **53**, p. 035024, <https://doi.org/10.1088/0741-3335/53/3/035024>.
- Sertoli, M., Dux, R., Pütterich and the ASDEX Upgrade Team. (2015). Modification of impurity transport in the presence of saturated  $(m, n) = (1, 1)$  MHD activity at ASDEX Upgrade, *Plasma Phys. Control. Fusion* **57**, p. 075004, <https://doi.org/10.1088/0741-3335/57/7/075004>.
- [84] Shen, Y., Dong, J-Q., Han, M. K., Sun, A. P. and Shi, Z. B. (2016). Isotope effects on instabilities driven by ion temperature gradient and tungsten ions in tokamak plasmas, *Nucl. Fusion* **58**, p. 076007, <https://doi.org/10.1088/1741-4326/aabcf9>.
- [85] Shen, Y., Dong, J-Q., Sun, A. P., Qu, H. P., Lu, G. M., He, Z. X., He, H. D. and Wang, L. L. (2016b). Isotope effects of trapped electron modes in the presence of impurities in tokamak plasmas, *Plasma Phys. Control. Fusion* **58**, p. 045028, <https://doi.org/10.1088/0741-3335/58/4/045028>.
- [86] Shen, Y., Dong, J-Q., Han, M. K., Sun, A. P. and Shi, Z. B. (2018). Isotope effects on instabilities driven by ion temperature gradient and tungsten ions in tokamak plasmas, *Nucl. Fusion* **58**, p. 076007, <https://doi.org/10.1088/1741-4326/aabcf9>.
- [87] Shibahara, K., Nosé, M., Fritz, T. A. and Niehof, J. (2010). A new generation mechanism of butterfly pitch angle distributions of energetic ions: Multiple pitch angle scattering in the stretched magnetic field, *J. Geophys. Res.: Space Physics* **115**, p. A07229, <https://doi.org/10.1029/2010JA015281>.
- [88] Smith, J. P. and Horton, W. (1998). Analysis of the bimodal nature of solar wind-magnetosphere coupling, *J. Geophys. Res. Space Phys.* **103**, pp. 14917–14923, <https://doi.org/10.1029/97JA02861>.
- [89] Tanaka, K., Michael, C. A., Vyacheslavov, L. N., Sanin, A. L., Kawahata, K., Akiyama, T., Tokuzawa, T. and Okajima, S. (2008). Two-dimensional phase contrast imaging for local turbulence measurements in large helical device, *Rev. Sci. Instrum.* **79**, p. 10E702, <http://dx.doi.org/10.1063/1.2988821>.
- [90] Tang, W. M. (1978). Microinstability theory in tokamaks, *Nucl. Fusion* **18**, p. 1089, <https://doi.org/10.1088/0029-5515/18/8/006>.

- [91] Tang, W. M., Bretz, N. L., Hahm, T. S., Lee, W. W., Perkins, F. W., Redi, M. H., Rewoldt, G., Zarnstorff, M. C., Zweben, S. J., Sydora, R. D., Dawson, J. M., Decyk, V. K., Naitou, H., Kamimura, T. and Abe, Y. (1989). Theoretical studies of enhanced confinement properties in tokamaks, *Plasma Phys. Control. Nucl. Fusion* **2**, 13 pp., <https://doi.org/10.2172/6527283>.
- [92] Troung, D. D. and Austin, M. E. (2014). High spatial resolution upgrade of the electron cyclotron emission radiometer for the DIII-D tokamak, *Rev. Sci. Instrum.* **85**, p. 11D814, <https://doi.org/10.1063/1.4889737>.
- [93] Villone, F., Barbato, L., Mastrostefano, S. and Ventre, S. (2013). Coupling of nonlinear axisymmetric plasma evolution with three-dimensional volumetric conductors, *Plasma Phys. Control. Fusion* **55**, p. 095008, <https://doi.org/10.1088/0741-3335/55/9/095008>.
- [94] Wade, M. R., Houlberg, W. A. and Baylor, L. R. (2000). Experimental confirmation of impurity convection driven by the ion-temperature gradient in toroidal plasmas, *Phys. Rev. Lett.* **84**, p. 292, <https://doi.org/10.1103/PhysRevLett.84.282>.
- [95] Wagner, F., Becker, G., Behringer, K., Campbell, D., Eberhagen, A., Engelhardt, W., Fussmann, G., Gehre, O., Gernhardt, J., Gierke, G. V., Haas, G., Huang, M., Karger, F., Keilhacker, M., Klüber, O., Kornherr, M., Lackner, K., Lisitano, G., Lister, G. G., Mayer, H. M., Meisel, D., Müller, E. R., Murmann, H., Niedermeyer, H., Poschenrieder, W., Rapp, H., Röhr, H., Schneider, F., Siller, G., Speth, E., Staebler, A., Steuer, K. H., Venus, G., Vollmer, O. and Yü, Z. (1982). Regime of improved confinement and high beta in neutral-beam-heated divertor discharges of the ASDEX Tokamak, *Phys. Rev. Lett.* **49**, pp. 1408–1412, <http://dx.doi.org/10.1103/PhysRevLett.49.1408>.
- [96] Wu, T., Nie, L., Xu, M., Yang, J., Chen, Z., Shi, Y., Wang, N., Li, D., Ke, R., Yu, Y., Gong, S., Long, T., Chen, Y., Liu, B. and J-TEXT Team 2. (2019). Effect of resonant magnetic perturbation on boundary plasma turbulence and transport on J-TEXT tokamak, *Plasma Sci. Technol.* **21**, p. 125102, <https://doi.org/10.1088/2058-6272/ab4369>.
- [97] Yamoto, S., Bonnin, X., Homma, Y., Inoue, H., Hoshino, K., Hatayama, A. and Pitts, R. A. (2017). Kinetic modeling of high- $Z$  tungsten impurity transport in ITER plasmas using the IMPGYRO code in the trace impurity limit, *Nucl. Fusion* **57**, p. 116051, <https://doi.org/10.1088/1741-4326/aa7fa6>.

# **Chapter 7**

## **Future for Fusion Power Machines**

### **7.1 Building small stars for producing power by “burning” hydrogen isotopes**

The effort to build plasma machines reproducing the methods of stars for producing power by “burning” hydrogen isotopes is progressing worldwide with an increasing number of machine designs. The tokamak approach used in the ITER machine is currently be tested in an international partnership in new facility on a mesa plateau near Aix en Provence, France. Next to the ITER site is the classified French nuclear power laboratory that builds the fission reactors used around the world in many countries.

### **7.2 The ITER machine will show “The Way”**

ITER is a name adopted from Latin to describe “the Way”. The meaning is that the International Toroidal Energy Reactor is the way to produce the first nuclear fusion power reactor. Mankind is attempting to reproduce mother nature’s way to vast, clean nuclear energy sources with plasmas confined by magnetic fields in large toroidal vacuum vessels. The search for best confinement vessels started as classified work under the Sherwood project in the USA and top secrete classified efforts in the Soviet Union and England until an international declassification agreement was reached in 1970s.

### **7.3 Solar nuclear burning fusion plasmas**

Solar nuclear burning fusion plasmas produce helium as the ash and high-energy neutrons that rapidly decay or combine to form heavier elements. The process produces a low level of radioactive

waste in contrast to fission nuclear reactions.

## 7.4 Complex magnetic fields configurations

In nature, like in our Sun and other stars, complex magnetic fields configurations develop from the electromagnetic dynamics of the high temperature rotating plasmas and the pull of gravity. In the laboratory scientists and engineers are developing complex magnetic geometries to achieve the confinement and burning of the low mass nuclear elements from lithium, beryllium, and boron to form carbon as the exhaust materials. The fusion nuclear reactions are hundreds of times stronger than the fission nuclear reactions and produce a much safer exhaust — helium — than the fission nuclear reactors that produce.

Nuclear fusion machines are complicated owing to the need to isolate the solar temperature plasmas and even higher temperature plasmas — from the machine walls and to absorb the very high energy neutrons admitted in the nuclear fusion reactions.

## 7.5 Isolating the burning plasma from the walls

Isolating the burning plasma from the walls of the confinement machine remains a challenging issue. Producing the controlled burning fusion of plasma is a critical problem for the next generation of physicists and engineers. Complex magnetic field vessels with special walls and plasma heating waves and beams will be needed and are being designed and tested in broad international and national activities. Safely confining and controlling the nuclear fusion “burning” plasma has proven to be a century-long research project. The exhaust products are high-energy alpha particles and neutrons.

### 7.5.1 Alpha particle plasma heating rates

Important parameters in the energy balance of thermonuclear plasmas are the alpha particle heating rates and the division of the alpha particle energy that is transferred between ions and electrons. Here we review the collective mechanisms for the transfer of alpha energy to the plasma fuel and point out that these collective wave mechanisms are much faster than the classical collisional transfer rates. The collisional alpha particle of mass  $m_\alpha$  and energy  $E_\alpha$  slowing-down time is  $\tau_s \simeq 3, m_\alpha m_e v_e^3 / [(2\pi)^{1/2} m_e z_\alpha^2 e^4 \ell n \Gamma]$  and is of order one second for  $n_e = 10^{14} \text{ cm}^{-3}$  and  $T_e \approx m_e v_e^2 \approx 10\text{-}20 \text{ KeV}$ .

Here we analyze the alpha particle energy distributions peaked around the source energy of 2.5 MeV there are electromagnetic instabilities with scale  $k^{-1} \simeq c/\omega_{pi}$  and electrostatic instabilities

with scale  $k^{-1} \gtrsim v_i/\omega_{ci} = \rho_i$  that grow on the ion cyclotron period time scale and lead to anomalous diffusion equations for the particle distribution functions. We review results for the electrostatic modes and the electromagnetic modes.

The stability of a plasma with Maxwellian ions and electrons and the high-energy alpha particle distribution  $f_\alpha(v^2)$  having various degrees of peaking about the source energy  $E_\alpha = 1/2m_\alpha v^2 = 3.5$  MeV is a function of  $E_\alpha/T_e$  and  $n_\alpha/n_e$ . The alpha particle distributions are parameterized by  $(p, n)$  as follows:

$$f_\alpha^n(v^2) = \frac{p^{2n+3}}{2\pi\Gamma(n+3/2)} v^{2n} e^{-p^2 v^2} \quad (7.1)$$

where  $E_\alpha = m_\alpha(2n+3)/4p^2$ . In the limit  $n \rightarrow \infty$  with  $n/p^2$  finite, the distribution is monoenergetic at  $E_\alpha$ .

For the electrostatic dispersion relation  $\varepsilon(\omega)$  with Maxwellian ions and electrons and calculating the fluctuating resonant alpha particle density contribution,  $\text{Im } \tilde{\rho}_\alpha, \rho_\alpha(k, \omega)$  for low alpha-particle concentration  $n_\alpha/n_e < 1$  one obtains the dispersion relation

$$\begin{aligned} k^2 \varepsilon_{\mathbf{k}}(\omega) = & i\pi\omega\omega_{p\alpha}^2 \sum_\ell \int dv j_\ell^2 \delta(\omega - k_\parallel v_\parallel - \ell\omega_{c\alpha}) \frac{\partial f_\alpha}{\partial v^2/2} \\ & \frac{i\pi\omega\omega_{p\alpha}^2 p^3}{|k_\parallel|\Gamma(n+3/2)} \sum_\ell e^{-p^2 c_\ell^2} \int_0^\infty 2y dy e^{-y^2} \\ & J_\ell^2 \left( \frac{l_{\parallel y}}{p\omega_{c\alpha}} \right) (n - p^2 c_\ell^2 - y^2) (p^2 c_\ell^2 - y^2)^{n-1} \end{aligned} \quad (7.2)$$

where  $c_\ell = (\omega - \ell\omega)/k_\parallel$ .

First we consider the mode at the deuterium cyclotron frequency  $\omega_{cD} = \omega_{c\alpha} = \omega_{ci}$  for wavelengths  $k_\perp \rho_i < 1$ . The mode frequency is  $\omega_{\mathbf{k}} \cong \omega_{ci}(1 - 1/2m_e k_\perp^2/m_i k^2)$  for  $k_\perp \rho_i < k_\parallel v_e/\omega_{ci} < 1$  and  $\omega_{\mathbf{k}} \cong \omega_{ci}(1 - 1/2k_\perp^2 \rho_i^2 T_e/T_i)$  for  $k_\parallel v_e/\omega_{ci} > 1$ . For  $k_\perp \rho_\alpha = k_\perp v_\alpha/\omega_{c\alpha} > 1$  with  $v_\alpha = p^{-1}$  the alphas with  $v_\perp < v_\alpha$  dominate the resonant contribution to  $\tilde{\rho}_\alpha$  and for these particles ( $v_\perp < v_\alpha$ ) the distribution in  $v_\parallel$  is double humped with the resonance destabilizing for  $|c_{\ell=1}| < v_\alpha$ . For this gyrofrequency mode the  $\alpha$ -particle contributions for the mildly-peaked  $n = 1$  distribution is

$$k^2 \varepsilon_{\mathbf{k}} = i \frac{4\omega_{ci}^2 \omega_{p\alpha}^3 p^4}{3|k_\parallel| |k_\perp|} \left( \frac{1}{2 - p^2 c_1^2} \right) \quad (7.3)$$

where  $c_1 = (\omega_{\mathbf{k}} - \omega_{ci})/k_\parallel = \delta\omega_{\mathbf{k}}/k_\parallel$ . In Fig. ? the resonant parallel particle velocity contours are shown in the  $k_\perp, k_\parallel$ -plane. The growth rate reaches a maximum in the  $k_\parallel v_e/\omega_{ci} < 1$  region between the curves  $2v_i < c_1 \lesssim 0.5v_\alpha$  and where  $k_\perp \rho_i \gtrsim v_i/v_\alpha$ . The maximum growth rate is of order  $\gamma/\omega_{ci} \simeq 0.2(n_\alpha/n_e)(m_e/M_i)^{1/3}$ .

The effect on the background distribution functions of a stationary turbulent spectrum of

fluctuations of these modes is given in Fig. ?. We model the wavenumber spectrum as

$$I(k_{\perp}, k_{\parallel}) = I_{\max} \exp \left[ -\frac{1}{2} (k_{\perp} - \bar{k}_{\perp})^2 / \Delta k_{\perp}^2 - \frac{1}{2} (k_{\parallel} - \bar{k}_{\parallel})^2 / \Delta k_{\parallel}^2 \right]. \quad (7.4)$$

The correlation function along the particle orbit is

$$C_{\mathbf{k}}(\mathbf{v}, t)(\mathbf{v}, t) \cong \langle \varphi^2 \rangle \sum_n J_n^2 \left( \frac{\bar{k}_{\perp} v_{\perp}}{\omega_c} \right) e^{-1/2} \Delta \omega_{\mathbf{k}t^2}^{\alpha} \cos [(\omega_{\bar{\mathbf{k}}} - \bar{k}_{\parallel} v_{\parallel} - n \omega_c) t] \quad (7.5)$$

where  $\Delta \omega_{\mathbf{k}}^2 = \Delta k_{\parallel}^2 v_{\parallel}^2 + \Delta k_{\perp}^2 (d\omega_{\bar{\mathbf{k}}}/d\bar{k}_{\perp})^2$ .

The velocity diffusion equation is

$$\frac{\partial f_j}{\partial t} = \frac{\partial}{\partial \mathbf{v}} \left( \tilde{D} \cdot \frac{\partial f_j}{\partial \mathbf{v}} \right) \quad (7.6)$$

where

$$\tilde{D} = \left( \frac{e_j}{m_j} \right)^2 \sum_n \int_{-\infty}^0 dt C_{\mathbf{k},n}(\mathbf{v}, t) \begin{pmatrix} \frac{n^2 \Omega^2}{v_{\perp}^2} & \frac{n \Omega k_{\parallel}}{v_{\perp}} \\ \frac{n \Omega}{v_{\perp}} & k_{\parallel}^2 \end{pmatrix}. \quad (7.7)$$

For the ions the velocity diffusion reduces to

$$D_{\perp}^i \simeq \left( \frac{\pi}{2} \right)^{1/2} \frac{e^2 \langle \varphi^2 \rangle \bar{k}_{\perp}^2}{m_i^2 \Delta \omega_{\mathbf{k}}} e^{-1/2} (\delta \omega_{\bar{\mathbf{k}}} - \bar{k}_{\parallel} v_{\parallel})^2 / \Delta \omega_{\mathbf{k}}^2. \quad (7.8)$$

From Eq. (7.6) one finds that the fast ions with  $v_{\parallel} = \delta \omega_{\bar{\mathbf{k}}} / \bar{k}_{\parallel}$  diffuse or heat at the rate

$$\tau_{D_i}^{-1} = D_{\perp}^i / v_{\perp}^2 = \omega_{ci} \frac{v_i^2}{v_{\perp}^2 v_{\alpha}^2} \frac{e^2 \langle \varphi^2 \rangle}{T_i^2}$$

and the thermal ions with  $v_{\parallel} \simeq v_i < \delta \omega_{\bar{\mathbf{k}}} / \bar{k}_{\parallel}$  heat at a rate reduced by  $\exp \left[ \frac{-1}{2} (\delta \omega_{\bar{\mathbf{k}}} / \Delta \omega_{\mathbf{k}})^2 \right]$

The alpha particles diffuse and cool at the rate

$$\tau_{D_{\alpha}}^{-1} = \frac{D_{\alpha}}{v_{\alpha}^2} \simeq \omega_{ci} \left( \frac{\omega_{ci}}{\bar{k}_{\perp} v_{\alpha}} \right) \frac{v_i^4}{v_{\alpha}^4} \frac{\langle \varphi^2 \rangle}{T_i^2}.$$

These collective heating rates compare to the classical collisional slowing-down time  $\tau_{\alpha}$  as

$$\frac{\tau_s}{\tau_{\alpha}} \simeq \frac{e^2 \langle \varphi^2 \rangle}{T_i^2} \frac{\omega_{ce}}{\omega_{pe}} (n_e \lambda_{De}^3). \quad (7.9)$$

### 7.5.2 Drift waves driven by ion pressure gradients

Ion pressure gradient–driven drift modes are analyzed for their parametric dependence on the magnetic shear, the toroidal aspect ratio, and the pressure gradient using the ballooning toroidal mode theory [*Horton, et al.* (1981)]. An approximate formula for the anomalous ion thermal conductivity is derived for the turbulent regime. In view of the high ion temperatures produced by powerful auxiliary heating in tokamaks, it is important to re-examine the ion pressure gradient driven drift modes along with their associated anomalous thermal transport  $\chi_i$ . In this chapter we analyze the mode structure of these pressure gradient driven modes using the methods developed for studying toroidal drift modes [*Choi and Horton* (1980), *Hastie, et al.* (1979), *Frieman, et al.* (1980), *Chen and Cheng* (1980), *Horton, et al.* (1978)]. The parametric variation of the turbulence with toroidal curvature, magnetic shear and the pressure gradient of the unstable mode characteristics, such as their angular width, average radial and parallel wavenumbers, is used for their identification in the laboratory plasmas fluctuation measurements.

### 7.5.3 Magnetic fluctuations and electron transport in the ionosphere

The scientific activity will be associated with a theoretical description of the generation of magnetic coherent structures and turbulence in the ionosphere. These structures mainly determine the turbulent spatial transport and heating of the electrons in these regions. The plasma data shows signatures of coherent structures that are a combination of magnetic waves and drift waves forming 3D structures. The nonlinear equations will be solved for the formation of the plasma structures.

One of the major problems of atmospheric and laboratory physics refers to the description of coherent structures in the ionosphere which are similar but more complex than those of the neutral gas atmosphere. By using nonlinear 3D computer simulations, we construct models for the ionosphere plasma dynamics and predictions of disruptive events.

Drift waves were originally discovered by *D'Angelo and Motley* (1963) and *Chen* (1965a,b, 1966, 1967); their properties were documented in detail by *Hendel, et al.* (1968) in *Q*–machine plasmas. The first detailed explanation of the nonlinear oscillations measured by Hendel's experiments is given by *Hinton and Horton* (1971). In that work, the square of the density gradient drives the growth rate of the waves through the electron resistivity and parallel thermal diffusivity in a plasma where ion collisional viscosity governs the high wavenumber damping. From these drift wave experiments it became clear that the Bohm diffusion [*Bohm, et al.* (1949)] was produced by the large convection in the drift waves driven by the plasma density gradients. The drift wave instability plays a key role in the turbulent transport of magnetized fusion plasmas, which makes the literature on this subject very extensive. For a review see, for instance, *Horton* (1999) and references therein. This instability, sometimes called universal instability, is present in most laboratory plasmas due to the necessary presence of density and temperature gradients in confined plasmas. However, the experimental study of drift wave instabilities and the associated turbulence and turbulent transport are not simple problems. This difficulty comes from

the fact that in order to obtain good plasma confinement a complex toroidal magnetic geometry is necessary. In addition, a complete experimental description of the fluctuations is not always possible either because of the high temperatures of fusion-grade plasmas or access limitations due to configurational constraints in the plasma confinement devices.

The Helimak is one of the classics of basic plasma experiments which manifests selected characteristics of a fusion plasma in a simpler geometry and with better diagnostics than are possible in major fusion confinement devices. The Helimak, now operating with numerous upgrades in China, is a finite realization of the cylindrical-sheared slab often used in theoretical calculations of plasma turbulence. This correspondence makes possible the comparison of well-understood theoretical and numerical models with experimental data. The additions of magnetic curvature and shear are the minimal additions to the ideal slab model required to introduce the effects of a confinement geometry. The field curvature generates a charge-dependent drift of the guiding centers which separates electrons from ions. This charge separation is also mathematically equivalent to the one that occurs from the gravitational field on the surface of the sun. Thus, the experiment can simulate the Rayleigh-Taylor instability.

The Helimak produces a spiraling toroidal magnetic field. The dominant toroidal field is of order 0.1 T with a weaker vertical field  $B_z$  which may be varied up to 10% of the toroidal field. The field lines are thus helices as shown spiraling from bottom to top of the two meter cylindrical chamber. The helical field line length may be varied from less than 10 m to more than 1 km. The height of the vacuum vessel is  $L_z = 2H = 2\text{m}$ , the inner radius is 0.6 m, and the outer radius 1.6 m. For most conditions, all the field lines terminate at both ends of the cylinder on sets of metal plates as shown. There are two sets of plates, top and bottom, 180° apart. For the steepest pitches, some field lines terminate on the vessel. Although each plate is electrically isolated, all are connected to the vacuum vessel in these experiments. The field lines impinge nearly normal to the plates, which are dotted with more than 700 surface-mounted Langmuir probes. The insert in the figure illustrates one probe tip with its ceramic insulator protruding through the plate into the plasma. The plasma is formed and heated with 6 kW of microwave power at the electron cyclotron frequency. The power is admitted through an open waveguide on the high-field side. Since the single-pass absorption is small in this experiment, the vacuum chamber forms an over-moded, low- $Q$  cavity similar to a microwave oven. In argon at a neutral density of  $4 \times 10^{11}$ , typical plasma parameters are  $n_e = 10^{11} \text{ cm}^{-3}$ ,  $T_e = 10 \text{ eV}$ , and  $T_i = 0.1 \text{ eV}$ . This configuration has a simple stable Magnetohydrodynamic (MHD) equilibrium [*Parail, et al. (1985)*, *Zimmerman and Luckhardt (1993)*, *Luckhardt (1999)*] in which the charge separation from vertical drifts is largely neutralized by a return  $j_{\parallel}$  and the small  $j_{\perp}$  required for force balance flows to the end plates and returns through the conducting vessel. The configuration has been used in other experiments described in *Müller, et al. (2004)* and *Rypdal and Ratynskaia (2005)*. The latter experiment also uses microwave power for plasma production and reports plasmas with similar equilibrium parameters. The Helimak experiment differs from these principally in size, having dimensions large compared with all scale lengths, including these for density and temperature gradients. This experiment operates in a steady state with stationary conditions for tens of seconds, giving excellent statistics for turbulence. It is a full realization of the cylindrical sheared slab plasma model.

Large-scale neutral gas wave motions have a significant influence on energy balance in the Earth's atmospheric circulation [Pedlosky (1987), Satoh (2004)]. However, the presence of charged particles in the electrically-conductive weakly-ionized ionosphere substantially enriches the conditions for the propagation of low-frequency wave modes that are different in nature. Numerous ground-based and satellite observations [Cavalieri, et al. (1974), Cavalieri (1976), Manson, et al. (1981), Hirooka and Hirota (1985), Randel (1987), Sorokin (1988), Sharadze, et al. (1988, 1989), Williams and Avery (1992), Forbes and Leveroni (1992), Bauer, et al. (1995), Zhou, et al. (1997), Lastovicka (1997), Smith (1997), Lawrence and Jarvis (2003), Burmaka, et al. (2006), Alperovich and Fedorov (2007), Fagundes, et al. (2005)] show that planetary-scale (with wavelength  $\lambda > 1000$  km and period of several days) wave perturbations of Electromagnetic (EM) origin regularly exist in different ionospheric layers. Increasing interest in planetary-scale Ultra Low Frequency (ULF) wave perturbations is caused by the fact that many ionospheric phenomena from the same frequency range can play the role of ionospheric precursors of some extraordinary phenomena (earthquakes, volcano eruptions, etc.) [Hajkowicz (1991), Liperovsky, et al. (1992), Cheng and Huang (1992)] and also appear as the ionospheric response to the anthropogenic activity [Pokhotelov, et al. (1995), Shaefer, et al. (1990), Burmaka and Chernogor (2004), Burmaka, et al. (2005)]. Forced oscillations of that kind, under the impulsive impacts on the ionosphere and during magnetospheric storms, were also observed [Hajkowicz (1991)].

In recent years, an increasing number of theoretical and experimental investigations have been devoted to the investigation of the dynamics of Rossby waves (induced by the spatial inhomogeneity of the Coriolis parameter) in the Earth's ionosphere. Dokuchaev (1959) first indicated the necessity of accounting for the interaction of an induced electric current with the Earth's magnetic field on the wind's dynamics. The next step was done by Tolstoy (1967), who pointed out the importance of global factor acting permanently in the ionosphere — the space inhomogeneity of the geomagnetic field on the dynamics of Rossby type waves in the Earth's ionospheric E-layer. The waves were entitled Hydromagnetic Gradient (HMG) waves. It was also shown that HMG waves can couple with the Rossby waves in the E-layer heights. He suggested that HMG waves may appear as traveling perturbations of the Sq current system producing from a few to several tenths of nT strong variations of the geomagnetic field.

A review of the mechanisms for the generation of zonal flows and magnetic field fluctuations by various coupled EM ULF waves in the Earth's ionospheric E-layer on the base of our investigations [Kaladze, et al. (2012a,b, 2013a,b)] are described in Kahlon and Kaladze (2015). Taking into the account a latitudinal inhomogeneity of Coriolis parameter and geomagnetic field propagation of Coupled Internal Gravity Alfvén (CIGA), Coupled Rossby–Khantadze (CRK) and Coupled Rossby–Alfvén–Khantadze (CRAK) waves is revealed and studied. In Kahlon and Kaladze (2015) it is shown that the instability of short wavelength turbulence of such coupled waves may lead to the excitation of low-frequency and large-scale perturbation of the sheared zonal flow and sheared magnetic field. The nonlinear mechanism of the instability is based on the parametric triple interaction of finite amplitude coupled waves leading to the inverse energy cascade toward the longer wavelength. The possibility of generation of the intense mean magnetic field is shown. Obtained growth rates are discussed for each case of the considered coupled waves.

## The objectives of the Helimak plasma project

The main goal of the project is to develop nonlinear equations for the formation of vortical structures in the Helimak and for mesoscale cyclones and anticyclones in the ionosphere, incorporating all features mentioned above. The present research assumes the use of the previous experience simpler plasmas. Here the new research relates to understanding the generation of coherent magnetic plasma structures and turbulence in the Helimak and their correspondence to plasma structures in the ionosphere. A part of the project will be dedicated to interpretation of laboratory, numerical, and observational studies of these structures in Helimak and their relation to structures in the ionosphere. A particular attention will be paid to the analysis of the ionospheric responses to the man-made activities and extraordinary natural phenomena (earthquake, storms, hurricanes etc.).

### The main objectives of the project are:

- To perform a theoretical investigation of the generation of magnetic coherent structures and turbulence in Helimak at The University of Texas and their corresponding structures in the ionosphere.
- To study the similarities between these coherent structures in Helimak and ionospheric plasmas. Dynamics of these structures in Helimak and ionospheric plasma will be developed.
- To provide a novel mechanism for the formation of vortical structures in the Helimak and for mesoscale cyclones and anticyclones in the ionosphere.
- To elucidate the role of the charged particles in the nonlinear dynamics of magnetic waves and drift waves.
- To apply the developed theory to the physics of laboratory and ionospheric atmospheres.

#### 7.5.4 Helicon waves and LHCD for controlling the toroidal currents

##### Helicon RF waves

Antennas are designed to drive helical RF to maintain the toroidal plasma currents in steady state or long pulse tokamaks. The method is used in the DIII-D tokamak plasmas to control the toroidal plasma current profiles and the current strength, with the aim of achieving a degree of confirmation between the theoretical models and the DIII-D plasma data. The Pinkser team developed 12 element Helicon antenna that is currently being tested on DIII-D.

Plans are to verify modeling of the helicon wave antennas as carried out earlier for the higher-frequency LHCD-driven plasmas in the Tore Supra tokamak; the theory and simulations of the interactions of the RF waves in turbulent plasma. The plasma inhomogeneity produces RF mode conversions. The Tore Supra team published [Horton, *et al.* (2013)] a modeled and successful experiment maintaining long plasma currents driving the fast RF waves by a complex 3 GHz RF antenna. The slow LHCD waves and fast wave helicon waves each have advantages for steady-state fusion plasmas. The RF simulation procedures are similar for a given turbulent tokamak plasma; however, the LHCD is smaller and easier to maintain the large fast wave antennas. Currently, validation of the fast-wave current drive model is taking place on DIII-D plasmas. The community would then have two RF methods to maintain steady-state toroidal plasma currents. Drift wave turbulence couples the two types — slow and fast — RF waves and needs to be taken into account in the plasma data analysis and modeling.

## LHCD in EAST

The EAST tokamak has successfully driven long steady-state tokamak plasma currents. Other RF-driven toroidal fusion plasmas include HL-2A and KSTAR machines that use Klystrons and Gyrotrons to maintain steady-state fusion plasmas. The comparisons of the results from EAST, KSTAR, WEST and DIII-D will be top priority in designing a steady-state ITER toroidal plasma.

The Department of Energy launched an emphasis on research for “Long Pulse Tokamak Research” to support and explore critical science and technology for long duration plasma discharges in ITER in 2017. It was stated that the specific areas of interest were to find and make achieving long-pulse high-performance plasmas. Then they numerated these items of concern: (i) studying and developing high-performance operating states that can be robustly produced, sustained, and controlled for long periods of time; (ii) establishing plasma confinement, stability and operational boundaries, (iii) understanding plasma core, pedestal, boundary, and scrape-off layer physics and (iv) developing and demonstrating divertor solutions that provide improved power handling.

### 7.5.5 Anomalous alpha particle plasma heating rates

Important parameters in the energy balance of thermonuclear plasmas are the alpha particle heating rates and the division of the alpha particle energy transferred between ions and electrons. Here we review the collective mechanisms for the transfer of the alpha particle energy to the plasma and point out that these collective wave transfer mechanisms are much faster than the collisional transfer rates. The collisional alpha particle  $m_\alpha, E_\alpha$  slowing-down time is  $\tau_s \simeq 3m_\alpha m_e v_e^3 / [(2\pi)^{1/2} n_e z_\alpha^2 e^4 \ell n \Lambda]$  and is of order one second for  $n_e = 10^{14} \text{ cm}^{-3}$  and  $T_e \approx 10 - 20 \text{ KeV}$ . Here we show that for alpha particle energy distributions peaked around the source energy of 2.5 MeV there are electromagnetic instabilities with scale  $k^{-1} \simeq c/\omega_{pi}$  and electrostatic instabilities with scale  $k^{-1} \gtrsim v_i/\omega_{ci} = \rho_i$  that grow on the ion cyclotron period time scale and lead to

anomalous diffusion equations for the particle distribution functions. We review results for the electrostatic modes and the electromagnetic modes.

# Bibliography

- [1] Alperovich, L. S. and Fedorov, E. N. (2007). *Hydromagnetic Waves in the Magnetosphere and the Ionosphere*, (Dordrecht: Springer, 2007), <https://ezproxy.cern.ch/login?url=http://dx.doi.org/10.1007/978-1-4020-6637-5>.
- [2] Bauer, T. M., Baumjohann, W., Treumann, R. A., Sckopke, N. and Lühr, H. (1995). Low-frequency waves in the near-Earth plasma sheet, *J. Geophys. Res.* **100**, pp. 9605–9617, <https://doi.org/10.1029/95JA00136>.
- [3] Bohm, D., Burhop, E. H. S. and Massey, H. S. W. (1949). The use of probes for plasma exploration in strong magnetic fields, *The Characteristics of Electrical Discharges in Magnetic Field* eds. A. Guthrie and R. K. Wakerling, (New York, McGraw-Hill).
- [4] Burmaka, V. P. and Chernogor, L. F. (2004). Clustered instrument studies of ionospheric wave disturbances accompanying rocket launches against the background of nonstationary natural processes, *Geomag. Aeron.* **44**, pp. 518–534.
- [5] Burmaka, V. P., Taran, L. F. and Chernogor, L. F. (2005). Results of investigations of the wave disturbances in the ionosphere by noncoherent scattering, *Adv. Mod. Radiophys.* **3**, pp. 4–35.
- [6] Burmaka, V. P., Lysenko, V. N., Chernogor, L. F. and Chernyak, Yu. V. (2006). Way-like processes in the ionospheric *F*-region that accompanied rocket launches from the Baikonur site, *Geomag.. Aeron.* **46**, pp. 742–759, <https://doi.org/10.1134/S0016793206060107>.
- [7] Cavalieri, D. J., Deland, R. J., Poterna, J. A. and Gavin, R. F. (1974). The correlation of VLF propagation variations with atmospheric planetary-scale waves *J. Atmos. Terr. Phys.* **36**, pp. 561–574, [https://doi.org/10.1016/0021-9169\(74\)90082-8](https://doi.org/10.1016/0021-9169(74)90082-8).
- [8] Cavalieri, D. J. (1976). Traveling planetary-scale waves in the *E*-region, *J. Atmos. Terr. Phys.* **38**, pp. 965–977, [https://doi.org/10.1016/0021-9169\(76\)90079-9](https://doi.org/10.1016/0021-9169(76)90079-9).
- [9] Chen, F. F. (1965a). Resistive over-stabilities and anomalous diffusion, *Phys. Fluids* **8**, p. 912, <http://dx.doi.org/10.1063/1.1761335>.
- [10] Chen, F. F. (1965b). Excitation of drift instabilities in thermionic plasmas, *J. Nucl. Energy Pt. C*, p. 399, <http://dx.doi.org/10.1088/0368-3281/7/4/305>.

- [11] Chen, F. F. (1966). Microinstability and shear stabilization of a low- $\beta$  rotating, resistive plasma, *Phys. Fluids* **9**, p. 965, <https://doi.org/10.1063/1.1761798>.
- [12] Chen, F. F. (1967). Nonlocal drift modes in cylindrical geometry, *Phys. Fluids* **10**, p. 1647, <https://doi.org/10.1063/1.1762340>.
- [13] Chen, L. and Cheng, C. Z. (1980). Drift-wave eigenmodes in toroidal plasmas, *Phys. Fluids* **23**, p. 2242, <https://doi.org/10.1063/1.862907>.
- [14] Cheng, K. and Huang, Y-N. (1992). Ionospheric disturbances observed during the period of Mount Pinatubo eruptions in June 1991, *J. Geophys. Res.* **97**, pp. 16995–7004, <https://doi.org/10.1029/92JA01462>.
- [15] Choi, D. I. and Horton, W. (1980). Weakly localized two-dimensional drift modes, *Phys. Fluids* **23**, p. 356, <https://doi.org/10.1063/1.862980>.
- [16] D'Angelo, N. and Motley, R. W. (1963). Low-frequency oscillations in a potassium plasma, *Phys. Fluids* **6**, p. 422, <http://dx.doi.org/10.1063/1.1706749>.
- [17] Dokuchaev, V.P. (1959). P. Influence of the earth's magnetic field on the ionospheric winds, *Izvestia AN SSSR Seria Geophysica* **5**, pp. 783–787, .
- [18] Fagundes, P. R., Pillat, V. G., Bolzan, M. J. A., Sahai, Y., Becker-Guedes, F., Abalde, J. R., Aranha, S. L. and Bittencourt, J. A. (2005). Observations of F-layer electron density profiles modulated by planetary wave type oscillations in the equatorial ionospheric anomaly region, *J. Geophys. Res.* **110**, p. A12302, <https://doi.org/10.1029/2005JA011115>.
- [19] Forbes, J. and Leveroni, S. (1992). Quasi 16-day oscillation in the ionosphere, *Geophys. Res. Lett.* **19**, pp. 981–984, <https://doi.org/10.1029/92GL00399>.
- [20] Frieman, E. A., Rewoldt, G., Tang, W. M. and Glasser, A. H. (1980). General theory of kinetic ballooning modes, *Phys. Fluids* **23**, p. 1750, <https://doi.org/10.1063/1.863201>.
- [21] Hastie, R. J., Hesketh, K. W. and Taylor, J. B. (1979). Shear damping of two-dimensional drift waves in a large-aspect-ratio tokamak, *Nucl. Fusion* **19**, p. 1223, <https://doi.org/10.1088/0029-5515/19/9/006>.
- [22] Hajkowicz, L. A. (1991). Global onset and propagation of large-scale traveling ionospheric disturbances as a result of the great storm of 13 March 1989, *Planet. Space Sci.* **39**, pp. 583–593, [https://doi.org/10.1016/0032-0633\(91\)90053-D](https://doi.org/10.1016/0032-0633(91)90053-D).
- [23] Hendel, H. W., Chu, T. K. and Politzer, P. A. (1968). Collisional drift waves — Identification, stabilization, and enhanced plasma transport, *Phys. Fluids* **11**, p. 2426, <http://dx.doi.org/10.1063/1.1691833>.
- [24] Hinton, F. L. and Horton, Jr., C. W. (1971). Amplitude limitation of a collisional drift wave instability, *Phys. Fluids* **14**, pp. 116–123, <http://dx.doi.org/10.1063/1.1693260>.

- [25] Hirooka, T. and Hirota, I. (1985). Normal mode Rossby waves observed in the upper stratosphere. Part II: Second antisymmetric and symmetric modes of zonal wavenumbers 1 and 2, *J. Atmos. Sci.* **42**, pp. 536–548, [https://doi.org/10.1175/1520-0469\(1985\)042<0536:NMRWOI>2.0.CO;2](https://doi.org/10.1175/1520-0469(1985)042<0536:NMRWOI>2.0.CO;2).
- [26] Horton, W., Estes, R., Kwak, H. and Choi, D-I. (1978). Toroidal mode coupling effects on drift wave stability, *Phys. Fluids* **21**, p. 1366, <https://doi.org/10.1063/1.862378>.
- [27] Horton, W., Choi, D-I. and Tang, W. M. (1981). Toroidal drift modes driven by ion pressure gradients, *Phys. Fluids* **24**, pp. 1077–1085, <https://doi.org/10.1063/1.863486>.
- [28] Horton, W. (1999). Drift waves and transport, *Rev. Mod. Phys.* **71**, p. 735, <http://dx.doi.org/10.1103/RevModPhys.71.735>.
- [29] Horton, W., Goniche, M., Peysson, Y., Decker, J., Ekedahl, A. and Litaudon, X. (2013). Penetration of lower-hybrid current drive waves in tokamaks, *Phys. Plasmas* **20**, p. 112508, <http://dx.doi.org/10.1063/1.4831981>.
- [30] Kahlon, L. Z. and Kaladze, T. D. (2015). Generation of zonal flow and magnetic field in the ionospheric E-layer, *J. Plasma Phys.* **81**, p. 905810512, <https://doi.org/10.1017/S002237781500080X>.
- [31] Kaladze, T. D., Kahlon, L. Z. and Tsamalashvili, L. V. (2012). Excitation of zonal flow and magnetic field by Rossby–Khantadze electromagnetic planetary waves in the ionospheric E-layer, *Phys. Plasmas* **19**, p. 022902, <https://doi.org/10.1063/1.3681370>.
- [32] Kaladze, T. D., Kahlon, L. Z., Tsamalashvili, L. V. and Kaladze, D. T. (2012b). Generation of zonal flow and magnetic field by coupled internal–gravity and Alfvén waves in the ionospheric E-layer, *J. Atmos. Sol.: Terres. Phys.* **89**, pp. 110–119, <https://doi.org/10.1016/j.jastp.2012.08.012>.
- [33] Kaladze, T. D., Horton, W., Kahlon, L. Z., Pokhotelov, O. and Onishshenko, O. (2013). Generation of zonal flow and magnetic field by coupled Rossby–Alfvén–Khantadze waves in the Earth’s ionospheric E-layer, *Phys. Scr.* **88**, p. 065501, <https://doi.org/10.1088/0031-8949/88/06/065501>.
- [34] Kaladze, T. D., Horton, W., Kahlon, L. Z., Pokhotelov, O. and Onishshenko, O. (2013b). Zonal flows and magnetic fields driven by large-amplitude Rossby Alfvén Khantadze waves in the E-layer ionosphere, *J. Geophys. Res.: Space Phys.* **118**, pp. 7822–7833, <https://doi.org/10.1002/2013JA019415>.
- [35] Lastovicka, J. (1997). Observations of tides and planetary waves in the atmosphere–ionosphere system, *Adv. Space Res.* **20**, pp. 1209–1222, [https://doi.org/10.1016/S0273-1177\(97\)00774-6](https://doi.org/10.1016/S0273-1177(97)00774-6).

- [36] Lawrence, A. R. and Jarvis, M. J. (2003). Simultaneous observations of planetary waves from 30 to 220 km, *J. Atmos. Solar-Terr. Phys.* **65**, pp. 765–777, [https://doi.org/10.1016/S1364-6826\(03\)00081-6](https://doi.org/10.1016/S1364-6826(03)00081-6).
- [37] Liperovsky, V. A., Pokhotelov, O. A. and Shalimov, S. L. (1992). Ionospheric earthquake precursors (Moscow: Nauka, 1992).
- [38] Luckhardt, S. (1999). The Helimak: A one dimensional toroidal plasma system, Technical Report, University of California, San Diego, 1999; <http://orion.ph.utexas.edu/~starpower>.
- [39] Manson, A. H., Heek, C. E., and Gregory, J. B. (1981). Winds and waves (10 min–30 days) in the mesosphere and lower thermosphere at Saskatoon (52°N, 107°W, L= 4.3) during the year, October 1979 to July 1980 *J. Geophys. Res.* **86**, pp. 9615–9625, <https://doi.org/10.1029/JC086iC10p0961>.
- [40] Müller, S. H., Fasoli, A., Labit, B., McGrath, M., Podesta, M. and Poli, F. M. (2004). Effects of a vertical magnetic field on particle confinement in a magnetized plasma torus, *Phys. Rev. Lett.* **93**, p. 165003, <https://doi.org/10.1103/PhysRevLett.93.165003>.
- [41] Parail, V. V., Pereverzev, G. V. and Vojtsekovich, I. A. (1985) in *Proceedings of the IAEA Conference on Plasma Physics and Controlled Thermonuclear Fusion* (London, 1985), Vol. I, p. 605.
- [42] Pedlosky, J. (1987). *Geophysical Fluid Dynamics*, 2nd Ed. (Berlin: Springer) *Science*.
- [43] Pokhotelov, O. A., Parrot, M., Fedorov, E. N., Pilipenko, V. A., Surkov, V. V. and Gladychev, V. A. (1995). Response of the ionosphere to natural and man-made acoustic sources, *Annales Geophysicae* **13**, pp. 1197–1210, <https://doi.org/10.1007/s00585-995-1197-2>.
- [44] Randel, W. J. (1987). A Study of planetary waves in the southern winter troposphere and stratosphere. Part I: Wave structure and vertical propagation, *J. Atmos. Sci.* **44**, pp. 917–935, [https://doi.org/10.1175/1520-0469\(1987\)044<0917:ASOPWI>2.0.CO;2](https://doi.org/10.1175/1520-0469(1987)044<0917:ASOPWI>2.0.CO;2).
- [45] Rypdal, K. and Ratynskaia, S. (2005). Onset of turbulence and profile resilience in the Helimak configuration, *Phys. Rev. Lett.* **94**, p. 225002, <https://doi.org/10.1103/PhysRevLett.94.225002>.
- [46] Satoh, M. (2004). *Atmospheric Circulation Dynamics and General Circulation Models* (Berlin: Springer) (2004).
- [47] Sharadze, Z. S., Mosashvili, N. V., Pushkova, G. N. and Iudovich, L. A. (1989). Long-period wave disturbances in the ionospheric  $\Gamma$ -region *Geomag. Aeron.* **29**, pp. 1032–1035, <http://adsabs.harvard.edu/abs/1989IonIs..46..123S>.

- [48] Shaefer, L. D., Rock, D. R., Lewis, J. P. and Warshaw, S. I. (1999). Detection of explosive events by monitoring acoustically-induced geomagnetic perturbations, Lawrence Livermore Laboratory 94550 (Livermore, CA, 1999), UCRL-ID-133240.
- [49] Sharadze, Z. S., Mosashvili, N. V., Pushkova, G. N. and Iudovich, L. A. (1989). Long-period wave disturbances in the ionospheric F-region, *Geomag. Aeron.* **29**, pp. 1032–1035, <http://adsabs.harvard.edu/abs/1989IonIs..46..123S>.
- [50] Smith, A. K. (1997). Stationary planetary waves in upper mesospheric winds, *J. Atmos. Sci.* **54**, pp. 2129–2145, [https://doi.org/10.1175/1520-0469\(1997\)054<2129:SPWIUM>2.0.CO;2](https://doi.org/10.1175/1520-0469(1997)054<2129:SPWIUM>2.0.CO;2).
- [51] Sorokin, V. M. (1988). Wave processes in the ionosphere associated with the geomagnetic field, Izv. Vyssh. Uchebn. Zaved., Radiofiz.; (USSR) **31**, pp. 827–836, <https://doi.org/10.1007/BF01040013>.
- [52] Tolstoy, I. (1967). Hydromagnetic gradient waves in the ionosphere, *J. Geophys. Res.* **72**, pp. 1435–1442, <https://doi.org/10.1029/JZ072i005p01435>.
- [53] Williams, C. R. and Avery, S. K. (1992). Analysis of long-period waves using the mesosphere–stratosphere–troposphere radar at Poker Flat, Alaska, *J. Geophys. Res.* **97**, p. 20,855–20,861, <https://doi.org/10.1029/92JD02052>.
- [54] Zhou, Q. H., Sulzer, M. P. and Tepley, C.A. (1997). An analysis of tidal and planetary waves in the neutral winds and temperature observed at low-latitude E-region heights, *J. Geophys. Res.* **102**, pp. 11491–11505, <https://doi.org/10.1029/97JA00440>.
- [55] Zimmerman, E. D. and Luckhardt, S. C. (1993). Measurement of the correlation spectrum of electrostatic potential fluctuations in an ECRH Helimak plasma, *J. Fusion Energy* **12**, pp. 289–293, <https://doi.org/10.1007/BF01079672>.

# Chapter 8

## Space Plasma Physics and the Global Navigation Satellite System

There are broad and intense international collaborations as well as private sector companies working to find ways to produce power from controlling nuclear fusion reactions. Fusion reactions are Mother Nature's way to produce the enormous power from billions of stars of all sizes in the universe. We must find a way to construct plasma confinement in vessels, that is, to build a star. This is the Grand Challenge problem for the future generation of scientists and engineers. Remember more than 99.9% of the universe is in the plasma state and there are billions of stars producing fusion energy. Understanding the universe requires understanding and controlling fusion power.

The early history of the search in the USA for the path to building a fusion reactor is detailed by Steve Dean in *Search for the Ultimate Energy Source, A History of the U.S. Fusion Energy Program* (Springer) ISBN:978-4611-6036-7.

### 8.1 Ionospheric plasma turbulence and satellite systems

The scintillation and tomography receiver in space (CITRIS) instrument will orbit the Earth near 560 km altitude to detect signals from the ground-based array of more than 50 DORIS UHF/S-band radio beacons established at sites around the world by the French Centre National d'Etudes Spatiales (CNES) and the Institut Géographique National (IGN). The CITRIS receiver is on the US Air Force Space Test Program satellite STPSAT1, which is scheduled for launch in November 2006. CITRIS will record ionospheric Total Electron Content (TEC) and radio scintillations with a unique ground-to-space geometry. The new instrument has been developed to study the ionosphere using data obtained with the UHF and S-band radio transmissions from the DORIS beacons because ionospheric radio scintillations can seriously degrade the performance of many space-geodetic systems, including the DORIS precise satellite orbitography system and Global Navigation Satellite Systems (GNSS). The ionospheric data will be based on radio signals sampled at a rate of 200 Hz by the CITRIS receiver. Numerical models have been used to predict that the DORIS signals measured by CITRIS may have 30 dB fluctuations in amplitude and 30 rad in phase

as the satellite flies over kilometer-scale ionospheric structures. The data from the space-based CITRIS receiver will help update and validate theories on the generation and effect of ionospheric irregularities known to influence radio systems. By using simultaneous beacon transmissions from DORIS on the ground and from low-Earth orbit beacons in space, the concept of reciprocity in a nonbilateral propagation medium like the ionosphere will be tested. Computer simulations are used to predict the magnitude of amplitude and phase scintillations that are expected to be recorded with the CITRIS instrument. Geostationary beacon transmissions to ground permit the recording of temporal variations in the ionosphere at a fixed-ground longitude. The Global Navigation Satellite Systems (GNSS), consisting of the current Global Positioning System (GPS), Global Navigation Satellite System (GLONASS), and future Galileo satellites, are placed in MEO near 20,000 km altitude with about a 12-h period. Ionospheric measurements made with these satellites have both spatial and temporal variations. With the presence of over 30 GNSS satellites, ionospheric data are provided in abundance with networks of ground-based receivers, e.g., [Saito, *et al.* (1998), Mannucci, *et al.* (1998), Garcia-Fernandez (2005)].

The ionosphere is a source of error and data loss for many communications, navigation, and radar systems. As satellite radio signals propagate from space through the ionosphere to the ground, they can become distorted by a large number of effects [Davies (1990)] including phase fluctuations, Faraday rotation, amplitude fluctuations, group delay, absorption, scattering, frequency shifts, and multipath (Fig. 9.1). Ionospheric characterization is needed to identify these influences, to predict their occurrence and, if possible, to mitigate their effects.

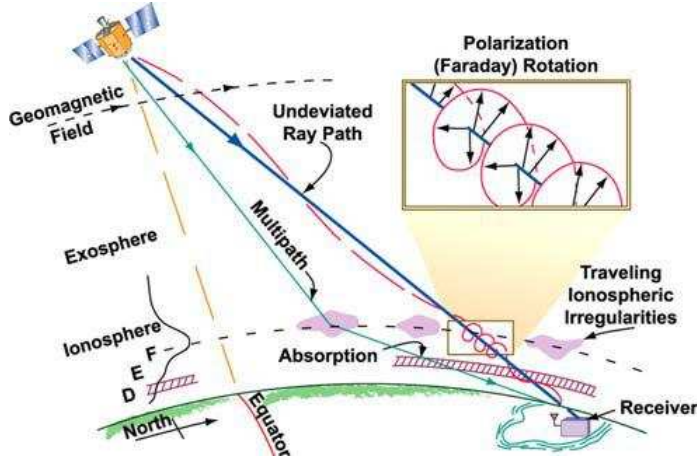


Figure 8.1: Diagram of the GNSS rays with rotation, scattering and refraction during propagation through the ionosphere layers with traveling ionosphere from the spacecraft to the ground-based receiver. Shows the distortions traveling through the F, E and D ionosphere with irregulars and the absorption layer [Bernhardt, *et al.* (2006)] [Adapted from Davies (1990)].

# Bibliography

- [1] Bernhardt, P. A., Siefring, C. L., Galysh, I. J., Rodilloso, T. F., Koch, D. E., MacDonald, T. L., Wilkens, M. R. and Landis, G. Paul (2006). Ionospheric applications of the scintillation and tomography receiver in space (CITRIS) mission when used with the DORIS radio beacon network, *J. Geodesy* **80**, pp. 473–485, <https://doi.org/10.1007/s00190-006-0064-6>.
- [2] Davies, K. (1990). *Ionospheric Radio*, Electromagnetic Waves Series **31** (Publisher: Peter Peregrinus Ltd., London, United Kingdom), ISBN:0-86341-186-X.
- [3] Garcia-Fernandez, M., Hernandez-Pajares, M., Juan, J. M., Sanz, J. (2005). Performance of the improved Abel transform to estimate electron density profiles from GPS occultation data, *GPS Solut.* **9**, pp. 105–110, <https://doi.org/10.1007/s10291-005-0139-5>.
- [4] Mannucci, A. J., Wilson, B. D., Yuan, D. N., Ho, C. H. Lindqwister, U. J. and Runge, T. F. (1998). A global mapping technique for GPS-derived ionospheric total electron content measurements, *Radio Science* **33**, pp. 565–582, <https://doi.org/10.1029/97RS02707>.
- [5] Saito, Y., Uemura, S. and Hamaguchi, K. (1998). Cathode ray tube lighting elements with carbon nanotube field emitters, *Jpn. J. Appl. Phys.* **37**, Part 2, p. L346, <https://doi.org/10.1143/JJAP.37.L346>.

# Chapter 9

## Turbulent Electron Thermal Transport in Tokamaks

The origin of anomalous electron thermal turbulence from spatial gradients in magnetized plasmas is described. Laboratory experiments demonstrating key features of drift waves are reviewed. The turbulent electromagnetic fields produce an anomalous transport that scales with both the gradient parameters and microscopic plasma scale length parameters. The change from the microscale dominated gyroBohm to the macroscale dominated Bohm scaling laws is discussed. The close correlations between the electron turbulent transport theory and the confinement properties measured in the steady-state hot-electron plasmas produced in tokamak devices are presented [Horton, *et al.* (2003)].

Plasma occurs in states of turbulence under a wide range of conditions including space and astrophysical plasmas as well as those produced in MHD stable laboratory confinement devices. The strength of the turbulence increases as the plasma is driven farther away from thermodynamic equilibrium. While there are many ways to drive the plasma away from equilibrium with particle beams, laser beams, and radio frequency waves, a universally-occurring departure from equilibrium is the existence of spatial gradients across an ambient magnetic field. The problem posed is then a classic one of determining the fluxes of particles, energy and momentum across an ambient magnetic field due to gradients in thermodynamic variables of density  $n_a$ , temperature  $T_a$  and flow velocity  $u_a$ .

Plasma distributions that are driven away from the thermodynamic equilibrium of a spatially uniform Maxwell–Boltzmann velocity distribution with densities  $n_a$  and temperatures  $T_a$  for the charge particles species  $(e_a, m_a)$  are said to have a free energy density  $W_f$  available to drive plasma turbulence. For the first free energy example, we estimate the energy density associated with the relative cross-field drift velocity  $u$  between the ions and the electrons driven by the pressure gradient. The cross-field drift is required to maintain force balance in the nonuniform magnetized plasma with  $j \times B = \nabla p$  when  $j_\perp = \sum_a e_a n_a u_{\perp a}$  for  $n_e = \sum_i Z_i n_i$  and  $p = \sum_i p_i + p_e$ . The free energy density is  $W_f = \frac{1}{2} \sum_a m_a n_a u_a^2$ . The condition for the onset of instability is determined by linear stability analysis which specifies the relations between the system parameters  $\rho_a/L_{Ta}, T_e/T_i, m_i/m_e$  for various forms (different modes or branches of  $\mathcal{E}_{ij}\tilde{E}_j(k) = 0$ ) of  $q$  unstable plasma waves. Here  $\rho_a = c(m_a T_a)^{1/2}/e_a B$  is the thermal gyroradius. The nature of the nonlinear

saturated state depends on how far into the unstable domain the system parameters reside which typically varies with space and time as the plasma turbulence reacts on the plasma distributions to push the system back toward one of the marginally stable states. The turbulence provides a mechanism for self-organization toward a relaxed dynamical state often containing a mixture of waves, vortices and zonal flows. The best high temperature, steady-state plasma confinement experiments are produced in tokamaks with large temperature gradients from the core plasma that is often more than twenty million degrees Kelvin surrounded by a room temperature wall no more than one meter away. These high-temperature gradients drive two well-known types of temperature gradient instabilities called the ITG and ETG modes for ion or electron temperature gradient instabilities. We will concentrate in this work on recent theoretical and experimental research on the electron temperature gradient driven turbulent transport. While much is known about these turbulence mechanisms there is still a need for more detailed formulas to make reliable predictions for operational regimes of future large tokamaks. Thus, we review the recent results on electron transport for the purpose of showing more clearly the areas that need further investigations to make predictions for the next generation of large tokamaks. Figure 9.1 shows a schematic of the temperature gradient that operates a Carnot engine through a plasma convection to liberate energy  $W$  over a correlation length  $l_c$ . The plasma simulations of turbulence show that there are many vortices and wave structures that carry out this transport of plasma energy across the magnetic field much faster than one would calculate from collisional transport mechanisms in the plasma. This rapid transport of thermal energy is what has prevented the last generation of tokamaks from reaching the burning plasma state when operating with deuterium and tritium fuels. We now define the correlation functions, and correlation times and lengths needed to discuss plasma turbulence and show a simple example of their measurement in a controlled steady-state laboratory plasma.

## Threshold $\nabla T$ for Convection

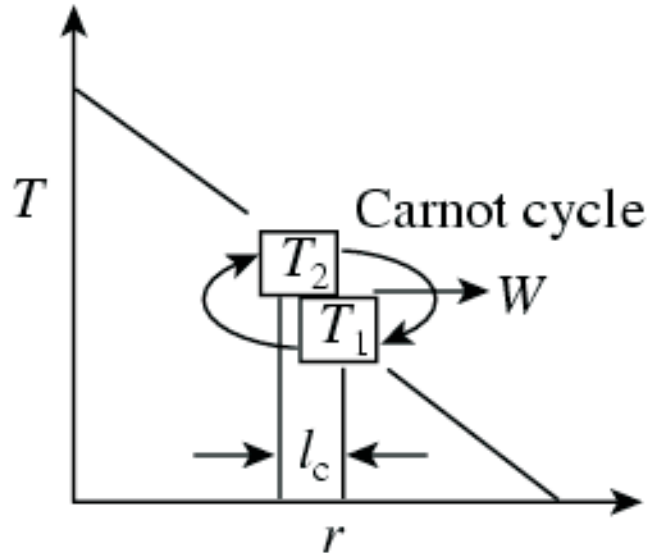


Figure 9.1: The thermodynamics of the Carnot cycle operating in a steep electron temperature gradient over correlation length  $l_c$  of the turbulent convection. The maximum energy density  $W$  to drive the turbulence occurs for a reversible Carnot cycle which gives  $W \leq P_c^2(dT_e/dr)(N_e dT_e/dr - (2/3)T_e dN_e/dr)/T_e$  for the electron gas of density  $N_e$  and temperature  $T_e$ .

## 9.1 Identifying Microinstabilities in Tokamak Pedestals

## 9.2 Application of gyrokinetic “fingerprints” in identifying microinstabilities in a DIII–D pedestal

### 9.2.1 Transport “fingerprints” of various gyrokinetic microinstabilities

Table 9.1: [Kotschenreuther, et al. (2019)]

Mode:	$\chi_i/\chi_e$	$D_e/\chi_e$	$D_z/\chi_e$	Inward Particle Pinches	Shear Suppressed?
MHD-like (e.g. KBM)	$\sim 1$	$\sim 2/3$	$\sim 2/3$	No	No
MTM	$\sim 0$	$\sim 0$	$\sim 0$	No	No
ETG	$\sim 0$	$\sim 0$	$\sim 0$	No	No
ITG/TEM $\geq 1$	$-0.2 - 1$	$\sim 1$	Sometimes	Usually	

### 9.2.2 Experimental observations in DIII–D shot 174082

Strong electromagnetic fluctuations with frequencies appear at  $\sim 420$  kHz and  $\sim 140$  kHz. Shot 174082 has no heating sourced by pellets or gas puffing, only NBI, and is used as the baseline shot in a study of the effects of fueling methods on transport characteristics and pedestal structure [Nelson, et al. (2018)].

$$P_{\text{NBI}} = 4.67 \text{ MW}, \quad \beta_N = 2.0$$

### 9.2.3 Equilibrium profile reconstructions using OMFIT software package

Inter-ELM equilibrium reconstruction uses OMFIT profiles, Osborne, and CAKE packages with Thomson scattering and charge-exchange recombination data. Iterative process on kinetic equilibria generates accurate equilibrium profiles, consisting of magnetic geometry, pressure,  $q$ -profile, pressure derivative, and toroidal current source. There is a small dip in the edge of the safety factor, indicating low shear in the pedestal, a characteristic of microtearing modes observed in previous studies. [Liu (2018)].

### 9.2.4 GENE simulations of the pedestal

High-resolution local linear, global linear, and local nonlinear simulations are performed across the pedestal, for a wide array of toroidal mode numbers. Nonlinear simulations are local, with minimum  $k_y \rho_i = 5$ , to find transport levels of the ETG. Global simulations focus on the range  $k_y \rho_i < 1$ , with toroidal mode numbers ranging from  $n = 3 - 14$ . Each species is fully kinetic. Global simulations make use of the block structured grids algorithm, which adjusts the velocity space grid based on the electron temperature amplitude.

Global runs require high resolutions in the radial direction. Simulations in this study have a grid size of  $(x, z, v_{\parallel}, v_{\perp}) = (256, 96, 32, 16)$ . Block structuring the velocity grids improves performance by resolving with lower resolution in velocity space. There is roughly a 30% increase in efficiency of runs using BSG. Simulations take into account  $\mathbf{E} \times \mathbf{B}$  shear using interferometer data provided by DIII-D team.

## Results

Magnetic and electrostatic potential eigenfunctions lead to minimal parallel electric field cancellation. Upon simulation, the “fingerprints” of the observed linear mode are collected and compared to the previous table. Global simulations indicate that a majority of heat transport is in the electron channel, and electromagnetic in character.

### 9.2.5 Identifying instabilities based on “fingerprints”

Global simulation (fingerprints”) correspond directly to the predicted behavior of microtearing modes.

### 9.2.6 Comparison between experimental and simulation results

Simulated microtearing modes have frequencies that correspond directly to the bands found in experiment. The real frequencies of the MTMs also agree well with the predictions of analytic theory. The fastest-growing simulated mode agrees well with the highest experimental frequency. There currently is work being done on global simulations of modified equilibria to see if the experimentally-observed gap in frequencies can be replicated.

### 9.2.7 Edge Modeling Analysis

Edge Modeling Analysis: SOLPS Diffusivities

Edge Modeling Analysis: Electron particle flux

### 9.2.8 Conclusions

The “fingerprints” method of instability identification categorizes modes based on physical characteristics of transport. In conjunction with simulations, this is a powerful tool that correctly identifies causes of pedestal microturbulence. Microtearing modes are proving to be a valid candidate as the major cause of experimentally–observed anomalous heat losses. Despite the multitude of modes driven unstable in the pedestal region, systematic simulations can accurately report the underlying physics of the fastest–growing mode in the linear regime. Taking into consideration a reasonable variation of equilibrium profiles leads to a significant increase in ETG transport, but not nearly enough to satisfy power balance.

Advances in gyrokinetic codes, along with analytic techniques for mode identification based on “fingerprints” method have found the significance of Microtearing Modes (MTM) and Electron Temperature Gradient (ETG) modes in driving the energy losses within the Edge Transport Barriers (ETB) of fusion experiments operating in the ELM My H–mode regime. Gyrokinetic simulations using the GENE code [Liu (2018)] are performed using equilibrium EFIT profiles constructed from experimental data. Nonlinear local simulations of DIII–D shots 174082 and 174092 have shown that electron heat flux has only minor contributions from ETG turbulence, allowing for the presence of MTM’s and neoclassical effects to account for observed energy losses. The increased particle sources in shot 174092 leads to additional transport mechanisms. The MTM instabilities found in simulations of shot 174082 are consistent with an observed magnetic fluctuation, having a frequency in the electron diamagnetic direction and range. Simulation results have also shown that Kinetic Ballooning Modes (KBM) can contribute to particle losses in pedestals. Fluctuations linked to KBM’s and MTM’s provides a useful “fingerprint” in distinguishing these two modes, and can be used in a quasilinear prediction of transport channels.

Following the analysis of *Halfmoon, et al.* (2019), we analyze the electromagnetic fluctuations and transport in the DIII–D tokamak showing how the drift wave turbulence produces the plasma transport in the plasma near and across the magnetic separatrix and how this relates to the experimental data.

For complex structured signals  $\varphi(x, t)$ , typical of what is meant by the term turbulence, the standard measure of the coherence of the signals is the two–point, two–time correlation function

$$C_{12}(x, t_1, x_2, t_2) = \langle \varphi(x_1, t_1) \varphi(x_2, t_2) \rangle \quad (9.1)$$

where the average  $\langle \rangle$  is the time average taken over a time period  $T$  that contains many oscillations

## 9.2. APPLICATION OF GYROKINETIC “FINGERPRINTS” IN IDENTIFYING MICROINSTABILITIES

of the associated field. The correlation functions for the plasma electric potential  $\varphi$  and the fluctuations of the electron density  $\delta n_e = n_e(x, t) - \langle n_e \rangle$  are the principal structure functions measured in laboratory plasma turbulence research. The dependence of  $C_{12}$  on  $r = x_1$  and  $\tau = t_2 - t_1$  is strong, decaying to small values for large  $r, \tau$  and weak on  $R = (r_1 + r_2)/2$  and  $t = (t_1 + t_2)/2$  for typical turbulent systems. In the physics idealization of homogeneous, stationary turbulence  $C_{12} \rightarrow C_{12}(r, \tau)$  independent of  $R$  and  $t$ . It is evident that  $C_{12}(r, \tau)$  is a maximum at  $r = 0, \tau = 0$  where  $C_{12}(0, 0) = \langle \varphi^2 \rangle$ . The space and time separation where  $C_{12}$  falls to low values for large  $|r| \geq \ell_c$  or  $|\tau| \geq \tau_c$  defines the correlation length  $\ell_c$ . These properties provide the definition of the correlation distances  $\Delta x_c, \Delta y_c, \Delta z_c$  and correlation time  $\tau_c$  by choosing a critical point for the fall-off of  $C_{12}/C_{12}(0, 0)$  often taken as the  $1/e$ -point. Often a theoretically more useful definition of the correlation length  $\Delta x_L$  or time  $\tau_c$  is the integral scale length such that  $\Delta x_L C_{12}(0, 0) = \int_{-\infty}^{+\infty} dx C_{12}(x, \tau)$  and  $\tau_c C_{12}(\tau = 0) = \int_0^{\infty} C_{12}(\tau) d\tau$ . Typically the subscripts on  $C_{12}$  are dropped and the particular fields used in the correlation functions are implied.

A clear example of the plasma turbulence correlation function for the electrostatic potential  $\varphi(x, t)$  turbulence is shown in Fig. 9.2 from the experiment of Stenzel (1978). In Fig. 9.2(a) the decay of the two-point correlation function of separation  $\Delta z$  of the two space points along the direction of the plasma current  $j = -enu$  driving the turbulence is shown for all other separations ( $\Delta x = \Delta y = \tau = 0$ ) equal to zero. In Fig. 9.2(b) the constant level contours of  $C_{12}$  of the correlation function for separations in  $\Delta z$  along the current and in an orthogonal direction  $\Delta y$  are shown. Note that the central maximum (approaching 40 units) occurs at the  $\Delta y = \Delta z = 0$  point and the correlation length ( $\Delta y_c \cong 6$  mm) perpendicular to the current is longer than the correlation parallel to the current  $\Delta z = 4$  mm. This anisotropy of the turbulence is a characteristic of plasmas due to the preferred directions of unstable wave propagation associated the geometry and the magnetic fields in the plasma systems.

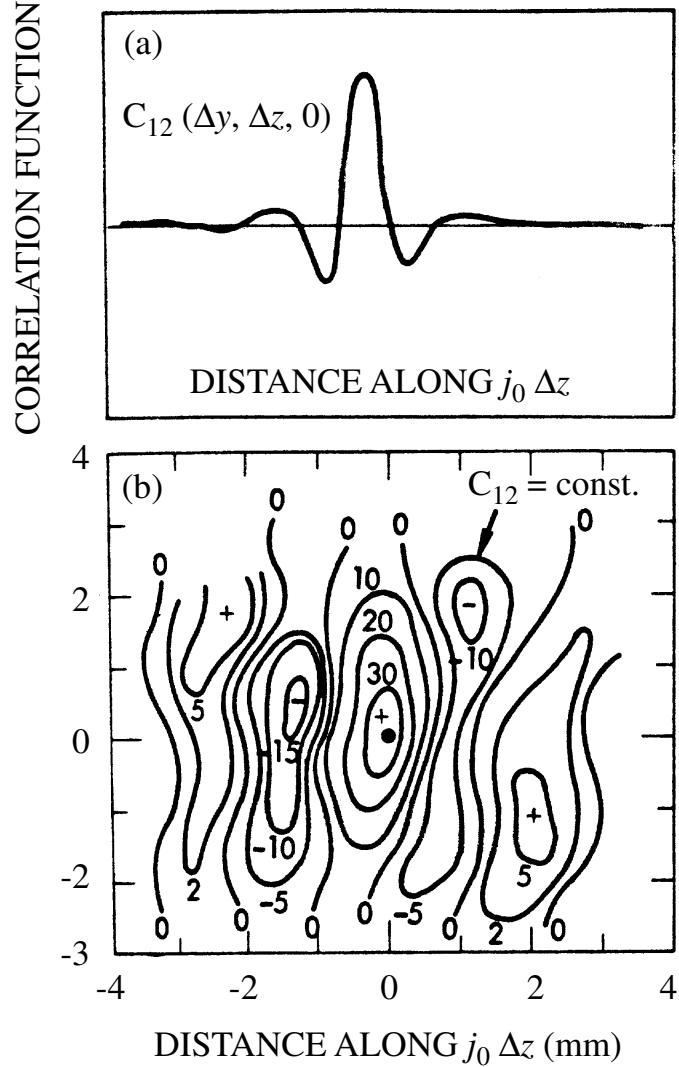


Figure 9.2: Characterization of the turbulent electrostatic potential by the two-point correlation function  $C_{12}$  in Eq. (9.1). (a) Decay of the correlation function with separation of the two points along an axial line parallel to the current; (b) Oscillatory decay of the correlations for two points in the  $y$ - $z$ -plane where the  $\hat{y}$ -direction is perpendicular to me current and  $\hat{z}$  is the parallel direction (courtesy of Stenzel).

For broad-band turbulence there is a simple rule for estimating the correlation time  $\tau_c$  and correlation lengths  $\Delta r_c$  from the spectral width of the power spectrum  $I(k\omega)$  defined by the Fourier transform of the correlation function  $C_{12}(r, \tau)$ . The correlation time is given by  $\tau_c = 1/\Delta\omega$  and the correlation length  $\Delta z = 1/\Delta k_z$  where  $\Delta\omega = \omega_{\max} - \omega_{\min}$ ,  $\Delta k_z = k_{\max} - k_{\min}$

## 9.2. APPLICATION OF GYROKINETIC “FINGERPRINTS” IN IDENTIFYING MICROINSTABILITIES

are the widths of the highest levels of the fluctuation power spectrum  $I(k, \omega)$ . As an example, the ion acoustic turbulence in the Stenzel experiment is shown in Fig. 9.3 where a spectrum consistent with turbulence theory has been reported. The spectral width from the  $1/e$  point is approximately 400 kHz consistent with the directly measured  $\tau_c = 2\mu\text{sec}$  correlation time. Physically, the correlation time  $\tau_c$  is the maximum time interval over which the field, in this case the electrostatic potential, maintains a given structure. In the next correlation time the complexion, or structure, of the field is qualitatively different.

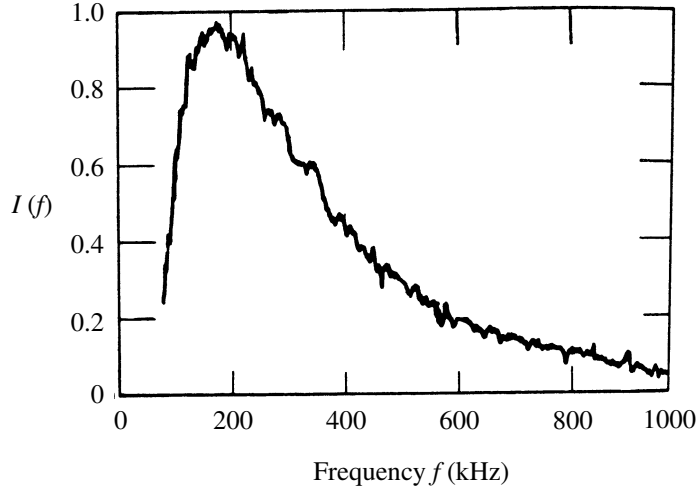


Figure 9.3: Frequency spectrum of ion acoustic turbulence showing the broadband potential fluctuation spectrum with short correlation time  $\tau_c = 1/\Delta\omega \simeq 0.4\mu\text{s}$ . The spectral distribution decreases slightly faster than  $1/\omega$  between the low-frequency cut-off due to nonlinear effects and a high frequency limit due to Landau damping on the thermal ions (courtesy of Stenzel).

The case of plasma turbulence produced by the spatial gradients from its confinement is described. The confinement or trapping of a plasma is produced both in the laboratory and space/astrophysics by magnetic fields that cause the charged particles to gyrate with radius  $\rho_a = m_a v_a / q_a B$  around the local magnetic field  $B(x)$ . The confinement along  $B$  occurs either due to the large increase of  $|B|$  giving rise to the magnetic mirror effect as in Earth’s magnetosphere or due to the field lines forming closed, nested toroidal surfaces as in solar current loops and the laboratory tokamak device. From over 30 years of laboratory research in the tokamak confinement studies of plasma there is a detailed understanding of the intrinsic, irreducible plasma turbulence that develops from spatial gradients. This turbulence is generically called drift wave turbulence and is driven by the cross-field gradients of the plasma density  $\nabla n = -(n/L_n)\hat{e}_x$  and temperature  $\nabla T = -(T/L_T)\hat{e}_x$ . While there are many detailed forms known for the turbulence depending on the plasma parameters, there are three generically distinct types of plasma cross-field diffusivities  $D[\text{m}^2/\text{s}]$  of particles and  $\chi[\text{m}^2/\text{s}]$  for thermal diffusivity. The three functionally distinct forms are: (1) the Bohm diffusivity  $D_B = \alpha_B(T_e/eB)$ , (2) the gyroBohm diffusivity from drift

waves  $D_{\text{dw}} = \alpha_{\text{dw}}(\rho_i/L_T)(T_e/eB)$  where  $\rho_i = (m_i T_i)^{1/2}/eB$  is the thermal ion gyroradius and the (3) collisional turbulence diffusivities  $D_r = \alpha_{\text{rg}}\nu_e\rho_e^2(L_S^2/L_T R_C)$  where  $\nu_e$  is electron-ion collision frequency associated with resistivity  $E_{\parallel} = \eta j_{\parallel}$  along the magnetic field. The Bohm diffusivity varies as  $T/B$  and is documented for the Joint European Torus (JET) in *Taroni, et al.* (1994) and *Erba, et al.* (1995). A modified form, called Taroni-Bohm, of the Bohm scaling of transport has been widely accepted as a standard empirical transport formula for the two large tokamaks JET and JT-60U for many years. The modification is required to get the dependence on the plasma current produced magnetic field to dominate over the externally applied magnetic field. The numerical coefficient  $\alpha_B$  is a low coefficient  $\alpha_B \sim 1/200$ . In contrast, the drift wave transport formulas vary as  $T^{3/2}/B^2 L$  and are documented in theory, e.g., *Horton* (1990) and gyrokinetic simulations with a coefficient  $\alpha_{\text{dw}} \sim 0.3$  [*Dimits, et al.* (2000)]. The third functional form of the diffusivity is that arising from resistive interchange instabilities where  $D_r$  varies as  $x_{\text{rg}} \sim n/T_e^{1/2} B^2$  and has a coefficient  $\alpha_{\text{rg}}$  of order unity [*Wakatani and Hasegawa* (1984), *Scott* (1998), *Rogers, et al.* (1998), *Hallatschek and Biskamp* (2001)]. The coefficients  $\alpha_B$ ,  $\alpha_{\text{dw}}$  and  $\alpha_{\text{rg}}$  are weak functions of many detailed plasma parameters such as  $T_e/T_i$ ,  $L_T/R$ ,  $\beta = 2\mu_0 p/B^2$  and more. Just as in neutral fluid turbulence, there are many degrees of freedom excited in plasma turbulence and there is difficulty in determining the details of these formulas either through theory or numerical simulations. Nonetheless, the years of experience with the tokamak confinement program have led to rather firm general conclusions about the turbulent diffusivities. The most successful approach to modeling the transport has been called the multi-mode approach where all relevant instabilities are assessed at each set of plasma system parameters. Now we give some details of the spatial gradient driven turbulence in magnetized plasma.

### 9.3 Spatial Gradient Driven Turbulence in Magnetized Plasma

In nonuniform, magnetized plasmas the ion acoustic waves are modified into two branches with different parallel phases velocities due to the presence of the diamagnetic currents  $j_a = e_a n_a u_{da}$  required from the  $j_a \times B = \nabla p_a$  force balance. Here, each charged particle species is designated by the subscript  $a$ . The relevant drift velocities  $u_{da}$  for driving the plasma turbulence are the small diamagnetic drift velocities  $u_{da} = T_a/e_a B L_{pa} = (\rho_a/L_{pa})v_{Ta}$  where  $L_{pa}^{-1} = -\partial_x \ln p_a(x)$ . Even for small values of  $\rho_a/L_{pa}$  these diamagnetic currents drive low-frequency ( $\omega \ll e_a B/m_a$ ) waves with  $k$  almost parallel to  $B \times \nabla p_a$  unstable. These waves are called drift waves and their effect is to produce a cross-field transport of particle, energy and momentum through the turbulent  $\mathbf{E} \times \mathbf{B}$  drifts.

## 9.4 Drift waves in the laboratory

The collisional drift waves with growth rates determined by the electrical resistivity  $\eta$  and thermal diffusivity  $\chi_e$  were the first drift waves to be discovered in *Chen* (1965) and thoroughly investigated in *Hendel, et al.* (1968). The identification was made in low temperature steady-state plasmas produced by thermal (contact) ionization of Alkali elements (principally Cesium and Potassium) in long cylindrical devices with closely-spaced Helmholtz coils. Correlations between the observed potential-density waves with the properties predicted by the linear dispersion relation and the single-wave finite amplitude formulas [*Hinton and Horton* (1971)] were used to establish that the radially localized, 10 kHz rotating wave structures were the drift waves. The dimensionless density  $\tilde{n}/n$  and potential  $e\tilde{\varphi}/T_e$  waves are approximately equal amplitude sinusoidal oscillation with  $\tilde{n}$  leading  $\tilde{\varphi}$  by 30° to 45° in phase. Figure 9.4 shows the drift wave potential and density isolines. Vortex dynamics has also been observed in the plasmas produced in these devices called *Q*-machines in the *Hendel, et al.* (1968) experiment. Here *Q* is for quiet, meaning that the plasma fluctuations are not as intense and broad-band as in the toroidal devices of that period. In the experiments of *Pecseli, et al.* (1984, 1985), externally excited vortices of like signs were shown to coalesce into one vortex. Vortices of opposite signs were reported to interact with each other forming a dipole vortex pair.

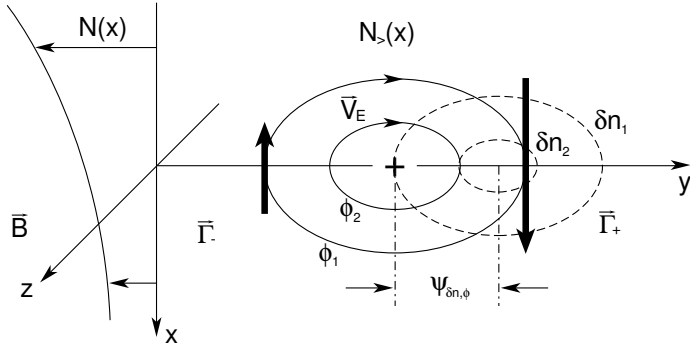


Figure 9.4: A segment of a drift wave fluctuation showing the variation of the electrostatic potential and the density perpendicular to the magnetic field at a given instant of time. The contours of  $\varphi$  in the plane perpendicular to  $B = B\hat{z}$  are the stream lines of the  $\mathbf{E} \times \mathbf{B}$  particle motion. The potential and the density variation are out of phase by  $\psi_{\delta n, \varphi}$ , producing the net downward flux.

A variety of drift-type instabilities relevant to toroidal magnetic fusion devices, including the trapped electron modes by *Prager, et al.* (1974), the trapped ion instability by *Slough, et al.* (1981), the collisionless curvature driven trapped particle mode by *Scarmozzino, et al.* (1986) have been produced and identified in the Columbia Linear Machine.

The drift wave driven by the radial ion temperature gradient in a Collisionless cylindrical plasma was demonstrated in the modified Columbia Linear Machine (CLM) by *Sen, et al.* (1991) by using biased wire screens to create a  $T_{i\parallel}(r)$  gradient sufficient to excite an  $m = 2, 10$  kHz (in the plasma frame) drift wave oscillation. The toroidal ITG mode driven by the magnetic curvature was also produced and identified by *Chen and Sen* (1995) in the same machine.

Drift waves were found in the transient plasmas produced in the multipole confinement machines that were both linear and toroidal devices with strongly varying  $B$ -fields from parallel conductors carrying large currents from external power supplies. The theory for the drift waves in the multipole takes into account the localization of the unstable oscillations to regions of unfavorable gradient- $B$  and curvature particle drifts and the shear in the helical  $\mathbf{B}(x)$ -field [*Ohkawa and Yoshikawa* (1967)]. These experiments provided further evidence for the universal appearance of drift waves in confinement geometries. The correlation of drift wave theory with the multipole and spherator experiments are described in Sec. 3.3 of the *Horton* (1990) review article. The main result to be noted here is that the experiments show that increasing the magnetic shear reduces the fluctuation amplitudes [*Okabayashi and Arunasalam* (1977)]. The multipole devices are unique in being able to continuously vary the magnetic shear parameter strength from zero to order of unity. Even with the strongest magnetic shear, however, the fluctuations were not eliminated.

The magnetic shear plays a central role in the linear and nonlinear theory of the cross-field transport consistent with the role of shear on the fluctuations measured in these experiments. In recent theory and experiments for tokamak confinement devices the combined roles of  $\mathbf{E}_r \times \mathbf{B}$  sheared flows and magnetic shear are known to produce enhanced confinement regimes [*Synakowski, et al.* (1997), *Burrell* (1997), *Hahm* (2002)]. The improved confinement occurs over narrow radial regions giving rise to new confinement regimes with internal transport barriers [*Koide, et al.* (1994), *Levinton, et al.* (1995), *Strait, et al.* (1995)]. The principal tools available for producing these changes in transport is the control of the drift wave turbulence in the system parameters through the programming of the plasma current to control the magnetic shear in  $\mathbf{B}(\mathbf{x})$  and the programming of the neutral beam injectors to control the mass flow shear in the plasma flow velocity  $\mathbf{u}(\mathbf{x})$ . The timing of the auxiliary power, the momentum injector with respect to the Ohmic transformer current is used to determine the plasma regime created.

In tokamaks the identification of drift waves in the core plasma came from the microwave scattering experiments [*Mazzucato* (1976)] and infrared CO<sub>2</sub> laser scattering experiments [*Surko and Slusher* (1976)]. These measured fluctuations were explained in the context of drift waves existing at the mixing-length level of saturation [*Horton, et al.* (1976)] taking into account the response of the trapped electrons in the drift-wave dissipation. Subsequently, many experiments around the world have observed the universal appearance of a broadband of drift wave fluctuations with  $\omega/2\pi \simeq 50$  kHz–500 kHz at  $k \perp = 1 \text{ cm}^{-1}$  to  $15 \text{ cm}^{-1}$  in toroidal confinement devices for both the tokamak and helical-stellarator systems. Many fluctuation and transport studies in toroidal confinement facilities around the world, including TFTR, Alcator, Tore Supra, TEXT, ATF, Heliotron, JFT2M, ASDEX were undertaken in the 1980s and 1990s that have referred these initial findings of drift wave turbulence and the associated radial transport. ASDEX Upgrade experiments have drawn attention to the role of a critical electron temperature gradient in the electron power balance analysis [*Ryter, et al.* (2001ab)]. In the present work we concentrate on

the recent electron transport experiments on Tore Supra where long time steady-state conditions are achieved with a well known power deposition profile and electron temperature profile. About 90% of the power goes through the electrons in the transport zone between the core and the edge plasma. This makes the system particularly simple compared to those regimes where the ions and electrons share the power transport in some complex manner. In addition there have been detailed microwave scattering experiments with polarized beams in these experiments which leads to knowledge of the electron density fluctuations and an less accurate but useful measurement of the magnetic fluctuations due a change in the polarization vector of the scattered microwave beams.

#### 9.4.1 Conditions for transport and propagation of disturbances

Now we analyze the motion of charged particles in the  $\mathbf{E} \times \mathbf{B}$  convection. For the small, localized excess of ion charge shown in Fig. 9.4 the convection

$$v_E = \frac{c\mathbf{E} \times \mathbf{B}}{B^2} \quad (9.2)$$

rotates plasma clockwise around the potential maximum  $\varphi > 0$  which is also the density and electron pressure maximum in the adiabatic response. The motion is clockwise when viewed down the magnetic field line  $\mathbf{B}$ . Now, if the ambient plasma is uniform ( $\partial_x n_z = \partial_x T_i = 0$ ) across the convection zone, then the cell rotates without plasma transport. When the plasma has an  $x$ -gradient of density (pressure), however, there is a rapid transport of the structure along the symmetry direction  $\hat{\mathbf{y}}$  with a small diffusive transport across an  $x = \text{const}$  surface. The speed of the localized structure in Fig. 9.4 along the symmetry direction is approximately the electron diamagnetic drift speed  $v_{de} \equiv cT_e/eBL_n$  where  $L_n^{-1} = -\partial_r \ell n N$ . The analytical description of the net convective flux particle and thermal fluxes across a given surface  $S$  is given by

$$\Gamma_e = \frac{1}{S} \int_S n_a \mathbf{v}_E \cdot d\mathbf{a} = -D_{11} \frac{dn_e}{dx} - D_{12} \frac{dT_e}{dx}, \quad (9.3)$$

$$q_e = \frac{3}{2S} \int_S n_a T_a \mathbf{v}_E \cdot d\mathbf{a} = -D_{21} \frac{dn_e}{dx} - n_e D_{22} \frac{dT_e}{dx}. \quad (9.4)$$

In the absence of the phase shift  $\psi_{\delta n, \varphi} = 0$  in Eq. (9.4), the particle transport vanishes. For different phase shifts the off-diagonal terms in Eqs. (9.3) and (9.4) can add or subtract from the diagonal terms. The situation is shown in Eqs. (9.4) where the heat flux is shown versus the electron temperature gradient. In Sec. 3 we show that the electron power balance studies show that the off-diagonal term produces an inward heat flux contribution that gives a critical gradient above which the heat flux rises to a high level. It should be understood that there are also collisional transport process that would contribute to  $\Gamma_e$  and  $q_e$  but that they are in generally smaller by one to two orders of magnitude than the turbulent fluxes [Shaing (1988)]. The collisional fluxes also exhibit off-diagonal structures [Balescu (1988)].

In the proper set of flux-driving gradient variables the transport matrix has Onsager symmetry [Shaing (1988), Sugama and Horton (1996)]. The matrix is positive definite with  $D_{11}D_{22} - D_{12}D_{21} > 0$ . The positive definiteness of the matrices relating conjugate pairs of driving forces and transport fluxes is developed in detail by Sugama in a series of works on turbulent transport. In typical particle and power balance experimental studies of steady-state discharges the particle and thermal fluxes  $\Gamma$  and  $q$  are determined from the input source of particles and energy and the resulting measured profiles of  $n, T$  to infer the required diffusivities  $D_{ij}$ . For different signs of  $D_{12}$  there are three types of thermal flux versus temperature gradient relations that occur in plasmas. Type I shows a process of transport that starts above a critical gradient, in Type II processes the flux vanishes when the gradient vanishes, and in Type III the flux is finite when the gradient vanishes. The Type III flux occurs when the turbulence is driven by other gradients such as the ion temperature or electron density gradient for ITG or TEM driven fluctuations. Figure 9.5 shows these relationships schematically. The Type I flux gradient relation applies to ETG turbulent transport where one of the linear theoretical formulas gives critical gradient.

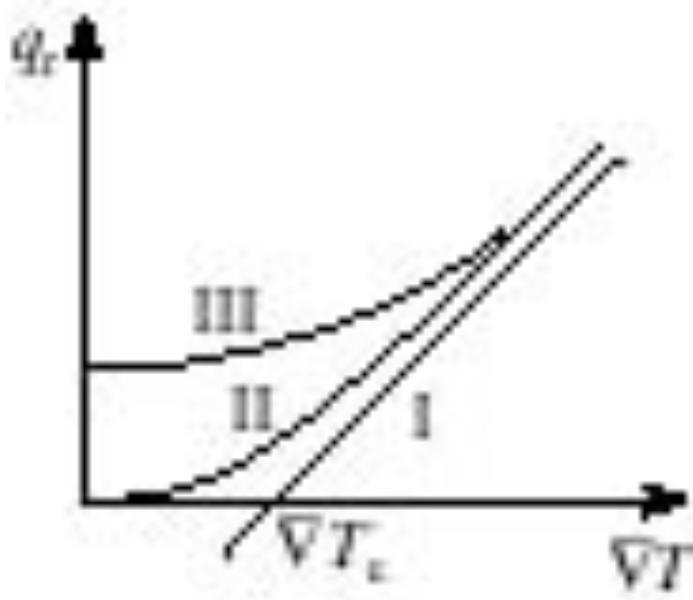


Figure 9.5: The three types of flux-gradient relations that arise in complex plasmas systems with off-diagonal transport diffusivities.

Consider the simple case shown in Fig. 9.4. For the positive electric potential structure in Fig. 9.4 the clockwise  $\mathbf{E} \times \mathbf{B}$  rotation brings higher density  $N_>$  (and higher pressure  $N_>T_e$ ) plasma to the right and lower density  $N_<$  (pressure) to the left resulting in a shift of the maximum density and potential, linked through the electron response by  $\delta n_e \cong n_e(e\varphi/T_e)$ , to the right. The speed of the translation is proportional to the gradient of the density  $L_n^{-1} = -\partial_r \ln N$  and inversely proportional to the strength of the magnetic field  $B$ . The speed also increases with electron

temperature  $T_e$  since the potential fluctuation  $e\varphi$  scales up with  $T_e$ . For a negative potential structure the  $\mathbf{E} \times \mathbf{B}$  rotation is counter-clockwise, but the structure moves to the right with same speed (in the limit of small  $e\varphi/T_e$ ) since now lower density plasma is brought to the right shifting the minimum in that direction. Now, the ion density at this location builds up in the time  $\delta t$  equal to that of the original electron maximum  $\delta n_e = N(e\varphi/T_e)$  when the condition

$$\delta n_i = -\frac{\delta tc\varphi}{B\delta y} \frac{\partial N}{\partial x} = N \frac{e\varphi}{T_e}, \quad (9.5)$$

is satisfied. In the last step we use quasineutrality, taking  $\delta n_i = \delta n_e = N(e\varphi/T_e)$  which is valid for fluctuations that are large compared to the Debye length. During the time  $\delta t$  the convection moves the maximum of the structure to the right by  $\delta y = v_{de}\delta t$  where

$$v_{de} = \frac{\delta y}{\delta t} = -\frac{cT_e}{eBN} \frac{\partial N}{\partial x}. \quad (9.6)$$

The  $x$ -displacement of the plasma during this motion is  $\xi_x = v_x\delta t = -\delta t\varphi/B\delta y$ . When this displacement becomes comparable to  $\delta x$  the motion is nonlinear leading to the formation of nonlinear vortex structures. Locally, the plasma is mixed over the length  $\delta x$  in one rotation period when the amplitude reaches the mixing length level  $\xi_x = \int^t dt' v_{Ex} = \delta x = l_c$ . The nonlinear problem is treated in *Chaos and Structures in Nonlinear Plasmas* by Horton and Ichikawa (1996).

#### 9.4.2 Drift wave diffusivities and the ion inertial scale length

It is conventional in the study of drift waves and transport to introduce gradient scale lengths and reference diffusivities. Thus, the length  $L_n$  is defined as the density gradient scale length through the relation  $1/L_n = -\partial_x \ln N$ . The temperature gradient scale length  $L_T$  is defined similarly. The spacetime scales of the waves lead to two different dimensional scalings for the plasma diffusivities. The reference diffusivities are the Bohm diffusivity

$$D_B = \frac{T_e}{eB}, \quad (9.7)$$

and the drift wave diffusivity

$$D_{dw} = \left( \frac{\rho_s}{L_n} \right) \left( \frac{T_e}{eB} \right), \quad (9.8)$$

also commonly called the gyroBohm diffusivity in reference to the factor  $\rho_s/L_n \ll 1$ . Here  $\rho_s = (m_i T_e)^{1/2}/eB$  is effective gyroradius parameters for hot electrons of  $T_e \gtrsim T_i$ . Clearly, the scaling of the Bohm and gyroBohm diffusivities are markedly different with  $D_B \propto T_e/B$  independent of the system size while  $D_{dw} = T_e^{3/2}/B^2 L$  decreasing with the system size. In short, the Bohm (9.7) scaling arises from *mesoscale* drift wave structures  $\Delta x = (\rho_s L_T)^{1/2}$  and thus is expected near marginal stability [Horton, et al. (1994), Kishimoto, et al. (1996), Garbet and Waltz (1996), Lin

(1998)]. With a minimal model of ITG, *Ottaviani and Manfredi* (1999) investigate the  $\rho_s$  scaling for a constant thermal flux through a turbulent annulus. They observed an inverse cascade to larger elliptical vortices but find that the flux scaling remains gyroBohm. When the convective cells size reduces to scale as  $\Delta x = \rho_s$  the drift wave diffusivity (9.8), commonly called gyroBohm, applies. In defining the dimensionless gyroradius parameter  $\rho_*$ , it is usual to replace the spacetime varying length  $L_n$  with the relatively constant value  $a$  of the plasma minor radius. Thus, a key issue is the scaling of plasma confinement with

$$\rho_* \equiv \frac{\rho_s}{a}. \quad (9.9)$$

[*Waltz, et al.* (1990), *Perkins, et al.* (1993)]. Drift wave theory is able to account for confinement scaling either as  $D_B$  or  $\rho_* D_B$ . Transport dependent on  $\rho_*$  depends on the average mass  $m_i$  of the working gas ions since  $\rho_s = (m_i T_e)^{1/2} / eB$ . The transition between the Bohm and the gyroBohm scaling is a difficult problem, both theoretically and experimentally, that has received recent attention. Simulations by *Furnish, et al.* (1999) give one picture of the transition and those of *Lin, et al.* (1998) give the results of even larger and higher resolution simulations. Both authors report that there is a transition at certain values of  $\rho_*$  which measures the ratio of the microscale size to the global size of the system. The role of large scale computing is settling such issues is made clear by *Lin, et al.* (1998). On the experimental side of the scaling problem, the scaling studies of *Perkins, et al.* (1993), *Petty, et al.* (1995), and *Erba, et al.* (1995) present evidence for the Bohm-like scaling of the turbulent transport. More recent power balance studies in the JET discharge up to 7 MA of plasma current use a model that adds the Bohm and gyroBohm contributions. This is called the JETTO model and is now widely used in transport predictions [*Erba, et al.* (1998)]. Roughly the JETTO model is obtained with  $\chi_e = \alpha_e q^2 (a/L_p) D_B$  and  $\chi_i = \alpha_i x_e + \chi_i^{\text{neo}}$  with  $\alpha_e = 2.1 \times 10^{-4}$  and  $\alpha_i = 3.0$  [*Erba, et al.* (1995)]. Here  $1/q(r) = RB_\theta/rB_T$  gives the local pitch of the helical magnetic sideline.

The relevant system parameters for Tore Supra (TS) and the large Tokamak Fusion Test Reactor (TFTR) are given in Table 9.2. The fluctuation measurement at wave numbers  $k_\perp \lesssim 1 \text{ cm}^{-1}$  requires the techniques of reflectometry [*Doyle, et al.* (1991), *Mazzucato and Nazikian* (1993)] and the indirect method of beam emission spectroscopy as in the *Durst, et al.* (1993)

Table 9.2: Plasma Drift Wave Parameters

Machine	TFTR	TS
magnetic field	4.8 T	2.7 T
major/minor radii	2.45 m/0.80 m	2.30 m/0.75 m
electron temperature	6 KeV	5 keg
density $n_e$ and	$4.0 \times 10^{13} \text{ cm}^{-3}$	$3.6 \times 10^{13} \text{ cm}^{-3}$
gradient length $L_n$	20 cm	20 cm
drift velocity $v_d$	$3 \times 10^5 \text{ cm/s}$	$1 \times 10^5 \text{ cm/s}$
$k$ scattering experiment	$1\text{-}20 \text{ cm}^{-1}$	$1.5\text{--}15 \text{ cm}^{-1}$
$\omega$ scattering experiment	10-500 kHz	10-1000 kHz
to 0.02	0.01 to 0.1	

experiment. Finally, it is important to point out parallels with other areas of physics. The closest and most important parallel to plasma drift waves is the analogy with the Rossby waves and vortices in geophysical atmospheric and oceanographic disturbances with periods long compared to the rotational period of the planet. *Hasegawa and Mima* (1977, 1978) and *Hasegawa, et al.* (1979) develop the limit in which the two models become isomorphic. The correspondence is due to the Coriolis force having the same mathematical form as the Lorentz force. The analogy was also recognized by *Petviashvili* (1977) which led to the first rotating parabolic water tank experiments by *Antipov, et al.* (1982, 1985) in Kurchatov in 1983 in Tbilisi. This aspect of the drift wave Rossby problem is found in the *Horton and Hasegawa* (1994) article in the special issue of CHAOS devoted to such geophysical vortex structures. A recent high resolution simulation of geophysical vortex turbulence is in *McWilliams, et al.* (1999).

### 9.4.3 Resistive drift wave and interchange turbulence

The collisional drift wave is a paradigm for anomalous transport that has been extensively investigated with many different modelings. A particularly simple 2D-model, called the *Hasegawa–Wakatani* (1983) model with an adiabaticity parameter  $\ell$  has been investigated by *Wakatani and Hasegawa* (1984), *Krommes and Hu* (1994), *Sugama, et al.* (1988), *Gang, et al.* (1991), *Koniges, et al.* (1992), *Biskamp, et al.* (1994), and *Hu, et al.* (1997). To understand the origin of the simple  $\alpha$  model and to appreciate its limits we briefly present the 3D resistive drift model. For finite resistivity  $\eta = m_e \nu_e / n_e e^2$  the parallel current carried by the electrons in Eq. (9.10) yields  $j_{\parallel} = -(n_e e^2 / m_e \nu_e) \nabla_{\parallel}(\varphi - T_e / e \ell n n)$  using the isothermal approximation  $\delta p_e = T_e \delta n_e$ . The collisional drift wave equation follows from the divergence of the current  $\nabla \cdot \mathbf{j} = 0$  with the divergence of the polarization current  $j_p$  balancing the divergence of  $j_{\parallel}$  through  $\nabla \cdot \mathbf{j}_p = -\nabla_{\parallel} j_{\parallel} = \eta^{-1} \nabla_{\parallel}^2 (\varphi - \frac{T_e}{e} \ell n n)$  and the electron continuity equation. In other words the dynamical equation for the field-aligned vorticity  $\zeta = \mathbf{b} \cdot \nabla \times \mathbf{v}_E = c \nabla_{\perp}^2 \varphi / B$  is given by the conservation of charge in the quasineutrality limit. The rotational part of the plasma momentum for the vorticity  $\nabla^2 \varphi$  is equivalent to the current closure equation. The vorticity equation and the electron continuity equation give, in dimensional form

$$\frac{m_i n c}{B_0} \frac{d}{dt} \nabla^2 \varphi = \frac{B_0}{c} \nabla_{\parallel} j_{\parallel} + \hat{\mathbf{z}} \cdot \nabla p_e \times \nabla \Omega, \quad (9.10)$$

$$\frac{d}{dt} (n_0 + n_1) = \frac{1}{e} \nabla_{\parallel} j_{\parallel} + \frac{c T_e n_0}{e B_0} \hat{\mathbf{z}} \cdot \nabla \left( \frac{n_1}{n_0} - \frac{e \varphi}{T_e} \right) \times \nabla \Omega, \quad (9.11)$$

where  $\nabla \Omega$  is the effective  $\mathbf{g}$ -force used to relate the curvature and gradient- $B$  effects to the classical Rayleigh–Taylor instability. The computation of  $\Omega(r)$  for the average curvature of the magnetic field line is extensively used in stellarator/heliotron research [*Carreras, et al.* (1987)]. The derivatives on the left side of Eqs. (9.10) and (9.11) are the  $\mathbf{E} \times \mathbf{B}$  convective derivatives defined by  $df/dt = \partial_t f + \mathbf{v}_E \cdot \nabla f$ .

The coupled vorticity and density equations Eqs. (9.10) and (9.11) have a conserved potential

vorticity  $\zeta$  given by

$$\zeta = \frac{m_i c^2}{e B^2} \nabla_{\perp}^2 \varphi - \ln n n_0 - \frac{n_1}{n_0} - \Omega, \quad (9.12)$$

which generalizes the conserved vorticity  $\nabla_{\perp}^2 \varphi$  in 2D Euler fluid. It is useful to first consider the dimensionless form of the model equations (9.10) and (9.11) in global coordinates before using the local drift wave units  $\rho_s$  and  $L_n/c_s$ . Using the minor radius  $a$  for the cross-field  $B_0 \hat{z}$  dimensions, the major radius  $R$  for the dimensionless  $z/R \rightarrow z$  and time in units  $\omega_{ci} t (\rho_s/a)^2 \rightarrow t$  [equivalent to  $(cT_e/eBa^2)t \rightarrow t$ ], one finds that the natural amplitude variables are  $e\varphi/T_e = \varphi$  and  $n_1/n_0 = n$ , and the dimensionless parameters of the model are  $\epsilon = a/R$ ,  $\rho = \rho_s/a$ ,  $\nu = \nu_e/\omega_{ce}$ . The dimensionless model is then

$$\rho^2 \frac{d}{dt} \nabla_{\perp}^2 \varphi = \frac{\epsilon^2}{\nu} \nabla_{\parallel}^2 (n - \varphi) - g \frac{\partial n}{\partial y} + \mu \nabla^2 \varphi, \quad (9.13)$$

$$\frac{dn}{dt} = \frac{\epsilon^2}{\nu} \nabla_{\parallel}^2 (n - \varphi) + \partial_x \ell n n_0 \frac{\partial \varphi}{\partial y} - g \frac{\partial}{\partial y} (n - \varphi) + D \nabla^2 n, \quad (9.14)$$

where  $g = d\Omega/dr$ . This 3D model has resistive drift waves driven by the density gradient  $(\partial_x n_0)^2$  through the charge separation from finite  $k_{\perp}^2 \rho_s^2$  and the resistive interchange driven modes from  $\omega_* \omega_D > 0$  where  $\omega_D = (ck_{\theta} T/eB)(d\Omega/dr)$  is the averaged grad- $B$ /curvature drift frequency [Chen, et al. (1980)]. The linear eigenmodes are of two types: localized to the rational surfaces where  $k_{\parallel} = 0$  and global modes [Sugama, et al. (1988), Hong, et al. (1991)].

The electric potential has the important property of developing an  $m = 0/n = 0$  component with a well-defined circular null surface. This  $\varphi_{0,0}(r, t) = 0$  surface partially blocks the turbulent losses from the core of the cylindrical model. For stellarators the  $m = 1, n = 1$  rational surface is near the edge of the plasma and the dominant modes in this simulation are the  $m = 3/n = 2$  and  $m = 2/n = 1$  fluctuations and the  $m = 0/n = 0$  background profile for  $v_{\theta} = -cE_r/B$ . These simulations with  $\nu_e/\omega_{ce} = 1.4 \times 10^{-4}$  are too collisional to apply to the edge of tokamaks with  $I > 1$  MA confinement devices (where  $\nu_e/\omega_{ce} \lesssim 10^{-6}$ ).

#### 9.4.4 The impact of rational surfaces on radial heat transport in TJ-II

In this work, we study the outward propagation of temperature perturbations. For this purpose, we apply an advanced analysis technique, transfer entropy, to ECE measurements performed in ECR heated discharges at the low-shear stellarator TJ-II. We observe that the propagation of these perturbations is not smooth, but is slowed down at specific radial positions, near ‘trapping zones’ characterized by long time lags with respect to the perturbation origin. We also detect instances of rapid or instantaneous (nonlocal) propagation, in which perturbations appear to ‘jump over’ specific radial regions. The analysis of perturbations introduced in a resistive magnetohydrodynamic model of the plasma leads to similar results. The radial regions corresponding to slow radial transport are identified with maxima of the flow shear associated with rational surfaces (mini-transport barriers). The nonlocal interactions are ascribed to MHD mode coupling effects

[*van Milligen, et al. (2017)*].

*Wakatani, et al.* (1992) extend the investigation of the model (9.13)-(9.14) to include an externally-imposed electric field  $E_r(r)$  exceeding the strength of self-consistently generated field from the  $m = 0/n = 0$  modes. The  $E_r < 0$  field suppresses the turbulence during the growth phases, but produces only a weak reduction of the flux in the saturated state. The collisionality dependence of the particle flux is shown to increase with  $\nu_e$  for  $\nu/\omega_{ce} < 10^{-3}$  and then to increase as  $\nu_e^{1/3}$  for  $\nu/\omega_{ce} > 10^{-3}$ . The numerical treatment of the stabilizing role of sheared flows is subtle in that the problem of resolving the low- $k$  modes giving fluctuating sheared flow requires a high density of small  $k_y$  modes. *Hallatschek* (2001) has carried out convergence studies and concludes that often the role of shear flow damping of the turbulence is over estimated since the  $L_y$  box size is not taken large enough to have adequate resolution of the low  $k_y$  condensation of turbulent energy. With resistive interchange turbulence Hallatschek carries out high resolution simulations and finds a condition for sufficient density of the low- $k$  modes. The nature of this turbulence interaction with the shear flow is investigated for toroidal ITG modes by *Li and Kishimoto* (2002). These authors confirm earlier theoretical studies that show there is a bursting or intermittent nature to the shear generation through the turbulent Reynolds stress. Thus, the  $\chi_i$  and the level of the turbulence generated component of the sheared flows undergo relaxation oscillations controlled by the strength of the instability and the magnitude of the shear flow damping. This generation of zonal flows behavior persists but is much weaker for the short scale electron temperature gradient driven turbulence.

In the widely-investigated 2D model of the Hasegawa-Wakatani equations (9.13)-(9.14) the operator  $\nabla_{\parallel}^2 \rightarrow -\bar{k}_{\parallel}^2$  or  $-1/\mathcal{L}_c^2$ , where  $\bar{k}_{\parallel}$  is the relevant mean parallel wave number and  $\mathcal{L}_c$  is the connection length to the divertor end plates in the scrape-off layer (open field lines) modeling. For the interior tokamak field lines this reduction seriously limits the applicability due to loosing the information on the closeness of the helical pitch of the magnetic field to the twists of the fluctuations following the toroidal direction. This resonance of the field pitch to that of the fluctuations is a key player in numerous effects including (1) the condensation of the turbulence to large-scale zonal flows described above and (2) the response of the density as adiabatic or MHD-fluid like. For 2D turbulence models the parameter  $c\ell = k_{\parallel}^2 T_e / m_e \nu_e \omega_0$  measures the parallel electron diffusion in a characteristic wave period  $(1/\omega_0)$ .

The space-time units are changed to the local scales of  $\rho_s$  and  $L_n/c_s$  in these 2D studies. The standard form of the Hasegawa-Wakatani 2D model is then

$$\frac{d}{dt}(\nabla^2 \varphi) = \alpha(\varphi - n) + \mu \nabla^4 \varphi, \quad (9.15)$$

$$\frac{dn}{dt} = -\kappa \frac{\partial \varphi}{\partial y} + \alpha(\varphi - n) + D \nabla^2 n, \quad (9.16)$$

where the viscosity  $\mu$  and  $D$  are taken small, but finite to absorb all fluctuation energy reaching the smallest resolved space scales in the simulation system. The system's strong turbulence features at small  $\alpha$  with  $\alpha/\bar{\omega} \sim 1$  where  $\bar{k}, \bar{\omega}, \bar{\gamma}$  are taken at the peak of the energy spectrum. Here the overbar on  $k, \omega, \gamma$  denotes a mean value near the peak of the energy spectrum  $E_k$ . One can show

that  $\bar{k} \approx \alpha^{1/3}$ ,  $\bar{\gamma} \approx \alpha^{1/3}$  and that  $E_{\bar{k}} \simeq \bar{\gamma}^2/\bar{k}^3 \simeq 1/\alpha^{1/3}$  [*Hu and Krommes (1994)*]. In the large  $\alpha$  limit the density  $n \rightarrow \varphi(1 + \mathcal{O}(1/\alpha))$  approaches the adiabatic limit and a weaker turbulence appears with  $E_k \simeq \bar{\gamma}\omega/\bar{k}^3 \approx 1/\alpha$  since  $\bar{\gamma} \sim 1/\alpha$ , and  $\bar{k} = \alpha^0$  and  $\bar{\omega} = \alpha^0$  independent of  $c\ell$ . These  $\alpha$ -scalings in the small- $\alpha$  and large- $\alpha$  regimes have been verified by direct numerical simulation and the statistical closure method.

In the quasi-2D equations (9.15)–(9.16), the new parameter  $\alpha = k_{\parallel}^2 T_e / m_e \nu_e \omega_0$  determines the properties of the waves. For  $\alpha \gtrsim 1$  the electrons tend to the Boltzmann distribution  $\bar{n} = e\varphi/T_e$  and the Hasegawa–Mima equation is recovered. The Hasegawa–Mima equation is isomorphic with the Rossby wave equation for high Rossby number geostrophic flow in the mid-latitudes [*McWilliams, et al. (1999)*]. There is a strong dual cascade in this equation with anisotropy in the north–south or radial direction. The anisotropy leads to zonal flows.

Plasma turbulence appears as ubiquitous as plasma itself. In space, solar and astrophysical plasmas show many varied forms of plasma turbulence ranging from large-scale Magnetohydrodynamic (MHD) turbulence [*Biskamp (1997)*] to the smallest Debye length scale Langmuir turbulence. For example, the magnetic energy released during solar flares heats and accelerates the plasma in the solar corona. Electrons on the open coronal magnetic field lines caused by large scale MHD reconnection events stream at relativistic speeds into the interplanetary plasma. The electrons beams drive Langmuir turbulence creating intermittent bursts of radio noise known as Type III radio sources. The peculiar intermittency of Langmuir turbulence called nonlinear wave collapse was first described by *Zakharov (1972)*. The phenomenon of nonlinear wave collapse is reviewed by *Robinson (1997)* for a wide range of laboratory and space physics settings. The general theoretical analysis of wave turbulence for plasmas and neutral fluids is given in *Zakharov, et al. (1992)*.

We have developed, based on the oscillating-center transformation, a general theoretical approach for self-consistent plasma dynamics including, explicitly, effects of nonlinear (higher-order) wave-particle resonances. A specific example is then given for low-frequency responses of trapped particles in axisymmetric tokamaks. Possible applications to transport as well as nonlinear wave growth/damping are also briefly discussed [*Chen and Zonca (2019)*].

#### 9.4.5 Short wavelength drift wave turbulence

Short wavelength fluctuations  $k \perp \rho_i \gg 1$  with finite electron inertia are driven unstable by the electron temperature gradient. The modes are electron analogs of the better studied ion temperature gradient modes often called ITG modes. Their properties are developed in *Lee, et al. (1987)* and *Horton et al. (1988)*. The short wavelength turbulence produces the electron thermal diffusivity given by

$$\chi_e = 0.3 \left( \frac{r}{R} \right)^{1/2} \frac{v_e}{R} \frac{c^2}{\omega_{pe}^2},$$

which explains the widely-observed  $\tau_E \propto n_E a^2 R$  scaling of the energy confinement time. Recently, there have been many simulation studies of the short wavelength turbulence to understand the

coupling to the electromagnetic fluctuations that produce coherent structures on the scale of the collisionless skin depth  $c/\omega_{pe}$ . In typical tokamaks this length is order a few millimeters and is smaller than the standard drift-wave turbulence that is on the scale of several centimeters. The reason the smaller scale turbulence can compete in its ability to transport plasma is that the correlation times are smaller since the modes involve electron dynamics. Studies of the electron transport in a spectrum of ETG electromagnetic waves shows the stochasticization of the guiding center orbits and the rapid transport of the electron thermal energy [Kim, et al. (1990)]. Recent self-consistent field simulations include *Idomura, et al.* (2000), *Jenko, et al.* (2000, 2001), *Dorland, et al.* (2000), and *Li et al.* (2002). It is found that, unlike in the analogous case of ITG turbulence, the turbulent electron heat flux significantly exceeds the simple mixing length estimate, using the scale length that maximizes the growth rate. The mechanism is identified as the formation of highly elongated radial vortices (“streamer”), instead of zonal flows as in the case of ITG, when the perturbations develop nonlinearly. The streamers lead to very effective cross-field transport while the zonal flows reduce it. This results in the discussion on the differences between ITG and ETG turbulence. The electromagnetic secondary instabilities in ETG turbulence are investigated in recent theoretical work of *Holland and Diamond* (2002). The possibilities of magnetic secondary instabilities (zonal magnetic fields and magnetic streamers) are studied as novel potential mechanisms for electron transport regulation and enhancement, respectively. A crucial issue raised in these works is that of pattern selection for both ITG and ETG turbulence, that is, whether zonal modes or streamers are preferentially generated. At this time, these issues are unsolved and remain open challenges to the magnetic fusion community.

A variational method is introduced to analyze the transmissivity of an electromagnetic wave propagating in the magnetized plasma sheath. The plasma density is modeled by two parabolic inhomogeneous regions separated by one homogeneous region. The Lagrangian density of the system is constructed based on the fluid energy density and the electromagnetic energy density. The total variation of the Lagrangian density is derived. The fluid and electromagnetic fields are numerically solved by expansion in piecewise polynomial function space. We investigate the effect of an external magnetic field on the transmissivity of the electromagnetic wave. It is found that the transmissivity is increased when an external magnetic field is applied. The dependence of transmissivity on the collision frequency between the electrons and the neutral particles has also been studied. We also show that the external magnetic field causes a shift in the critical frequency of the plasma sheath [*Chen, et al.* (2019)].

In the efforts to understand the differences and possible correlation between the short wave length ( $k\rho_e \sim 1$ ) and the intermediate wave length ( $k\rho_i \sim 1$ ) instabilities and turbulence, the instabilities of continuous wavelength spectrum from the short to the intermediate are studied by *Smolyakov, et al.* (2002) and *Hirose, et al.* (2002). The unstable modes of  $k_y\rho_{i,e} > 1$  are identified as short wavelength ITG and ETG modes, respectively. In contrast to the conventional ITG and ETG modes, the new modes require both ion and electron temperature gradient higher than certain thresholds. In addition, the short wavelength modes in toroidal geometry require a minimum magnetic shear as a driving force. It is claimed that the short wavelength ITG modes driven turbulences may induce higher electron thermal transport than the ETG turbulence does and, therefore, are responsible for the anomalous electron thermal transport experimentally

observed.

The dependence of the critical temperature gradient on other plasma parameters such as temperature ratio ( $T_e/T_i$ ) , magnetic shear and safety factor for toroidal ETG instability is studied and formulas are given by *Jenko, et al.* (2001) and *Dong, et al.* (2002a,b) . An interesting point from *Dong, et al.* (2002a,b) is that the critical electron temperature gradient increases from  $R/L_{Te} \sim 3$  to  $R/L_{Te} \sim 10$  dramatically when the temperature ratio  $T_e/T_i$  increases from 1/3 to 3. This is in great favor of  $\alpha$  particle heated burning plasmas if it is verified by future high  $T_e/T_i$  experiments. In addition, a brief estimate for ASDEX Upgrade and Tore Supra experiments [*Ryter, et al.* (2001a,b), *Hoang, et al.* 2001)] on the critical gradient is given and compared with the results from solving the integral eigenvalue problem for the ETG modes. The theoretical results are in the range of the experimental observations.

The electron thermal transport experiments on eight tokamak devices (ASDEX–Upgrade, COMPASS–D, FT–U, JET, TCV, Tore Supra, RTP and AUG) are summarized by *Ryter, et al.* (2001a). The critical gradients, above which the measured electron thermal diffusivity and the calculated growth rates of drift instabilities increase dramatically, are identified as  $R/L_{Te} \sim 8\text{--}12$  that falls right into the range of calculated critical electron temperature gradient for toroidal ETG instabilities by *Dong, et al.* (2002a).

Tokamak Fusion Test Reactor (TFTR) discharges with high core temperatures  $T_{e0} \lesssim 8\text{ KeV}$ ,  $T_{i0} \lesssim 25\text{ KeV}$  from the improved confinement regime (enhanced reversed shear) and high neutral beam heating power (28 MW) has small scale fluctuations at  $k_\perp \cong 0.85\omega_{pe}/c \sim 5\rho_i^{-1} \simeq 9\text{ cm}^{-1}$  [*Wong, et al.* (1997)]. These electron density fluctuations  $\langle \delta n_e^2 \rangle_k$  are measured by scattering a microwave beam with  $|\Delta\mathbf{k}| = k_\perp = 8.9\text{ cm}^{-1}$  from the core plasma continuously in time. Power balance studies are then performed to determine the electron thermal diffusivity  $\chi_e(r, t)$  required to give the measured  $n_e, T_e(r, t)$  profiles from the fraction of the beam power deposited into the electrons. The resulting  $\chi_e(r, t)$  is shown to track the fluctuation level over a period of one second while  $\chi_e$  varies from 0.5 to  $4\text{ m}^2/\text{s}$ .

A related instability based on the electron inertial in the nonlinear Ohm's law and a single pressure field driving interchange instability in the unfavorable magnetic curvature is called the current diffusive ballooning mode. *Yagi and Horton* (1994) develop the properties of this turbulence estimating the thermal diffusivity as

$$\chi = f(s) \frac{c^2 q^2 v A}{\omega_{pe}^2 R} \left( -R \frac{d\beta}{dr} \right)^{3/2}$$

where  $f(s)$  is a complicated function of magnetic shear  $s$  obtained from the ballooning mode calculation of  $\langle k_x^2 \rangle$ . Evaluation of the current diffusive  $\chi$ , in the form given by *Fukuyama, et al.* (1994), is compared with a standard ITG transport model for a high–beta poloidal JT–60U discharge is given in *Horton, et al.* (1997). The importance of the electron transport at the  $c/\omega_{pe}$  scale has been pointed out and investigated by many authors: *Ohkawa* (1978), *Kadomtsev and Pogutse* (1979), *Lee, et al.* (1987), *Horton, et al.* (1988, 1989, 1990b, 2000), *Connor* (1993), *Itoh, et al.* (1994), *Fukuyama, et al.* (1994), *Idomura, et al.* (2000), *Hirose and Elia* (2002), *Holland and Diamond* (2002), and *Dong, et al.* (2002a,b) . It is the authors' view that these

fluctuations are the standard mechanism, albeit independently understood, for electron thermal transport. If this is indeed the case, then the electron fluctuations may be responsible for holding the electron temperature down in discharges where the ion confinement is improved dramatically. Low electron temperatures in the large D-T fusion experiments are one of the main reasons that those experiments fell short of expectations. Due to the importance of the electron turbulent transport, we discuss the Tore Supra experiments in the next section. Tore Supra has optimal plasma conditions for the study of turbulent electron transport.

#### 9.4.6 Tore Supra Hot Electron Plasma Transport Data Analysis

Tokamak discharges with core electron heating dominating ion heating provide valuable models for the transport regimes in a burning fusion reactor where alpha particle slowing down through electron collisions is the dominant heating power  $P_{\alpha e}$ [MW/m<sup>3</sup>] for thermal plasmas. The long-time steady-state discharges produced in Tore Supra with dominant, core localized electron heating provide a unique opportunity for the study of electron transport under conditions similar to burning plasmas in fusion reactor of a tokamak confinement system. In general, Radio Frequency (RF) heating systems in Tore Supra provide flexibility of driving up the plasma temperature and of controlling plasma current profiles. The Fast Wave Electron Heating (FWEH) provides high-performance discharges with the largest increase of the core electron temperature over the ohmic temperature  $T_e^{\text{OH}}$ , compared with the alternative Ion Cyclotron Resonant Heating (ICRH) and the Lower Hybrid (LH) wave heating mechanisms. FWEH shows the longest plasma energy confinement times  $\tau_E$  [Hoang, *et al.* (1998)]. The universal feature of toroidal confinement arising from temperature gradient driven turbulence controlling the diffusivities is that the total electron stored energy  $W_e$  and the global energy confinement time  $\tau_E$  show a strong degradation as the total input heating power  $P$ , taken as the sum of ohmic and injected RF powers, increases. This behavior is shown in the standard empirical L-mode scaling law for the global energy confinement time as a function of the system parameters. A large international database supports the standard L-mode laws of tokamak operation. Improved confinement is then measured by defining the H-factor through the ratio  $H = \tau_E / \tau_E^L$ . Here H stands for “high confinement” and the H-factor is the ratio of the improved  $\tau_E$  to the standard  $\tau_E^L$ . By varying current profile and peaking density profile tokamaks can achieve H-factor from 1.6 to 2.0 and even higher for special advanced operational scenarios. For Tore Supra with FWEH, the discharge parameters range over  $2 \text{ MW} \leq P \leq 10 \text{ MW}$  with  $0.4 \text{ MA} \leq I_p \leq 0.9 \text{ MA}$  at two values of the toroidal magnetic field  $B_\varphi = 2.0 \text{ T}$  and  $2.8 \text{ T}$ . The scaling results show that an improved confinement factor  $H \simeq 1.6$  is obtained when the global energy confinement time is compared with the ITER97-L-mode [Kaye (1997)] thermal energy confinement scaling law. The improved confinement arises from controlling magnetic shear through RF heating. The current profiles that produce low central magnetic shear and high outer confinement zone ( $\rho = r/a > 0.6$ ) shear produced the largest H-factors. The ETG thermal diffusivity  $\chi_e$  formula, based on the existence of critical electron temperature gradient, is shown to be consistent with the power balance  $\chi_e^{\text{PB}}$  when  $\nabla T_e$  exceeds the critical value  $(\nabla T_e)_{\text{crit}}$ , by a factor of two or more [Hoang, *et al.* (2001)]. There is clear evidence in both the power balance  $\chi_e$

and the measured density and magnetic fluctuations for a critical electron temperature gradient of about 3 KeV/m in the FWEH database. The critical gradient is observed to increase with magnetic shear and be independent of the magnetic field, that is consistent with what is known from electromagnetic drift wave theory [*Horton, et al.* (1988, 2000)]. The electromagnetic drift wave turbulence theory successfully interprets the high-power FWEH Tore Supra database of more than 40 well-documented discharges. The working gas is typically helium and the plasma pressure satisfies  $m_i\beta_e/m_e \approx 40$  at the mid-radius  $r = a/2$ . Thus,  $v_A \ll v_e$  and the drift wave is electromagnetic, with an associated  $\delta B_x/B \sim 10^{-5}$  fluctuation.

Gas spark gap is widely used in any pulsed power system as the key element which directly determines its repetitive performance and output characteristics. Among many factors of three-electrode gas spark gap, background pressure is of much importance in determining the gap performance parameters such as the delay and jitter, and relevant studies have been rarely performed. A magnetohydrodynamic model of the arc in gas spark gap is built and the effects of background pressure on the arc characteristics are discussed in this paper. It is demonstrated that a higher background pressure may result in radial compression of the arc column, a higher arc voltage, and a lower declination rate of arc resistance in the first quarter cycle. Relevant simulation data would be helpful for the optimization of the design of gas spark gap [*Huang, et al.* (2019)].

#### 9.4.7 Electron transport theory

The existence of a broadband of drift-type fluctuations in Tore Supra is documented by the laser scattering experiments [*Devynck, et al.* (1993)]. The long wavelength end of the scattering measures the region of the ITG trapped electron spectrum while the short wavelength end measures the ETG type of turbulence. If one assumes that the modes are electrostatic in nature, then the stability analysis of *Ross, et al.* (1977) applies. One finds that the modes are unstable for both zero electron temperature gradient and for a finite electron temperature gradient. There is a strong increase of the short wavelength electrostatic growth rate with  $\eta_e$  that leads those authors to state that for  $\eta_e > 2/3$  the short wavelengths modes are strongly unstable. They search for stabilization by including the ion-ion collisions.

In contrast, the ion temperature gradient is the dominant controlling parameter for the long wavelengths as is easily seen in the work of *Rewoldt and Tang* (1990). In that work the growth rate is shown to have a substantial value down to zero temperature gradient ( $\eta_i = \eta_e = 0$ ) for the long wavelength modes. The Rewoldt and Tang stability analysis is historically interesting in that it shows clearly the improved confinement properties of the proposed high field burning plasma experiment called the Compact Ignition Tokamak or CIT for short. This same theme has emerged again and a new more advanced high field compact ignition tokamak is shown to lead to ignition in *Hu, et al.* (2002). Rewoldt and his collaborators show how the growth rates and ratios of the particle and thermal fluxes vary for realistic tokamak models. Due to the renewed interest in the compact high field ignition experiments a timely work to revisit is *Rewoldt and Tang* (1990) in which the growth rates were worked out for CIT tokamak. In this work they used MHD equilibria

coupled with BALDUR transport values of  $\eta_i$  and  $\eta_e$  to study the collision and the  $\eta_i$  dependences of the complete matrix eigenvalue problem for coupled ITG and trapped electron modes. They clearly show that the growth rates are greatly suppressed for the high-density regime of a compact ignition tokamak in their figures 1 and 2. For high densities, where the bounce frequency of trapped electrons is lower than the collision frequency, the growth rate threshold appears in  $\eta_i$  as in the classical adiabatic electron ITG theory. When the density is lowered to that typical of the standard 5t field tokamaks like TFTR and JET, the drift waves remain unstable with a substantial growth rate even at zero values of the  $\eta_i$  parameter due to the density gradient. This is due to the wave changing to rotate in the electron diamagnetic direction and being destabilized with the trapped electron resonant wave interactions. The ballooning mode eigenfunctions are reported along with the ratios of the particle flux and the electron heat flux divided by the larger ion thermal flux. By taking these ratios of the turbulent fluxes the uncertainty in the amplitude of the fluctuations is reduced although not entirely eliminated due to the nonlinear shift of the spectrum to wavelengths longer than those that maximize the growth rate. The subject was studied again by Dong, *et al.* (1997). In toroidal collisionless high temperature plasmas, ITG and Trapped Electron (TE) modes are shown to be weakly (strongly) coupled when both the temperature gradients and the driving mechanism of the TE are moderate to strong (weak but finite). In the regime of strong coupling, there is a single hybrid mode unstable for all ITG in plasmas with positive magnetic shear. In the weak coupling case, two independent unstable modes, one in the ion and the other in the electron diamagnetic direction, are found to coexist. In either situation, a negative magnetic shear exerts a strong stabilizing influence; the stabilizing effect is considerably enhanced by the presence of trapped particles. It is predicted that for plasmas of given parameters, it will be much hard to simultaneously excite the two modes in a toroidal magnetic field with negative shear.

In view of recent short wavelength theory and simulations, it is clear that these small scale modes are a key mechanism for producing the universally observed anomalous electron thermal losses in tokamaks that was found from the beginning of tokamak history [Kadomtsev (1992)]. We analyze the turbulent electron heat loss in Tore Supra under the hypothesis that the short wavelength electromagnetic fluctuations arise from the well-known mechanisms of the temperature gradient driven toroidal drift wave instabilities [Horton, *et al.* (1988, 2000)]. The overview of the drift-wave fluctuation spectrum given in Fig. 6 of Horton, *et al.* (1988) is evaluated here in detail for TS to show the multiple space-time scales. Four important wavelengths scales shown along the  $x$ -axis in that figure are computed for a typical Tore Supra plasma (TS shot # 19542). Now we investigate the properties of these fluctuations in Tore Supra. Two of the characteristic cross-field wavelengths are given by the wave numbers  $k_y^m$  that maximize the linear theory growth rates  $\gamma_{k_y}^{\text{ITG}}$  and  $\gamma_{k_y}^{\text{ETG}}$  for the ion and electron temperature gradient driven instabilities respectively. The third major scale lengths corresponds to the wavelengths that mark the transition from the short scale  $\nabla T_i$  and  $\nabla T_e$  directly driven turbulence that is well described within the framework of quasi-two-dimensional plasma turbulence to the longer wavelength regime where the three dimensionality of the turbulence dominates. The 2D to 3D transitional cross-field scale length is given by the conditions  $\omega_{*i} = k_{\parallel} v_i$  for ITG and by  $\omega_{*e} = k_{\parallel} v_e$  for ETG where  $k_{\parallel} = 1/qR$  is fixed by the toroidal geometry and  $q = rB_T/RB_\theta$ . The inverse cascade of the quasi-two-dimensional system is arrested at this  $k_{\perp}$ -scale since the fluctuations become intrinsically three-dimensional at this and larger

cross-field scale lengths. The FLR fluid simulations [Horton (1990)] show that the  $k_y$  wavenumber spectrum changes shape, developing a flat local maximum at this transitional scale where  $k_{\perp} \simeq \ell_c^{-1}$ . Physically, it is clear that the nonlinear dynamics of fluctuations changes character when the time to propagate the ion or electron acoustic wave around the torus is shorter than the corresponding drift wave period. The nonlinear matrix elements for the mode coupling become dominated by  $k_{\parallel}^2$  rather than  $k_{\perp}^2$  when the turbulence scale satisfies  $k_{\perp} < \ell_c^{-1}$ . Evidently, high  $q$  extends the range of the quasi-two-dimensional turbulence producing a higher turbulent thermal diffusivity through the extended range of the inverse cascade  $\ell_c = qR/\Delta k_y L_t = q\ell_c R/L_T$ . Further discussion of this inverse cascade effect is given in Ottaviani and Manfredi (1999). With the inverse cascade ITG turbulence spectrum, two successful applications with interpretative simulations for discharges in the ITER profile database are reported by Redd, *et al.* (1997). Subsequently, Erba, *et al.* (1999) confirm and extend these investigations. These inverse cascaded transport formulas are called the OHE (Ottaviani-Horton-Erba) model [Ottaviani, *et al.* (1997)] for the ion transport channel. Simulations of ETG show the same type of inverse cascade effect which appears generic to the  $\mathbf{E} \times \mathbf{B}$  convective nonlinearities. Thus the same type of formula larger than that for mixing length estimate must be included in turbulent electron transport. For ETG there are two larger scales where the turbulent energy can accumulate. The electron transport driven by the ETG turbulence is less well documented than the ITG turbulence. An experiment supporting the role of the ETG turbulence is found in Wong, *et al.* (1997). The key formulas are that the maximum growth rate is given by

$$\gamma_{\max}^{\text{ETG}} = \frac{v_e}{(L_{T_e} R)^{1/2}}, \quad (9.17)$$

where  $v_e = (T_e/m_e)^{1/2}$ , and occurs at  $k_y \gg k_x$  with

$$k_y^m = \frac{1}{\rho_e} \left( \frac{1 - 2L_{ne}/R}{1 + \eta_e} \right)^{1/2}, \quad (9.18)$$

where  $\rho_e = v_e/\omega_{ce}$ . The electrostatic inverse cascade limit defines the electron mixing length  $P_{c,e}$  as

$$\ell_{c,e}^{es} = q\rho_e \frac{R}{L_{T_e}}. \quad (9.19)$$

The derivation of this electrostatic scale  $\ell_{c,e}$  applies for low plasma  $\beta_{pe}$ . For higher  $\beta_{pe}$  the collisionless skin depth  $\delta_e = c/\omega_{pe}$  is the relevant breakpoint in the spectrum. If we compare formula with  $\ell_{c,e}$  in Eq. (9.19) with

$$\ell_{c,e}^{em} = \delta_e = \frac{c}{\omega_{pe}}, \quad (9.20)$$

to find the critical  $\beta_e^{\text{crit}} = L_{T_e}^2/q^2 R^2$  or  $\beta_p^{\text{crit}} = 2L_{T_e}^2/a^2$  for the transition defined by  $\ell_{ce}^{es} = \ell_{c,e}^{em}$ . The experiments have  $\ell_{c,e}^{em} > \ell_{c,e}^{es}$  for  $r/a \lesssim 0.3$ . The scale length  $\delta_e$  in Eq. (9.20) arises from the solution of the fluctuating component of Ampere's law

$$\nabla_{\perp}^2 \tilde{A}_{\parallel} = -4\pi \tilde{j}_{\parallel}^e/c = 4\pi n_0 e \tilde{u}_{\parallel}/c, \quad (9.21)$$

as explained in *Horton, et al.* (1988). Here  $\tilde{u}_{\parallel}$  is the fluctuating parallel electron flow velocity. Three 3D partial differential equations are given and solved for simulations of the finite  $\beta_e$  ETG turbulence in *Horton* (1990). The results show that at the scale  $P_{c,e}$  the cross-field turbulence has become approximately isotropic in the  $x-y$ -plane. The vortex or coherent structures are much larger than the electron gyroradius scale. The toroidal gyrokinetic simulations of *Idomura, et al.* (2000) reconfirm these findings of large-scale structures supporting large thermal fluxes. The region between  $\ell_{c,e}$  and  $1/k_y^m$  is sufficiently large that we may look for a spectral index to roughly characterize this region. It is to be noted, however, that in general, there is some degree of linear growth and damping throughout  $\mathbf{k}$ -space so that Kolmogorov exponents are not strictly defined, since there are no source/sink-free transport regions in  $\mathbf{k}$ -space. For completeness we note that the corresponding ITG time-space scales are

$$\gamma_{\max}^{\text{ITG}} = \frac{c_s}{(L_{T_i} R)^{1/2}} \quad (9.22)$$

$$k_y^m = \frac{1}{\rho_s} \left( \frac{1 - 2L_{n_i}/R}{1 + \eta_i} \right)^{1/2} \quad (9.23)$$

and

$$\ell_{c,i} = q\rho_s \frac{R}{L_{T_i}}. \quad (9.24)$$

Note that for flat density profiles where  $2L_{n_i}/R \rightarrow 1$  another formula applies for  $k_y^m$ . The derivation and interpretation of these time spaces is given in *Ottaviani, et al.* (1997), and *Redd, et al.* (1997). The ion temperature does not become high enough for finite ion  $\beta$  effect being important in those experiments. For plasma states well above the critical gradient for the instability the threshold is relatively unimportant and the turbulent diffusivities are given by

$$\chi_e = C_e \ell_{c,e}^2 \gamma_{\max}^{\text{ETG}} \quad (9.25)$$

and

$$\chi_i = C_i \ell_{c,i}^2 \gamma_{\max}^{\text{ITG}}. \quad (9.26)$$

The coefficients  $C_i = 0.014$  from *Ottaviani, et al.* (1997) for a JET discharge and  $C_e = 0.1$  is determined by *Horton, et al.* (2000) for a Tore Supra discharge. The theoretical meaning of  $C_i$  and  $C_e$  is the fraction to which the ITG and ETG turbulence reach the levels given by the mixing length level of  $e\tilde{\varphi}/T_e \simeq \ell_c/L_T$ . The *Hoang, et al.* (1998) power balance studies indicate that magnetic shear  $s = rq'/q$  is an important parameter. Strong magnetic shear leads to electron Landau damping and is known to provide a threshold gradient above the adiabatic value. *Hoang, et al.* (1998, 2001) investigate the question as to the experimental evidence for the existence of a critical electron gradient  $(\nabla T_e)_c$ . *Hoang, et al.* (1998) found evidence for a critical electron temperature gradient near  $(\nabla T_e)_c \simeq 3 \text{ KeV/m}$  and attempted to correlate the  $(\nabla T_e)_c$  inferred from heating experiments with the *Rebut, et al.* (1990) model. Serious difficulties with the toroidal magnetic field dependence and magnetic shear independence of the RLW formula are reported. Thus the emphasis has changed to the thresholds for ITG and ETG turbulence. There are well-developed formulas for critical threshold gradients for the ITG and ETG turbulence since these values are

from the linear dispersion relation. Here we examine the effects of magnetic shear dependence of  $(\nabla T_e)_c$  formula. The resulting ETG electron diffusivity is

$$\chi_e^{es} = C_e^{es} q^2 \left( \frac{R}{L_{T_e}} \right)^{3/2} \left( \frac{c\rho_e}{eB} \right) \left[ \frac{T_e}{L_{T_e}} - C_L \left( \frac{|s|T_e}{qR} \right) \left( 1 + \frac{T_e}{T_i} \right) \right], \quad (9.27)$$

with two parameters  $C_e$  and  $C_L$ . Formula (9.27) is the straightforward generalization of the ion turbulent thermal diffusivity formula in OHE model to the electron turbulence. The dependence of Eq. (9.27) on  $q^2$  and  $R/L_{T_e}$  reproduces features shown in Hoang, et al. (1998) for  $\chi_e$  from power balance. The critical gradient also agrees in magnitude (few KeV/m) and in the observed increase of  $(\nabla T_e)_c$  with magnetic shear reported from both the power  $\chi_e$  and the fluctuation levels in Tore Supra. Recent documentation of this agreement between theory and electron power balance inferred values of the critical gradient are presented in Hoang, et al. (2001). For the core region of the discharge the electrostatic  $\chi_e$  in Eq. (9.27) transforms to an electromagnetic turbulent transport given by

$$\chi_e^{em} = C_e^{em} \frac{c^2}{\omega_{pe}^2 (L_{T_e} R)^{1/2}} \frac{v_e}{\beta_{pe}} \quad \beta_{pe} > \beta_{crit}. \quad (9.28)$$

Because of the fewer electromagnetic transport simulations, less is known about the details of Eq. (9.28). The independence of  $\chi_e^{em}$  on  $B_T$  appears strange but is explained by the requirements that  $\beta_e^{crit} = L_{T_e}^2/q^2 R^2 (\beta_{pe} > \beta_{pe}^{crit} \sim (L_{T_e}/a)^2)$  and  $q \geq 1$ . Analyzing the difficult region between the high and low beta regimes we find that a good working formula to span the two regimes is

Table 9.3: TS High- $\beta_p$  Experiment #19542 at  $t = 6$  s

$R/a$	2.3 m/0.75 m
$B_\phi$	2.7 T
$I_p$	0.69 MA
$P_{RF}$	3.4 MW
$n_e(0)$	$3.6 \times 10^{19} \text{ m}^{-3}$
$T_e(0)/T_i(0)$	4.3 KeV/0.55 KeV
$n_D \tau_E T_e$	$3.7 \times 10^{18} \text{ m}^{-3} \cdot \text{s} \cdot \text{KeV}$
$v_\phi(0)$	-20 km/s

given by

$$x_e^{em} = \frac{x_e^{es}}{[1 + (C_e^{es} \beta_e / C_e^{em} \beta_e^{crit})]}.$$

This new composite formula has the same high and low beta limits and keeps the desirable property of reducing to the electrostatic gyroBohm scaling at low plasma pressure. This feature is probably necessary in modeling the LHCD experiments where the density is low and use of Eq. (9.28) would yield too high a transport rate.

### 9.4.8 Theory Comparison With Power Balance Analysis

#### A Reference TS Shot

Here we analyze TS shot #19542 for the time interval  $t = 5.0\text{--}6.35$  due to the previous detailed study in Hoang, *et al.* (1998) and its availability on the ITER profile database. The characteristics of this 0.685 MA/2.71 T discharge are given in Table 9.3. The profiles of the electron temperature  $T_e$ , ion temperature  $T_i$  and electron density are shown in Fig. 9.6. In the fast wave Radio Frequency RF heating power is absorbed by electron Landau damping ( $\omega^{\text{RF}} \simeq k_{\parallel}^{\text{RF}} v_e$ ) and is exponentially localized ( $P_e^{\text{RF}} \exp(-r/L_p)$ ) to the core of this discharge with the  $1/e$  width  $L_p = 4.3$  cm. In this discharge the net integrated power deposited is 3.4 MW. The strong localization of the deposited power is important for producing the high electron temperature gradient shown in Fig. 9.7 that reaches a maximum value of 12 KeV/m at  $\rho = r/a \simeq 0.3$ . Also, shown in Fig. 9.7 is the critical electron temperature gradient computed from Eq. (9.27). We see that in the core out to  $\rho \simeq 0.8$  the electron temperature gradient exceeds this critical gradient by factor from 5 to 2 in going from  $\rho = 0.3$  to 0.8. Thus, in our first analysis we choose to compute the thresholdless  $\chi_e$  formula with one parameter  $C_e$  to the power balance  $\chi_e$ .

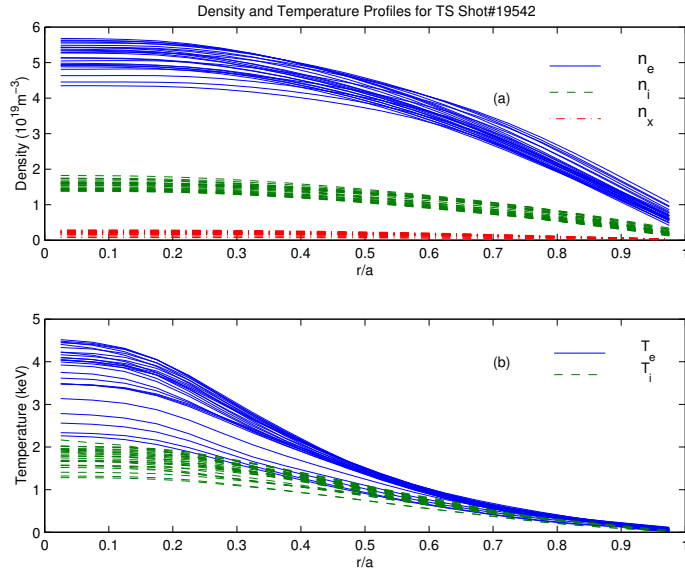


Figure 9.6: The (a) temperature and (b) density profiles from  $t = 5$  s to 6.35 s in Tore Supra shot # 19542. [Reprinted with permission from W. Horton, *et al.* (2000), Copyright 2002, American Institute of Physics].

The steady-state power balance equations in the core plasma are

$$\frac{1}{r} \frac{\partial}{\partial r} (rq_e) = P_e^{\text{RF}} + j_{\parallel} E_{\parallel} - Q_{ei}, \quad (9.29)$$

$$\frac{1}{r} \frac{\partial}{\partial r} (rq_i) = P_i^{\text{RF}} + Q_{ei}. \quad (9.30)$$

Beyond  $\rho > 0.8$  the radiation losses in electron channel and the atomic physics processes in the ion channel may become dominant. Thus, we limit the transport analysis to  $\rho_1 < \rho < \rho_2$  typically choosing  $\rho_1 = 0.1$  and  $\rho_2 = 0.8$ . The electron-ion energy transfer term  $Q_{ei}$  is subdominant to  $P = P_e^{\text{RF}} + P_e^{\Omega}$ , but is the dominant input term in the ion power balance equation. More than 90% of the RF input power is coupled to the electron, and since  $T_e \gg T_i$ ,  $Q_{ei}$  depends mainly on  $T_e$ .

The integration of Eqs. (9.29) and (9.30) from  $\rho = 0$  to  $\rho$  gives the power balance fluxes shown in Fig. 9.8. The peak flux  $q_e$  occurs at the edge of the FEWH deposition profile and then falls approximately as  $1/r$  until  $r/a \simeq 0.74$  where the lower temperature  $T_e$  provides a strong sink into the ion channel. The power balance thermal diffusivities are defined as

$$\chi_e^{\text{PB}} = -\frac{q_e}{n_e \left( \frac{dT_e}{dr} \right)} \quad (9.31)$$

$$\chi_i^{\text{PB}} = -\frac{q_i}{n_i \left( \frac{dT_i}{dr} \right)} \quad (9.32)$$

following Eq. (4) of *Hoang, et al.* (1998).

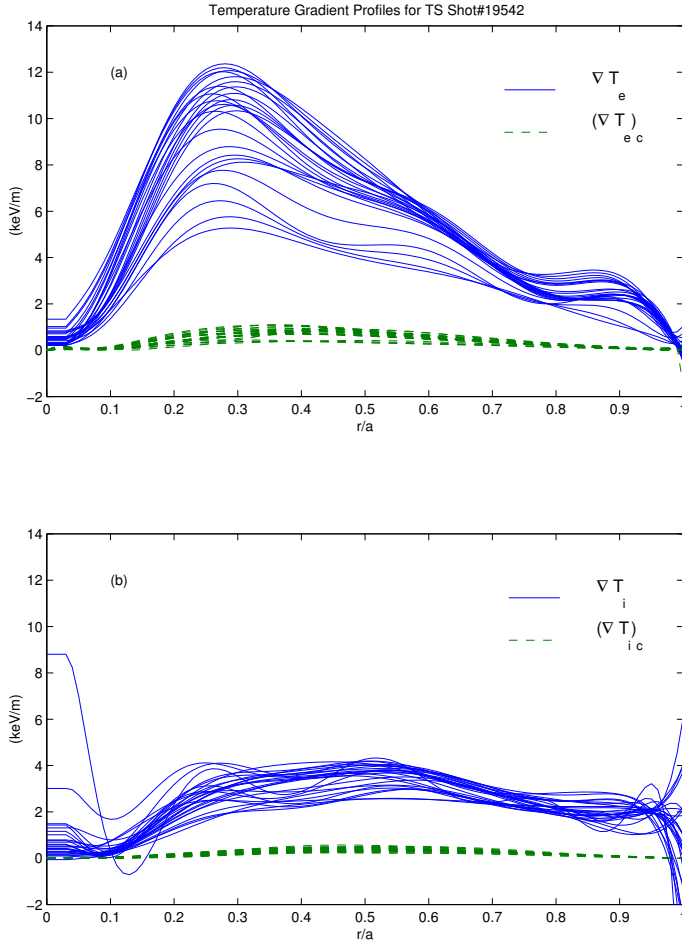


Figure 9.8: (a) The deposition profiles for the fast wave heating  $P_{\text{ICRHE}}(r)$  are highly peaked in the core as given in the  $U$ -files. The heating of the ions is from the electron-ion coupling  $Q_{ei}(r)$  with a small fraction from the fast wave heating. (b) The steady-state power balance heat fluxes. All the profiles are for  $t = 5\text{ s}$  to  $6.35\text{ s}$  in Tore Supra shot #19542. [Reprinted with permission from W. Horton *et al.* (2002), Copyright 2002, American Institute of Physics].

The values obtained for the power balance diffusivities (9.31) and (9.32) compared with the computations from Eqs. (9.26) and (9.27). In constructing this comparison we choose  $C_e$  and  $C_i$  by minimizing the mean-square deviation of the model  $\chi_S$  with the power balance  $\chi_S$ . The resulting values are  $C_e = 0.1$  and  $C_i = 0.015$  with the mean square deviations given by  $\sigma_{C_e} = 0.3$  and  $\sigma_{C_i} = 0.5$ . The value of the  $C_e$  is consistent with earlier theoretical estimates. The value of  $C_i$  is consistent with that value obtained for the JET shot # 19649, which is used in calibration of the OHE model [Ottaviani, *et al.* (1997)] to within the limits of the large errors in  $x_i$ . The

Probability Distribution Functions (PDF) of  $\chi_e^{\text{expt}}/\chi_e^{\text{model}} = \chi_e^{\text{PB}}/\chi_e^{\text{em}}$  are not gaussian, but have a skewness to large values of  $\chi_i^{\text{PB}}/\chi_i$  and  $\chi^{\text{PB}}/\chi_e^{\text{em}}$ . These heavy tails on the PDFs lead to the large values of  $\sigma_{C_e}$  and  $\sigma_{C_i}$ .

## TS–98 Database

A database of approximately fifty discharges has been assembled and used for power balance analysis. The toroidal magnetic field  $B_\phi$  and plasma current  $I_p$  range from a minimum of 2.1 T/0.4 MA to a maximum of 2.8 T/0.9 MA. The electron density from 1.2 to  $5.2 \times 10^{19} m^{-3}$  with a range of mixture of deuterium and helium as working gas. Figure 9.9 shows the range of the key instability quantities  $L_{T_e}/R$  and  $L_{ne}/R$  over the database. Also shown are the stability boundaries in the two limiting cases of peaked density profile, given by the oblique line of slope  $\eta_e = 2/3$ , and flat density profile, which is given by the vertical line at abscissa  $L_{T_e}/R = [\pi/2(1 + Z_{\text{eff}}T_e/T_i)]^{-1}$ . Clearly almost all the database points fall in the unstable region. We will show below that the wide range of variations is reduced to a narrow spread of values by the electromagnetic  $\chi_e^{\text{EM}}$  formula.

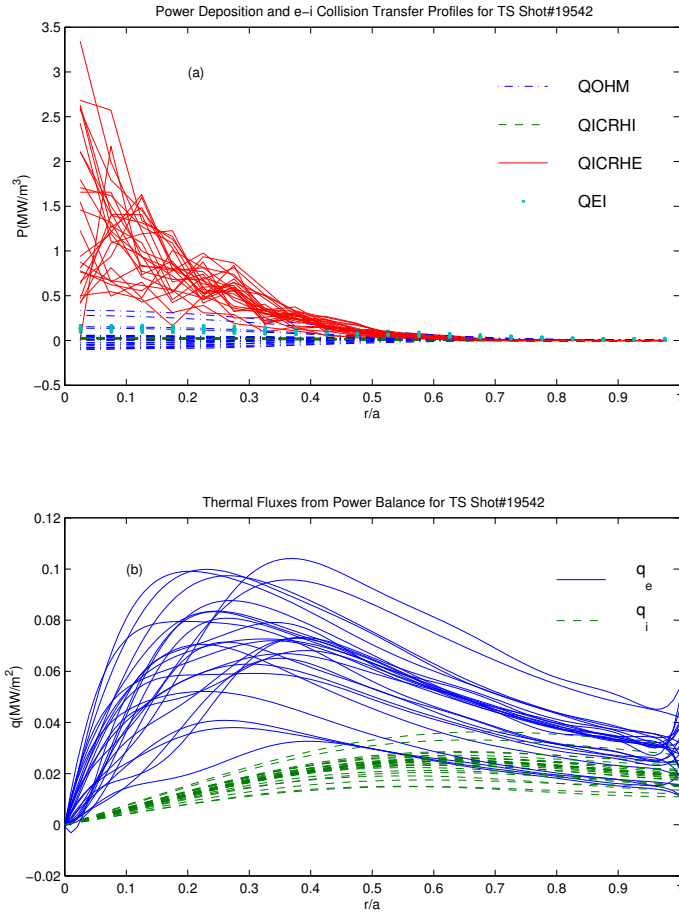


Figure 9.9: ETG stability boundaries and database points in the  $(L_{T_e}/R, L_{ne}/R)$  plane. [Reprinted with permission from W. Horton *et al.* (2000), Copyright 2002, American Institute of Physics]

For each of the independent time slices distributed over different TS shots, we obtain a coefficient  $C_e^{es}$  in Eq. (9.27) and a coefficient  $C_e^{em}$  in Eq. (9.28) by minimizing the square deviation between the model diffusivities and the ones obtained from power balance equations, as we did in the analysis of the reference shot in the previous section. In this way we get two distributions from the two sets of coefficients, with 48 samples in each for various values of  $\nu = 1$  and 2 in the exponent of  $q$  in  $\chi_e^{es}$  and  $\chi_e^{em}$  formulas. The mean square deviation of the data from the ETG model is minimized for  $\nu = 0$  to 1 for the  $\chi_e^{em}$  and  $\nu = 0$  for the  $\chi_e^{es}$  models, and  $C_e^{em}$  has much smaller relative deviation than  $C_e^{es}$  for all variations of  $\nu$ . The best fit values are  $C_e^{em} = 0.1$  and  $C_e^{em} = 0.15$  with error measure for the  $\chi_e^{es}$  more than twice that of the  $\chi_e^{em}$  formula. The results suggest that the electromagnetic turbulence formula [Eq. 9.28] gives a better model for the

turbulent electron thermal diffusivity, when only one correlation length formula is used. Predictive simulations have confirmed this suggestion from Fig. 9.9.

Finally, we find that in terms of global energy confinement time scaling, the electromagnetic  $\chi_e^{\text{ETG}}$  formula reproduces pretty well the improved confinement which is almost of H-mode equality. This is shown in Fig. 9.10, where the H-factor  $H = W^{\text{tot}}/W_L^{\text{tot}}$  of these discharges ranges between  $H = 1.4$  and  $H = 1.7$ . Here  $W_L$  is the ITER L-mode scaling [Kaye (1997)]

$$W_L^{\text{tot}} = 0.023\kappa^{0.64}R^{1.83}(R/a)^{0.06}I_p^{0.96}B_\phi^{0.03}\bar{n}_e^{0.40}M_{\text{eff}}^{0.20}P^{0.27}. \quad (9.33)$$

In contrast, we find that the low  $\beta_{pe}$ , electrostatic  $\chi_e^{\text{ETG}}$  formula predicts L-mode quality performance, which is too pessimistic for these discharges.

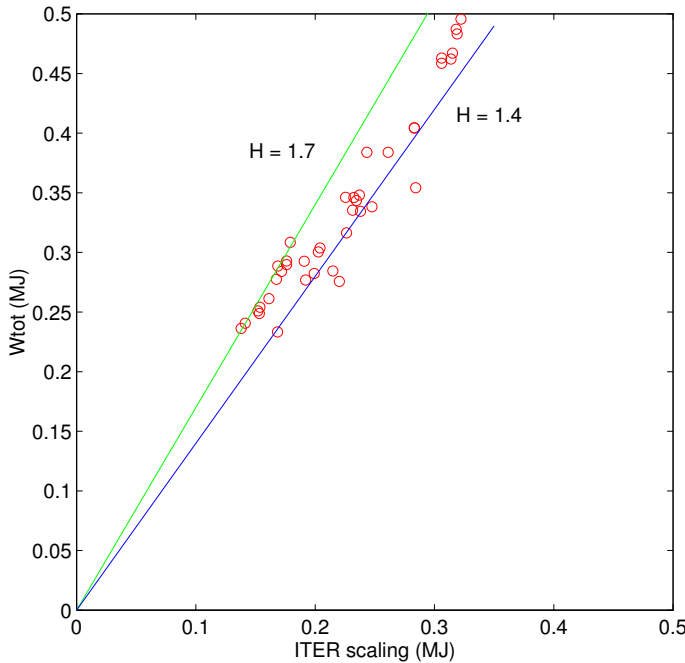


Figure 9.10: Comparison of the measured total plasma energy with the ITER-97 L-mode scaling prediction for the 48 Tore Supra shots. [Reprinted with permission from *W. Horton, et al. (2000)*, Copyright 2002, American Institute of Physics].

#### 9.4.9 Interpretive Transport Simulations

Now, we test the theory for the electron transport making simulations in the LOCO transport code in the interpretive configuration. By interpretive simulations one means transport runs on a database shots with theoretical formulas used for  $\chi_e$  and  $\chi_i$  that yield the evolution of  $T_e(r, t)$  for

the model to compared with the measured profiles. The comparisons are more demanding than the steady-state power balance since these is a ramp-up and ramp-down of the driving radio frequency heating power. For this model of electron thermal transport the measured electron density is used in the simulation to eliminate uncertainties associated with the particle transport processes. Such runs allow one to interpret and assess the space-time evolution of the temperature profiles given by the theoretical electron thermal diffusivity formula. Here we show one comparisons from the database that demonstrates well the accuracy to which the space-time evolution of the electron temperature profile is reproduced by the  $\chi_e^{\text{ETG}}$  formula. In *Horton, et al.* (2000) and *Hoang, et al.* (2001) many more discharges are analyzed and statistical distributions of the deviations between theory and the power balance inferred  $\chi_e$  are presented.

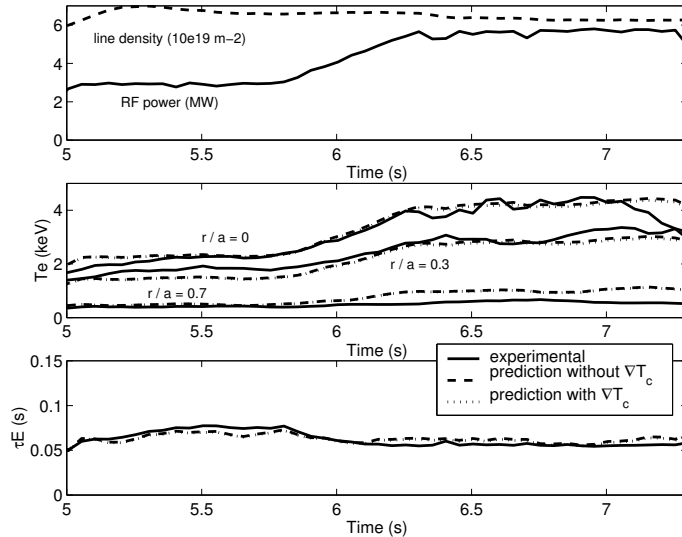


Figure 9.11: Interpretive simulation for shot 18368. (a) Applied FWEH heating ramp from 3 MW to 6 MW for  $\Delta t = 0.5$  s at  $t = 5.8$  s. (b) The rise and saturation of  $T_e$  at  $r/a = 0$ ,  $r/a = 0.3$  and  $r/a = 0.7$  from the experiment (solid), and from the model without (dashed) and with (dotted) a critical gradient term. (c) Evolution of  $\tau_E$  from the experiment (solid) and from the model without (dashed) and with (dotted) a critical gradient term [Reprinted with permission from *W. Horton, et al.* (2000), Copyright 2002, American Institute of Physics].

### Shot 18368, $I_p = 0.65$ MA, $P_{\text{ICRH}} = 3$ MW → 6 MW

This discharge has a step-up over a period  $\Delta t = 0.5$  s ( $\sim 5\tau_E$ ) from the RF driving level of 3 MW to 6 MW shown in Fig. 9.11a. The net stored electron energy increase from 0.2 MJ to 0.35 MJ with the model following closely the measured increase of electron thermal energy. The tracking of the modeled  $T_e$  profile at  $r/a = 0, 0.3$ , and 0.7 with the measured profile is shown in Fig. 9.11b. The

model over-predicts the core temperature somewhat significantly. There are some large 100 ms oscillations on the core temperature which are not in the model  $T_e$  and may account for the discrepancy. The model tracks the measured profile well at  $r/a = 0.3$  and 0.7 through the step-up in the RF power.

The top panel of Fig. 9.11 shows that the model prediction for the stored energy tracks well the measured stored energy over the step-up in the RF power. The core oscillations shows up as  $\Delta W_e \leq 50$  kJ excursions of the model  $W_e$  above that from the measured profiles for which  $\Delta W_e \leq 300$  kJ.

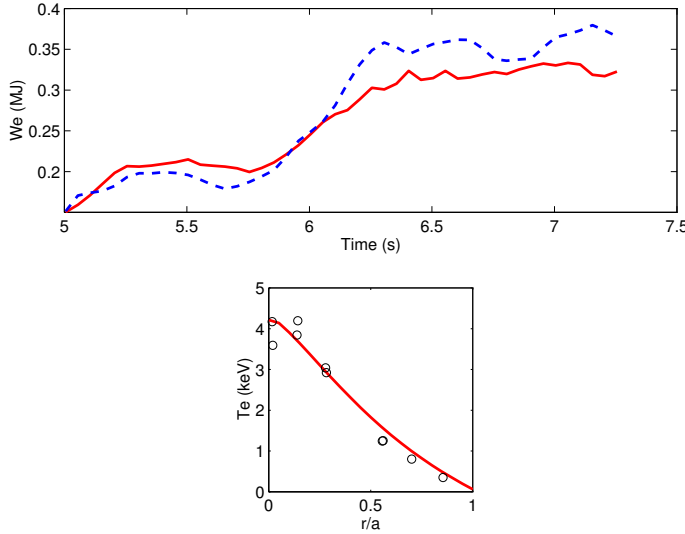


Figure 9.12: Interpretive simulation for shot 18368.(a) The stored electron energy  $W_e$ , from the experiment (solid) and from the simulations (dashed). (b) The temperature profile at  $t = 6.5$  s, from the experiment (circles)and from the simulations (solid). [Reprinted with permission from W. Horton *et al.* (2002), Copyright 2002, American Institute of Physics.]

This and other similar interpretive simulations establish that the theoretical  $\chi_e$  model tracts well both the radial and time variations of the electron temperature profile in the RF heated plasma. The histograms for ratios of  $C_e = x_e^{\text{PB}}/\chi_e$  (model) are shown for the FWEH database of 48 shots in *Horton, et al.* (2000) and for a larger set of competing theoretical models in *Hoang, et al.* (2001). The conclusion is that the ETG transport formulas work well to provide a predictive tool for determining the electron temperature in tokamaks.

#### 9.4.10 Summary

The theoretical and experimental status of turbulent plasma transport in tokamaks is reviewed with an emphasis on the electron turbulent transport. The degree of the electron anomaly is the

largest and, historically, the longest standing transport anomaly in the controlled fusion research program. We show that recent developments in theory and simulations allow the formula for  $\chi_e$  to be used and tested for confidence with steady-state electron data. While the best approach for describing turbulent transport is explicitly that of the multi-mode approach where all possible instabilities are assessed and applied as dictated by theory, we report here tests of the electron transport in plasma where the power flow is dominantly through the electron channel and thus most sensitive to the  $\chi_e$  formula. The power balance analysis of the hot electron TORE SUPRA plasmas is unusually clear due to the direct, local deposition of radio frequency power into core electrons through the FWEH mode of operation. As a consequence, there is a multi-megawatt thermal flux conducting through the electron channel in the radial region from  $\rho = \rho_1 \simeq 0.2$  to  $\rho = \rho_2 \simeq 0.7$ . Since the electron temperature profile is accurately measured for these discharges there is a well-defined electron thermal diffusivity  $\chi_e$  called the power balance thermal diffusivity. The data analysis presented here shows clear evidence for the short scale length electron temperature gradient drift wave turbulence, providing a basic physics explanation for the mechanism producing the observed thermal diffusivity. This hypothesis is tested with transport codes with the local heating deposition profiles and edge boundary conditions given. The results show that the ETG formula is able to reproduce well the accurately-known electron temperature profiles. The theory gives that the turbulent correlation scale length changes character in going from the high electron pressure core to the lower pressure outer zone plasma. The degree to which the data supports the  $\chi_e$  formula based on the correlation lengths  $\ell_{c,e}^{em} = c/\omega_{pe}\ell_{c,e}^{es} \simeq q\rho_e R/L_{T_e}$  is presented. The interpretation and predictions resulting from theoretical turbulence  $\chi_e$  formulas is then compared with the well-documented empirical formula based on the database — the Taroni–Bohm formula. The conclusion that it is the electromagnetic turbulent electron thermal diffusivity that explains well the power balance  $\chi_e^{\text{PB}}$ . This explanation is consistent with the report of *Colas, et al.* (1998) that reports the presence and role of internal magnetic fluctuations on electron heat transport. The *Colas, et al.* (1998) transport analysis uses the internal magnetic fluctuations  $\delta B_r$  measured with cross-polarization scattering technique [Zou, *et al.* (1995)]. The magnetic turbulence at short wave length  $k_\perp = 12.6 \text{ cm}^{-1}$  is measured at  $r/a = 0.55$ . Power scans show that the intensity at this wavenumber and position increases as  $(\delta B_r/B)^2 \cong 10^{-8}(8\text{m}^{-1}/L_{T_e})$  in experiments where  $\nabla T_e \leq 7 \text{ KeV/m}$ . The corresponding maximum electron thermal flux is  $0.1 \text{ MW/m}^2$  which exceeds considerably the values shown in Fig. 9.8 for shot TS19542 ( $t = 6 \text{ s}$ ). The  $\chi_e$  formulas used by *Colas, et al.* (1998) are not self-consistent collective electromagnetic field transport formulas; rather they are the test particle diffusivities of electrons in a given spectrum of purely magnetic fluctuations. More realistic test particle diffusivities for electrons are in *Kim, et al.* (1990), keeping both the electric fields and the magnetic fluctuations. The motion of electron guiding center is strongly influenced by both the electric and magnetic components of the fluctuations. For very low fluctuation levels the Coulomb collisional pitch-angle scattering and the electromagnetic drift wave fluctuation spectrum act together to determine the electron diffusion in tokamak geometry. In very low amplitude fluctuation limit, one recovers [*Kim, et al.* (1990)] the neoclassical banana-plateau diffusion coefficient. At the fluctuation levels given by the mixing length amplitudes, the anomalous transport formulas for the electron turbulent transport in Eqs. (9.26)–(9.27) are recovered.

## Momentum–energy transport from turbulence driven by parallel flow shear

The low-frequency  $\mathbf{E} \times \mathbf{B}$  turbulence driven by the shear in the mass flow velocity parallel to the magnetic field is studied using the fluid theory in a slab configuration with magnetic shear. Ion temperature gradient effects are taken into account. The eigenfunctions of the linear instability are asymmetric about the mode rational surfaces. Quasilinear Reynolds stress induced by such asymmetric fluctuations produces momentum and energy transport across the magnetic field. Analytic formulas for the parallel and perpendicular Reynolds stress, viscosity and energy transport coefficients are given. Experimental observations of the parallel and poloidal plasma flows on TEXT–U are presented and compared with the theoretical models [Dong, et al. (1998)].

Since it was first studied in the early 1970s [Antipov, et al. (1982)] the instability driven by the cross-field gradient (shear) of the plasma mass flow velocity parallel to the magnetic field in an inhomogeneous plasma has been investigated extensively in fusion [Antipov (1985), Antonova (1983), Balescu (1988), Biskamp (1997), Biskamp) et al. (1994)] as well as in space plasmas [Burrell (1997), Carreras, et al. (1987)]. Such instability can be strongly driven by neutral-beam injection in tokamak discharges. In addition, a strong gradient of the flow velocity may appear near the plasma boundary due to the presence of the limiter or divertor which is known to dramatically alter the plasma dynamics in the scrape off layer (the shadow of the poloidal limiter or the divertor region) from that in the bulk. In space plasmas, high streaming velocities parallel to the magnetic field and rapid variation of the parallel flow velocity with the distance perpendicular to the magnetic field are measured in the plasma sheet boundary layer due to the influence of the solar wind on the plasma sheet [Carreras, et al. (1987), Chen (1965a)].

Such turbulence driving mechanisms are understood and the characteristics of the instability are well documented [Antipov, et al. (1982a, 1985) , Antonova (1983), Balescu (1988), Biskamp (1997), Biskamp, et al. (1994), Burrell (1997), Carreras, et al. (1987), Chen (1965a)]. In this work the emphasis is not on the study of the instability itself but rather on momentum and energy fluxes described by the turbulence induced Reynolds stress. From the Reynolds stress parallel and perpendicular to the magnetic field we determine the associated viscosity and energy transport coefficients generated by the turbulence of the instability. The transport coefficients are characterized both by their magnitude at the mixing length level of the turbulence and by their dimensionless ratios, the Prandtl numbers, which are independent of the turbulence level.

It was first observed on the TEXT tokamak [Chen and Sen (1995)] that a poloidal flow shear is formed at the plasma edge. Such flow shear may suppress the plasma density fluctuations and affect the local plasma confinement improvement. Later, the L-mode to H-mode (L–H) transition in tokamak plasma confinement was found to be related to the presence of the poloidal flow shear near the plasma edge [Chen and Cheng (1980)]. Theoretical work has been carried out to study the poloidal flow shear effect on the plasma turbulence [Colas, et al. (1998)].

Several possible sources for the generation of such poloidal flow shear have been proposed [Connor (1993), Devynck, et al. (1993), Dimits, et al. (2000), Dong, et al. (1997) , Dorland, et al. (2000), Doyle, et al. (1991)]. Among them two models are widely studied. One is the

particle losses caused by the interaction with the limiter or divertor [*Connor* (1993), *Devynck, et al.* (1993)]. An alternative explanation is the Reynolds stress produced by the turbulence in the plasma [*Dimitis, et al.* (2000), *Dong, et al.* (1997)]. This latter mechanism requires a physical driving force for the turbulence. A few physical models such as drift-resistive ballooning mode [*Dorland, et al.* (2000a)], resistive pressure-gradient driven mode [*Doyle, et al.* (1991)] have been proposed and studied.

In this work, the parallel velocity shear, combined with the ion temperature gradient, is proposed as the driving mechanism for the poloidal sheared flow. It has been pointed out by several authors [*Dimitis, et al.* (2000), *Doyle, et al.* (1991)] that there must be a symmetry breaking mechanism such as boundary conditions in drift waves, or some symmetry breaking seed introduced in the study of pressure-gradient driven turbulence in order to generate nonzero Reynolds stress from fluctuations. One of the features for the model proposed in this work is that the mode eigenfunction is intrinsically asymmetric about the mode rational surface so that the Reynolds stress generation is independent of, or at least not sensitive to, boundary conditions. Symmetry breaking seeds are not needed even in the nonlinear simulations [*Biskamp, et al.* (1994)].

Experimental measurements of the parallel and poloidal flows are carried out on Texas Experimental Tokamak Upgrade (TEXT-U) and some of the results are presented in this work. The measurements from a Mach probe show that there is a strong radial gradient of the parallel ion mass flow at about the same region as the poloidal shear layer. The sharp spatial gradient may be created and maintained by the transition from a confined interior plasma to a scrape-off layer plasma regulated by the cold plasma sheath surrounding the limiter. The sheath condition on the net parallel plasma electric current requires the build up of a parallel ion velocity to a fraction of the ion acoustic speed. The turbulence is now driven by the free energy associated with the radial gradient of the parallel flow velocity, and in turn, produces an acceleration in the poloidal direction. The preliminary evidence that the plasma parallel velocity changes at about the same radial position as the poloidal shear layer supports this scenario for the poloidal shear flow generation. The theoretical results are compared with and shown to be in reasonable agreement with the experimental observations if a neoclassical damping mechanism is introduced to balance the driving force from the Reynolds stress.

In large tokamaks the toroidal velocity gradients are measured by spectroscopic techniques and may be driven in the interior by parallel beam injection. In a recent analysis of the high poloidal beta discharge regime on JT-60U [*Durst, et al.* (1993)], a transport barrier is reported at the  $q = 3$  surface where the toroidal velocity gradient, measured in terms of the dimensionless stability parameter defined here, has a value close to that found in the TEXT-U scrape-off layer. We speculate that same physical processes proposed here for local confinement improvement on TEXT-U may be involved in the transport barrier generation on JT-60U.

The remainder of this work is organized as follows. In Sec. 2 the physics model is described, and the eigenmode equation is given and solved analytically. Analytic formulas for the Reynolds stress are derived in Sec. 3 and the numerical evaluations are presented in Sec. 4. In Sec. 5 the experimental observations on TEXT-U are presented and possible correlation of the theoretical results obtained in this work with these experiments are discussed in detail while Sec. 6 is devoted to the conclusions of this study.

### 9.4.11 Physics Model and Eigenmode Equation

We consider a slab magnetic configuration  $\mathbf{B} = B_0(\hat{\mathbf{z}} + \frac{x}{L_s}\hat{\mathbf{y}})$ , where  $L_s$  is the scale length of magnetic shear. Here the  $x$ -,  $y$ -, and  $z$ -directions in the sheared slab geometry are defined as the radial, poloidal and toroidal directions in the tokamak configuration. Fluid theory is used to describe the ion motion and the electrons are adiabatic. Equilibrium parallel velocity shear  $dv_{\parallel}(x)/dx = \text{const}$  is considered and ion temperature gradient ( $\eta_i$ ) effects are included in the instability study. The perturbed electrostatic potential is expressed as  $\tilde{\phi}(x, y, t) = \text{Re}\{\phi(x) \exp(ik_y y - i\omega t)\}$ . Under these assumptions it is straightforward to derive the linear eigenmode equation for the function  $\phi(x)$  as follows,

$$\frac{d^2\phi(x)}{dx^2} - b_s\phi(x) + \frac{1 - \hat{\omega}}{\hat{\omega} + K}\phi(x) + \left[ \frac{s^2 x^2}{\hat{\omega}^2} - \frac{\hat{v}'_{0\parallel} s x}{(\hat{\omega} + K)\hat{\omega}} \right] \phi(x) = 0, \quad (9.34)$$

where  $b_s = k_y^2 \rho_s^2$ ,  $\hat{\omega} = \omega/\omega_{*e}$ ,  $K = (1 + \eta_i)/\tau$ ,  $\tau = T_e/T_i$ ,  $\eta_i = d \ln T_i / d \ln n$ ,  $\omega_{*e} = k_y \rho_s c_s / L_n$  is the electron diamagnetic frequency,  $x$  is normalized to  $\rho_s = c_s/\Omega = (T_e/m_i)^{1/2}/\Omega = c(m_i T_e)^{1/2}/eB$ ,  $\Omega$  is the ion gyrofrequency;  $\hat{v}'_{0\parallel} = L_n dv_{\parallel}/c_s dx$ ,  $s = L_n/L_s$  with  $L_n$  being the density gradient scale length. Here  $T_e$  and  $T_i$  are the electron and ion temperature, respectively. Equation (9.34) is valid in the hydrodynamic-like limit and the full kinetic equation is also given in Ref. 4.

The dispersion relation obtained from (9.34) is

$$\left[ -b_s + \frac{1 - \hat{\omega}}{\hat{\omega} + K} - \frac{\hat{v}'_{0\parallel}^2}{4(\hat{\omega} + K)^2} \right] \frac{\hat{\omega}}{is} = 2n + 1. \quad (9.35)$$

The corresponding eigenfunction is

$$\phi^{(n)}(x) = \phi_0^{(n)} \frac{\hat{\omega}}{is} H_n \left( is/\hat{\omega} \right)^{1/2} (x + \Delta) e^{-is(x+\Delta)^2/2\hat{\omega}}, \quad (9.36)$$

where  $H_n$  is the Hermite function of order  $n$  and

$$\Delta = -\frac{\hat{v}'_{0\parallel} \hat{\omega}}{2s(\hat{\omega} + K)}. \quad (9.37)$$

In the rest of this work only the  $n = 0$  mode will be considered.

It is easy to notice that the mode growth rate is independent of the sign of  $\hat{v}'_{0\parallel}$  from Eq. (9.37). However, the asymmetry element, the shift  $\Delta$  of the position of the maximum  $\phi^{(0)}(x)$  from the mode rational surface ( $x = 0$ ), depends on the sign of  $\hat{v}'_{0\parallel}$  and is important for the Reynolds stress calculation. For cold ion approximation ( $K \rightarrow 0$ )  $\Delta$  is a real shift in  $x$ -space. In general  $\Delta$  is complex and introduces a deformation of the eigenfunction given by  $\text{Re}\{\phi^{(n)}(x) \exp(ik_y y - i\omega t)\}$  as well as the shift.

### 9.4.12 Equations for Reynolds Stress

The general expression for the perturbed electrostatic potential is  $\tilde{\phi} = \text{Re} \left\{ \sum_{k_y} \phi_0 \phi(x) \exp(-i\omega t + ik_y y) \right\}$ . The  $\mathbf{E} \times \mathbf{B}$  drift velocity is

$$\tilde{v}_x = -\frac{c}{B} \frac{\partial \tilde{\phi}}{\partial y}, \quad \tilde{v}_y = \frac{c}{B} \frac{\partial \tilde{\phi}}{\partial x}, \quad (9.38)$$

where  $B$  is the toroidal magnetic field and  $c$  is the speed of light. In the representation of  $\tilde{\phi}$  we use  $\phi_0$  to characterize the rms fluctuation level and  $\phi(x)$  the normalized wave function. Now we introduce the two components of the micro-Reynolds stress that measure the radial flux of the parallel and perpendicular momentum,

$$\pi_{xy}(x) = \tilde{v}_x^* \tilde{v}_y + \tilde{v}_x \tilde{v}_y^*, \quad (9.39)$$

$$\pi_{x\parallel}(x) = \tilde{v}_x^* \tilde{v}_\parallel + \tilde{v}_x \tilde{v}_\parallel^*, \quad (9.40)$$

where in the quasilinear approximation  $\tilde{v}_\parallel = (\epsilon s_c/T_e \hat{\omega}) x \tilde{\phi}$ . In writing Eqs. (9.6) and (9.7) we leave implicit the summation over all poloidal mode numbers and all rational surfaces determined by the toroidal mode number spectrums. It is straightforward to obtain the analytic expressions for Eqs. (9.6) and (9.7), using Eqs. (9.3) and (9.5), as follows:

$$\pi_{xy} = |\phi_0|^2 \frac{c^2}{\rho_s B^2} \frac{2k_y}{s} (2x\hat{\omega}_r + \Delta\hat{\omega}^* + \Delta^*\hat{\omega}) e^{is[\hat{\omega}(x+\Delta^*)^2 - \hat{\omega}^*(x+\Delta)^2]/2|\hat{\omega}|^2}, \quad (9.41)$$

$$\pi_{x\parallel} = |\phi_0|^2 \frac{cc_s e}{BT_e s} (-2k_y \gamma) e^{is[\hat{\omega}(x+\Delta^*)^2 - \hat{\omega}^*(x+\Delta)^2]/2|\hat{\omega}|^2}, \quad (9.42)$$

where  $*$  stands for complex conjugate,  $\hat{\omega}_r$  and  $\gamma$  are the real and imaginary part of  $\hat{\omega}$ , respectively. For energy transport we need the radial flux  $q_x(x)$  of the ion pressure fluctuation

$$q_x(x) = \tilde{v}_x^* \tilde{p} + \tilde{v}_x \tilde{p}^* = |\phi_0|^2 \frac{P_0(1+\eta_i)c^2}{\rho_s c_s B^2} \frac{2\gamma k_y}{s^2} e^{is[\hat{\omega}(x+\Delta^*)^2 - \hat{\omega}^*(x+\Delta)^2]/2|\hat{\omega}|^2}, \quad (9.43)$$

where again we use the quasilinear approximation  $\tilde{p} = -\tilde{v}_x dP_0/i\omega dx$  for the perturbation of the pressure. Here  $P_0$  is the equilibrium pressure and the equilibrium pressure gradient is  $dP_0/dx = -KP_0/L_n$ .

All the quantities given in Eqs. (9.8)–(9.10) are function of  $x = r - r_0$  with  $r_0$  being the position of the mode rational surface. In order to obtain the effects of these quantities on the macro-motion, or background motion, these micro-fluxes that are localized to small layers around the resonant surfaces ( $x + \Delta = 0$ ) must be integrated over  $x$ . The results are the corresponding

values used in the macro-motion equation on the mode rational surface. In this way we have

$$\langle \pi_{xy} \rangle = \int_{-\infty}^{+\infty} (\tilde{v}_x^* \tilde{v}_y + \tilde{v}_x \tilde{v}_y^*) dx = -|\phi_0|^2 \frac{c^2 k_y}{B^2 \rho_s} \sqrt{\pi} |\hat{\omega}|^3 K \hat{v}'_{0\parallel} s^{5/2} \gamma^{1/2} |\hat{\omega} + K|^2 e^{\gamma \hat{v}'_{0\parallel}^2 K^2} 4s |\hat{\omega} + K|^4, \quad (9.44)$$

$$\langle \pi_{x\parallel} \rangle = \int_{-\infty}^{+\infty} (\tilde{v}_x^* \tilde{v}_{\parallel} + \tilde{v}_x \tilde{v}_{\parallel}^*) dx = -|\phi_0|^2 \frac{cc_s e}{BT_e s^{5/2}} \sqrt{\pi} \frac{k_y \gamma^{1/2} |\hat{\omega}|^3 \hat{v}'_{0\parallel}}{|\hat{\omega} + K|^2} e^{\gamma \hat{v}'_{0\parallel}^2 K^2 / 4s |\hat{\omega} + K|^4}, \quad (9.45)$$

and

$$\langle q_x \rangle = \int_{-\infty}^{+\infty} (\tilde{v}_x^* \tilde{p} + \tilde{v}_x \tilde{p}^*) dx = |\phi_0|^2 \frac{P_0(1 + \eta_i) c^2}{\rho_s c_s B^2} \frac{(\pi \gamma)^{1/2} |\hat{\omega}| k_y}{s^{5/2}} e^{\gamma \hat{v}'_{0\parallel}^2 K^2 / 4s |\hat{\omega} + K|^4}. \quad (9.46)$$

In Eqs. (9.11)–(9.13) the mode growth rate  $\gamma$  and real frequency  $\hat{\omega}_r$  must be obtained from the mode dispersion equation (2) (with  $\hat{\omega} = \hat{\omega}_r + i\gamma$ ), for each  $k_y$  and the mean fluxes summed over all  $k_y$ . Apparently,  $\langle \pi_{xy} \rangle$  and  $\langle \pi_{x\parallel} \rangle$  vanish linearly with  $\hat{v}'_{0\parallel} \rightarrow 0$  while  $\langle q_x \rangle$  does not. Considering that the ion temperature gradient is taken into account, the instability is still possible under such limit. This clearly shows the importance of the parallel velocity shear for the momentum transport from turbulence in the quasilinear theory.

With this presentation of  $\langle \pi_{xy} \rangle$ ,  $\langle \pi_{x\parallel} \rangle$ , and  $\langle q_x \rangle$  we are giving the intensity for per unit spectrum of the fluctuations at the specified  $k_y$ . The complete flux is then the integral of the intensity over the spectral distribution of the fluctuations  $\int I(k_y) dk_y$ . When one scale dominates the fluctuation spectrum it is adequate to take  $\phi_0^2$  as the rms amplitude and choose  $k_y$  corresponding to the dominant scale.

In integrating the micro-fluxes over  $x$  we obtain the weight for a single rational surface. To obtain the total flux across the sheared magnetic field, we must introduce the mean density of the rational  $\rho_{k_y}(r) = (6|q'|/\pi^2 q^2) k_Y r$  and define  $\langle \pi_{xy} \rangle = \sum_{k_y} \int \rho_{k_y}(r) \pi_{xy} dr$ . Note that  $\rho_{k_y}(r)$  varies only on the scale of  $q(r)$  and is then essentially constant over the shear flow layer and the mode width. The total fluxes is given by the integrated formulas Eqs. (9.11)–(9.13) multiplied by the function  $\rho_{k_y}(r)$  and summed over all  $k_y$ . Here we report the flux per unit of these weighting factors. The momentum transport coefficients  $\mu_{\perp}$  and  $\mu_{\parallel}$  are defined by

$$\mu_{\perp} = \frac{\langle \pi_{xy} \rangle}{-\frac{dv_{\parallel}}{dx}} = |\phi_0|^2 \frac{c^2 k_y (\pi)^{1/2} |\hat{\omega}|^3 K L_n}{c_s B^2 \rho_s s^{5/2} \gamma^{1/2} |\hat{\omega} + K|^2} e^{\gamma \hat{v}'_{0\parallel}^2 K^2 / 4s |\hat{\omega} + K|^4}, \quad (9.47)$$

and

$$\mu_{\parallel} = \frac{\langle \pi_{x\parallel} \rangle}{-\frac{dv_{\parallel}}{dx}} = |\phi_0|^2 \frac{ce k_y (\pi)^{1/2} |\hat{\omega}|^3 L_n \gamma^{1/2}}{BT_e s^{5/2} |\hat{\omega} + K|^2} e^{\gamma \hat{v}'_{0\parallel}^2 K^2 / 4s |\hat{\omega} + K|^4}. \quad (9.48)$$

The energy transport coefficient  $\chi$  is defined as

$$\chi = \frac{\langle q_x \rangle}{-\frac{dP_0}{dx}} = \frac{L_n}{P_0(1 + \eta_i)} \langle \tilde{v}_x^* \tilde{p} + \tilde{v}_x \tilde{p}^* \rangle = |\phi_0|^2 \frac{c^2 L_n |\hat{\omega}| k_y (\pi \gamma)^{1/2}}{c_s B^2 \rho_s s^{5/2}} e^{\gamma \hat{v}'_{0\parallel}^2 K^2 / 4s |\hat{\omega} + K|^4}. \quad (9.49)$$

The transport coefficients ( $\mu \perp$ ,  $\mu \parallel$ ,  $\chi$ ) are proportional to the square of the fluctuation level  $\langle \bar{\phi}^2 \rangle$ . It is important to consider the ratio of the coefficients for which the dependence on  $\tilde{\phi}$  is removed. The ratios of the energy transport coefficient to the momentum transport coefficients are,

$$\frac{\chi}{\mu \perp} = \frac{\gamma |\hat{\omega} + K|^2}{|\hat{\omega}|^2 K} \quad (9.50)$$

$$\frac{\chi}{\mu \parallel} = \frac{|\hat{\omega} + K|^2}{|\hat{\omega}|^2}. \quad (9.51)$$

The ratios in Eqs. (9.17) and (9.18) are the reciprocal of the perpendicular and the parallel Prandtl numbers for the turbulent plasmas. The approximate solution for the dispersion equation can be written as

$$\gamma \simeq \frac{sK}{1 - \frac{\hat{v}'_{0\parallel}}{4K}} \quad (9.52)$$

if  $\frac{1}{2}|\hat{v}'_{0\parallel}| \leq sK$ , which is generally true in tokamak plasmas nowadays. As a result, in this parameter regime we have

$$\frac{\chi}{\mu \perp} \sim \frac{1 - \frac{\hat{v}'_{0\parallel}^2}{4K}}{s} + sK^2,$$

and

$$\frac{\chi}{\mu \parallel} \sim \frac{\left(1 - \frac{\hat{v}'_{0\parallel}^2}{4K}\right)}{s^2} + 1.$$

The comparison with the Prandtl numbers for Coulomb collision plasma will be given in Sec. 9.4.13.

#### 9.4.13 Numerical Evaluation of the Transport Coefficients

The dispersion equation (9.2) is solved numerically. Typical mode growth rates and frequencies are shown in Fig. 1. The reference parameters are  $s = 0.1$ ,  $b_s = 0.1$ , and  $\tau = 1$ . In Fig. 1a the mode growth rate is shown as function of  $\hat{v}'_{0\parallel} = L_n dv_{\parallel}/c_s dx$  for  $\eta_i = 0.5, 1.0, 1.5$ , and  $2.0$ . It is clear in the figure that there are two regimes for the mode development. In the first regime, where  $\hat{v}'_{0\parallel} \sim 1$  and the growth of the mode is dominated by the ion temperature gradient, the mode growth rate increases slowly with  $\hat{v}'_{0\parallel}$ . In the second regime, where  $\hat{v}'_{0\parallel} \sim 2$  and the growth of the mode is dominated by the parallel velocity shear, the mode growth rate increases rapidly with  $\hat{v}'_{0\parallel}$ . The approximate mode growth rate is given by Eq. (9.19) in the first regime. The higher the  $\eta_i$  value [deeper  $T_i(r)$  profile or flatter density profile  $n(r)$ ] or the lower the  $\tau$  value (lower  $T_e$  or higher  $T_i$ ), the flatter the curves  $\gamma$  versus  $\hat{v}'_{0\parallel}$ .

In the second regime the approximate solution of the dispersion equation (2) is

$$\widehat{\omega} = \frac{1}{2(1+b_s)} \left\{ 1 - is + \left[ (1-is)^2 - (1+b_s)\widehat{v}'_{0\parallel}^2 \left( 1 - \frac{2K(1+b_s)^{1/2}}{i|\widehat{v}'_{0\parallel}|+1} \right) \right]^{1/2} \right\} \quad (9.53)$$

if  $K$  is small compared with  $|\widehat{v}'_{0\parallel}|$ . For small magnetic shear Eq. (9.20) gives

$$\gamma \simeq \frac{1}{2(1+b_s)^{1/2}} \left( |\widehat{v}'_{0\parallel}| - \frac{K+s}{|\widehat{v}'_{0\parallel}|} \right). \quad (9.54)$$

The mode real frequency exhibits two flat regimes and a transition regime. The higher the  $\eta_i$  value the larger the difference between the two flat regimes. Generally speaking, the mode rotates in the ion diamagnetic direction and frequency increases with  $|\widehat{v}'_{0\parallel}|$ . The frequency in the laboratory frame is Doppler shifted from what is given here where  $v_\parallel(x=0)=0$ .

The micro-Reynolds stress  $\pi_{xy}$  without the factor  $|\phi_0|^2 c^2 / \rho_s B^2$  is plotted in Fig. 9.2 as function of  $x$  for  $\eta_i = 1, \tau = 1, b_s = 0.1$ . In Fig. 9.2(a)  $s = 0.1$  and  $\widehat{v}'_{0\parallel} = -1.5, -1.0, -0.5$  and 0.0. It is easy to see that  $\pi_{xy}$  is antisymmetric about the  $x = 0$  surface for  $\widehat{v}'_{0\parallel} = 0$  and that the asymmetry develops dramatically with the increasing of  $|\widehat{v}'_{0\parallel}|$ . In addition, the magnitude of the micro-Reynolds stress  $\pi_{xy}$  increases significantly with  $|\widehat{v}'_{0\parallel}|$ . In Fig. 9.2(b)  $s = 0.5$  and  $\widehat{v}'_{0\parallel} = -1.5, -0.5, 0.5$ , and 1.5. Comparison of the two cases with  $\widehat{v}'_{0\parallel} = -1.5$  shows that the asymmetry is higher while the amplitude is lower for  $s = 0.5$  than that for  $s = 0.1$ .

The Reynolds stress  $\langle \pi_{xy} \rangle$  [Eq. (9.11)] without the factor  $|\phi_0|^2 c^2 / \rho_s B^2$  is given in Fig. 9.3 as function of  $\widehat{v}'_{0\parallel}$  for  $\tau = 1, b_s = 0.1$ . In Fig. 9.3a  $\eta_i = 1.0, s = 0.1, 0.2, 0.3$ , and 0.4. It is shown that for the same  $\widehat{v}'_{0\parallel}$ ,  $|\langle \pi_{xy} \rangle|$  decreases with the magnetic shear  $s$ , and that for all the  $s$  values studied here the Reynolds stress increases with the parallel velocity shear  $|\widehat{v}'_{0\parallel}|$ . The sign of  $\langle \pi_{xy} \rangle$  is opposite to the sign of  $\widehat{v}'_{0\parallel}$ . In Fig. 9.3(b)  $s = 1, \eta_i = 2, 3, 4$ , and 5. It is seen that  $|\langle \pi_{xy} \rangle|$  increases with the increasing of  $\eta_i$  for  $\widehat{v}'_{0\parallel} \leq 1.5$  where the ion temperature gradient is the dominant driving force. For  $\widehat{v}'_{0\parallel} \sim 2$  it is the opposite,  $|\langle \pi_{xy} \rangle|$  increases with the decreasing of  $\eta_i$ .

The micro-Reynolds stress  $\pi_{x\parallel}$  without the factor  $|\phi_0|^2 c_s e / B T_e$  as function of  $x$  is plotted in Fig. 9.4 for  $\tau = 1, b_s = 0.1, s = 0.1$ . In Fig. 9.4a  $\eta_i = 1, \widehat{v}'_{0\parallel} = -1.5, -1.0, -0.5$ , and 0. Similar to  $\pi_{xy}$ , the stress  $\pi_{x\parallel}$  is inversely symmetric about the  $x = 0$  surface when  $\widehat{v}'_{0\parallel} \neq 0$  and such symmetry breaks as long as  $\widehat{v}'_{0\parallel} \neq 0$ . In Fig. 9.4(b)  $\widehat{v}'_{0\parallel} = -1.5, \eta_i = 1, 2, 3$ , and 4. Both the amplitude and the asymmetry of  $\pi_{x\parallel}(x)$  increase with parallel velocity shear  $|\widehat{v}'_{0\parallel}|$  as well as with the ion temperature gradient  $\eta_i$  for the parameters studied here.

The Reynolds stress  $\langle \pi_{x\parallel} \rangle$  [Eq. (9.12)] is plotted as function of parallel velocity shear  $\widehat{v}'_{0\parallel}$  in Fig. 9.5 for  $\tau = 1, b_s = 0.1$ . In Fig. 9.5(a)  $s = 0.1, \eta_i = 2, 3, 4$  and 5. The Reynolds stress  $\langle \pi_{x\parallel} \rangle$  increases with the increasing of  $\eta_i$  for  $|\widehat{v}'_{0\parallel}| \gtrsim 1.5$ . For  $|\widehat{v}'_{0\parallel}| \gtrsim 2$  it decreases while  $\eta_i$  increases. In Fig. 9.5(b)  $\eta_i = 3, s = 0.1, 0.2, 0.3$  and 0.4. The Reynolds stress  $\langle \pi_{x\parallel} \rangle$  increases when the magnetic shear  $s$  decreases. For  $\eta_i \sim 1$  the Reynolds stress  $\langle \pi_{x\parallel} \rangle$  is not sensitive to the magnetic shear  $s$ . In addition,  $\langle \pi_{x\parallel} \rangle$  has the opposite sign to the flow shear  $\widehat{v}'_{0\parallel}$ .

A common feature of  $\langle \pi_{xy} \rangle$  and  $\langle \pi_{x\parallel} \rangle$  is that both of them are equal to zero for  $\widehat{v}'_{0\parallel} = 0$  and that the magnitudes increase with the increasing of the flow shear  $\widehat{v}'_{0\parallel}$ .

The micro-thermal flux  $q_x$  is given in Fig. 9.6 for  $\tau = 1$ ,  $b_s = 0.1$ , and  $s = 0.1$ . In Fig. 9.6(a)  $\widehat{v}'_{0\parallel} = -1.5$ ,  $\eta_i = 1, 2, 3$ , and 4. In contrast to the momentum fluxes  $\pi_{xy}$  and  $\pi_{x\parallel}$ , the energy flux is always positive and increases with  $\eta_i$ . In Fig. 9.6(b)  $\eta_i = 1$ ,  $\widehat{v}'_{0\parallel} = -1.5, -0.5, 0.5$ , and 1.5. It is easy to notice that the curve for  $\widehat{v}'_{0\parallel} = -1.5$  is identical to the curve for  $\widehat{v}'_{0\parallel} = 1.5$  but shifts towards the left. It is the same for the curves of  $\widehat{v}'_{0\parallel} = -0.5$  and 0.5.

The integrated energy flux  $\langle q_x \rangle$  [Eq. (9.13)] is shown in Fig. 9.7 as function of the parallel flow shear  $\widehat{v}'_{0\parallel}$  for  $\tau = 1$ ,  $b_s = 0.1$ . For given magnetic shear  $s = 0.1$  the energy flux increases with the increasing of  $\eta_i$  [see Fig. 9.7(a)] while for  $\eta_i = 1$  it decreases with the increasing of the magnetic shear  $s$  [see Fig. 7(b)]. The momentum fluxes  $\langle \pi_{xy} \rangle$  and  $\langle \pi_{x\parallel} \rangle$  are zero while the energy flux is not for  $\widehat{v}'_{0\parallel} = 0$ .

All the above mentioned variations of  $\langle \pi_{xy} \rangle$ ,  $\pi_{xy}$ ,  $\langle \pi_{x\parallel} \rangle$ ,  $\pi_{x\parallel}$ ,  $\langle q_x \rangle$  and  $q_x$  with the parameters  $(s, \eta_i, \widehat{v}'_{0\parallel})$  are like at a fixed  $\phi_0^2$  so that additional variation through the dependence of  $\phi_0^2$  on the parameters must be calculated by other means in a comparison with a real physics system.

The ratio of the energy transport coefficient  $\chi$  over the poloidal momentum transport coefficient  $\mu \perp$  (the inverse Prandtl number) is independent of  $\phi_0^2$  and given in Fig. 9.8 as function of  $\widehat{v}'_{0\parallel}$  for  $\tau = 1$ ,  $s = 0.1$ . In Fig. 9.8(a)  $\eta_s = 0.1$ ,  $\eta_i = 1, 2, 3$ , and 4. One interesting point of the result is that  $\chi/\mu \perp$  decreases when  $\eta_i$  increases for  $|\widehat{v}'_{0\parallel}| \lesssim 1$  while it is the opposite for  $|\widehat{v}'_{0\parallel}| \gtrsim 1.5$ : lower  $\eta_i$  corresponds to lower  $\chi/\mu \perp$ . In Fig. 9.8(b)  $\eta_i = 1$ ,  $b_s = 0.1, 0.2, 0.3$ , and 0.4. The ratio  $\chi/\mu \perp$  monotonously decreases for increasing  $b_s$ . Not shown here is the results we obtained that  $\chi/\mu \perp$  monotonously increases for decreasing magnetic shear  $s$ . The common feature is that  $\chi$  and  $\mu \perp$  are always positive and the value  $\chi/\mu \perp$  decreases with the increasing of the parallel flow shear  $|\widehat{v}'_{0\parallel}|$ . Figure 9.9 shows the inverse Prandtl number defined with respect to the parallel turbulent viscosity  $\chi/\mu_\parallel$ . The results are similar except that  $\chi/\mu_\parallel$  is more than one order of magnitude higher than  $\chi/\mu \perp$ , which means that  $\mu \perp$  is much higher than  $\mu_\parallel$ .

For Coulomb collisions the corresponding inverse Prandtl numbers are

$$\frac{\chi}{\mu_1} \simeq 7, \quad \frac{\chi}{\mu_2} \simeq 1.7.$$

Here  $\mu_2$  corresponds to  $\mu_\parallel$  in the turbulence case and  $\mu_1$  is perpendicular viscosity coefficient with no direct correspondence to the turbulent viscosities given here. Thus the turbulent Prandtl numbers ( $\simeq 0.01$ ) are small compared with the Coulomb collisional values ( $\simeq 0.6$ ). There are no parameters in the theory based on the Coulomb collision corresponding to  $\mu \perp$ . The parameter  $\mu \perp$  introduced in this work is unique for the theory of turbulence driven by velocity shear.

#### 9.4.14 Discussion

It is widely recognized by fusion physicists [Dorland, *et al.* (2002), Erba, *et al.* (1995, 1999)], that the plasma dynamics in the bulk region and in the Scrape-Off Layer (SOL) are significantly

different from each other. As a consequence there must be a transition region around the edge of the limiter or the Last Closed Flux Surface (LCFS), where some of the plasma parameters change rather rapidly across the region. In other words, the edge plasma is characterized by a rapid radial dependence of the plasma parameters such as parallel plasma flow. Particles may move freely along the magnetic field lines in the bulk plasma while such freedom does not exist in SOL due to the presence of limiter or divertor plates.

Experimentally, a poloidal flow shear has been observed in the vicinity of a material limiter [Chen and Sen (1995)], in a ohmically-heated plasma. The poloidal velocity shear is important in the L–H transition [Chen and Cheng (1980)]. We present evidence that the plasma parallel velocity changes at about the same radial location as the poloidal shear flow layer. These measurements were taken on the TEXT–U tokamak with plasma conditions  $B_T = 2.5$  T,  $I_p = 220$  kA, and a line-averaged density,  $\bar{n}_e = 3.0 \times 10^{13}$  cm $^{-3}$ , using a reciprocating probe array. The plasma was defined by three rail limiters located at  $r = 27$  cm. The probe array was mounted on the top of the vessel separated from the limiters by 247.5° in the plasma current direction. The toroidal magnetic field was in the same direction as the plasma current, and the ion grad- $B$  drift was upwards. In Fig. 9.9(a) we show a radial profile of the parallel flow Mach number  $M = v_{\parallel}/c_d$  measured with a Mach probe with two collecting electrodes biased with –180 V to collect ion saturation currents from upstream and downstream. The current ratio can then be used to calculate the flow Mach number [Fukuyama, et al. (1994), Furnish, et al. (1999), Gang, et al. (1991)] with the assumption that the ion temperature is equal to the electron temperature. We used the Hutchinson model [Gang, et al. (1991)] which includes diffusion and viscosity into the probe presheath. The ion flow direction is in the direction of the toroidal magnetic field and plasma current. Figure 9.9(b) presents the normalized radial derivative of the ion parallel velocity. In Fig. 9.10(c) we show a radial profile of the poloidal phase velocity,  $v_{\text{phase}}$ , used to define the shear layer [Chen and Sen (1995)]. The phase velocity is derived from the power spectrum measured with a two-point correlation technique,  $v_{\text{phase}} = \sum_{k,\omega} \frac{\omega}{k} S(\omega, k) / \sum_{k,\omega} S(\omega, k)$ , where  $S(k, \omega)$  is the measured power spectra [Garbet and Waltz (1996)] as a function of wavenumber and frequency. Since the phase velocity measurements were not taken on the same shot as the data on parallel flow velocity, it is important to note that the conditions were similar and the location of the velocity shear layer is generally robust for the plasma conditions used. We estimate the uncertainty in position for the location of the flow shear layer to be of order 4 mm. To within the limits of plasma reproducibility the maximum gradient of the parallel ion flow occurs at the same radial position as the velocity shear in the perpendicular direction.

In order to make detailed comparison possible the quasilinear saturation amplitude is estimated in the following. Suppose that the mixing length saturation level is determined by the condition that

$$x \frac{dv_{\parallel}}{dx} \sim \tilde{v}_{\parallel}(x), \quad (9.55)$$

which is valid if  $|\tilde{v}'_{0\parallel}| \gtrsim 1 + \eta_i$ . Noting from the motion equation in the parallel direction that

$\tilde{v}_\parallel = (\text{esc}_s/T_e \hat{\omega}) x \tilde{\phi}$ , then it is straightforward to have

$$\phi_0 \sim \frac{T_e}{e} \frac{\rho_s}{L_n} \tilde{v}'_{0\parallel}. \quad (9.56)$$

For  $\tilde{v}'_{0\parallel} < 1 + \eta_i$  the saturation level is  $\phi_0 \simeq (\eta_i - \eta_{ic})/\langle k_x^2 \rangle^{1/2} \simeq (\eta_i - \eta_{ic})/\langle k_y^2 \rangle^{1/2}$

Substituting Eq. (9.23) into Eqs. (9.11)–(9.13) gives the approximate formulas as follows

$$\begin{aligned} \langle \pi_{xy} \rangle &= -\frac{c^2 T_e^2}{e^2 B^2 L_n^2} \frac{(\pi)^{1/2} k_y \rho_s}{s^{5/2}} \frac{\gamma^{1/2} |\hat{\omega}|^2 K \tilde{v}_{0\parallel}^3}{|\hat{\omega} + K|^2} \\ &= -\left(\frac{c T_e}{e B L_n}\right)^2 F_\perp(\eta_i, \tau, s, \tilde{v}'_{0\parallel}, b_s), \end{aligned} \quad (9.57)$$

$$\begin{aligned} \langle \pi_{x\parallel} \rangle &= -\frac{c^2 T_e^2}{e^2 B^2 L_n^2} \frac{(\pi)^{1/2} k_y \rho_s}{s^{5/2}} \frac{\gamma^{1/2} |\hat{\omega}|^3 \tilde{v}_{0\parallel}^3}{|\hat{\omega} + K|^2} \\ &= -\left(\frac{c T_e}{e B L_n}\right)^2 F_\parallel(\eta_i, \tau, s, \tilde{v}'_{0\parallel}, b_s), \end{aligned} \quad (9.58)$$

$$\begin{aligned} \langle q_x \rangle &= \frac{c^2 T_e^2}{e^2 B^2 L_n c_s} P_0 (1 + \eta_i) (\pi \gamma)^{1/2} k_y \rho_s L_n s^{5/2} |\hat{\omega}| \tilde{v}_{0\parallel}^2 \\ &= -\left(\frac{\rho_s^2 c_s}{L_n}\right) G(\eta_i, \tau, s, \tilde{v}'_{0\parallel}, b_s) \frac{dP_0}{dx}. \end{aligned} \quad (9.59)$$

To obtain the fluxes as function of system parameters the value of  $\hat{\omega} = \hat{\omega}_r + i\gamma$  must be calculated from Eq. (9.2) and substitute into Eqs. (9.24)–(9.26). The dimensionless functions  $F_\perp$ ,  $F_\parallel$ , and  $G$  are given by

$$\begin{aligned} F_\perp(\eta_i, \tau, s, \tilde{v}'_{0\parallel}, b_s) &= \frac{(\pi)^{1/2} k_y \rho_s}{s^{5/2}} \frac{\gamma^{1/2} |\hat{\omega}|^2 K \tilde{v}_{0\parallel}^3}{|\hat{\omega} + K|^2} \\ F_\parallel(\eta_i, \tau, s, \tilde{v}'_{0\parallel}, b_s) &= \frac{(\pi)^{1/2} k_y \rho_s}{s^{5/2}} \frac{\gamma^{1/2} |\hat{\omega}|^3 \tilde{v}_{0\parallel}^3}{|\hat{\omega} + K|^2} \end{aligned}$$

and

$$G(\eta_i, \tau, s, \tilde{v}'_{0\parallel}, b_s) = \frac{(\pi \gamma)^{1/2} k_y \rho_s}{s^{5/2}} |\hat{\omega}| \tilde{v}_{0\parallel}^2.$$

The equation for generation of the poloidal velocity  $\langle v_\theta \rangle$  is

$$\frac{\partial}{\partial t} \langle v_\theta \rangle = -\frac{1}{r} \frac{\partial}{\partial r} (r \langle \pi_{xy} \rangle). \quad (9.60)$$

In our case, suppose that the parameters are constant except  $\hat{v}'_{0\parallel}$ , then

$$\begin{aligned}\frac{\partial}{\partial x} \langle \pi_{xy} \rangle &= -\frac{c^2 T_e^2}{e^2 L_n^3 B^2} \frac{k_y \rho_s(\pi)^{1/2}}{s^{5/2}} \frac{\gamma^{1/2} |\hat{\omega}|^2 K}{|\hat{\omega} + K|^2} \left( 3 + \frac{\gamma K^2 \hat{v}_{0\parallel}^2}{2s |\hat{\omega} + K|^4} \right) \hat{v}_{0\parallel}^2 \hat{v}_{0\parallel}'' \\ &= -\frac{c^2 T_e^2}{e^2 L_n^3 B^2} H(\eta_i, \tau, s, b_s, \hat{v}'_{0\parallel}, \hat{v}_{0\parallel}''),\end{aligned}\quad (9.61)$$

where  $\hat{v}_{0\parallel}'' = L_n^2 d^2 v_{\parallel}/c_s dx^2$  and

$$H(\eta_i, \tau, s, b_s, \hat{v}'_{0\parallel}, \hat{v}_{0\parallel}'') = \frac{k_y \rho_s(\pi)^{1/2}}{s^{5/2}} \frac{\gamma^{1/2} |\hat{\omega}|^2 K}{|\hat{\omega} + K|^2} (3 + \frac{\gamma K^2 \hat{v}_{0\parallel}^2}{2s |\hat{\omega} + K|^4}) \hat{v}_{0\parallel}^2 \hat{v}_{0\parallel}''.$$

Equations (9.27) and (9.28) clearly show that the driving force for the poloidal velocity is independent of the sign of  $\hat{v}'_{0\parallel}$  but depends on the sign of  $\hat{v}_{0\parallel}''$ . Such dependence of the driving force on  $\hat{v}_{0\parallel}''$  determines the dependence of  $\langle v_\theta \rangle$  on  $\hat{v}_{0\parallel}''$  and will be discussed later. In general, the functions  $F_\perp$ ,  $F_\parallel$ ,  $G$ , and  $H$  should be replaced by  $F_\perp A$ ,  $F_\parallel A$ ,  $GA$ , and  $HA$ , where the exponential part  $A = \exp(\gamma \hat{v}_{0\parallel}^2 K^2 / 4s |\hat{\omega} + K|^4) \sim 1$  since for a real system  $\gamma \hat{v}_{0\parallel}^2 K^2 / 4s |\hat{\omega} + K|^4 \simeq \gamma \hat{v}_{0\parallel}^2 / 4s K^2 \ll 1$  when  $\gamma$  is given by Eq. (9.19).

Measurements from the TEXT-U experiment show [Hahm (2002)] that the measured poloidal plasma velocity shear increases with plasma current, decreases with chord average density and the toroidal magnetic field. The shear layer width is a constant over a range of discharge conditions. There is no explicit dependence on plasma density  $\bar{n}$  and current  $I_p$  in Eq. (9.28). However, both the decrease of density  $\bar{n}$  and the increase of current  $I_p$  correspond to an increase of electron temperature  $T_e$  in the shear layer which explicitly appears in Eq. (9.28). The poloidal driving force given in Eq. (9.28) is inversely proportional to  $B^2$ . In summary, the driving force given in Eq. (9.28) is qualitatively in agreement with the measured scaling if the damping mechanism is approximately independent of those parameters. There is no simple scaling for the shear layer width from this model. Physically, it is reasonable to think that the poloidal shear layer width is approximately the same as of the parallel flow shear.

Some damping mechanism must be introduced to estimate the steady state poloidal velocity driven by the turbulence. As an example the magnetic damping is considered as the only damping mechanism and equilibrium poloidal velocity is included. Under these conditions the plasma motion equation in the poloidal direction, Eq. (9.27) will be modified as follows [Biskamp, et al. (1994), Dorland, et al. (2002), Doyle et al. (1991)]

$$\frac{\partial}{\partial t} \langle v_\theta \rangle = -\frac{1}{r} \frac{\partial}{\partial r} (r \langle \pi_{xy} \rangle) - \nu^{nc} (\langle v_\theta \rangle - v_\theta^{nc}) \quad (9.62)$$

where  $v_\theta^{nc}$  is the equilibrium poloidal velocity, and

$$\nu^{nc} = \frac{\nu_{ii}}{\epsilon^{3/2} (1 + \nu_*) (1 + \epsilon^{2/3} \nu_*)} \quad (9.63)$$

with  $\nu_* = \nu_{ii}qR/v_\theta\epsilon^{3/2}$  and  $\epsilon$  is the inverse aspect ratio,  $q$  the safety factor,  $R$  the major radius and  $\nu_{ii}$  the ion-ion collision frequency. In steady state Eq. (9.29) reduces to

$$\langle v_\theta \rangle - v_\theta^{\text{nc}} = -\frac{1}{\nu^{\text{nc}}} \frac{\partial}{\partial x} \langle \pi_{xy} \rangle. \quad (9.64)$$

For the dimensionless parameters  $(\eta_i, s, \tau, \hat{v}'_{0\parallel}, b_s)$  of order unity the poloidal acceleration from the divergence of the momentum flux is of the magnitude  $(cT_e/eBL_n)^2/L_n \simeq v_{de}^2/L_n$  compared with the neoclassical damping rate  $\nu^{\text{nc}}$ .

In order to make further comparison it is assumed that the equilibrium poloidal velocity  $v_\theta^{\text{nc}}$  is negligible, and that the plasma is around the boundary between the Pfirsch-Schlüter and the plateau regimes with  $l \sim qR$  so that  $\nu^{\text{nc}} \simeq \nu_{ii}$ . Then the steady-state poloidal velocity [Eq. (9.31)] reduces to

$$\langle v_\theta \rangle = \frac{1}{\nu_{ii}} \frac{v_{de}^2}{L_n} H(\eta_i, \tau, s, b_s, \hat{v}'_{0\parallel}, \hat{v}''_{0\parallel}). \quad (9.65)$$

For the typical discharge parameters:  $T_e = T_i = 40 \text{ eV}$ ,  $B = 20 \text{ kG}$ ,  $n = 3 \times 10^{12}/\text{cm}^3$ ,  $L_n = 3 \text{ cm}$ , it turns out that

$$\frac{1}{\nu_{ii}} \frac{v_{de}^2}{L_n} \simeq 2.1 \times 10^5 \text{ cm/s.}$$

The function  $H$  is sensitive to  $\hat{v}'_{0\parallel}$ . For the parameters used in this study, i.e.  $s = 0.1, b_s = 0.1, \eta_i \sim 1, \tau = 1$ , the results are given in Fig. 11.  $H$  versus  $\hat{v}''_{0\parallel}$  is given in Fig. ?? for  $\hat{v}'_{0\parallel} = 0.5$ . The maximum value of  $H$  is about 10 for  $\hat{v}'_{0\parallel} = 1$ . These numbers are in reasonable agreement with the experimental observations,  $\langle v_\theta \rangle \sim -3$  to  $+3 \times 10^5 \text{ cm/s}$ . It should be noted that the suppression effect of the poloidal velocity shear on the fluctuation is not considered in this work. In this regard the driving force from the turbulent Reynolds stress is overestimated. On the other hand, however, the saturation level evaluation [Eq. (9.23)] is made without taking the ion temperature gradient ( $\eta_h$ ) effect into account. This may lead to underestimation of the driving force. These two factors may compensate each other so that the theoretical numbers are well in the regime of the experimental observations.

According to Eq. (9.32) the dependence of  $\langle v_\theta \rangle$  on  $\hat{v}''_{0\parallel}$  is the same as given Eq. (9.28) for the driving force and is qualitatively in agreement with the experimental observations given in Fig. 10 from TEXT-U tokamak. Roughly speaking,  $\langle v_\theta \rangle$  has the same sign as that of  $\hat{v}''_{0\parallel}$  and changes sign at the same location where  $\hat{v}''_{0\parallel} \simeq 0$ . The correlation between  $\langle v_\theta \rangle$  and  $\hat{v}''_{0\parallel}$  is very impressive though the data shown here are not from the same discharge. To further study the profile of the turbulence driven  $\langle v_\theta \rangle$ , the profile of the derivative of the parallel velocity can be modeled as  $\hat{v}'_{0\parallel}(x) = -0.5 \operatorname{sech}(\alpha x)$ , with  $\alpha$  being a constant of order unity and  $x = 0$  the position where  $\hat{v}'_{0\parallel}(x)$  has minimum. Then the function  $H(x)$  is given in Fig. 10(b). It is reasonable to assume that  $v_{de}^2/\nu_{ii}L_n$  is roughly a constant in the velocity shear layer. Under these assumptions the poloidal velocity profile from this model is approximately the same as that given in Fig. 10(b) which is similar to the experimental results given in Fig. 9(c) and Hahm (2002).

The width of the velocity shear layer can be estimated as

$$\Delta \simeq \frac{\langle \pi_{xy} \rangle}{\nu_{ii} \langle v_\theta \rangle} \sim \frac{4 \times 10^9}{3.2 \times 10^9} \sim 1 \text{ cm} \quad (9.66)$$

and is in good agreement with the experimental observations.

To close this section we would like to say a few words about the L–H transition from the point of view of the model suggested in this work. One typical feature of the L–H transition is that  $v_\theta$  and  $|v'_\theta| = |dv_\theta/dr|$  increase very rapidly ( $\sim 100\mu\text{s}$ ) during the transition. The driving force given in Eq. (28) exponentially increases with  $\widehat{v}_{0\parallel}^2 K^2 / |\widehat{\omega} + K|^4$ . Usually  $|\widehat{\omega}| < K$  so that such increase is slow as long as  $|\widehat{v}'_{0\parallel}| < K$ . However, the acceleration increases very rapidly when  $|\widehat{v}'_{0\parallel}| \gtrsim K$ . It may be possible that the condition  $|\widehat{v}'_{0\parallel}| \gtrsim K$ , (i.e.  $|v_\parallel/dx| \gtrsim c_s(L_n + L_T)T_i/L_n L_T T_e$ ) somehow is achieved and triggers the L–H transition. Another concern is how the acceleration process is stopped. It has been demonstrated [Antipov, et al. (1985), Antonova (1983), Balescu (1988), Colas, et al. (1998)] that the mode growth rate will decrease after the poloidal flow is driven up. The driving force in Eq. (9.28) is proportional to the  $\frac{3}{2}$ -power of the mode growth rate so that the acceleration stops when the mode becomes marginally stable. This stopping effect can be modeled by taking  $\gamma = \gamma_0(1 - v_\theta'^2/v_{\theta\text{crit}}^2)$ . Another mechanism to stop the acceleration is that  $L_n$  becomes very small in the shear flow layer after L–H transition so that the dimensionless driving force parameter  $\widehat{v}'_{0\parallel} = L_n dv_\parallel/c_s dr$  is negligibly small even though  $dv_\parallel/dr$  does not change very much. Of course, the plasma will eventually enter into a steady state if other drag forces such as the magnetic damping are taken into account.

#### 9.4.15 Conclusions

The instability driven by parallel flow shear is studied within the fluid approximation in a local slab configuration with magnetic shear. Ion temperature gradient  $\eta_i$  is taken into account. The dimensionless parameter set of the problem is  $(\eta_i, \tau, s, \widehat{v}'_{0\parallel}, b_s)$ . The quasilinear expressions for the radial fluxes of the parallel momentum  $\langle \pi_{x\parallel} \rangle$ , the perpendicular momentum  $\langle \pi_{xy} \rangle$  and the thermal energy  $\langle q_x \rangle$  are derived using the exact linear eigenfunction. The perpendicular and parallel momentum fluxes, called Reynolds stress, are shown to vanish when the dimensionless parameter  $\widehat{v}'_{0\parallel} = 0$  due to the symmetry feature of the mode structure about the rational surface. Such symmetry property is broken leading to nonzero parallel and perpendicular momentum transport as long as  $\widehat{v}'_{0\parallel} \neq 0$ . This dependence on the parallel velocity shear does not hold for the thermal energy flux:  $\langle q_x \rangle$  does not vanish when  $\widehat{v}'_{0\parallel} = 0$ . The Reynolds stress exponentially increases with  $(T_e L_n L_T / T_i (L_n + L_T) c_s)^2 (dv_\parallel/dx)^2$ , while it is proportional to the square of the electron temperature  $T_e^2$  and inversely proportional to the square of the toroidal magnetic field  $B^2$ . Experimental measurements of the parallel and poloidal plasma flows on TEXT–U tokamak are carried out and the results support the interpretation that the poloidal shear flow is generated through the turbulence driven by parallel sheared plasma flow. The theoretical models are compared and shown to be of reasonable agreement with the experimental observations for scalings as well as for

magnitudes when the neoclassical damping mechanism is introduced to balance the driving force from the Reynolds stress.

The transport coefficients ( $\mu \perp, \mu_{\parallel}, \chi$ ) induced by the  $\mathbf{E} \times \mathbf{B}$  turbulence of the instability are obtained analytically. They are always positive. The positivity of the turbulent transport means that entropy production from the transformation of the ordered flows into the turbulent fluctuations is positive definite. The ratio of the energy transport coefficient to the viscosity coefficient is obtained and studied numerically.

The suppression effects of the poloidal velocity gradient on the fluctuations are not considered in this work. In *Biskamp, et al.* (1994) hydrodynamic simulations show the evolution of  $\tilde{v}_{\parallel}$ -driven turbulence and the reaction of the turbulence through  $\pi_{xy}$  and  $\pi_{xz}$  on the mean shear flows including the creation of  $\mathbf{E} \times \mathbf{B}$  shear flow. A self-consistent study about the poloidal flow generation by the turbulence and the fluctuation suppression by the poloidal velocity shear is in progress and will be published in a separate work.

As is pointed out in *Erba, et al.* (1999), the tokamak plasma is a complex physical system. The edge region, where more physics processes take place than in the bulk region, is the most complex subsystem. The model suggested in this work does not exclude other models for the subject of the sheared flow generation. The parallel flow shear is only one of the physical phenomena which exhibit and influence the plasma behavior in the edge region. The emphasis here is that a parallel velocity shear does exist in the edge region and provide a free energy source for turbulence, as well as a symmetry breaking element which is necessary for the poloidal sheared flow generation by turbulence in the quasilinear theory.

## Impurity-induced micro-electromagnetic instabilities in toroidal plasmas

Impurities are important elements in tokamak plasmas. Impurities affect stability, transport, confinement, and safety. Impurity effects on ITG, TEM and AITG modes, and the by impurity-induced electrostatic modes have been studied in tokamak and RFP plasmas [*Antipov, et al.* (1982, 1985), *Antonova* (1983), *Balescu* (1988), *Biskamp* (1997)]. Kinetic shear Alfvén and kinetic ballooning instabilities have been investigated without the effects of impurities. The impurity induced electromagnetic instabilities (KSA and KBM) are studied in this work [*Zhong, et al.* (2016)].

### 9.4.16 Double critical gradients of impurity density HL-2A for exciting edge electromagnetic turbulence

- (a) Divertor Da and edge  $n_z$
- (b)  $B_{\theta}$  fluctuations measured with Mirnov coil

- (c)  $n_e$  fluctuations from reflectometry (ped. top)
  - (d) Coherence ( $B_\theta$  and  $n_e$  fluctuation)
  - (e) Evolution of integrated coherence for EM turbulence
  - (f) Filtered  $B_\theta$  fluctuation of EM turbulence in H-mode
  - (g) EM turbulence intensity in H-mode
  - (h) Edge impurity accumulation occurrence of EM turbulence (50-150 kHz)
  - (i) I: LCOs  $\rightarrow n_z$  decreases  $\rightarrow$  EM turbulence is replaced by ES turbulence
- Coherence is noticeably higher in H-mode  $\rightarrow$  EM turbulence is localized around the pedestal top; Exponential growth and then saturation of the EM turbulence.

#### 9.4.17 Preliminary comparison between experimental and HD7 results with C<sup>+4</sup> impurity ions considered

The strong asymmetry of the two critical gradients is consistent with the experimental observation [Zong, et al. (2016)].

#### 9.4.18 Questions

Do these results have general meaning? The modes are really induced by impurities? They are EM modes or ES modes with finite beta effects? What kind of instabilities they are?

#### 9.4.19 Physics Model and Equations

Axisymmetric toroidal configurations of circular flux surfaces with Shafranov shift ( $s--\alpha$  model); Ballooning mode representation;

Gyrokinetic theory retaining:

Full main and impurity ion transit  $k_p v_p$ ;

Curvature and magnetic gradient drifts for main and impurity ions  $\omega_D(v_\perp^2, v_p^2, \theta)$ ;

Finite Larmor radius effects;

Ion magnetic trapping is neglected;

Electrons are assumed to be massless.

Quasineutrality condition

$$\sum_x Z_s n_x^{0/0} = 0$$

Parallel component of Ampère's law:

$$\nabla_\perp^2 \infty$$

$$A_p = -\frac{4\pi}{c} \sum_s j_s^{0/0}$$

$s = 1, z, e$  for hydrogen, impurity, and electron

$$n_s^{0/0} = \int f_s d^3v, \quad J_{sp}^{0/0} = q_s \int \nu_p f_s d^3v, \quad f_s = -\frac{q_s F_{Ms}}{T_s} \phi^{0/0} + h_s J_0(\delta_s)$$

$$i \frac{\nu_p}{qR} \frac{\partial}{\partial \theta} h_s + (\omega - \omega_{Ds}) h_s = (\omega - \omega_{*sT}) J_0(\delta_s) F_{Ms} \frac{q_s n_{0s}}{T_s} \left( \phi^S(\theta) - \frac{\nu_p}{c} \mu_{Ap}(\theta) \right).$$

Eigenmode equations

$$\begin{aligned} [1 + \tau_i(1 - f_z) + \tau_z Z f_z] \phi^S(k) &= \int_{-\infty}^{+\infty} \frac{dk'}{\sqrt{2\pi}} \left\{ (K_{11}^i(k, k') + K_{11}^z(k, k')) \phi^S(k') \right. \\ &\quad \left. + \left[ (K_{12}^i(k, k') + K_{12}^z(k, k')) + K_{12}^e(k, k') \right] \mu_{Ap}(k') \right\}, \\ \frac{k_\perp^2}{2\tau_i} \mu_{Ap}(k) &= \int_{-\infty}^{+\infty} \frac{dk'}{\sqrt{2\pi}} \left\{ [(K_{21}^i(k, k') + K_{21}^z(k, k')) + K_{21}^e(k, k')] \phi^S(k') \right. \\ &\quad \left. + \left[ (K_{22}^i(k, k') + K_{22}^z(k, k')) + K_{22}^e(k, k') \right] \mu_{Ap}(k') \right\}, \end{aligned}$$

where  $f_z = Z n_z n_e$  is the impurity charge concentration.

$$K_{m,n}^{s(s=i,z)}(k, k') = -i \int_{-\infty}^0 \omega_{*e} d\tau H_{m,n}^s(\tau, k, k'),$$

and

$$\begin{aligned} H_{11}^s(\tau, k, k') &= \sqrt{2} f_s e^{-i\omega\tau} \frac{\exp[-(k, k')^2/4\lambda_s]}{\sqrt{a_s}(1+a_s)\sqrt{\lambda_s}} \times \left\{ \omega \tau_s Z_s + L_{es} \left[ 1 + \tau_s \left( -\frac{3}{2} + \frac{2}{1+a_s} \right) \right] \right. \\ &\quad \left. + L_{es} \eta_s \left[ \left( \frac{(k, k')^2}{4a_s \lambda_s} - \frac{k_\perp^2 + k'^2_\perp}{1+a_s} \frac{\mu_s}{\tau_s Z_s^2} \right) + \frac{2k_\perp k'_\perp}{1+a_s} \frac{\mu_s}{\tau_s Z_s^2} \frac{I_1}{I_0} \right] \right\} \Gamma_{0s}(k_\perp, k'_\perp), \\ H_{12}^s(\tau, k, k') &= \frac{k - k'}{2\sqrt{a_s \lambda_s}} H_{11}^s(\tau, k, k'), \\ H_{21}^s(\tau, k, k') &= -\beta_s \frac{(k - k')}{2\sqrt{a_s \lambda_s}} H_{11}^s(\tau, k, k'), \\ H_{22}^s(\tau, k, k') &= -\beta_s \frac{(k - k')^2}{4a_s \lambda_s} H_{11}^s(\tau, k, k'), \end{aligned}$$

$$\begin{aligned}
K_{12}^e(k, k') &= \frac{iq\sqrt{\pi\tau_i}}{2\sqrt{2}\varepsilon_n S}(\omega - 1)\text{sgn}(k, k'), \quad K_{12}^e(k, k') = -\beta_i K_{12}^e, \\
g(\theta, \theta') &= (s + 1)(\sin \theta - \sin \theta') - s(\theta \cos \theta - \theta' \cos \theta') - \frac{\alpha}{2}(\theta - \theta' - \sin \theta \cos \theta + \sin \theta' \cos \theta'), \\
\lambda_s &= \frac{\tau_*^2 \omega_{*e}^2}{a_s} \frac{1}{\tau_s \mu_s} \left( \frac{s}{q} \varepsilon_n \right)^2 a_s = 1 + i \frac{2\varepsilon_n}{\tau_s Z_s} \frac{g(\theta, \theta')}{(\theta - \theta')} \omega_{*e} \tau, \\
\Gamma_{0s} &= I_0 \left( \frac{k_\perp k'_\perp}{(1 + a_s) \tau_s Z_s^2} \frac{\mu_s}{\mu_s} \right) \exp \left[ -\frac{k_\perp^2 + k'^2_\perp}{2(1 + a_s) \tau_s Z_s^2} \frac{\mu_s}{\mu_s} \right], \\
k_\perp^2 &= k_\theta^2 + k^2, \quad k'^2_\perp = k_\theta^2 + k'^2, \quad k = k_\theta(s\theta - \alpha \sin \theta), \quad k' = k_\theta(s\theta' - \alpha \sin \theta'), \\
\alpha &= -R_0 q^2 \frac{d\beta}{dr} = \frac{q^2 \beta_e}{\varepsilon - n} \left\{ \frac{L_{ei}(1 - f_z)}{\tau_i} (\eta_i + 1) + (\eta_e + 1) + \frac{L_{ez} f_z}{Z_c \tau_c} (1 + \eta_z) \right\}.
\end{aligned}$$

**Typical parameters:**

$$\begin{aligned}
\eta_i &= \eta_e = 0, 0, \quad q = 4.0, \quad 1/L_{ns} = -\partial \ln n_s / \partial r, \\
T_e/T_i &= \tau_i = T_e/T_z = \tau_z = 1, \quad k_\theta \rho_s = 0.3, s = 2.0, \\
m_i/m_e &= 1836, \quad \beta_e = 0.01, \quad f_z = Z n_z / n_e = 0.3.
\end{aligned}$$

#### 9.4.20 Numerical tool:

Code HD7: 1D integral eigenmode equations

1. ions: complete gyrokinetic description;
2. electron: massless (in this version);
3. electrostatic and electromagnetic;
4. two ion species

Benchmark:

1. Electrostatic
2. Electromagnetic version
3. Numerical Results

Positive impurity density gradient

$$L_{ez} = L_{ne}/L_{nz} = -7, \quad \varepsilon_n = \varepsilon_{ne} = 0.15,$$

Negative impurity density gradient

$$L_{ez} = L_{ne}/L_{nz} = 5, \quad \varepsilon_n = \varepsilon_{ne} = 0.04,$$

$$R/L_{ns} = -R\partial \ln n_s / \partial r,$$

Double critical impurity density gradients

Positive  $\partial \ln n_z / \partial r$

1. The larger the impurity mass, the higher the growth rate;
2. The larger the impurity charge, the higher the growth rate;
3. The higher  $\partial \ln n_z / \partial r$ , the higher the growth rate and frequency;
4. ITG destabilizing;

Negative  $\partial \ln n_z / \partial r$ ,

1. Impurity mass effect is weak;
2. The larger the impurity charge, the higher the growth rate;
3. The higher  $\partial \ln n_z / \partial r$ , the higher the growth rate and lower frequency;
4. ITG effect variant;

Critical impurity charge concentration

$\beta_e$  and  $\alpha$  dependences of the modes

Positive  $\partial \ln n_z / \partial r$ ,

1. Critical  $\beta_e$  and  $\alpha$  for the modes to grow;
2. Kinetic ballooning features;
3. The real frequency decreases with  $\beta_e$  and  $\alpha$

Negative  $\partial \ln n_z / \partial r$ ,

1. Critical  $\beta_e$  and  $\alpha$  for the modes to grow;

2. Kinetic ballooning features;
3. The real frequency increases with  $\beta_e$  and  $\alpha$

Poloidal wave vector spectrum

Mode structure

1. Impurity induced electromagnetic instabilities are demonstrated numerically;
2. Double critical gradients of impurity ion density for exciting the modes are confirmed;
3. The impurity charge concentration has critical values for the excitation of the instabilities;
4. The instabilities are identified as kinetic ballooning and kinetic shear Alfvén modes, respectively, instead of electrostatic modes with finite beta effects;
5. The modes are unstable in the first and second stable regimes of the ideal MHD ballooning modes;
6. The dynamic difference between the main and impurity ions may provide new free energy for the collective plasma motions.
7. More detailed analysis is needed for the modes.

## Nonlinear MHD Simulations of Pellet Triggered ELM for ITER Plasma Scenarios

ITER operation in its high-fusion performance DT scenarios relies on the achievement of the H-mode confinement regime, which is expected to lead to the quasi-periodic triggering of Edge Localized Modes (ELMs) [Futatani, *et al.* (2017)]. The energy fluxes associated with natural (or ‘uncontrolled’) ELMs are expected to produce excessive erosion and/or superficial surface damage on the plasma facing component and large W influxes due to sputtering during the ELMs. Controlled triggering of ELMs by the injection of small deuterium–ice pellets at frequencies significantly exceeding those of uncontrolled ELMs is one of the foreseen schemes to control ELM energy losses, divertor power fluxes and W production during ELMs. Although the technique has been demonstrated to decrease ELM energy loss successfully in ASDEX Upgrade [Lang, *et al.* (2004)], JET [Lang, *et al.* (2013)], and DIII-D [Baylor, *et al.* (2013)], uncertainties still remain regarding the physics understanding as well as of the consequence of its application, such as localized power loads associated with this technique [Wenninger, *et al.* (2011)]. The nonlinear MHD simulations with the JOREK code [Huijsmans and Czarny (2007), Futatani, *et al.* (2014)] have been performed to study the dependence of the pellet size required to trigger an ELM in ITER plasma, and also the dependency of the threshold on the pedestal plasma pressure when the

pellet is injected; based on the assumption of that the pedestal pressure leading to spontaneous ELM triggering is 150 kPa pedestal pressure of 75 kPa and 112.5 kPa have been studied. The work contributes the estimation of the requirement of the pellet injection condition to control ELMs in ITER 15 MA operation scenarios.

## Implemented pellet modeling in JOREK

The nonlinear MHD code JOREK includes a model for the density source coming from the ablation of an injected deuterium pellet [*Huijsmans and Czarny (2007)*, *Futatani, et al. (2014)*, *Futatani (2016)*]. The pellet is assumed to travel along a straight line with a given fixed velocity. The amplitude of the space and time varying density source is such that the integrated source rate is consistent with the Neutral Gas Shielding (NGS) pellet ablation model [*Gal, et al. (2008)*]. With nonlinear MHD equations, the pellet ablation process is calculated self-consistently. The ablation of the pellet as it travels into the plasma causes a large local, moving density source. Since the deuterium pellet injection is mostly adiabatic, the temperature at the location of the density source will drop such that the local pressure stays constant initially. Due to the large heat conductivity, the region over which the density perturbation extends will be quickly heated up. This results in a strong local increase of the pressure which triggers an ELM.

## Pellet triggered ELM in ITER 15 MA/5.3 T $Q = 10$ operation scenarios

The ITER plasma equilibrium profiles which have the pressure of 150 kPa, 112.5 kPa and 75 kPa at the pedestal top are prepared as shown in Fig. . The distance to the edge MHD stability limit of the target plasma is varied by changing the pedestal pressure gradient, and, self-consistently, the pedestal bootstrap current in a given number of steps (at 50% and 75% of the maximum stable condition which corresponds to the 150 kPa of the pressure at the pedestal top). There will be three pellet injection ports in ITER plasma as shown in Fig. . In JOREK, the initial pellet locations are chosen to be located slightly outside of the separatrix.

The dependence of ELM size on the pellet size has been studied for the pedestal pressure of 75 kPa. The pellet injection velocity is 300 m/s, and the injection location is the X-point region. Simulations of the pellet injection from the X-point region have been performed with the toroidal modes  $n$  of  $n = 0 - 10$ . The pellet size has been varied from  $1.0 \times 10^{21} D/\text{pellet}$  (3.0 mm of cylindrical pellet) to  $4.0 \times 10^{21} D/\text{pellet}$  (4.7 mm), with pellet injection speed of 300 m/s; the time of injection of the pellet is  $t = 2443.1 \mu\text{s}$ . The pellet ablation rate profile versus normalized flux is shown in Fig. . The pellet ablation profiles show some oscillations in the vicinity of the time of the maximum pellet ablation rate. This is due to the interaction between the pellet ablated particles and the local plasma temperature. Figure shows the time evolution of the magnetic energies of toroidal modes of  $n = 8 - 10$ . The pellet triggering ELM appears at  $2800 \mu\text{s}$  for the largest pellet case,  $4.0 \times 10^{21} D$ . The duration of the ELM crash due to the pellet triggered ELM

is  $600\mu\text{s}$ - $800\mu\text{s}$  which is a reasonable value. The pellet injections in the plasma which is in the MHD stability limit, i.e. the  $112.5\text{kPa}$  at the pedestal top have been carried out. The parameters of the pellet injection is identical with the studies of  $75\text{kPa}$ . The pellet size has been varied for two sizes,  $1.0 \times 10^{21}\text{D/pellet}$  and  $2.0 \times 10^{21}\text{D/pellet}$ . The pellet ablation rate profile versus time and versus normalized flux is shown in Fig. . The  $112.5\text{kPa}$  plasma has higher temperature profile than the one of  $75\text{kPa}$ , therefore the pellet ablation rate is higher than the one of  $75\text{kPa}$  case. Figure shows the magnetic energies of  $n = 8 - 10$  after the pellet injection. The pellet  $2.0 \times 10^{21}\text{D}$  increases the MHD activity strongly.

The time evolution of the energy content inside of the separatrix is compared for  $75\text{kPa}$  and  $112\text{kPa}$  plasmas as shown in Fig. and Fig. , respectively. The energy content in the plasma decreases due to the pellet-triggered ELM. The  $75\text{kPa}$  shows that the energy loss has a nonlinear dependence on the pellet size as shown in Fig. . It means the smaller pellets, such as  $1.0 \times 10^{21}\text{D}$  and  $2.0 \times 10^{21}\text{D}$  do not trigger an ELM while  $4.0 \times 10^{21}\text{D}$  pellet triggers an ELM which leads to a large energy release from the plasma. The pellet of  $1.0 \times 10^{21}\text{D}$  in  $112.5\text{kPa}$  plasma leads the energy loss of  $0.1\%$  of the total plasma in  $100\mu\text{s}$ . The pellet injection of the pellet size  $2.0 \times 10^{21}\text{D}$  in  $75\text{kPa}$  plasma leads  $0.23\%$  of the total energy in  $100\mu\text{s}$  while the pellet of  $2.0 \times 10^{21}\text{D}$  leads  $0.47\%$  of the energy loss in  $1000\mu\text{s}$ .

The nonlinear MHD simulations with the JOREK code show that the size of the pellet required to trigger an ELM depends on the pedestal plasma pressure when the pellet is injected; for  $15\text{MA}$  plasmas it is necessary to increase the pellet size by a factor of 1.5 (in number of particles) to trigger ELMs for a pedestal pressure of  $75\text{kPa}$  compared to  $112.5\text{kPa}$  (note that for the pedestal assumptions in these simulations the pedestal pressure leading to spontaneous triggering of ELMs is  $150\text{kPa}$ ). In these simulations it has also been found that the magnitude of the ELM energy loss is strongly correlated with the pedestal plasma pressure (lower at lower pressures) rather than with the size of the pellet that is required for triggering (larger at lower pressures). The next important step is to investigate the pellet triggered ELM in the presence of realistic plasma flows including diamagnetic drift, neoclassical effects, and toroidal rotation which had been neglected in previous studies.

Auroral beads indicate that shear-flow interchange instability in nightside magnetotail triggers substorm onset *Derr, et al.* (2019). A geometric wedge model of the near-earth nightside plasma sheet is used to derive a wave equation for long-wavelength buoyancy waves which transmit  $\mathbf{E} \times \mathbf{B}$  sheared zonal flows along magnetic flux tubes. Discrepancies with the wave equation result in *Kalmoni, et al.* (2015) for shear-flow ballooning instability are discussed. The shear-flow interchange instability is responsible for substorm onset. The wedge wave equation is used to compute dispersion relations and growth rates in the midnight region of the nightside magnetotail around  $9\text{-}12\text{RE}$  where the instability develops for comparison with the growth rates of auroral beads characteristic of geomagnetic substorm onset. Stability analysis is performed for the shear-flow interchange modes, and a brief discussion of nonlinearity follows.

When the interplanetary magnetic field originating at the sun contains a southward magnetic field component, the solar wind can cause magnetic reconnection on the dayside of the earth, followed by nightside reconnection in the magnetotail “Interplanetary magnetic field and the auroral zones”, n.d.). This deposits energy in the magnetotail and disrupts the equatorial current

sheet, initiating a sequence events which leads to the formation of aurorae in the E-layer of the ionosphere by accelerating plasma towards the polar regions of the earth [Coppi, *et al.* (1966), Kivelson and Russell (1995), Wolf (1995), Angelopoulos, *et al.* (2008a,b), De Zeeuw, *et al.* (2004), Zou, *et al.* (2010), McPherron, *et al.* (2011), Sergeev, *et al.* (2011) Forsyth, *et al.* (2014)]. Such a sequence of events is referred to as a magnetic substorm. At the onset of magnetic substorms, the most equator-ward auroral arc suddenly brightens, followed by breakup of the arc and pole-ward expansion [Akasofu (1964) Donovan, *et al.* (2008)]. In the minutes leading to the breakup, small periodic fluctuations in the aurora aligned with magnetic longitude form [Nishimura, *et al.* (2014)]. These fluctuations have come to be called (auroral beads). Henceforth, “longitudinal” will be used to refer to magnetic longitude. Auroral beads have been found to be likely pervasive in onset arcs, and the exponential growth of the beads indicates that a plasma instability in the magnetosphere is responsible for substorm onset [Gallardo-Lacourt, *et al.* (2014), Kalmoni, *et al.* (2017)].

All-Sky Imagers (ASIs), which are a part of the NASA THEMIS mission to uncover the sequence of events which occur in the first few minutes of substorm onset, are distributed across North America, as seen in Fig. . They have a 1 km spatial resolution, and 3 s cadence image capturing capacity, and respond to 557.7 nm emissions. This spatio-temporal resolution is succinct to capture the pertinent data for analyzing auroral bead structures for the green emissions corresponding to aurora at an altitude of approximately 110 km, namely the E-layer [Mende, *et al.* (2008), Burch and Angelopoulos (2008)].

Motoba, *et al.* (2012) used ASI data from auroral beads in the northern and southern hemispheres, and proposed a common magnetospheric driver. Ultra-low frequency waves occurring within minutes of substorm onset are observed in the magnetosphere at frequencies similar to those of the auroral beads, and a single event was analyzed by Rae, *et al.* (2010) to demonstrate that the beading is characteristic of a near-earth magnetospheric instability triggering a current disruption in the central plasma sheet. Of the examined instabilities, cross-field current instability and shear-flow ballooning instability were the only two consistent with the analytical results. Kalmoni, *et al.* (2015) used the ASI data for substorm events over a 12-hour time span throughout the auroral oval (pre-midnight sector) across Canada and Alaska to perform an optical-statistical analysis that yielded maximum growth rates for the beads as a function of longitudinal wavenumber, which were compared with theoretical calculations for growth rate dependence on wavenumber for various instabilities. Ultimately, the two mechanisms which remained unrefuted were the shear-flow ballooning instability and the cross-field current instability.

The statistical analysis involved first spatially Fourier transforming longitudinal keograms to obtain the power spectral density. The longitudinal wavenumbers  $k_{y,E}$  measured in the ionosphere lay within the interval  $k_{y,E} \in [0.5 \times 10^{-4} \text{ m}^{-1}, 1.5 \times 10^{-4} \text{ m}^{-1}]$  during initial beading. The logarithm of the power spectral density was then plotted against time to determine the intervals of exponential growth for each wavenumber during onset. This is shown for one wavenumber in Fig. . Since the exponential growth of each mode had a unique well-defined growth rate during the interval until the breakup, only one instability is operating to produce the growth for each event. The growth rates were then examined as a function of wavenumber for determination of the most unstable waves. The maximum growth rates lie in the range  $[0.03 \text{ s}^{-1}, 0.3 \text{ s}^{-1}]$  with median growth rate

$$\gamma \sim 0.05 \text{ s}^{-1}.$$

Note that wave propagation direction (eastward vs. westward) differed for the individual substorm events, but growth rates are independent of propagation direction [Nishimura, *et al.* (2016)].

Subsequently, Kalmoni, *et al.* (2015) used the T96 model [Tsyganenko (1995, 1996a,b)] to map the wavenumbers back to the equatorial magnetosphere to obtain the corresponding magnetospheric wavenumbers  $k_y\epsilon$  [ $2.5 \times 10^{-6} \text{ m}^{-1}$ ,  $3.75 \times 10^{-6} \text{ m}^{-1}$ ], or wavelength interval  $\lambda_\perp\epsilon$  [1700 km, 2500 km]. The T96 model underestimates field-line stretching (and spatial scales) during the substorm growth phase, but the error is systematic, so the spatial scales can be compared between events. The arcs map to the equatorial plane mostly in the range of 9–12 RE, with field strengths less than 20 nT. The growth rates were normalized so that the spatial scales in the magnetosphere were not an artifact of the T96 mapping. Normalization presupposes that most events were caused by the same instability. If each event was caused by a different instability, normalization would be unjustified.

Of the two instabilities which were not ruled out by the Kalmoni, *et al.* (2015) analysis, the shear flow ballooning instability provided the best explanation of the observed beading results, corroborating previous findings along these lines [Friedrich, *et al.* (2000)]. This instability was first characterized in Voronkov, *et al.* (1997). This instability is a hybrid of the Kelvin–Helmholtz and Rayleigh–Taylor instabilities with larger growth rates operating on shorter growth time scales than pure Kelvin–Helmholtz instability. The former are driven by shear flows and the latter by earthward pressure gradients. An extensive linear analysis of such hybrid instabilities and their relation to substorms has been conducted by Yamamoto (2008, 2009). In particular, it was found that the hybrid waves can grow in the presence of an earthward particle energy density gradient. The auroral arc is tied to the boundary between the stretched field 91 lines and the depolarized field lines at the inner edge of the near–Earth plasma sheet. This is 92 where pressure gradients are most relevant. The spatial scale of the shear flow ballooning instability varies inversely as the size of the shear–flow region. Kalmoni, *et al.* (2015) determined that for this instability, the growth rates peak at  $0.2 \text{ s}^{-1}$  in the wavenumber regions specified above.

After setting up a simple geometric wedge model following Wolf, *et al.* (2018) for which perturbations will entail earthward flowing waves which carry the effects of the magnetospheric disturbance back to the ionosphere, we derive a wave equation for the plasma wedge which differs from that of both his original paper [Wolf, *et al.* (2018)], and that from which Kalmoni, *et al.* (2015) extracted the equation governing the shear flow ballooning instability, namely Voronkov, *et al.* (1997). Voronkov, *et al.* (1997) treated the coupling of shear flow and pressure gradient instabilities, but incorrectly perturbed the momentum equation. Wolf, *et al.* (2018), on the other hand, neglected the shear flow effect, thus obtaining low–frequency buoyancy waves which are not coupled to shear flow. Either of these alterations shifts the growth rates and, more importantly, fails to capture some of the essential qualitative features of the instability mechanism.

We will begin with the linearization of the MHD field equations from which all equations under consideration can be derived by the addition of various constraints and assumptions. We will first diverge to discuss the way in which Voronkov, *et al.* (1997) obtained the shear flow ballooning wave equation by a particular misuse of the momentum equation. Then, we will return

to the linearized field equations less the continuity equation, which is an unnecessary constraint if one utilizes the flux tube volume given in terms of the magnetic field strength. Upon combining these equations to obtain an ordinary radial differential equation for the radial component of the velocity, we take several limits to obtain a reduced low-frequency shear flow–interchange wave equation. Occasionally, we pause to mention the equation obtained by *Wolf, et al.* (2018) for the buoyancy waves in the absence of velocity shear, in general, and under the limits.

The primary result is the shear–flow interchange wave equation which delivers the instability which occurs in the magnetotail. The shear flow ballooning instability equation is incorrect, and therefore eliminated as a proposal, and the interchange wave equation absent shear flow lacks the generality of the full shear flow interchange wave equation. Shear flow–interchange instability should replace shear flow ballooning instability proposals to explain magnetospheric phenomena in the appropriate limits. What was a destabilizing ballooning term is really seen to be replaced by a stabilizing interchange term. The shear flow couples to the interchange instability in a way which reduces the growth rates relative to shear flow ballooning instability, and a fortiori to pure Kelvin–Helmholtz instability. Growth rates and dispersion relations in the regions under consideration are obtained and discussed, and stability analysis is performed.

In summary, it appears that a shear–flow interchange instability in the midnight region of the nightside magnetopause is the more plausible link the causal chain of events which initiate substorm onset via earthward traveling buoyancy waves, and results in the aurorae in the E–layer of the ionosphere. After perturbations drive an instability, the linear equations and dispersion relations become invalid, and the full nonlinear dynamical analysis becomes necessary. This will be the nature of future work on the ballooning interchange dynamics of the flux tubes in the wedge model.

## Wedge Model for Local Nightside Geomagnetic Tail Plasma

First, we set up a cylindrical coordinate system in the near–earth nightside plasma sheet, seen to the right in Fig. 5. The center of the magnetosphere is taken to be the origin of cylindrical coordinates  $(r, \phi, y)$ . The  $y$ –axis is that of standard SM or GSM coordinates, perpendicular to the magnetic dipole and the earth–sun line. Distance from the  $y$ –axis is given by the  $r$ –coordinate, which specifies the distance of the tubes of magnetic flux from the center of the magnetosphere, and hence the local magnetic curvature. The transformation to the coordinates of *Voronkov, et al.* (1997) is simple in the local plasma sheet region, but globally aligns more naturally with the magnetospheric structures of interest.

Following *Wolf, et al.* (2018), the simplest geometry has been chosen which still allows magnetic tension to support magnetic buoyancy oscillations to drive earthward flow, so that analytical solution for the eigenvalues is possible. Our more general equation includes coupling to shear flow velocity without sacrifice to this point. The two places at the upper and lower boundary (at  $\pm\Delta\phi/2$ ) of the wedge represent the northern and southern ionospheres, taken by approximation to have no conductance or resistive damping owing to the absence of a field–aligned current.

The system is taken to be at rest in equilibrium. We consider small perturbations which do

not induce motion in the  $\phi$ -direction, so that  $k_\phi = k_{\parallel} = 0$ . Note that this implies that the field lines remain concentric circles. Background equilibrium quantities are labeled with “0” subscripts, and “ $\delta$ ” signifies perturbations. Magnetic field lines are approximated by concentric circles, and density, pressure, and magnetic field strength vary radially. The pressure dynamics are modeled as adiabatic, entropy  $K := PV^\Gamma$  constant, with adiabatic gas constant  $\Gamma = (f + 2)/f$ , where  $f$  is the number of degrees of freedom, and  $V(r) = r\Delta\phi/B(r)$  for the flux tube volume. Equilibrium force balance is given by:

$$-\nabla \left( P_0 + \frac{B_0^2}{2\mu_0} \right) + \frac{B_0^2}{\mu_0 r} = 0. \quad (9.67)$$

Note that the flux tube has a curvature towards the center of the earth in the equatorial region, and the flux tube radius  $r$  is just the local radius of magnetic curvature.

Background parameters take the following form in this model:

$$\mathbf{B}_0 = B_0(r)\hat{\phi} \quad (9.68)$$

$$\mathbf{v}_0 = v_0(r)\hat{y} \quad (9.69)$$

$$\rho_0 = \rho_0(r) \quad (9.70)$$

$$P_0 = P_0(r). \quad (9.71)$$

So we assume that all equilibrium quantities are static and depend only on radius. The velocity has the form of an axially-directed  $\mathbf{E} \times \mathbf{B}$  shear flow. More details about this model, such as the specific radial profiles of the background parameters and some of the perturbations which result under the assumption of no shear velocity (only buoyancy waves) can be found in *Wolf, et al.* (2018).

## Linear Dynamics of Geomagnetic Tail Plasma

We begin with the MHD field equations:

$$\frac{\partial}{\partial t} \left( \frac{P}{\rho^\Gamma} \right) + \mathbf{v} \cdot \nabla \left( \frac{P}{\rho^\Gamma} \right) = 0 \quad (9.72)$$

$$\frac{\partial \mathbf{B}}{\partial t} - \nabla \times (\mathbf{v} \times \mathbf{B}) = 0 \quad (9.73)$$

$$\rho \frac{\partial \mathbf{v}}{\partial t} + \rho \mathbf{v} \cdot \nabla \mathbf{v} = -\nabla \left( P + \frac{B^2}{2\mu_0} \right) + \frac{\mathbf{B} \cdot \nabla \mathbf{B}}{\mu_0} \quad (9.74)$$

$$\frac{\partial \rho}{\partial t} + \nabla \cdot (\rho \mathbf{v}) = 0. \quad (9.75)$$

A flowchart of the inferential pathways and corresponding assumptions for all equations to be analyzed is included below for reference. It should facilitate a global view of the interrelations.

## Voronkov Treatment of Momentum Equation

Before proceeding with the derivation of the appropriate wave equation, I will first briefly discuss the way in which the *Voronkov, et al.* (1997) results from inconsistencies due to a misleading grouping of terms in the momentum equation.

Let us examine Voronkov's treatment of the momentum equation. Equilibrium force balance can be written in general as:

$$-\nabla \left( P_0 + \frac{B^2}{2\mu_0} \right) + \frac{B^2}{\mu_0 r} = \frac{\rho_0 v_\phi^2}{r}. \quad (9.76)$$

Voronkov recasts this in the following way:

$$\rho_0 g \nabla \left( P_0 + \frac{B^2}{2\mu_0} \right), \quad (9.77)$$

where

$$\rho_0 g := \frac{B^2}{\mu_0 r} - \frac{\rho_0 v_\phi^2}{r}. \quad (9.78)$$

Notice that  $g$  contains both a force term and an acceleration term.

Subsequently, the momentum equation gets perturbed with a  $\rho g$  term acting as a source, rather than  $\mathbf{B} \cdot \nabla \mathbf{B}/\mu_0$ . This is not a gravitational term, but a term with the  $g$  defined implicitly as above. There is no obvious reason that  $g$  in this form would remain constant during the perturbation. For example, the magnetic field term gets perturbed everywhere except within the  $\rho g$  term. Also, equilibrium quantities are said to be in agreement with ours, contradicting the previous assumption of an azimuthal component of the background velocity. It is unclear how to fully characterize the discrepancy, but it is clear that the perturbation of the momentum equation is performed incorrectly.

### 9.4.21 Linearized MHD Equations for Wedge Flux Tube

Now, let's return to the derivation at hand, within the wedge formalism. Let's survey each equation and discuss. We can from the start bypass the continuity equation which *Voronkov, et al.* (1997) uses as an additional constraint by assuming the form of the density to be that of a flux tube:

$$\rho = \frac{B}{r\Delta\phi} \quad (9.79)$$

in the adiabatic pressure dynamics equation. Note that the  $\Delta\phi$  is a constant. It is fitting to define the entropy:

$$K := PV^\Gamma = \frac{P}{\rho^\Gamma} \quad (9.80)$$

for future use in eliminating pressure and more intuitively representing interchange dynamics of the flux tubes under consideration. The adiabatic pressure dynamics using the convective time derivative:

$$\frac{D}{Dt} \left( \frac{P}{\rho^\Gamma} \right) \quad (9.81)$$

thus take the following form for a flux tube in the wedge formalism:

$$\frac{D}{Dt} \left( P \left( \frac{r}{B} \right)^\Gamma \right) = 0. \quad (9.82)$$

Substituting the total fields and linearizing, we obtain the equation which governs the pressure fluctuation dynamics:

$$\left( \frac{\partial}{\partial t} + v_0 \frac{\partial}{\partial y} \right) \left( \frac{\delta P}{P_0} - \frac{\delta B}{B_0} \right) + \frac{K'_0}{K_0} \delta v_r = 0. \quad (9.83)$$

Henceforth, partial radial derivatives will be indicated by primes when convenient.

The magnetic field dynamics in the flux tube are governed by Faraday's law with  $\mathbf{E} = -\mathbf{v} \times \mathbf{B}$ , owing to the high conductivity in the region:

$$\frac{\partial \mathbf{B}}{\partial t} = -\nabla \times (\mathbf{b} \times \mathbf{B}). \quad (9.84)$$

Substituting the total fields and linearizing, we obtain:

$$\frac{\partial \delta B_r}{\partial t} = -v_0 \frac{\partial \delta B_r}{\partial y} \quad (9.85)$$

$$\frac{\partial \delta B_\phi}{\partial t} = -v_0 \frac{\partial \delta B_\phi}{\partial y} - B_0 \frac{\partial \delta v_y}{\partial y} - B_0 \delta v'_r = B'_0 \delta v_r \quad (9.86)$$

$$\frac{\partial \delta B_y}{\partial t} = \frac{v_0}{r} \delta B_r + v'_0 \delta B_r + v_0 \delta B'_r. \quad (9.87)$$

Now we examine the momentum equation, which governs the plasma dynamics:

$$\rho \frac{\partial \mathbf{v}_r}{\partial t} + \rho \mathbf{v} \cdot \nabla \mathbf{v} = -\nabla \left( P + \frac{B^2}{2\mu_0} \right) + \frac{\mathbf{B} \cdot \nabla \mathbf{B}}{\mu_0}. \quad (9.88)$$

Substituting the total fields and linearizing, we obtain:

$$\rho_0 \frac{\partial \delta v_r}{\partial t} + \rho_0 v_0 \frac{\partial \delta v_r}{\partial y} = -\frac{\partial}{\partial r} \left( \delta P + \frac{B_0}{\mu_0} \delta B_\phi \right) - \frac{2B_0}{\mu_0 r} \delta B_\phi \quad (9.89)$$

$$\rho_0 \frac{\partial \delta v_\phi}{\partial t} + \rho_0 v_0 \frac{\partial \delta v_\phi}{\partial y} = \frac{B_0}{\mu_0 r} \delta B_r + \frac{B'_0}{\mu_0} \delta B_r \quad (9.90)$$

$$\rho_0 \frac{\partial \delta v_y}{\partial t} + \rho_0 v_0 \frac{\partial \delta v_y}{\partial y} + \rho_0 v'_0 \delta v_r = -\frac{\partial \delta B}{\partial y} - \frac{B_0}{\mu_0} \frac{\partial \delta B_\phi}{\partial y}, \quad (9.91)$$

which governs the plasma acceleration.

In the wedge formalism, the continuity equation is unnecessary, as the density is already expressed in terms of the magnetic field. Thus, the density perturbations are implicit in magnetic field fluctuations of flux tubes via flux freezing.

## Magnetospheric Wave Equation for Plasma Wedge

Now, we assume all perturbations take the form of axially-propagating waves  $e^{ik_y y - i\omega t}$  in the plasma sheet, denoting the Doppler-shifted frequency:

$$\tilde{\omega}(r) := \omega - k_y v_0(r), \quad (9.92)$$

as these are the waves which will map back to the ionosphere to cause the longitudinally-directed auroral beads. Note that this converts primes into total rather than partial radial derivatives.

Substituting this form into our self-consistent set of dynamical equations (17)–(25) and (26) (for Voronkov, *et al.* (1997)), we obtain:

$$i\tilde{\omega} \left( \frac{\partial P}{P_0} - \Gamma \frac{\delta B}{B_0} \right) = \frac{K'_0}{K_0} \delta v_r \quad (9.93)$$

$$-i\tilde{\omega} \delta B_r = 0 \quad (9.94)$$

$$-i\tilde{\omega} \delta B_\phi = -ik_y B_0 \delta v_y - B'_0 \delta v_r - B_0 \delta v'_r \quad (9.95)$$

$$-i\omega \delta B_y = \frac{v_0}{r} \delta B_r + v'_0 \delta B_r + v_0 \delta B'_r \quad (9.96)$$

$$-i\tilde{\omega} \rho_0 \delta v_r = -\frac{\partial}{\partial r} \left( \delta P + \frac{B_0}{\mu_0} \delta B_\phi \right) - \frac{2B_0}{\mu_0 r} \delta B_\phi \quad (9.97)$$

$$-i\tilde{\omega} \rho_0 \delta v_\phi = \frac{B_0}{\mu_0 r} \delta B_r + \frac{B'_0}{\mu_0} \delta B_r \quad (9.98)$$

$$-i\tilde{\omega} \rho_0 \delta v_y + \rho_0 v'_0 \delta v_r = -ik_y \delta P - ik_y \frac{B_0}{\mu_0} \delta B_\phi. \quad (9.99)$$

We can now see that (9.94), (9.96), and (9.98) imply the following perturbation components:

$$\delta \mathbf{B} = \delta B_\phi \hat{\phi} \quad (9.100)$$

$$\delta \mathbf{v} = \delta v_r \hat{r} + \delta v_y \hat{y}. \quad (9.101)$$

So three of the equations are now implicitly taken into account, and from the remaining Eqs. (9.93)–(9.99) we obtain the following system:

$$i\tilde{\omega} \left( \frac{\partial P}{P_0} - \Gamma \frac{\delta B}{B_0} \right) = \frac{K'_0}{K_0} \delta v_r \quad (9.102)$$

$$i\tilde{\omega} \frac{\delta B_\phi}{B_0} = ik_y \delta v_y + \delta v'_r + \frac{B'_0}{B_0} \delta v_r \quad (9.103)$$

$$i\tilde{\omega} \rho_0 \delta v_r = \frac{\partial}{\partial r} \left( \delta P + \frac{B_0}{\mu_0} \delta B_\phi \right) + \frac{2B_0}{\mu_0 r} \delta B_\phi \quad (9.104)$$

$$i\tilde{\omega} \rho_0 \delta v_y - \rho_0 v'_0 \delta v_r = ik_y \delta P + ik_y \frac{B_0}{\mu_0} \delta B_\phi. \quad (9.105)$$

From now on, it will be convenient to make frequent use of the Alfvén speed, sound speed, and fast mode wave speeds given by  $c_A^2 := B_0^2/\mu_0 \rho_0$ ,  $c_s^2 := \Gamma P_0/\rho_0$ , and  $c_f^2 := c_A^2 + c_s^2$ , respectively. Now, for convenience, the equilibrium force balance equation can be recast as a condition to eliminate  $B_0$  in lieu of  $K_0$ :

$$\frac{B'_0}{B_0} = \frac{1}{c_f^2} \left( -\frac{c_s^2}{\Gamma} \frac{K'_0}{K_0} + \frac{c_s^2 - c_A^2}{r} \right) \quad (9.106)$$

which will make manifest the interchange instability.

Eliminating  $\delta v_y$ ,  $\delta P$ , and  $\delta B_\phi$ , we obtain the differential equation for the radial velocity fluctuations  $\delta v_r$ , written in a form which most resembles that of *Wolf, et al. (2018)*:

$$\begin{aligned} \tilde{\omega} \delta v_r &= \frac{\tilde{\omega}}{\rho_0} \frac{d}{dr} \left( -\frac{\delta v_r \rho_0 \tilde{\omega} (c_s^2 - c_A^2)}{r(\tilde{\omega}^2 - k_y^2 c_f^2)} - \frac{d\delta v_r}{dr} \frac{c_f^2 \rho_0 \tilde{\omega}}{\tilde{\omega}^2 - k_y^2 c_f^2} - \frac{\delta v_r \rho_0 v'_0 k_y c_f^2}{\tilde{\omega}^2 - k_y^2 c_f^2} \right) \\ &\quad + \frac{2c_A^2}{r} \left( \frac{\delta v_r}{\Gamma c_f^2} \left[ c_s^2 \frac{K'_0}{K_0} - \frac{\tilde{\omega}^2 \Gamma (c_s^2 - c_A^2)}{r(\tilde{\omega}^2 - k_y^2 c_f^2)} \right] - \frac{d\delta v_r}{dr} \frac{\tilde{\omega}^2}{\tilde{\omega}^2 - k_y^2 c_f^2} - \frac{\delta v_r k_y \tilde{\omega} v'_0}{\tilde{\omega}^2 - k_y^2 c_f^2} \right). \end{aligned} \quad (9.107)$$

Indeed, in this form, it is easy to see that dropping velocity shear terms yields precisely the equation in *Wolf, et al. (2018)*:

$$\begin{aligned} \omega^2 \delta v_r &= \frac{\omega}{\rho_0} \frac{d}{dr} \left( -\frac{\delta v_r \rho_0 \omega (c_s^2 - c_A^2)}{r(\omega^2 - k_y^2 c_f^2)} - \frac{d\delta v_r}{dr} \frac{c_f^2 \rho_\omega}{\omega^2 - k_y^2 c_f^2} \right) \\ &\quad + \frac{2c_A^2}{r} \left( \frac{\delta v_r}{\Gamma c_f^2} \left[ c_s^2 \frac{K'_0}{K_0} - \frac{\omega^2 \Gamma (c_s^2 - c_A^2)}{r(\omega^2 - k_y^2 c_f^2)} \right] - \frac{d\delta v_r}{dr} \frac{\omega^2}{\omega^2 - k_y^2 c_f^2} \right). \end{aligned} \quad (9.108)$$

Note that the frequencies are no longer Doppler-shifted (there is no shear velocity to supply the shift!). The objective of *Wolf, et al.* (2018) was to study buoyancy waves in the magnetosphere, and velocity shear terms were thus neglected in order to facilitate a clearer understanding of the interchange-induced buoyancy waves, with buoyancy force arising from magnetic tension rather than gravity. This equation still describes both fast mode longitudinal and buoyancy waves in the plasma wedge, but the former are easily eliminated, which we will demonstrate in what follows.

### Reduced low-frequency wedge-wave equation

We now eliminate fast modes, assuming  $\tilde{\omega}^2 \ll k_y^2 c_f^2$ , retaining only those modes which play a substantial role in substorm onset. We also assume that the length scales for  $\delta v_r \sim \delta$ , but are small compared to  $r$  and variations in  $P_0, v_0, \rho_0 \sim L$  (from which the scale for  $B_0$  follows from equilibrium force balance). In short, we assume small shear flow width. Care must be taken to ensure that terms which involve ratios of the small parameters are not hastily dropped.

The resulting reduced low-frequency equation gives the long wavelength buoyancy waves in the nightside wedge:

$$\delta v''_r + \left( \frac{v_0''}{k_y \tilde{\omega}} + \frac{1}{\omega^2 \Gamma r} \frac{2}{c_f^2} \frac{c_A^2 c_s^2}{K_0} \frac{K' - 0}{K_0} - 1 \right) k_y^2 \delta v_r = 0 \quad (9.109)$$

with the  $\mathbf{E} \times \mathbf{B}$  shear flow velocity  $v_0(r)$  and local magnetic curvature determining the dynamic stability conditions. This equation for low-frequency waves in the wedge captures the most general dynamical phenomena relevant to the causal chain of events which we aim to describe.

Though it does not pertain to the more general analysis at hand, it should be mentioned that these limits, taken in the appropriate order, agree with those in *Wolf, et al.* (2018), barring what appear to be minor typographical errors (determined by performing a unit check) on his part. The buoyancy frequency, which was thoroughly discussed in *Wolf, et al.* (2018), is given by the next-to-last term in our equation. Let us perform this check. Dropping the shear velocity term, we obtain:

$$\delta v''_r + \left( \frac{1}{\omega^2 \Gamma r} \frac{2}{c_f^2} \frac{c_A^2 c_s^2}{K_0} \frac{K'_0}{K_0} - 1 \right) k_y^2 \delta v_r = 0. \quad (9.110)$$

Thus the first term yields immediately the buoyancy frequency for waves in a wedge:

$$\omega_b^2(r) = \frac{2}{\Gamma r} \frac{c_A^2 c_s^2}{c_f^2} \frac{K'_0}{K_0}. \quad (9.111)$$

The speed  $c_A c_s / c_f$  is just that of the slow mode buoyancy waves which result from interchange oscillations.

Recast in the above notation, the *Voronkov, et al.* (1997) result (obtained in a methodologi-

cally identical way) utilized by *Kalmoni, et al.* (2015) is:

$$\delta v_r'' + \left( \frac{v_0''}{k_y \tilde{\omega}} - \frac{g}{\tilde{\omega}^2} \frac{\rho'_0}{\rho_0} - \frac{1}{\tilde{\omega}^2} \frac{g^2}{c_f^2} - 1 \right) k_y^2 \delta v_r = 0. \quad (9.112)$$

As written by *Voronkov, et al.* (1997), this has the form:

$$\delta v_r'' + \left( \frac{v_0''}{k_y \tilde{\omega}} + W \frac{1}{\tilde{\omega}^2} - 1 \right) k_y^2 \delta v_r = 0, \quad (9.113)$$

where

$$W := -\frac{g\rho'_0}{\rho_0} - \frac{g^2}{c_f^2}, \quad (9.114)$$

with effective acceleration defined above. The term  $W$ , obtained by *Voronkov, et al.* (1997), was taken to be an analog of the buoyancy frequency,  $\omega_b^2$ .

## Examination of Stability Conditions

The second derivative and velocity-shear terms are the same. The density-gradient terms differ, but the main effective difference is in the ballooning/interchange terms. Near the inner edge of the plasma sheet, at approximately  $9-12 R_E$ , the analysis of *Kalmoni, et al.* (2015) indicates that these terms are destabilizing, whereas the above analysis reveals these terms to be stabilizing. This is due to differences between ballooning and interchange, where the former is often treated as localized and the latter is globally distributed along the magnetic field lines.

Shear flow-balloonning dispersion relation:

$$\omega^2 + \left( \frac{k_y v_0}{1 - k^2 - \delta^2} \frac{\delta^2}{L^2} - 2k_y v_0 \right) \omega + \left( \frac{k_y^2 \delta^2}{1 - k_y^2 \delta^2} W - \frac{k_y^2 \delta^2}{1 - k_y^2 \delta^2} \frac{v_0^2}{L^2} + k_y^2 v_0^2 \right) = 0. \quad (9.115)$$

Now, we let  $\omega = \omega_r + i\gamma$ , and obtain a real equation and an imaginary equation, which can be jointly solved for  $\omega(k_y)$  and  $\gamma(k_y)$ :

$$\frac{\omega_r \delta}{v_0} = k_y \delta - \frac{1}{2} \frac{k_y \delta}{1 - k_y^2 \delta^2} \frac{\delta^2}{L^2} \quad (9.116)$$

$$\frac{\gamma \delta}{v_0} = \frac{k_y \delta}{1 - k_y^2 \delta^2} \sqrt{\left(1 - k_y^2 \delta^2\right) \frac{\delta^2}{v_0^2} W - \frac{1}{4} \left(\frac{\delta^2}{L^2}\right)^2}. \quad (9.117)$$

Ballooning dispersion relation:

$$\omega^2 - 2k_y v_0 \omega + \left( \frac{k_y^2 \delta^2}{1 - k_y^2 \delta^2} \frac{2(1 - \Gamma)}{\Gamma L r} \frac{c_A^2 c_s^2}{c_f^2} + k_y^2 v_0^2 \right) = 0. \quad (9.118)$$

Now, we let  $\omega = \omega_\Gamma + i\gamma$ , and obtain a real equation and an imaginary equation, which can be jointly solved for  $\omega(k_y)$  and  $\gamma(k_y)$ :

$$\frac{\omega_r \delta}{v_0} = k_y \delta \quad (9.119)$$

$$\frac{\gamma \delta}{v_0} = \frac{k_y \delta}{1 - k_y^2 \delta^2} \sqrt{(1 - k_y^2 \delta^2) \frac{2(1 - \Gamma)}{\Gamma L r} \frac{c_A^2 c_s^2}{c_f^2 v_0^2} \delta^2}. \quad (9.120)$$

Shear flow–interchange dispersion relation:

$$\omega^2 + \left( \frac{k_y v_0}{1 - k_y^2 \delta^2} \frac{\delta^2}{L^2} - 2k_y v_0 \right) \omega + \left( \frac{k_y^2 \delta^2}{1 - k_y^2 \delta^2} \frac{2(1 - \Gamma)}{\Gamma L r} \frac{c_A^2 c_s^2}{c_f^2} - \frac{k_y^2 \delta^2}{1 - k_y^2 \delta^2} \frac{v_0^2}{L^2} + k_7^2 v_0^2 \right) = 0. \quad (9.121)$$

Now, we let  $\omega = \omega_r + i\gamma$ , and obtain a real equation and an imaginary equation, which can be jointly solved for  $\omega(k_y)$  and  $\gamma(k_y)$ :

$$\frac{\omega_r \delta}{v_0} = k_y \delta - \frac{1}{2} \frac{k_y \delta}{1 - k_y^2 \delta^2} \frac{\delta^2}{L^2} \quad (9.122)$$

$$\frac{\gamma \delta}{v_0} = \frac{k_y \delta}{1 - k_y^2 \delta^2} \sqrt{(1 - k_y^2 \delta^2) \frac{2(1 - \Gamma)}{\Gamma L r} \frac{c_A^2 c_s^2}{c_f^2 v_0^2} \delta^2 - \frac{1}{4} \left( \frac{\delta^2}{L^2} \right)^2}. \quad (9.123)$$

Parameters used for the plotting were chosen to match the analyses of both Voronkov, *et al.* (1997) and Kalmoni, *et al.* (2015). In particular, we utilized a plasma density  $\rho_0 = 4.06 \times 10^{-21} \text{ kg/m}^3$ , and pressure of  $P_0 4nPa$ , and a magnetic field strength in the plasma sheet of  $B_0 = 40 \text{ nT}$ . Following Kalmoni, *et al.* (2015), the shear flow region was taken to be localized with a width  $\delta = 650 \text{ km}$ . The ion drift velocity in the region is approximately  $v_i = 100 \text{ km/s}$ . Gradient length scales are those of Voronkov, *et al.* (1997), namely  $L 5000 \text{ km}$ . For convenience, this implies speeds of  $c_s = 1380 \text{ km/s}$ ,  $c_A = 560 \text{ km/s}$ , and  $c_f = 560 \text{ km/s}$ .

Growth rate reduction (growth rates and implications) Type of instability. . . Recent K paper 1 paragraph about relations, 1 paragraph about stability, 2 paragraphs conclusions.

Details:  $R_E$  adjust Parameter Sensitivity Nonlinear Analysis Wolf/Xing for interchange stuff Wedge Conductivity Comments Bibliography, Proofread, “/”, Acknowledgments Comments on dropping gravity and centrifugal velocity.

## 9.5 Turbulent Electron Thermal and Impurity Transport

### 9.5.1 Validation of electron temperature gradient turbulence in the Columbia Linear Machine [Fu, et al. (2012)]

### 9.5.2 Schematic of CLM Validated ETG Transport

Figure 9.13: Columbia Linear Machine — Main features: steady state, collisionless, no trapped electrons flexibility for wide range of parameter variations.

### 9.5.3 Control of Electron Temperature Profile

The experiment can change the electron temperature profile by adjusting the D.C. voltage of the Disc Mesh 5 V to 20 V.

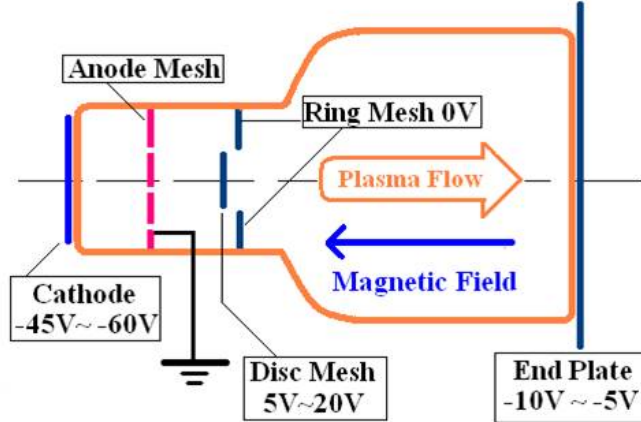


Figure 9.13: Typical Plasma Parameters: Plasma Density:  $n \sim 5 \times 10^8 - 3 \times 10^9 \text{ cm}^{-3}$ ; Magnetic Field in Cell Region:  $B_{rmcell} \cong 1 \text{ kG}$ ; Electron Temperature:  $T_e \sim 8 - 20 \text{ eV}$ ; Ion Temperature:  $T_i \sim 3 \text{ eV}$ ; Plasma Cell Length:  $L \sim 10 \text{ cm}$ .

### 9.5.4 CLM Profiles of Electron/Ion Temperature and Plasma Density

With the appropriate values of neutral pressure, D.C. accelerating voltage, we obtain the radial profiles of plasma density and electron/ion temperature as shown in the panel below (left). The typical power spectrum from the high frequency twin probes is also shown (right). For flat density profile the  $L_{T_e}$  is the relevant parameter.

### 9.5.5 Eigenmodes from the Dispersion Relation

If we keep only the first-order term from the electron gyroradius and take the flat-density limit  $\omega_{ne}^* \rightarrow 0$ : The high frequency dispersion reduces to the fluid-like equation

$$\frac{T_e}{T_i} + (k_\perp \lambda_{De})^2 + b + b \frac{\omega_{Te}^*}{\omega} - \frac{k_p^2 v_e^2}{\omega^2} (1 - b) + \frac{\omega_{Te}^* k_p^2 v_e^2}{\omega^3} (1 + b) = 0.$$

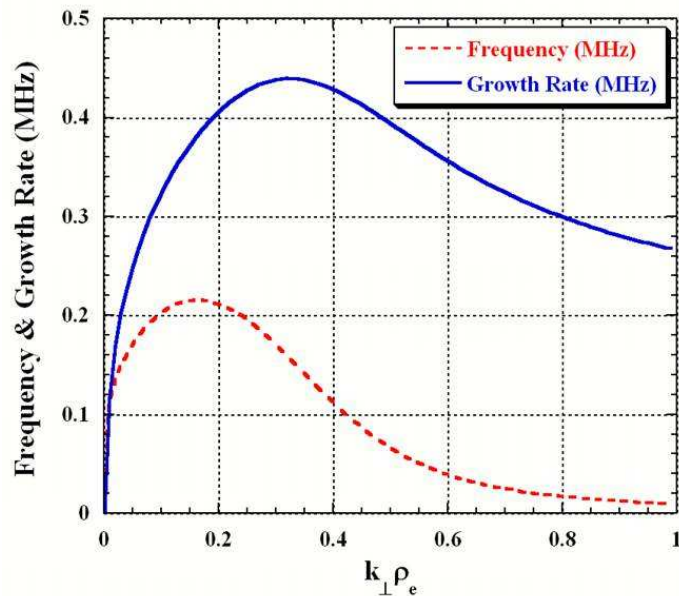


Figure 9.14: The solution of this dispersion relation is shown for measured  $L_{T_e} = 0.4$  cm.

### 9.5.6 GTC Simulation Results from UT–UCI SciDAD

#### GTC Simulation Results from UT-UCI SciDAC

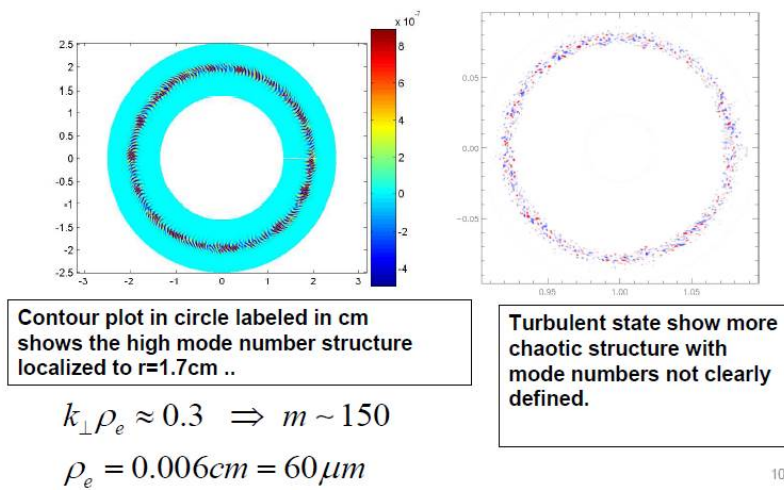


Figure 9.15: Contour plot in circle labeled in cm shows the high mode number structure localized to  $r = 1.7\text{ cm}$ . (b) Turbulent state shows more chaotic structure with mode numbers not clearly defined.

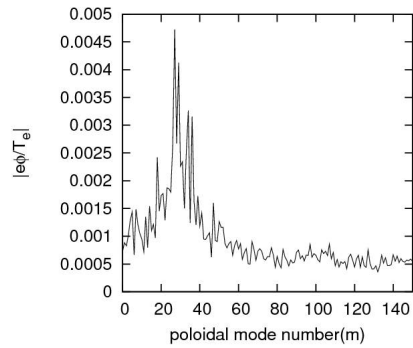


Figure 9.16: GT simulation data for model of CLM experiments.

### 9.5.7 Nonlinear quasi-steady state for $L_{Te} = 0.5 \text{ cm}$

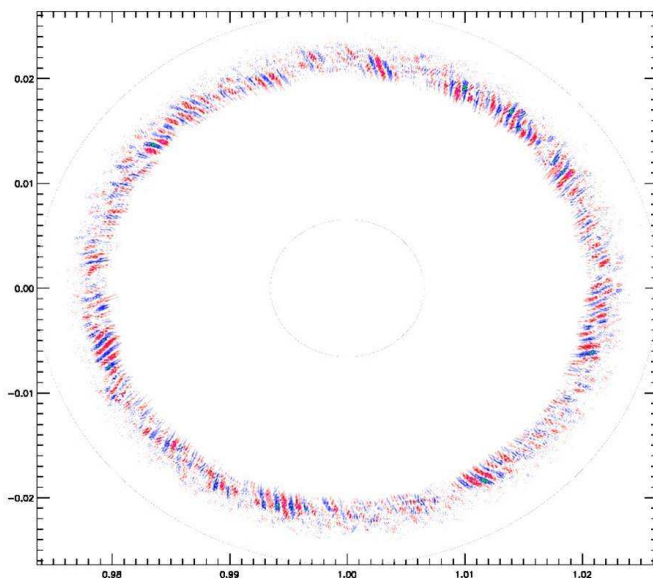


Figure 9.17: Nonlinear Quasi–Steady State for  $L_{Te} = 0.5 \text{ cm}$ . Contours of electric potential fluctuations in the nonlinear state of the ETG simulation using the GTC code. Red and Yellow = positive values. Blue and Green = negative values.

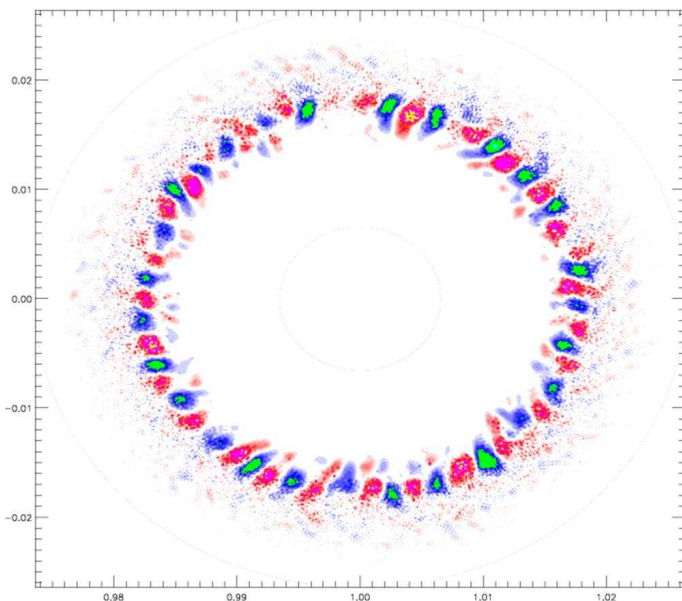


Figure 9.18: Nonlinear Quasi–Steady State for  $L_{Te} = 0.5$  cm. Run on Teragrid Ranger TACC University of Texas. 4096 cores running 10 hours. Grid size of the simulation: 400 (radial)  $X$ , 2000 (poloidal),  $X$  32 (parallel).

Fig. 9.19:Turbulent spectrum and radial mode structure in nonlinear state.

### 9.5.8 Radial profiles of potential fluctuation

#### Radial Profiles of Potential Fluctuation

The maximum fluctuation level is located at the point of the sharpest electron temperature gradient ( $L_{Te}$  smallest), as predicted by theory. The width is from eigenmodes.

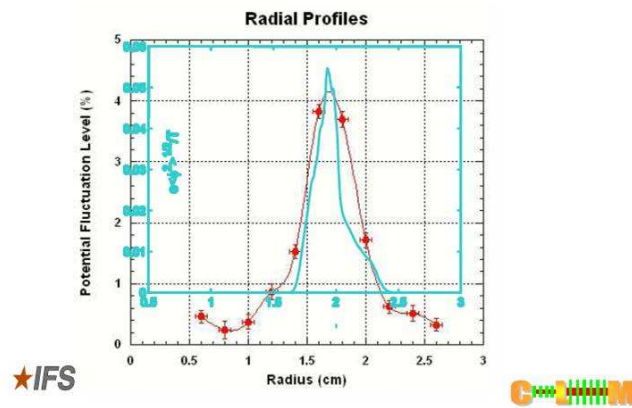


Figure 9.19: The maximum fluctuation level is located at the point of the sharpest electron temperature gradient ( $L_{Te}$  smallest), as predicted by theory. The width is from eigenmodes.

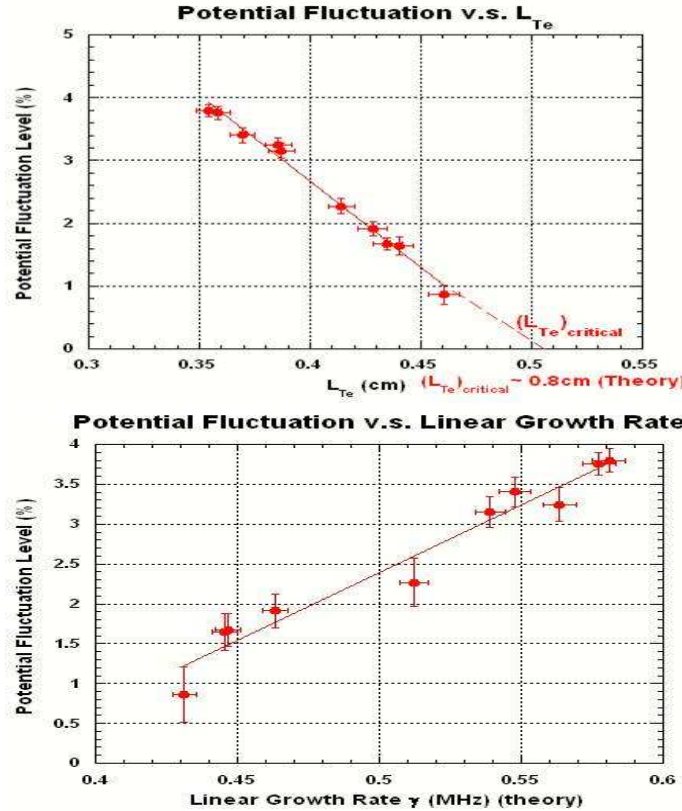


Figure 9.20: a) Temperature gradient  $L_{Te}$  Scaling. Potential fluctuation vs.  $L_{Te}$ . b) Potential fluctuation vs. linear growth rate.

### 9.5.9 Conclusions ETG Validation with CLM data

Potential fluctuations at  $\sim 0.7$  MHz are due to the steep electron temperature gradient at relative weak density gradient. The frequency spectrum is consistent with the simulation for the ETG mode with the measured  $T_e$  profile.

Maximum growth rate is at  $m \sim 90$ . The inverse cascade transforms spectrum to wave numbers  $m \sim 14\text{-}16$  as observed in the experiment. The cascade stops.

Simulations and experiments show fluctuations peak for  $k_y \rho_i \geq 1$ .

Unstable Modes  $k_{\parallel} L_{Te} = 0.02 \text{ cm}^{-1} \times 1 \text{ cm} = .02 \langle k_y \rho_e \rangle$  for ETG instability.

The potential fluctuation amplitude increases linearly with  $1/L_{Te}$ .

The radial location of the maximum amplitude of the mode coincides with the steepest electron temperature gradient.

With the signatures described above, the ETG mode is firmly identified in the CLM with the GTC simulations.

Measurements of electron thermal conductivity indicates  $\chi_{\perp e}$  is about  $3-8 \text{ m}^2/\text{s} \approx 20\chi_{e,\text{GB}}$  consistent with the GTC simulations

Thus, there is validation of the GTC simulations by the ETG experiment.

## 9.6 Impurity Transport from drift waves

### 9.6.1 Impurity transport data and theory

Alcator C–Mod work with Boron and Argon

LHD, EAST, WEST with trace amounts of Heavy Metals

### 9.6.2 General features of impurity experiments

Alcator C Mod with  $R/a = 0.67 \text{ m}/0.22 \text{ m}$ ,  $B = 5.4 \text{ T}$  — confinement times  $30 \text{ m}$

Large Helical Device  $R/a = 3.6 \text{ m}/0.4 \text{ m}$ ,  $B = 2 - 3 \text{ T}$  — confinement times  $50 \text{ m}$

### 9.6.3 Structure of Drift Wave equations with impurities

## 9.7 General Features of Impurity Experiments

Alcator C–Mod with  $R/a = 0.67 \text{ m}/0.22 \text{ m}$ ,  $B = 5.4 \text{ T}$  — confinement times  $30 \text{ ms}$  Large Helical Device  $R/a = 3.6 \text{ m}/0.4 \text{ m}$ ,  $B = 2 - 3 \text{ T}$  — confinement times  $50 \text{ ms}$ .

## 9.8 Structure of Drift Wave Equations with Impurities

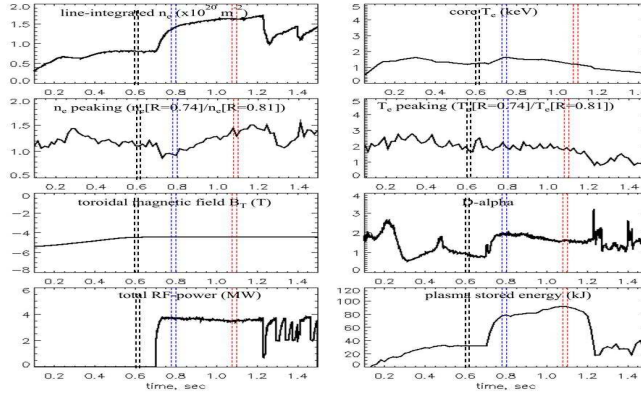


Figure 9.21: aL-mode, H-mode and ITB data in C-Mod discharge.

H-mode is triggered by off-axis ICRF at 0.7 s

H-mode evolves to ITB after 300 msec of RF heating

$B^{5+}$  density profiles start accumulating in L-mode (black), and become hollow H-mode (blue), and peaked in ITB (red) in a single discharge [Futatani, et al. (2010)].

## 9.9 LHD Doped Pellet Injection Data Impurity Transport Experiments [Sudo, et al. (2012)]

$B = 2.7 \text{ T}$ ,  $R_{\text{ax}} = 3.7 \text{ m}$ , up to 20 MW NBI makes

$T_e \sim 2 \text{ KeV}$  and high density  $\sim 2 \times 10^{21} / \text{m}^3$

Tracer impurity deposition from doped Pellet Ablation

1 mm pellets with Fe(+26/22) and Sn(+50/21 and 18) and  $T_i(+22/18)$  and Carbon injection. H-Z elements have clear spectral lines 13 nm, 16 nm, 17 nm, 19 nm with 0.6 mm spatial resolution for each pixel.

Images of  $2D + t$  dynamics of the pellet spreading

Exploration of High Density Operation — Internal Diffusion Barrier at  $q = 2$  surface..(20 MW at 2.5 T)

## 9.10 Features of C-Mod and LHD Experiments

CMOD and LHD reach densities well above the  $1020/\text{m}^3$

Accumulation of Boron or Carbon in some phases of discharge inward flow velocity  $V_z$  and diffusion  $-d \ln n_z/dr \equiv 1/L_{nz} \sim V_z/D_z$

Reaching critical condition  $V_z$  can reverse and  $Z$  flow outward.

Both machines show the  $D$  and  $V$  are above the neoclassical values and infer that drift waves are responsible [also shown in TEXT in *Horton and Rowan* (1994)].

The problem requires a multi-mode approach owing to several collisionality regimes in  $r, t$  and ITG vs. TEM vs CDW.

Complex set of eigenmodes and eigenvectors with a new mode from  $dn_z/dr = -n_z/L_{nz}$   
Positive and negative  $L_{nz}$ .

Phase relations between the plasma density fluctuations and the potential fluctuations determine the  $D_z$  and  $V'_z$ .

## 9.11 Theory-Simulation of Turbulent Impurity Transport

Three-component plasmas ( $i, z, e$ ) have additional degrees of freedom. Now, the electrons are not tied to the fuel ions.

For each  $k$ -vector, there are three eigenmodes from the pde system:

- 1) hydrogen ion density, 2) impurity density, 3) electron density and 4) plasma potential

$$\omega_\alpha(k, \mu_n) = \omega_k + i\gamma_k \quad \text{polarization } X(k, \mu_n)$$

Quasineutrality (QN) reduces the system to three dynamical fields with  $a = 1, 2, 3$  eigenmodes.  $10 - \dim \mu_n$  parameter vector.

Eigenmodes are worked out in detail for four generic types of discharges: L-mode, the H-mode, ITB and I-mode plasmas.

Recall ITER wall is  $800 \text{ m}^2$  Beryllium-coated metal tungsten.

Recall Li, Be, B, N, O with  $Z = 3, 4, 5, 6, 7, 8$  respectively.

Impurity transport at an internal transport barrier in Alcator C-Mod [*Rowan, et al.* (2008)],

## 9.12 Simulation with Atomic Physics and Impurity Fluxes in C-MOD

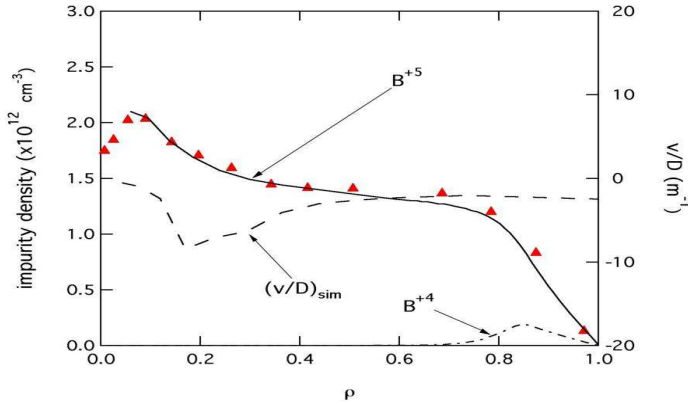


Figure 9.22: Transport Dynamics.

$$\frac{\partial n_j^z}{\partial t} + \nabla \cdot \Gamma_j^z = S_j^z$$

fixed background  $n_e(r, t), n_i(r, t), T_e(r, t), T_i(r, t)$

$$\Gamma_z = -D_z \frac{\partial n_z}{\partial r} + n_z v$$

$$S_j^z = -II_n^z n_j^z n_e + I_{j-1}^z n_{j-1}^z n_e + a_{j+1}^z n_{j+1}^1 n_e - a_j^z n_j^z n_e + S_B^z$$

L-Mode:

Relatively Flat  $B^{5+}$  profile.  $Z_{\text{eff}} = 1 - 1.1$  and  $T_i < T_e$

H-Mode:

Hollow  $B^{5+}$  profile.  $Z_{\text{eff}} = 1.3-1.4 \rightarrow T_i < T_e$

ITB:

Peaked  $B^{5+}$  profile.  $T_i \approx T_e$

## 9.13 Carbon Transport in LHH

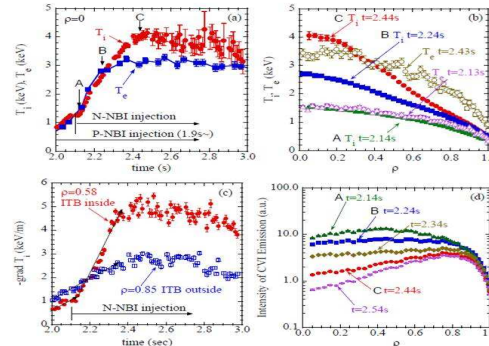


FIG. 1. (a) Time evolution of ion temperature and electron temperature. (b) Radial profiles of ion temperature and electron temperature. (c) Time evolution of ion temperature gradient. (d) Radial profiles of charge exchange emission of carbon.

Figure 9.24: (a) Time evolution of ion temperature and electron temperature. (b) Radial profiles of ion temperature and electron temperature. (c) Time evolution of ion temperature gradient. (d) Radial profiles of charge exchange emission of carbon.

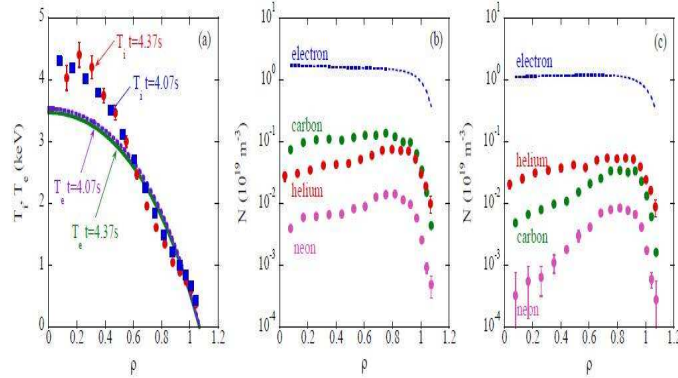


Figure 9.25: (a) Evolution of Impurity Holes LHD.

*Yoshinuma, et al.* (2010) state as their conclusion: “Thus the observations of the impurity hole can not be explained uniformly by the neoclassical transport. The turbulence transport therefore can be the next candidate for the dominant player of the impurity transport in the high ion temperature discharges in LHD.”

## 9.14 Nonlinear 3–Component Drift Wave Model

Particle Dynamics:  $n_i(x, t) + Zn_z(x, t) = n_e(x, t)$

$$\begin{aligned}\frac{dn_i}{dt} + \frac{2n_i v_x}{R} + \nabla_p n_i v_i - \nabla \bullet \left( \frac{m_i n_i}{eB^2} \frac{d}{dt} \nabla \phi \right) + \mu_i \frac{m_i}{eB^2} \nabla^4 \phi &= 0 \\ \frac{dn_z}{dt} + \frac{2n_z v_z}{R} + \nabla_p n_z v_z - \nabla \bullet \left( \frac{m_z n_z}{ZeB^2} \frac{d}{dt} \nabla \phi \right) + \mu_z \frac{m_z}{eB^2} \nabla_\perp \phi^4 &= 0\end{aligned}$$

Generalized Ohm's Law:  $\frac{dn_e}{dt} + \frac{2T_e}{eBR} \frac{\partial n_e}{\partial y} = \frac{1}{e} \nabla_\parallel \bullet J_\parallel$

$$J_\parallel = \sigma_\parallel \left( E_\parallel + \frac{1}{en_e} \nabla_{PPe} \right) = \sigma_P^{\text{kinetic}} \left( \frac{\partial \phi}{\partial z} + \frac{1}{en_e} \frac{\partial (n_e T_e)}{\partial x_P} \right)$$

gives rise to two drift waves at diamagnetic frequencies  $\omega_{j*}$  and scales  $\rho_{*jj}$ .

## 9.15 Nonlinear Drift Wave Impurity Fluxes

The particle fluxes are:

$$\Gamma_z = \text{Re} \sum_k \frac{ik_y \phi_k^*}{B} \delta n_z = -n_e \frac{T_e}{eB} \sum_k \frac{k_y |e\phi_k|^2}{T_e^2} \text{Im} \hat{X}_1(k)$$

$$\Gamma_i = \text{Re} \sum_k \frac{ik_y \phi_k^*}{B} \delta n_i = -n_e \frac{T_e}{eB} \sum_k \frac{k_y |e\phi_k|^2}{T_e^2} \text{Im} \hat{X}_2(k)$$

$$\Gamma_e = \text{Re} \sum_k \frac{ik_y \phi_k^*}{B} \delta n_e = -n_e \frac{T_e}{eB} \sum_k \frac{k_y |e\phi_k|^2}{\tau^2} \text{Im} \hat{X}_3(k)$$

$$\hat{X}_k^r = \begin{bmatrix} \frac{\delta n_i}{n_e} & / & \frac{e\phi}{T_e} \\ \frac{\delta n_z}{n_e} & / & \frac{e\phi}{T_e} \\ \frac{\delta n_e}{n_e} & / & \frac{e\phi}{T_e} \end{bmatrix}$$

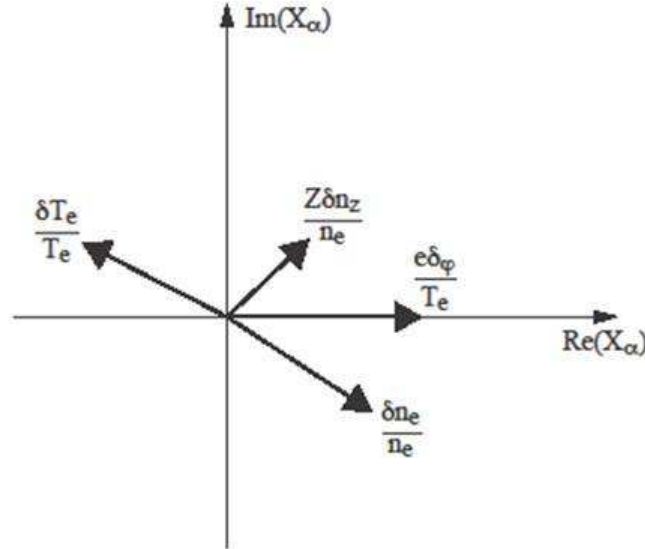


Figure 9.26: Evolution of Impurity Holes LHD.

## 9.16 Eigenvectors with Phases give D and V

Cross correlations of  $v_x = -\frac{\partial \varphi}{B \partial y}$  with  $\delta n_s$  and  $\delta T_s$  yields the turbulent fluxes.

For particle fluxes the phase relations determine the direction of the fluxes. Introducing the phases and the neoclassical driving forces  $X_\alpha$  gives

$$\Gamma_s = -D_s \frac{dn_s}{dx} + V_s n_s = -D_{\text{turb}}(W) \sum_\alpha [L_{s,\alpha}] [X_\alpha] \quad (9.124)$$

$$\Gamma_z = -D_z \frac{dn_z}{dx} + V_z n_z = -D_{\text{turb}}(W) \frac{dn_z}{dx} + \sum c_{z,n_e} \frac{R}{L_{n_e}} \quad (9.125)$$

Physically, the  $\hat{X}$  vector describes the “polarization” of density waves related to the electrostatic

wave. The particle fluxes are given by

$$\begin{aligned}\Gamma_i &= \operatorname{Re} \sum_k \frac{ik_y \phi_k^*}{B} \delta n_i = -n_e \frac{T_e}{eB} \sum_k \frac{k_y |e\phi_k|^2}{T_e^2} \operatorname{Im} \hat{X}_1(k) \\ \Gamma_z &= \operatorname{Re} \sum_k \frac{ik_y \phi_k^*}{B} \delta n_z = -n_e \frac{T_e}{eB} \sum_k \frac{k_y |e\phi_k|^2}{T_e^2} \operatorname{Im} \hat{X}_2(k) \\ \Gamma_e &= \operatorname{Re} \sum_k \frac{ik_y \phi_k^*}{B} \delta n_e = -n_e \frac{T_e}{eB} \sum_k \frac{e|\phi_k|^2}{\tau^2} \operatorname{Im} \hat{X}_3(k)\end{aligned}$$

Quasineutrality gives  $\Gamma_e = \Gamma_i + Z\Gamma_z$ . The impurity flux is given by

$$\Gamma_z = -D_z \frac{\partial n_z}{\partial x} + V_z n_z \quad (9.126)$$

where

$$D_z = \sum_k \frac{v_x^2(k)\gamma}{B^2(\omega^2 + \gamma^2)} \quad (9.127)$$

$$V_z = \sum_k \frac{v_x^2(k)\gamma}{\omega^2 + \gamma^2} \left( \frac{\omega(k)eB}{k_y T_e} \right) k_\perp^2 \rho_s^2. \quad (9.128)$$

## 9.17 Eigenmodes — Eigenvectors

Eigenmodes and eigenvectors of the linearized dynamical equations: fluctuations

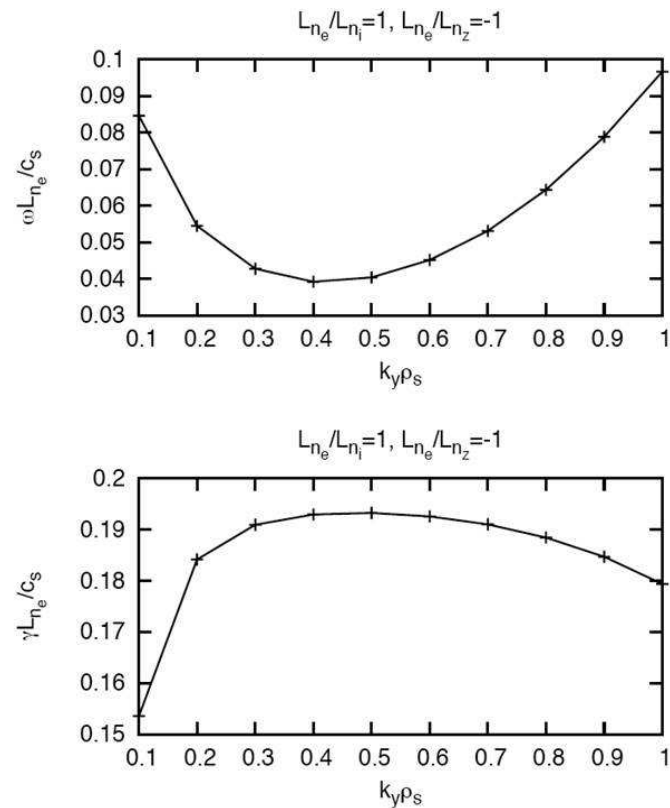
$$f_{k\omega} \exp(ik \bullet x - i\omega t)$$

Dynamics yield the  $a$  matrix  $A(k, \omega)$  for the field vector  $X^T$

$$A(k, \omega) X^T = 0 \quad X^T = \left( \delta n_i/n_e, \delta n_z/n_e, \delta n_e/n_e, \frac{e\phi}{T_e} \right)$$

$$\begin{bmatrix} 1Z & -1 & 0 & \\ -i\omega & 0 & 0 & -i\omega k_{\perp}^2 \rho_{s,i}^2 + i\omega_i^* - \mu_i k_{\perp}^4 \\ 0 & -i\omega & 0 & -i\omega k_{\perp}^2 \rho_{s,z}^2 + i\omega_z^* - \mu_z k_{\perp}^4 \\ 0 & 0 & -i\omega + i\omega_{De} + k_{\parallel}^2 D_{\parallel} & i\omega^* - k_{\parallel}^2 D_{\parallel} + \mu_i k_{\perp}^4 \end{bmatrix} \begin{bmatrix} \frac{\delta n_i}{n_e} \\ \frac{\delta n_z}{n_e} \\ \frac{\delta n_3}{n_e} \\ \frac{e\phi}{T_e} \end{bmatrix} = 0$$

$$\begin{aligned} \omega_z^* &= k_y \frac{T_e}{ZeB} \frac{1}{n_e} \frac{dn_z}{dx} & \omega_i^* &= k_y \frac{T_e}{eB} \frac{1}{n_e} \frac{dn_i}{dx} \\ \omega_i^* &= -k_y \frac{T_e}{eB} \frac{1}{n_e} \frac{dn_e}{dx} & \omega_{D\alpha} &= k_y \frac{2T_{\alpha}}{eBR} \cos \theta \end{aligned}$$

Figure 9.28: Hollow Impurity Profile:  $L_{ne}/L_{ni} = 1$ ,  $L_{ne}/L_{nz} = -1$ .

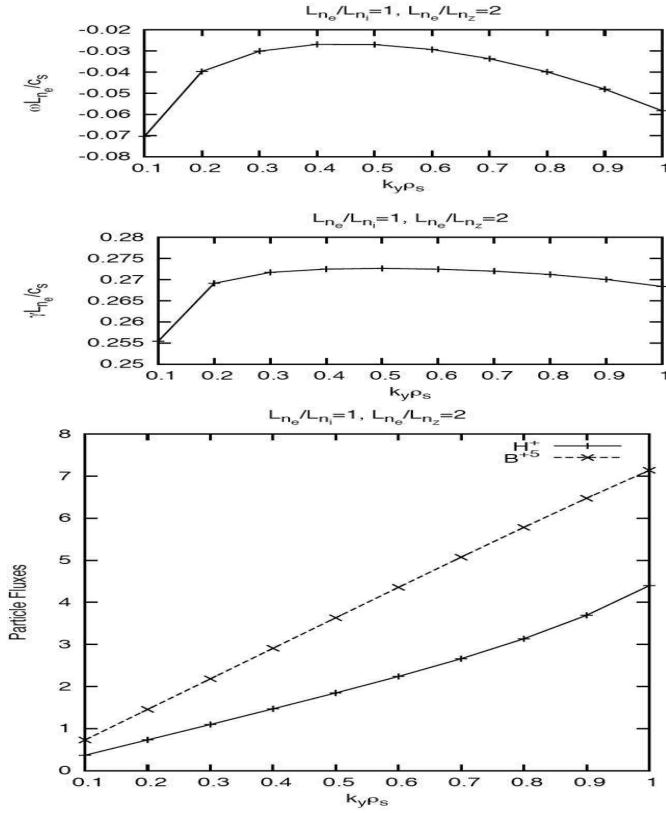


Figure 9.29: Inward Peaked Impurities:  $L_{ne}/L_{ni} = 1$ ,  $L_{ne}/L_{nz} = +2$ .

## 9.18 High-Z Trace Impurity Transport as Passive Scalar

$$\Gamma_z = -D_z dn/dr + \mu_z n Z e E_r \quad (\text{Horton-Rowan, 1994})$$

Radial electric field gives the impurity transport — Scandium blow-off in TEXT and Pellet Injection in LHD with V, Mn and Co.

For the  $E_r > 0$ , the impurity convection is outward and the impurity density is hollow due to the positive radial electric field.

$E_r(r, t)$  is complicated and largely unmeasured. High-ion temperature gradient gives negative  $E_r < 0$  with inward convection of impurities in C-Mod and others.

Analysis shows  $D \sim (20\rho_s)^2/2 \times 50 \text{ a/cs} = 4D_{\text{GB}}$  and  $V \sim 10\rho_s/50a/\rho_s \sim 0.2(\rho_s/a)$  and  $V_t$  gas releases.

## 9.19 Summary and Conclusions

Impurity Flux  $\Gamma_z$  is parameterized by two functions: the diffusivity  $D_z$  and advective  $V_z$  velocity  $\Gamma_z = -D_z \nabla n_z(r, t) + V_z n_z(r, t)$ .

Turbulence Theory yields structure for the impurity flux with explicit formulas for  $D_z$  and  $V_z$  from the eigenmode/eigenvector polarizations.

Neoclassical impurity fluxes are low. Need drift waves to explain data in both C-Mod and LHD.

Impurity transport with TESPEL experiments measured and explained by theory.

## 9.20 Ion ITB discharge on LHD–Impurity Transport

Impurity transport with TESPEL experiments measured and explained by theory.

LHD has three high-energy beam lines.

Negative-NBI beam energy of 180 KeV injected parallel  $B$  provides electron heating.

2 Positive NBI beams with energy of 40 KeV energy beams injected more nearly perpendicular to  $B$  provides ion heating and CX Spectroscopy.

Ion temperature, toroidal flow velocity, and poloidal flow velocity are inferred from the charge exchange emission CXRS from carbon.

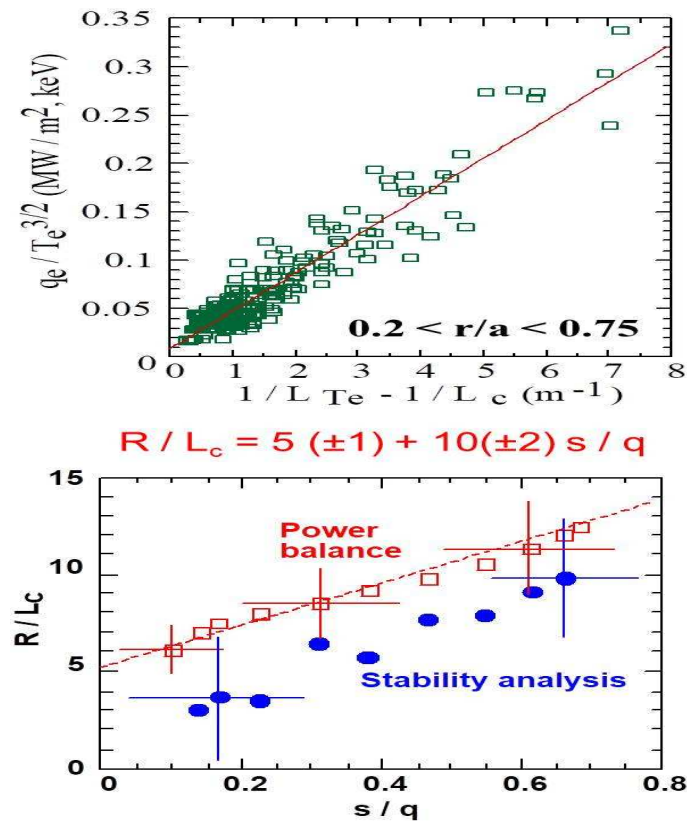


Figure 9.31: Simulation of Fast-Wave Heating with ETG Transport in Tore Supra.

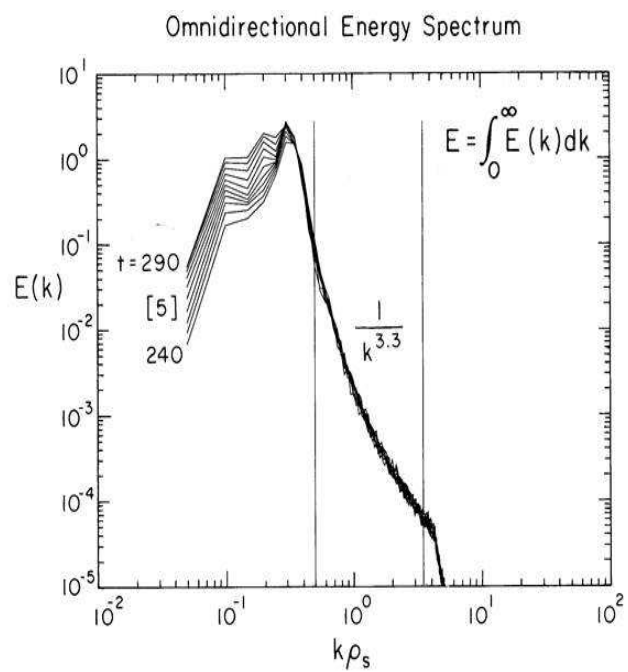
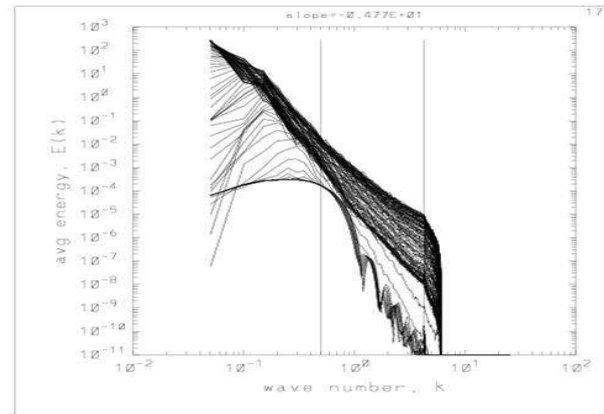


Figure 9.32: Inverse cascade from  $\rho_e$  to  $\rho_s$  and  $c/\omega_{pe}$ .

Electron Continuity Equation gives

$$e\delta(nu_{\parallel}) = \frac{\omega - \omega_{*e}}{k_{\parallel}}e\delta n.$$

Ampere's Law given

$$\delta B_x = \frac{1}{ik_y}\mu_0\delta j_{\parallel} \simeq \frac{\mu_0en(\omega - \omega_{*e})}{ik_yk_{\parallel}}\frac{\delta n}{n}.$$

So for TS we estimate

$$\delta j_{\parallel} \sim 5 \times 10^6 \text{ A/m}^2 \left( \frac{\delta n}{n} \right)$$

and

$$\delta B_x = 5 \times 10^{-2}T \left( \frac{\delta n}{n} \right)$$

The fractional perturbation is

$$\frac{\delta B_x}{B} = \frac{\mu_0en\omega_*}{2k_yk_{\parallel}}\frac{\delta n}{n} = \frac{\mu_0nT_e}{2B^2} \frac{1}{k_{\parallel}L_n} \frac{\delta n}{n} = \frac{1}{4} \frac{\beta_e}{k_{\parallel}L_n} \frac{\delta n}{n} \sim 5 \times 10^{-4}$$

Magnetic Stochastic Transport

$$\chi_e^{\text{RR}} = \frac{\pi v_e}{|k_{\parallel}|} \left( \frac{\delta B_x}{B} \right)^2 \sim \frac{\pi 10^7 \text{ m/s}}{10^{-2} \text{ m}^{-1}} 25 \times 10^{-8} \sim 10^2 \text{ m}^2/\text{s}$$

## 9.21 ETG Modeling of NSTX with HHFW Heating in High–Beta Regime

$$\chi_e^{\text{RR}} = \frac{\pi v_e}{|k_{\parallel}|} \left( \frac{\delta B_x}{B} \right)^2 \sim \frac{\pi 10^7 \text{ m/s}}{10^{-2} \text{ m}^{-1}} 25 \times 10^{-8} \sim 10^2 \text{ m}^2/\text{s}$$

ETG gyrofluid simulations for modeling high- $k$  scattering data at  $k_x\rho_e = 0.13$  and  $k_y\rho)e \approx 0$ . Mazzucato scattering on NSTX 2008, 2009. ETG plays an important role in determining electron transport at low  $B_T$  NSTX.

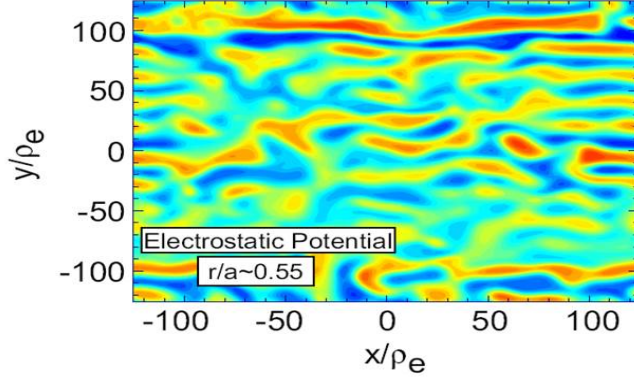


Figure 9.36: Nonlinear simulations indicate formation of radial streamers (up to  $200 \rho_e$ ): FLR-modified fluid code (Horton, *et al.* 2005).

Good agreement between experimental and theoretical saturated transport level at 0.35 T.

Experimental  $\gamma_e$  profile consistent with that predicted by e-m ETG theory (Horton, *et al.* (2004) at  $B = 0.35$  T–high beta discharge. Simulations for ETG fluctuations in TCV.

## 9.22 ETG and ITG–TEM Driven Electron Thermal Fluxes

For  $\eta_e > \eta_{e,\text{crit}}$

$$q_e = C_e^{em} n_e T_e \frac{c^2}{\omega_{pe}^2} \frac{v_e}{R^2} \left( \frac{R}{L_{T_e}} - \frac{R}{L_c} \right)$$

$$\beta_{e,\text{crit}} = \text{const} \times \frac{L_{T_e}^2}{q^2 R^2}$$

For  $\eta_e > \eta_{e,\text{crit},e,\text{crit}}$

$$q_e = C_e^{es} n_e T_e q^2 \left( \frac{\rho_e^2 v_e}{L_{T_e}^2} \right) \left( \frac{R}{L_{T_e}} - \frac{R}{L_c} \right)$$

ITG-TEM  $e$ -flux

$$q_e = -n_e f_{tr,e} c^{ITG} \sigma_{Ti} \frac{c_s q^2 \rho_s^2}{L_{T_i} R} \left( \frac{R}{L_{T_i}} - \frac{R}{L_c} \right)$$

[Ottaviani, *et al.* (1997)].

## 9.23 Conclusions and opportunities

Electron Temperature Gradient Driven Turbulence documented in basic physics experiments in steady-state, linear CLM experiments.

First Principles GTC (gyrokinetic simulations with generalized PIC methods) validated with the CLM data.

Nonlinear states with Coherent Structures (CS): vortices, streamers and nonlinear spreading of the fluctuations to linearly stable regions.

Experiments in Tore Supra, NSTX and TCV all show ETG.

Nonlinear states have mixed interchange and tearing mode symmetries as also reported in resistive- $g$  and ITG turbulence.

## 9.24 Electron Transport Results and Future Plans

ETG has become the standard model: plays key roles in NSTX, MAST, FTU, C-Mod, DIII-D, TCV and Tore Supra.

Full ETG Model includes microtearing modes.

Consistent with  $\delta B_{\perp}^2 \propto \nabla T_e = (\nabla T_e)_{\text{crit}}$  from Cross-Polarization Scattering in TS

Ion-scale turbulence (TEM and ITG) produces further turbulence. Controlled by  $E_r$ -shear: vortices, streamers, and zonal flows and by ICRF heating. Ion transport in NSTX and MAST is near neoclassical.

New tools such as GS2 and GKV (Watanabe) are being used to give detailed data on the structure of ETG and Micro-tearing modes — NSF TeraGrid, NERSC and Earth Simulator machines

## 9.25 Electron Transport Results and Future Plans

ETG has become the standard model: plays key roles in NSTX, MAST, FTU, C-Mod, DIII-D, TCV and Tore Supra.

Full ETG Model includes microtearing modes.

Consistent with  $\delta B_{\perp}^2 \propto \nabla T_e = (\nabla T_e)_{\text{crit}}$  from Cross-Polarization Scattering in TS

Ion-scale turbulence (TEM and ITG) produces further turbulence. Controlled by  $E_r$ -shear: vortices, streamers, and zonal flows and by ICRF heating. Ion transport in NSTX and MAST is near neoclassical.

New tools such as GS2 and GKV (Watanabe) are being used to give detailed data on the structure of ETG and Microtearing modes — NSF TeraGrid, NERSC and Earth Simulator machines

Theory of reversed magnetic shear induced electron transport barrier by *Horton and Morrison* [PoP, 3910, 1998] continuing with Caldas, et al. <http://orion.ph.utexas.edu/~starpowerhttp://pecos.ph.utexas.edu/~vortex>

## 9.26 Simplified Solution and Critical Value of $L_{Te}$

The fluid limit of the  $Z$ -functions gives a cubic linear dispersion relation for the slab ETG instabilities:

$$\omega^3 \approx -\tau \cdot k_{\parallel}^2 \cdot v_e^2 \cdot \omega_{Te}^*, \quad \text{or} \quad \omega_{\text{ETG}} \approx \frac{1}{2} (k_{\parallel}^2 \cdot v_e^2 \cdot \omega_{Te}^*/\tau)^{1/3} + i \frac{\sqrt{3}}{2} (k_{\parallel}^2 \cdot v_e^2 \cdot \omega_{Te}^*/\tau)^{1/3}.$$

Requirement for the ETG instabilities:  $\eta_e d \ln T_e/d \ln n \sim 2$

–with density gradient: the threshold controlled by  $L_p/L_{Te} = L_p(-dT_e/dr)/dr)/T_e$ ; 20

–flat density profiles: the threshold.

When we take the limit of the linear growth rate  $\rightarrow 0$ , the critical value of the electron temperature gradient scale length  $L_{Te}$  required by the slab ETG instabilities with flat density profiles can be obtained as:

$$(k_{\parallel} L_{Te})_{\text{critical}} \leq 0.14 \quad \text{from probe data: } 0.02 \text{ cm}^{-1} \times 0.8 \text{ cm} = 0.016$$

For instabilities, the electron temperature gradient scale length should be below this critical value.

## 9.27 Ohm's Law and Frozen in Motion

Electron Dynamics:

$$\frac{m_e}{e} \frac{\partial j_{\parallel}}{\partial t} + enE_{\parallel}^{(A)} + \frac{B_x}{B} \frac{dp_e}{dx} + enE_{\parallel}^{(ES)} + \nabla_{\parallel} p_e = en\eta j_{\parallel}$$

Ampere's Law

$$\begin{aligned} j_{\parallel} &= -\frac{1}{\mu_0} \nabla^2 A_{\parallel} \\ E_{\parallel}^{(A)} &= -\frac{\partial A_{\parallel}}{\partial t} \quad \text{and} \quad E_{\parallel}^{(ES)} = -\nabla_{\parallel} \phi \\ \frac{T_1}{T_2} \quad \frac{m_e}{en\mu_0} \frac{1}{L^2} &\rightarrow \frac{k_{\perp}^2 c^2}{\omega_p^2} = \begin{cases} = 0 \text{ MHD} (m_e = 0) \\ \gg 1 \text{ ES -- DWS} \end{cases} \end{aligned}$$

$$\begin{array}{ll}
\text{at } k_{\perp} \sim 1/\rho_s & = \frac{m_e}{m_i \beta_e} \\
A_{\parallel} - \text{resonance} & T_1 + T_2 + T_3 = 0 \\
\phi - \text{DW} & T_4 + T_5 + T_6 = 0 \\
\text{Frozen in Dynamics} & T_2 + T_4 = 0
\end{array}$$

## 9.28 ETG-Tearing modes with Closure for Parallel Electron Heat Flux

$$\begin{aligned}
nv \cdot \nabla T_e + \nabla_{\parallel} q_{e\parallel} &= 0 \\
\frac{\delta T_e}{T_e} &= -i \frac{\omega_{*Te}}{\chi_{\parallel} k_y^2} \frac{e\phi}{T_e} \\
Bg \nabla_{\parallel} T_e &= B_y(x) \frac{\partial \delta T_e}{\partial y} + \delta B \cdot \nabla T_e = 0 \\
\frac{\delta T_e}{T_e} &= \frac{\omega_{*Te}}{ck_y} \frac{ce\psi}{T_e}
\end{aligned}$$

## 9.29 Energy Release from Carnot Cycles

## 9.30 Nonlinear equations for Impurity

### 9.30.1 Standard drift waves and trapped electron mode

For the first model of drift wave impurity turbulence dimensionless partial differential equations are

$$\begin{aligned}
\frac{\partial \tilde{n}_i}{\partial \tilde{t}} + \frac{R}{L_{n_i}} \frac{\partial}{\partial \tilde{y}} \tilde{\phi} + [\tilde{\phi}, \tilde{n}_i] - \left( \frac{\partial}{\partial \tilde{t}} \tilde{\nabla}_{\perp}^2 \tilde{\phi} + [\tilde{\phi}, \tilde{\nabla}_{\perp}^2 \tilde{\phi}] \right) &= 0 \\
\frac{\partial \tilde{n}_z}{\partial \tilde{t}} + \frac{R}{L_{n_z}} \frac{\partial}{\partial \tilde{y}} \tilde{\phi} + [\tilde{\phi}, \tilde{n}_z] - \frac{A}{A} \left( \frac{\partial}{\partial \tilde{t}} \tilde{\nabla}_{\perp}^2 \tilde{\phi} + [\tilde{\phi}, \tilde{\nabla}_{\perp}^2 \tilde{\phi}] \right) &= 0 \\
\frac{\partial \tilde{n}_e}{\partial \tilde{t}} + \frac{R}{L_{n_e}} \frac{\partial}{\partial \tilde{y}} \tilde{\phi} + [\tilde{\phi}, \tilde{n}_e] + \frac{m_i}{m_e} \frac{c_s}{R \nu_{ei}} \tilde{\nabla}_{\parallel} (-\tilde{\nabla}_{\parallel} \tilde{n}_e + \tilde{\nabla}_{\parallel} \tilde{\phi}) &= 0
\end{aligned}$$

For linear analysis, we can assume fluctuation in the form of  $\exp(i\mathbf{k} \cdot \mathbf{x} - i\omega t)$ , drop nonlinear terms (Poisson brackets), and rewrite linearized equations in the following matrix form

$$\mathbf{A}(\mathbf{k})\mathbf{X} = -i\omega\mathbf{B}(\mathbf{k})\mathbf{X}, \quad \text{where} \quad \mathbf{X} = \begin{bmatrix} \frac{\delta n_i}{n_i} \\ \frac{\delta n_{z1}}{n_{z1}} \\ \frac{\delta n_{z3}}{n_{z2}} \\ \frac{e\phi}{T_e} \end{bmatrix}$$

### 9.31 Kinetic Simulation of FRC Stability and Transport

Magnetic confinement fusion offers the prospect of a carbon–neutral, environmentally responsible and inexhaustible energy source. The present mainline approach to magnetic fusion energy is via the tokamak concept relying on a strong toroidal (doughnut-shaped) magnetic field to confine plasma at temperatures characteristic of the interior of stars ( $\sim 100$  million°K). The hydrogen isotopes deuterium (D) and tritium (T) fuse at these temperatures, releasing energy mainly in the form of neutrons. The most advanced tokamak to date, the International Thermonuclear Experimental Reactor, is presently under construction, to test and demonstrate the sustained production of fusion energy for the first time.

The magnetic field-reversed configuration (FRC) employs its magnetic field more efficiently, characterized by a much higher ratio  $\beta$  of the plasma kinetic pressure to the external magnetic field energy density, with averaged  $\beta \sim 0.9$ . This magnetic configuration is of great interest as a fusion reactor concept due to its compact, axisymmetric geometry and the potential for aneutronic fusion based on advanced fuels, such as the proton–boron fusion reaction (p–B11). A major advantage of this fuel is that there are vast quantities of Boron in the US and around the world, in contrast with Tritium, a hydrogen isotope not found naturally on Earth.

Over nearly 20 years, TAE has raised over \$500M of private capital, allowing it to pioneer and refine the FRC approach over a succession of experimental research devices, leading up to the present C–2W experiment, shown in Figure 1. Our long–term computational research goal is to do Whole Device Modeling, which will combine models working on many scales, with calibration and verification with experimental data from C–2W and its successors. In conjunction with experiments this will lead to a commercial fusion power plant. How quickly this will happen depends, in part on our ability to do “virtual science”.

### 9.31.1 INCITE Impact on TAE Business Strategy

From a business point of view, the proposed INCITE work will accelerate learning and help to deliver scientific milestones which are required to unlock further private capital. The work will also help to mitigate experimental risk, which equates to mitigating capital risk; a key component of responsible stewardship of our invested capital. And the validated tools will allow strategic planning for the large scale funding round required for construction of the successor to C-2W, TAE’s next experimental reactor concept.

TAE funds and participates in multiple supporting research and development efforts, with domestic public partners including UC Irvine, PPPL, LLNL, TUNL, UCLA, U. Wisconsin, U. Washington, and U. Florida, and funded international partners including Nihon University, Japan, and Budker Institute of Nuclear Physics, Russia. This brings the benefits of parallelism and community resources to bear on the problem to increase the pace of research progress. It was with help from these partners that the TAE C-2 (2008–2015) and C-2U (2015–2016) programs discovered a High Performance Field Reversed Configuration regime [*Binderbauer, et al. (2015)*] and addressed along the way many of the issues regarding Compact Tori (CT) outlined in the US DOE sponsored Toroidal Alternates Panel report (2008) [*Hill (2008)*] and Research Needs Workshop [*Hazeltine (2009)*].

We propose to establish a collaboration with the Argonne Leadership Computing Facility to help us achieve our corporate goals, through the vehicle of the INCITE program.

### 9.31.2 Broader Scientific Impact and Context

The physics that we are studying at Tri Alpha Energy has important relevance for the publicly-funded fusion plasma science sector, because many of the concepts are complementary to those being explored in public facilities such as the NSTX-U experiment at Princeton Plasma Physics Laboratory, and the GDT experiment at Budker Institute.

The Field Reversed Configuration has no central conductor, which greatly simplifies the engineering of a reactor concept compared to a tokamak. Important physics consequences are that there is no externally imposed toroidal direction to the magnetic field, and, in the FRC, the magnetic field increases on the outside of the torus, rather than decreasing as in the tokamak, which leads to favorable stability properties. The fraction of large orbit particles, known to have favorable stability properties [*Rosenbluth, et al. (1962)*] is also larger in the FRC. Despite these differences, a very important quantitative similarity has been discovered, which is that the energy transport scalings found on the larger Spherical Tokamak and FRC experiments are very similar, with  $B\tau_E \sim v_{e*}^{-0.8 \text{ to } -1.0}$  for NSTX [*Kaye, et al. (2007, 2013)*], and  $B\tau_E \sim v_e^{-1}$  for C-2U [*Binderbauer, et al. (2015)*]. The meaning of these approximately  $1/v_e$  scalings is that the energy confinement per magnetic field improves as the temperature increases, which is ideal for a fusion reactor. Both NSTX-U and C-2W experimental programs have plans to study these transport scalings to see how well they extend into higher electron temperature parameter regimes, and a

public/private collaboration (see below) has already been proposed to allow synergistic interaction between the two programs.

In C–2W the core toroidal magnetic field region is enveloped in an open magnetic field line region of plasma known as the Scrape–Off Layer (SOL), which is confined between two magnetic mirrors. Particles that escape the mirrors move into the divertor expander vessels (see Fig. 2) where the magnetic field lines flare outward as in the Gas Dynamic Trap (GDT) experiment [*Ivanov and Prikhodko (2013)*]. There is an active collaboration between TAE and the GDT teams which is advancing the understanding of mirror plasma physics. The resulting scientific insights could have significant wider technological benefit, as there are several organizations that are exploring mirror devices as commercializable neutron sources for use in materials testing and remote sensing [*Ryutov (1990), Horton, et al. (2010)*]. The scientific community has taken note of these interesting points of comparison between the CW experiment and the NSTX–U and GDT experiments. These were highlighted at the recent DOE–backed 2016 US–Japan Compact Tori Workshop [*Tajima and Asai (2016)*], where members of the tokamak, Compact Torus, and mirror communities gathered to discuss synergistic physics research topics. Of particular relevance to the current INCITE proposal, this workshop concluded with a call to create a community–wide collaboration to develop the capability for high fidelity simulation of Compact Torus plasmas, a category which includes FRCs such as TAE’s C–2W, and Spherical Tori (ST) such as PPPL’s NSTX–U.

To meet this need, the lead PI on the present INCITE proposal also led in 2017 (under the auspices of UC Irvine) a multi–institution SciDAC proposal to create a Center for Whole Device Modeling of Compact Tori (WDMCT) to support US domestic research into high beta plasmas for fusion applications. This was in response to the SciDAC Whole Device Modeling FOA [*SciDAC (2017)*]. Our proposal was to create a public–private partnership, where TAE would fully fund about 10 FTE members of its Computational Modeling group to participate, and SciDAC would fund about 10 FTE non–TAE scientists at universities, national labs, and private companies. Co–PIs on the SciDAC proposal included Jan Egedal of U. Wisconsin, Kai Germaschewski of University of New Hampshire, Burlen Loring of LBNL, and representatives of private research companies including Sergei Galkin of Far–Tech Inc, Robert Harvey of CompX Co, Yuri Omelchenko of Trinum Research, and Dale Welch of Voss Scientific. Representatives of numerous public institutions signed on to be unfunded collaborators to assist with theoretical support and experimental validation of the developed models. Unfunded theoretical and computational collaborators included Daniel C. Barnes of Coronado consulting, Elena Belova of PPPL, Toshikazu Ebisuzaki of RIKEN, Walter Guttenfelder of PPPL, Yasuaki Kishimoto of Kyoto University, Zhihong Lin of UC Irvine, and the TAE team. Unfunded experimental collaborators included Stan Kaye of the Core Science Team of NSTX–U at PPPL, Peter Bagryansky of the GDT team at Budker Institute of Nuclear Physics, Michael Brown of the SSX group at Swarthmore College, and Tomohiko Asai of the FAT–CW experimental team at Nihon University, and the TAE C–2W experimental team.

The multi–institution collaborators on the SciDAC proposal agreed that two of the highest priorities of the WDMCT Center would be the simulation of kinetic microturbulence and global stability. Regardless of the funding status of the SciDAC proposal, TAE’s efforts on these most strategically important components of the WDM continue. These components have both been

under development since 2013 and are the subject of the present INCITE proposal: the ANC kinetic microturbulence code, and the FPIC kinetic global stability code.

### 9.31.3 ANC and FPIC Codes in Context

The ANC code [*Fulton* (2017)] is a specialization of the GTC code [*Lin, et al.* (1998), *Holod, et al.* (2009)], and is developed in collaboration between Tri Alpha Energy and Professor Zhihong Lin, PI of the GTC project, at UC Irvine. ANC and GTC are the first and only codes that we know of that are being used to simulate turbulent transport in the Field Reversed Configuration. There is, essentially, no competing work on that topic, and all planned work is completely novel. GTC is the first fusion code to reach the teraflop in 2001 on the Seaborg computer at NERSC [NERSC (2001), *Lin, et al.* (2002)] and the petaflop in 2008 on the Jaguar computer at ORNL in production simulations [*Xiao and Lin* (2009)]. Through collaborations with computer scientists from hardware vendors including NVIDIA and Inspur/Intel, the GTC production version was the first large scale fusion code to fully utilize the heterogeneous architectures using GPU (graphic processing unit) accelerators on Tianhe-1A [*Meng, et al.* (2013)] and Titan, and using MIC (many integrated core) co-processors on Tianhe-2 [*Dongarra* (2013)]. GTC has been selected by the DOE Center for Accelerated Application Readiness (CAAR), a program to prepare prominent codes across all DOE supported science research portfolio for the emerging exascale computers [CAAR] such as the next generation computer Summit at ORNL. GTC has recently been ported to SummitDev, the prototype computer of Summit. GTC has received large time allocations on the supercomputers at NERSC and ORNL through the SciDAC, INCITE, ALCC, and CAAR projects.

In the DOE-funded space of turbulent plasma transport codes, the only other code which may have the capacity for global turbulence study of the FRC is the XGC-I code [*Chang and Ku* (2008)] at the Center for Edge Physics Simulation hosted at PPPL.

FPIC is not the first hybrid Particle-In-Cell (PIC) code to be used for global stability studies of FRCs. The HYM code [*Belova, et al.* (2001)] has been used very extensively to study FRC global stability in the past, including specific applications to TAE problems. Review of existing FRC stability studies makes it clear that the global stability properties of an FRC depend intricately on the end boundary conditions [*Belova* (2015)], the shape of external current distributions [*Yamada, et al.* (2007)], the shape of the separatrix and the plasma profiles [*Parks and Schaffer* (2003)], and the level of kinetic influence [*Milroy, et al.* (2008), *Barnes and Milroy* (1991)]. All of these parameters may change during an FRC discharge; some of them are external actuators which may be used for feedback control. FPIC has been developed by TAE because feedback and control of global stability is a requirement for the C-2W experimental program, and it has to work in order for us to achieve our strategic goal. To our knowledge, the feedback and control capability of FPIC is unique in the area of global stability PIC codes.

## 9.32 RESEARCH OBJECTIVES AND MILESTONES

### 9.32.1 Research objectives

The overarching goals of the present proposal are to accelerate the scientific progress of the C-2W experimental program, and to commence predictive simulations for future fusion reactor prototype concepts. The strategic simulation development goal to allow this is to develop the Whole Device Model (WDM) mentioned in Sec. 1.3. This is already well underway.

The main goal of the C-2W experimental program is to increase the temperature of the magnetically-confined plasma, to see if the energy confinement scaling  $B\tau_E \sim v_e^{-1}$  discovered on C-2U continues to hold. The experimental strategy to accomplish this is to use known methods to form the plasma in C-2U conditions, and then to ramp up the plasma parameters using external actuators. Plasma parameters will then pass from a known state space, to a new state space. This imparts some element of risk: the global stability properties of the plasma may change in the process, so feedback and control systems are built into C-2W to keep the plasma macroscopically stable. Macroscopic stability is a prerequisite for the study of the energy confinement scaling. TAE's C-2U experiment was only able to demonstrate the favorable confinement scaling after macroscopic stability had been mastered.

The two elements of the WDM to be used in this INCITE proposal are the ANC and FPIC codes. Together they can be used to find stable operating points in new parameter regimes, and to make quantitative predictions of the turbulent transport levels at those points. With computing resources provided by an INCITE allocation, we propose to use the codes in close collaboration with the C-2W experimental program to validate the codes against the experiment, mitigate experimental risk inherent in the exploration of new parameter regimes, accelerate the optimization of experimental operating scenarios, and use validated models to predict stable and efficient operating points for future FRC reactor design concepts.

The physics problem is fundamentally hierarchical and represents a multi-year undertaking. In this section, an overall strategy to achieve the goals will be outlined, and milestones within the scope of this INCITE proposal will be highlighted.

### 9.32.2 Motivation for the Choice of Tools

Transport in magnetically-confined plasmas is determined by underlying microturbulence, which is characterized by length and time scales less than the ion Larmour radius and cyclotron frequency. In the FRC, overall confinement time depends on a balance between the cross-field and parallel-to-field transport, and between the topologically distinct core and open field-line Scrape-Off Layer (SOL), making transport intrinsically global. Further, global features, such as current or pressure gradient, also provide sources of free energy which drive the microturbulence. Due to the difficulty of resolving the wide range of time scales involved, a pragmatic approach is to apply

two separate simulation codes, one for long time scale macro-stability and the other for short time scale microturbulence. This is our motivation for using FPIC and ANC. The FRC magnetic configuration has special features mentioned in Sec. 1.3, including zero magnetic field regions, ion orbits comparable to the device size, and high beta self-organization, which place requirements on the models which are more stringent than in tokamak codes. To meet these requirements, both ANC and FPIC codes use fully kinetic ion orbits, and cannot make use of magnetic field aligned coordinate systems. A high level comparison of the two codes is in Table 9.4, and the codes are described in the following subsections.

### 9.32.3 Macro stability code, FPIC

The Finite Electron Mass Particle-In-Cell) (FPIC) code [*Detrick, et al. (2015)*] is a 3D global plasma stability code. Fully kinetic ions are used to capture the kinetic stabilization and destabilization of global modes which is known to occur [*Milroy, et al. (1989), Belova, et al. (2003)*]. Electron energy is represented by an equation of state, and a generalized Ohm's law is used with an optional finite electron mass correction term consisting of a vector Laplacian pre-multiplied by the ion skin depth squared. This correction affects the plasma/vacuum boundary which is usually treated by ad hoc resistivity tuning in hybrid codes. Particular care has been taken to allow realistically shaped boundaries, which can be either conducting or resistive.

FPIC will be used to study shape and position instabilities in general Compact Tori in the presence of conducting or resistive boundaries, including kinetic ion effects, multiple ion species, and other actuators on stability such as neutral beam injection and electrode biasing. It will be used to simulate feedback and control of those instabilities using coils as magnetic actuators in the C-2W experiment.

An example of successful application of the FPIC code [*Ceccherini, et al. (2016)*] is shown in Fig. : the stability of the tilt mode as a function of the ion kinetic parameter  $E/S^*$  (large  $E/S^*$  is more kinetic). The left panel shows evolution of the tilt mode followed by nonlinear saturation (c.f.) [*Belova, et al. (2004)*]. The right panel shows the results of modal analysis of 13 separate simulations, compared to analytic theory [*Steinhauer (2011)*].

### 9.32.4 Micro-stability code, ANC

A New Code (ANC) is a first-principles, integrated PIC microturbulence code. ANC is based on the Gyrokinetic Toroidal Code (GTC) at UC Irvine, but designed specifically for FRC magnetic geometry, to capture large-orbit ion dynamics, and cross-separatrix transport. It has been developed to investigate transport in TAE's FRC devices C-2, C-2U, and C-2W, and future reactor prototype designs.

ANC's physics model is electrostatic, solving the Vlasov–Poisson system, including a fully-kinetic or gyrokinetic ion advance, gyrokinetic or adiabatic electrons, and corresponding Poisson

solvers. The particle species distribution functions are modeled using a perturbative ( $\delta f$ ) formulation for substantially reduced particle noise. ANC's formulation uses cylindrical coordinates rather than magnetic coordinates in order to treat dynamics crossing the magnetic separatrix as well as magnetic field nulls. Since the code is tailored to simulate FRC magnetic geometry, ANC simulations are initialized from numerically specified equilibrium in a TAE specific HDF5 format, which is shared with FPIC.

Development of ANC is ongoing. A major part of development is continuing cross-code verification with GTC, which is developing an FRC transport model in tandem. To date, the gyrokinetic ion model in ANC has been applied to perform global linear and nonlinear simulations in C-2U geometry, for comparison to turbulent fluctuation measurements [Schmitz, *et al.* (2016)] as well as prior single-flux-surface GTC simulations [Fulton, *et al.* (2016a,b), Lau, *et al.* (2017)].

Table 9.4: High-level comparison of ANC and FPIC code features. Items marked as \* are future plans.

	ANC	FPIC
target physics	microturbulence	global stability; stability and control
fields	electrostatic, electromagnetic*	electromagnetic
particle model	perturbative (“delta $f$ ”), fully kinetic ions, drift kinetic electrons	nonperturbative (“full $f$ ”), fully kinetic ions, fluid electrons
domain	2+1 D, cylindrical+Fourier; local in Fourier mode	3D Cartesian Yee mesh; global
time scale mitigation	Adiabatic or orbit averaged electrons; Light waves not tracked in electromagnetic model;	Quasineutrality; Darwin model; Faraday subcycling; Implicit methods*
length scales	Debye length; ion gyroradius; electron gyroradius	ion inertial length; ion gyroradius
inter-node parallelism	MPI Group parallel	MPI domain decomposed
intra-node parallelism	MPI, OpenMP	MPI, OpenMP, CUDA

### 9.32.5 Research and Development Milestones (3 year)

There are two milestones per year, listed 1 to 6 below. Below, each milestone is described in text. In subsection 3.1 milestones are also broken into Research and Development tasks, recorded as subitems a,b,c etc. Year in which task or milestone is to be accomplished is designated by Y1, Y2, or Y3.

1. Verification of model components (Y1). Both ANC and FPIC will undergo additional analytical and cross-code verifications, to ensure that the model implementations accurately reflect their physics formulations. In ANC, some early optimization work on the spline algorithm will also be performed, to speed up the subsequent milestones.
2. Validation of model components against experiment (Y1). ANC and FPIC simulations will be compared to experimental data to validate that their models are sufficient to describe the real FRC. ANC transport simulations will be compared to fluctuation data from the completed C-2U campaign as well as prior GTC simulations, and FPIC will perform a positional stability scan against data from the new C-2W device.
3. Initial C-2W stability and transport calculations (Y2). The crux of this proposal is supporting the new C-2W device at TAE. In this milestone, ANC will perform a complete global, nonlinear transport calculation, providing values for heat and particle flux, while FPIC will study stability dependence on a variety of equilibrium properties and C-2W actuators.
4. Refinement of models and algorithms (Y2). The model will enter a development phase, based on difficulties discovered in milestones 2 and 3. Key items we anticipate adding are magnetic perturbations in ANC and an implicit algorithm in FPIC which may provide  $\sim 10 \times$  speedup.
5. Advanced C-2W stability and transport calculations (Y3). The C-2W simulations performed in Milestone 3 will be re-performed using the refined model, including all new actuators in FPIC and magnetic perturbations in ANC.
6. Future reactor prototyping simulations (Y3). The FRC stability and transport model will be applied to future reactor concepts in an exploratory fashion, primarily to direct future code development and mitigate experimental risk.

### 9.32.6 Prospective Publications

After a long history of operating in stealth, TAE has grown to value interaction with the wider plasma physics community. In addition external university collaborations and conference participation, peer-reviewed publications provide a major avenue for engaging colleagues in the research community.

Following recent published work on transport in C-2U [Schmitz, *et al.* (2016)], the work proposed herein could potentially culminate in a number of papers. Topics under consideration include respective formulations of ANC and FPIC, comparison of gyrokinetic and fully-kinetic ion models in the FRC, simulation of drift-wave turbulence in global FRC geometry, beam driven instabilities, and feedback and control simulations.

## 9.33 Computational Readiness

### 9.33.1 Use of Resources Requested

In the following, we describe the jobs that will be run for each task that contributes to the milestones listed in section 2.3. Only production runs are listed; smaller exploratory runs are absorbed into the production run estimates. CPU requirements are listed as MCH (Million Core Hours) on Theta. In the milestones table, they are converted to MCH on Mira, using the 3.25 conversion factor.

1. Verification of model components (Y1)
2. FPIC-4 MCH-10-run parameter scan to verify CAM dispersion relation, and 20 runs to study parameterization of tilt stability criterion in long FRC
3. ANC-0.4 MCH-initial optimization of splines, vectorization
4. ANC-0.1 MCH-I run simple ion acoustic wave, GTC cross-code verification
5. ANC-0.1 MCH-I run simple ion Bernstein wave, GTC cross-code verification
6. Validation of model components against experiment (Y1)
7. FPIC-6 MCH-25 runs for a coarse 2D parameter scan varying FRC length and pressure profile parameter.
8. ANC-validation of global simulation against C-2U fluctuation data [Schmitz, *et al.* (2016a,b)]
9. 9.4 MCH-10 runs for linear dispersion scan, compared to GTC
10. 20 MCH-2 nonlinear runs to compare C-2U Doppler backscatter data
11. Initial C-2W stability and transport calculations (Y2)
12. FPIC-Global FRC stability dependence on equilibrium properties
13. 2.5 MCH-10 runs to vary external field profiles-end mirror effects
14. 2.5 MCH-10 runs to study stability on C-2W ramp-up paths from 0.07 to 0.3
15. FPIC-Study external actuators
16. 2.5 MCH-10 runs to vary end-biasing parameters in C-2W
17. 2.5 MCH-10 runs to study neutral beam actuator in isolation

18. 2.5 MCH–10 runs to study magnetic coil actuators in isolation
19. 2.5 MCH–10 runs to study resistive wall actuator in isolation
20. ANC–global domain simulation calculation of electrostatic turbulent transport in C–2W
21. 9.6 MCH–10 runs to scan linear dispersion in C–2W equilibrium
22. 25 MCH–2 runs to compute nonlinear fluxes in C–2W equilibrium
23. Refinement of models and algorithms (Y2)
24. ANC–0.4 MCH–Electromagnetic solver, axial boundaries, equilibrium rotation
25. FPIC–2.5 MCH–implementation of implicit algorithm (which may provide
26.  $\sim 10 \times$  speedup) and repeat of many above simulations for regression testing
27. FPIC–2.5–finite electron mass effect–regression testing
28. Advanced C–2W stability and transport calculations (Y3)
29. FPIC–10 MCH–Exploratory feedback and control simulations with all actuators.
30. ANC–35 MCH–Revised nonlinear simulation, incorporating newly implemented physics features including magnetic perturbation, realistic axial boundaries, etc.
31. Future reactor prototyping simulations (Y3)
32. FPIC–10 MCH–Scale code to  $640x$  larger problem, and exploratory studies with shorter simulations. Depends on implicit time advance development task 4b.
33. ANC–5 MCH–Exploratory linear dispersion scans in prototype reactor equilibrium.

For ANC, estimates using 2048 nodes, so a 1 MCH linear simulation would take approximately 7.6 hours on 2048 nodes, while nonlinear simulations would be very intensive, taking approximately 150 hours on 2048 nodes. Restarts and check pointing are implemented and will be utilized for longer ANC simulations. For FPIC, planned usage is with 512 Theta nodes. Typical production run requires 0.5 M core hours, or 512 nodes for approximately 15.3 hours.

Time estimates for the ANC simulations are generated using a value of [MCH/time step] determined empirically by running the representative case discussed in Subsection 3.3.1 and in Fig. 7. This case uses a realistic FRC magnetic geometry, with an intermediary problem grid size. Time estimates are scaled proportionally to the number of grid points appropriate for C–2W or C–2U equilibrium and with sufficient physics resolution (approximately  $10 \times \lambda_{\text{Debye}}$ ) which is conservatively sufficient for the formulation. For linear simulations, the number of required time steps is then estimated by assuming the time step size is (1/20) of the ion gyroperiod, and that the physical time elapsed is (5) oscillation periods of the real frequency,  $\omega_r$ , of the phenomenon of

interest. This results in a total number of time steps  $0.01 \times \Omega_{ci}/\omega_r$ . In the case of ion acoustic waves and ion Bernstein waves  $\omega_r$  is estimated analytically. For the linear C-2U and C-2W scans,  $\omega_r$  is estimated from experimental observations and from prior gyrokinetic simulations. Nonlinear ANC simulations are very roughly estimated to be  $(10x)$  more expensive than their linear counterparts. This is based on using the same grid resolution, with  $5x$  longer simulation in physical time, to allow several linear growth times followed by nonlinear saturation, and  $2x$  more particles per cell, which are often required to reduce noise in the nonlinear case.

FPIC time requirements for typical C-2W production simulations are estimated from the strong scaling studies in Sec. 3.3. Optimal node count is determined from the sweet spot in Figure 8, which is at 512 Theta nodes, at which point each time step takes about 5 seconds (reading from the figure). This is for a typical production scenario which has  $10^6$  cells and  $10^9$  particles advanced for  $0.54e$  steps. There are  $\sim 10^6$  cells because the ion skin depth is  $\sim 3$  cm and the simulation domain is 1.6 m diameter and 8 to 12 meters long. There are  $\sim 10^3$  particles per cell because FPIC is nonperturbative and electromagnetic. And there are  $\sim 0.5e4$  time steps per run because the time advance is explicit, the time step is determined by the fastest Alfvén speed which is set by high-field, low-density regions under the mirror, making the time step around  $10^{-8}$  seconds, and the code should be integrated for  $\sim 10^{-4}$  seconds in order to observe linear growth of instabilities and subsequent saturation. A typical  $10^6$  cell,  $10^9$  particle,  $0.5e4$  time step production run takes 5 seconds per step and therefore requires 7 hours of wall time, and approximately 0.25 million Theta core hours (0.75 million Mira core hours equivalent) on 512 nodes. As a rule of thumb, a typical one-dimensional parameter scan on C-2W involving ten simulations would take 3 days of wall time and require 2.5 million Theta core hours (7.5 million Mira core hours).

Problem size estimates for both ANC/FPIC are intentionally a little large so that the net request can allow for smaller exploratory runs also, which are always be performed before any large production scan. Because of ongoing model development and verification, as well as the schedule of the C-2W experimental campaign, we anticipate that core hours will be burned slowly at first, with usage peaking towards the end of the year.

It should be clear that leadership class computing facilities are crucial to this project. To make scientific progress, a week is a practical turnaround time for a parameter scan for FPIC or a linear dispersion scan in ANC. If the computer had 100 times fewer nodes (TAE's commodity cluster has  $\sim 2$  MCH/year), it would be impossible to make progress or execute simulations necessary to support the C-2W campaign.

## I/O Requirements

Typical outputs from a production sized FPIC run consists of mesh and particle snapshots. Mesh snapshots are relatively small with respect to particle snapshots but are saved more frequently. For each production run we anticipate 60 GB and 20 GB of mesh and particle data, respectively. In most cases mesh snapshots do not need to persist in the project directory more than a few weeks. Particle snapshots are retained for at least a few months, to be able to restart partial runs. A parameter scan consisting of 20–30 production runs would result in storage of approximately

600-900 GB. Unlike FPIC, ANC uses a  $\delta f$  representation of the particle distribution, requiring significantly fewer particles per physical volume. Similar to FPIC, 3D mesh snapshots dominate storage requirements, although these are often analyzed in code, reducing them to 2D or even 1D outputs and minimizing IO. Promptly applying analysis can also reduce FPIC mesh data size from 60 to 10 GB or less. A heavy output ANC production run, resulted in 26 GB of total output in storage.

Our strategy to mitigate storage build up in project directory is to archive all simulation output on an annual basis. Over the lifetime of this proposal, data in archival tape storage would likely be  $< 10$  TB. In the event that more output is produced from either model component, frequency of tape backups would be increased to keep project storage under 1 TB, or transferred off-site via Globus. In the long term, in-situ visualization and analysis will be pursued. Other than the case of excess archived data, all transfers out of the center will use common tools such as ‘scp’ or ‘rsync’ for transfer of small data  $< 2$  GB. Our python based post-processing suite can be used directly at the center. Both codes would benefit from access to a center-hosted Jupyter server.

## Computational Approach ANC Numerical Methods

ANC is an electrostatic,  $\delta f$ , first principles particle-in-cell simulation code. It uses a magnetic field-null-spanning cylindrical coordinate mesh, on which an equilibrium magnetic field, density, and temperatures for each particle species are specified. The axial boundary of this grid is periodic, and the outer radial boundary is reflective to particles, and forced to zero for the Poisson solver. The  $\delta f$  technique, in which an equilibrium particle distribution,  $f$ , is assumed for each species and a perturbation,  $\delta f$ , is dynamically simulated, is applied. This technique substantially reduces particle noise at the cost of having to supply an input equilibrium. ANC requires use of the HDF5 library to read in equilibria, numerically specified in the  $R$ - $Z$ -plane. The particle distribution is assumed arbitrary in  $R$ - $Z$ , and may be initialized uniformly or to single harmonic mode in the azimuthal direction. The velocity distribution of the particles is assumed Maxwellian, however, non-Maxwellian distributions may be achieved by superimposing Maxwellians.

ANC implements both gyrokinetic and fully-kinetic particles in a polymorphic particle type, which is automatically handled in the particle advance routine. In its current implementation, it accommodates three species: ions, electrons, and test particles. Ions may be initialized as gyro or fully-kinetic and electrons may be initialized as gyrokinetic or adiabatic.

## FPIC Numerical Methods

FPIC uses a Cartesian Yee mesh with  $\mathbf{E}, \mathbf{J}, \mathbf{V}, \mathbf{A}$  vector fields defined on the cell edges,  $\mathbf{B}$  field defined on the faces, and densities defined at the vertices. Fully kinetic ions are advanced using the Boris method [Birdsall and Langdon (2004)], and their current is deposited in such a way as

to respect continuity [*Esirkepov* (2001)], using quadratic spline shaped particles. Electron energy is represented by an equation of state, and a generalized Ohm's law is used with an optional finite electron mass correction term. The Dey–Mittra cut cell method [*Dey and Mittra* (1997)] is used to model shaped conducting boundaries, and boundaries may also be periodic in one or more dimensions. Finite resistivity of the conducting boundary is implemented by coupling free-space exterior solutions to the cut–cell edges. The cut–cell implementation has been benchmarked against TEM spherical cavity modes for both conducting and resistive boundaries, and the full PIC code has been benchmarked against normal modes of a cylindrical uniform plasma [*Detrick, et al.* (2015) and against the FRC tilt mode [*Ceccherini, et al.* (2016)]. Initial conditions for the code are read from 2D ( $r, z$ ) cylindrically symmetric fluid equilibrium models [*Galeotti, et al.* (2011)] and converted to 3D Cartesian representation on the Yee mesh, with Maxwellian particles sampled from the fluid description. Explicit time advance of the field solver is performed by a second order Adams Bashforth method with magnetic field subcycling.

Two other state–of–the–art hybrid PIC codes which have been used to simulate FRCs are the HYM code developed by E. Belova at PPPL [*Belova, et al.* (2001)], and the HYPERS code developed by Y. Omelchenko at Trinum research [*Omelchenko and Karimabadi* (2014)]. Both codes are massively parallel, like FPIC. The HYM code has the advantage of maturity over FPIC, and has more flexible plasma models, including MHD, MHD+ minority kinetic, and hybrid PIC (like FPIC). The HYPERS code has the advantage of a sophisticated event–driven spatially adaptive time step which allows simulation of a domain where multiple time–scale phenomena are present simultaneously. Of the three codes, FPIC has the most sophisticated boundary model and is the only one with the resistive wall physics that will be necessary to model C–2W. HYM and HYPERS are not open source, so from a strategic planning point of view, FPIC is the best option for our studies.

## Parallelism

Both codes use distributed memory MPI for inter–node parallelism, and both solvers are domain decomposed using PETSc [*Balay, et al.* (2013)]. FPIC is MPI decomposed in 3D using the PETSc DM<sub>DA</sub> object for simplicity, and the particle set is also 3D decomposed onto the same subdomains, with explicit MPI particle passing used to keep particles on the right MPI rank as they cross subdomain boundaries. Load balancing is complicated somewhat because the field solver and the particle push have different optimal domain layouts. This is because the FRC separatrix radius is typically half of the wall radius, so the simulation domain includes a significant volume of low–particle density, typically at least 75% of the volume. Therefore, FPIC uses the particle distribution as the load balance weighting function.

In the ANC case, The Poisson solver is domain decomposed in the  $R$ – $Z$ –plane and spectrally decomposed in the azimuthal coordinate. After decomposing the 3D field into azimuthal harmonics, each harmonic is given its own PETSc solver, which has been pre–initialized before entering the main time–step loop. Particles are group decomposed using MPI, and each MPI process corresponding to a particle group receives a copy of the entire field after the Poisson solve. This does

not scale indefinitely with grid size, but is very efficient for problem sizes where the field grid fits in memory. Particle domain decomposition will be implemented in ANC for grid sizes above a threshold determined by the architecture memory.

Using the above inter-node parallelism methods, one or more subdomains may be allocated to a single node. Thus a combination of distributed memory and shared memory parallelism can be used for intra-node parallelism. On Theta, both codes use OpenMP to thread the particle push on each MPI subdomain. For FPIC, this approach was developed during an ALCF Director’s Discretion allocation on Theta, and was found to scale linearly to 64 cores of one node of Theta. See Sec. 3.3 for details.

Field output is performed in parallel using the PETSc HDF5 VecView methods with Vizschema attributes added to enable 3D visualization of staggered Yee mesh quantities in VisIt [*Childs, et al. (2012)*]. For code restart/checkpointing, particle output is performed by direct Parallel HDF5 calls.

ANC’s parallelization strategy is largely inherited from GTC, and as such is adaptable to many state of the art parallelization techniques. It will continue to leverage parallelism advances in GTC, including CUDA/OpenACC, and work collaboratively with the GTC team to develop exascale strategies.

## Visualization and Analysis

Interactive 3D VisIt visualization is helpful, but for efficient work flow, it is crucial to have batch job visualization methods. Our post-processing work-flow tools include automated python scripts that enable batch job 3D VisIt visualization. Another python based batch job visualization tool takes a mid-plane slice along each axis for all datasets in the output data file. We also have batch scripts for extracting “virtual diagnostics” from FPIC’s datasets for apples-to-apples comparison to experimental results.

Because FPIC is 3D and generates a vast amount of data, it is extremely important to find ways to reduce the dimensionality of the data for analysis. One way to do this is through mode analysis, which reduces the 3D data to OD mode amplitudes, from which we compute real frequency and growth rates of instabilities such as internal tilt, radial shift, ballooning, interchange and rotational modes. An example is in Figure 6 below where the growth rate of the tilt mode can be derived from the velocity antisymmetry  $v_z^+(r, z) = v_z(r, z) + v_z(r, -z)$ . Reduction of the 3D data to 2D and 1D is possible also. To do this, a field line tracing code which is used to calculate the connection length (from wall to wall) of the field line passing through every point. Iso-surfaces of connection length then provide an approximation to flux surfaces. This is similar to methods used for separatrix identification [*Albanese, et al. (2015)*] in tokamak simulation. The resulting ability to convert some 3D scalar fields, such as density, into approximate 2D and 1D profiles greatly facilitates the comparison of results with theory and allows buildup of intuition. A visualization of the connection length iso-surfaces is shown in Figure 6.

## Parallel Performance

Once the physics parameters for a simulation have been selected, the characteristic length scales such as ion inertial length (FPIC) or electron gyroradius (ANC) set the upper limit on cell size, determining the number of cells. The characteristic times scales such as Alfvén frequency (FPIC) or ion gyrofrequency (ANC) then determine the upper limit on timestep. The goal then is to execute the fixed size simulation as quickly as possible, so strong scaling studies are favored. We demonstrate that FPIC and ANC are computationally ready for Theta, with strong scalings for representative problem sizes showing near ideal performance up to 512 nodes for FPIC, and 2048 nodes for ANC, i.e. 15–30% of the size of Theta.

Other scaling studies (not shown here) show that the point at which the total wall time saturates is determined by the number of cells. This field-solver saturation will not be a bottleneck in the context of TAE’s strategic plans, because we plan higher magnetic fields and densities in larger machines. The ion inertial length in prototype reactor conditions is about 4 times smaller than C-2W, meaning that the maximum cell size is about 43 times smaller, and the volume of the domain is at least 10 times bigger, meaning that there would be 640 times as many cells. In such conditions the field solver will most likely saturate at much higher node count.

### 9.33.2 Developmental Work

In preparation for this INCITE application, a Director’s Discretion grant on Theta was obtained. Using this resource, the OpenMP intra-node particle parallelism methodology of ANC and GTC was also integrated into FPIC, leading to the strong scaling shown in Figure 8. For both codes we intend to see if we can use OpenMP to accelerate local loops of the field solvers, to improve overall performance. In the FPIC case, saturation in the strong scaling is caused by saturation in the field solver, so threading the field solver could make a big difference.

Experiments are planned to study the efficient use of memory layout and vectorization in both codes:

Particle sort to avoid cache thrashing [*Bowers (2001)*]

Analysis with Vector Advisor of memory alignment/High Bandwidth Memory (HBWM)

Use of OpenMP SIMD pragmas

Use of HBW API, e.g `std::vector<T, hbw::allocator>::allocatei`

We will explore these computational improvements during the remainder of our existing Theta Director’s Discretion award, and throughout the INCITE project. Intra-node optimization studies will not require significant computational resources because the development and early testing of the methods can be performed with single node runs. Validation of these strictly computational changes will be performed by performance benchmarking and regression testing against well studied simulations.

### 9.33.3 Development plan for next-generation systems

Because ANC is closely related to GTC, it will be able to leverage many of the computer science advances that are being developed in the CAAR program and the SummitDev preparations for Summit. ANC's development for next generation systems will largely rest on top of these very significant public investments in GTC development. FPIC parallelization plans for next generation systems include improving load balance by replacing the PETSc DM<sub>D</sub>A representation with a more general decomposition based on the PETSc Index Set (IS) and Application Ordering (AO) concepts. Both codes will experiment with porting the OpenMP methods developed on KNL to OpenACC methods for deployment on GPU, for next generation systems that use accelerators. I/O performance could be a significant limiting factor for both codes on next generation systems, so we are exploring the possibility of leveraging recent ASCR funded advances in in-situ visualization such as the SENSEI project [Ayachit, *et al.* (2016)]. This is part of our recent SciDAC proposal, in collaboration with LBNL Data Analytics and Visualization Group, and we are continuing to look for ways to find support for this effort with our LBNL colleagues.

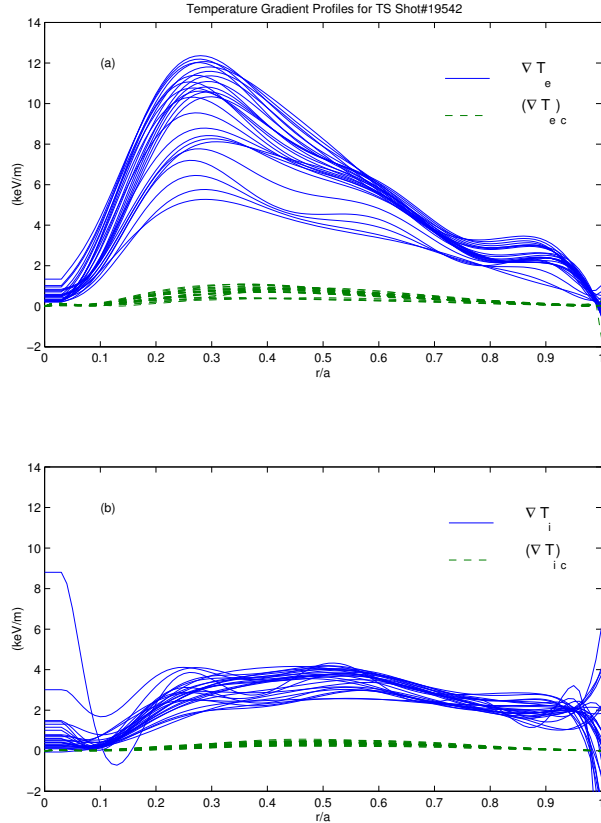


Figure 9.7: (a) The gradient of the electron temperature compared with critical gradient  $(\nabla T_e)_c = -1.88(|s|T_e/qR)(1 + T_e/T_i)$ . (b) The gradient of the ion temperature compared with critical gradient  $(\nabla T_i)_c = -1.7(|s|T_i/qR)(1 + T_i/T_e)$  for ITG modes. All the profiles are for  $t = 5$  s to  $6.35$  s in Tore Supra shot #19542. [Reprinted with permission from Horton, et al. (2002), Copyright 2002, American Institute of Physics.]

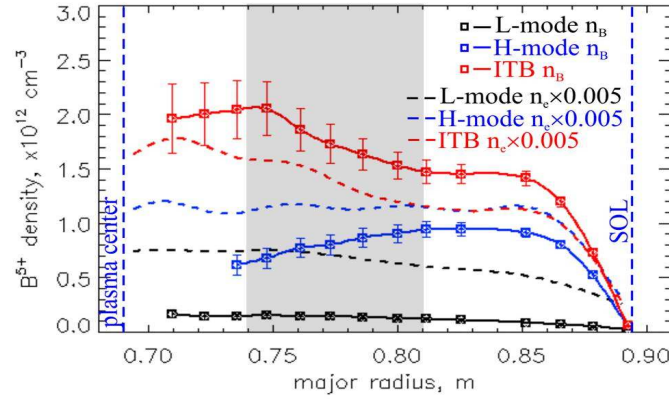


Figure 9.23: Boron n and T profiles from CXRS on DNB. Fully stripped boron ion,  $B^{5+}$  is the only boron ion present for  $R < 0.5 \text{ m}$ .

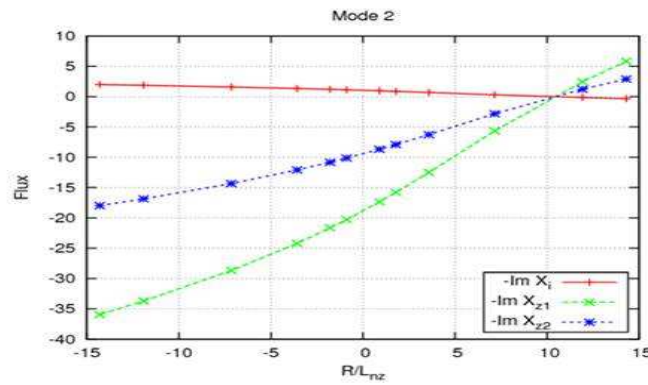


Figure 9.27: D and V Formulas from Fluxes.

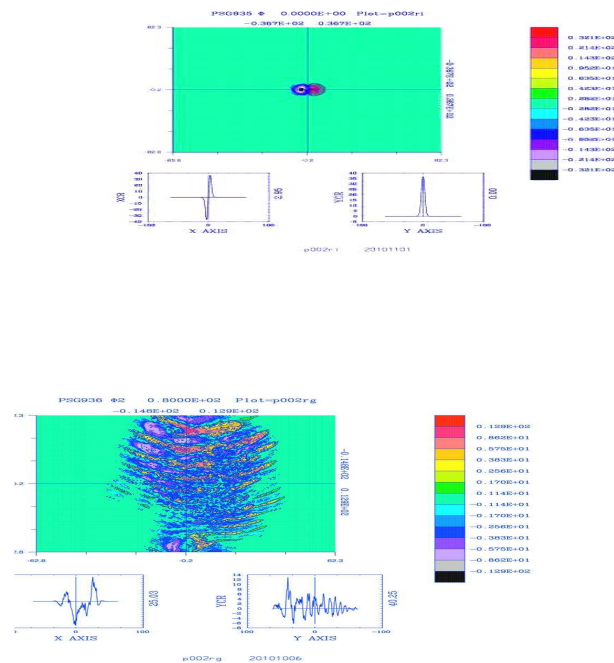


Figure 9.30: Turbulent Simulation for Spread of Impurities. Simulations from small injected “spot” of impurities as in pellets.

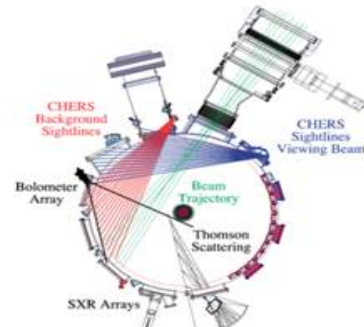
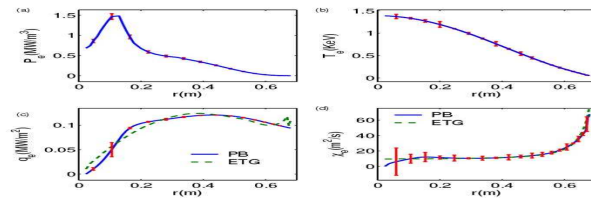


Fig. 2

Figure 9.33: a) 106194 discharge from *Le Blanc, et al. Nucl. Fusion* (2004) and *Horton, et al. Nucl. Fusion* (2005). b) RF heating is up to an order of magnitude larger than the Ohmic heating. The plasma current is essential to the confinement properties.

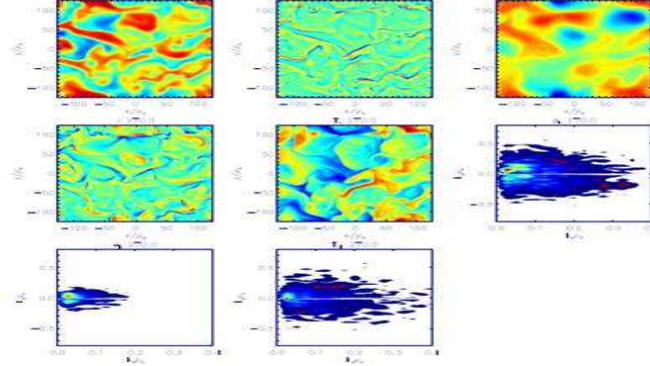


Figure 9.34: Shows formation of streamers both in the flow field and in the perpendicular magnetic field. Multi-scale turbulence with intermittency in the turbulent heat flux  $q_e(t)$ . Thermal diffusivity reaches 50 to 60 times the electron-gyroBohm level. Box size is  $3\rho_i \times 3\rho_i (\sim 126\rho_e)$  time scale  $500 L_{T_e} / V_e \sim 100\mu\text{s}$  (Mazzucato, et al. PoP, 2009 and PRL 101, 075001, 2008).

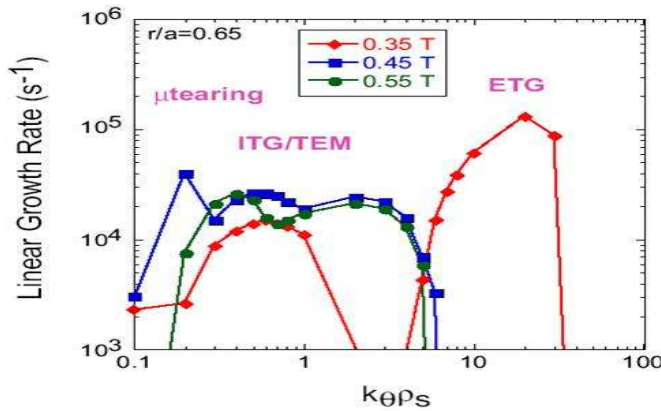


Figure 9.35: ETG linearly unstable only at lowest  $B_T$ .  $-0.35\text{ T}$  :  $R/L_{T_e}$  20% above critical gradient.  $-0.45, 0.55\text{ T}$ :  $R/L_{T_e}$  20–30% below critical gradient.

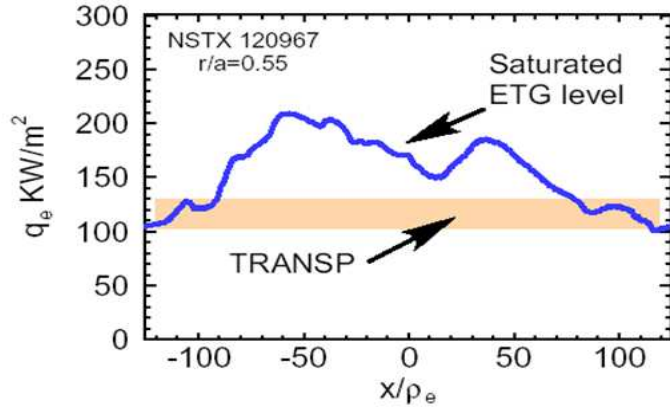


Figure 9.37: Spectral densities of  $\langle \delta n_e \delta n_e \rangle$  and the radial heat flux from  $\langle v_x \delta T_e \rangle \sim \text{Re}[ik_y \varphi(k) * \delta T_e(k)]/B$ .

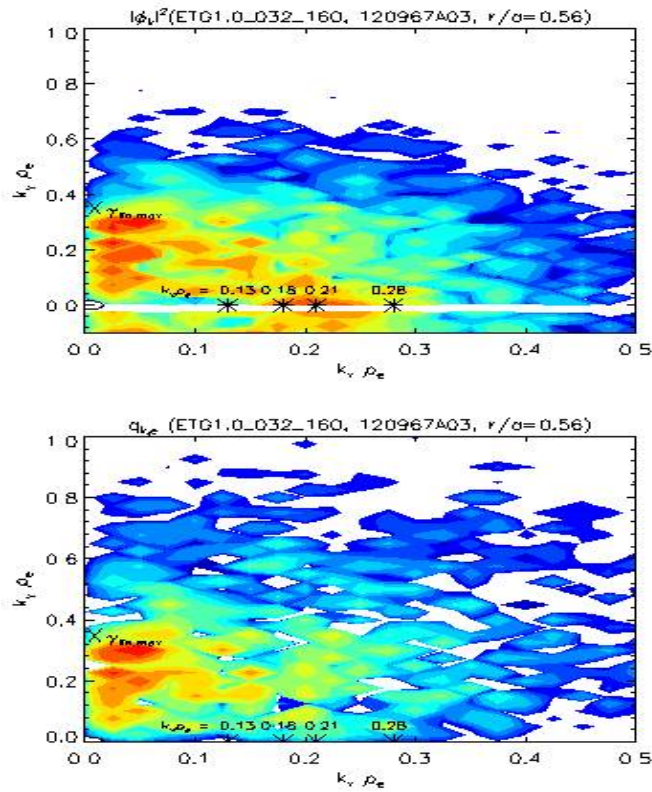


Figure 9.38: NSTX scattering data from H. Park in S. Kaye, et al. Chengdu IAEA, NF.

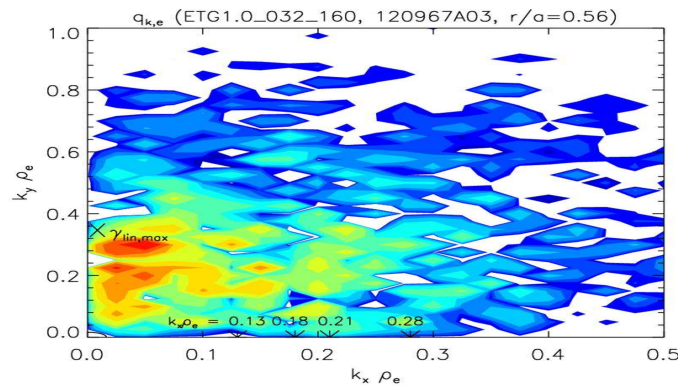


Figure 9.39: Diffusivity from Heat Flux  $q$  divided by local temperature gradient.

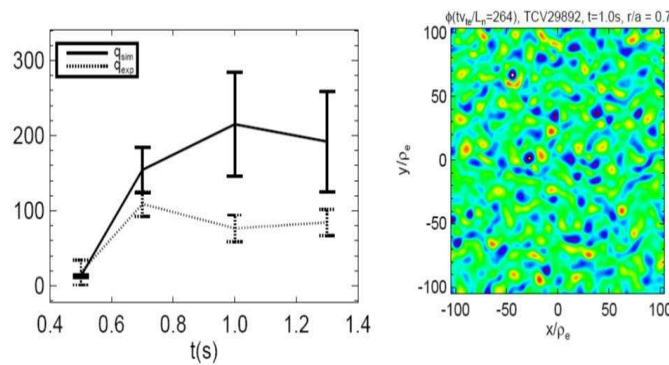


Figure 9.40:  $\chi_e$  from Modulated ECH in Frascati Tokamak FTU Analysis supports ETG transport.

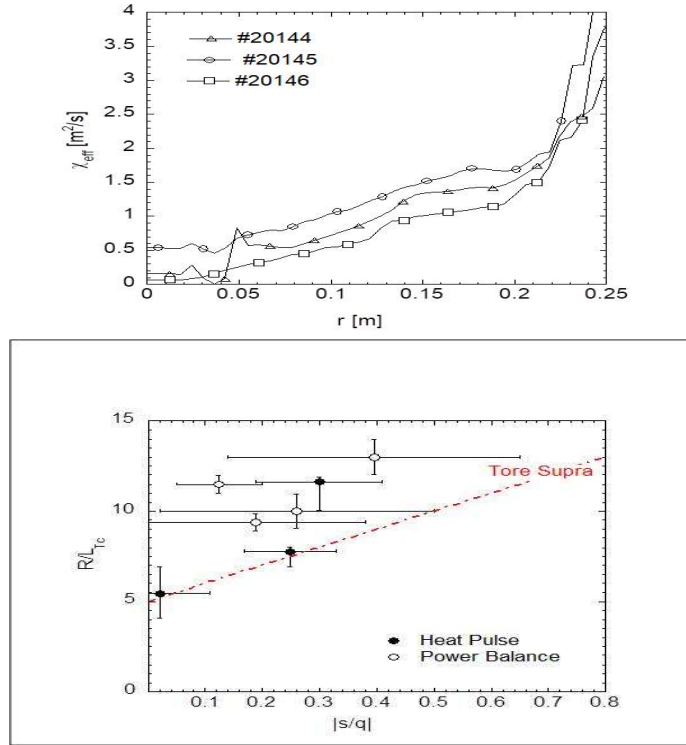


Figure 9.41: Reduction of fluctuation is well correlated with improved confinement. High- $k$  scattering shows significant level of turbulence that remains without ITG turbulence.

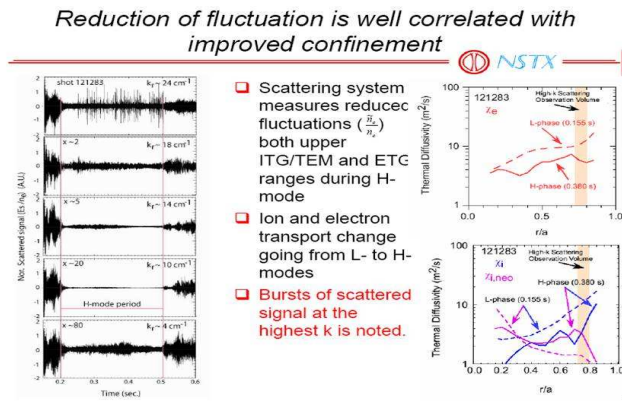


Figure 9.42: Record shot with D-D with equivalent  $Q$  for  $-T$  (factor 220 in n/s) of  $Q_{\text{fusion}}^{\text{eq}} \sim 1$ . Reversed magnetic shear [Ishida, et al., PRL 1997] and Fujita, et al. Nucl. Fusion, 1999.]

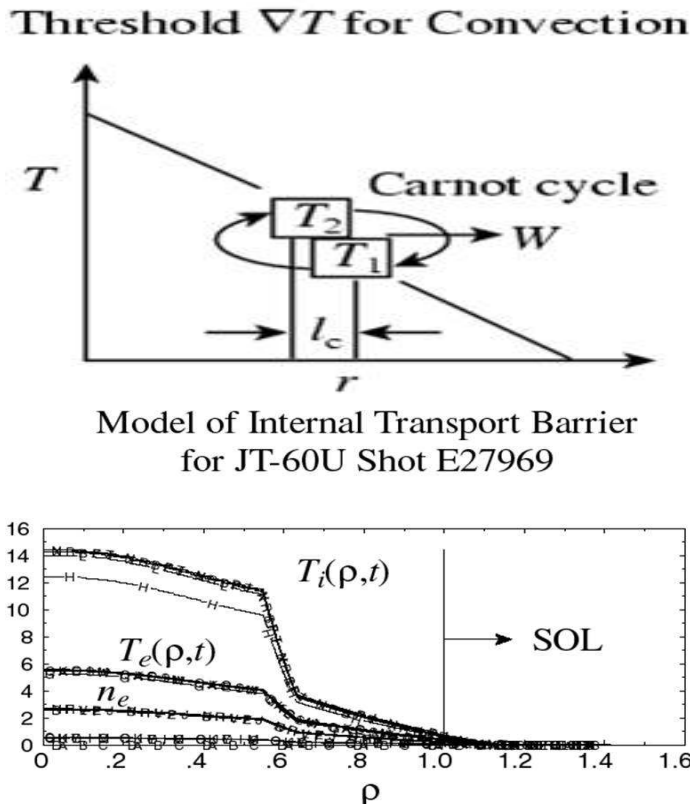


Figure 9.43: Boundaries of collisional and turbulent diffusivities.

# Bibliography

- [1] Akasofu, S.-I. (1964). The development of the auroral substorm, *Planet. Space Sci.* **12**, pp. 273–282, [https://doi.org/10.1016/0032-0633\(64\)90151-5](https://doi.org/10.1016/0032-0633(64)90151-5).
- [2] Albanese, R., De Magistris, M., Fresa, R., Maviglia, F. and Minucci, S. (2015). Accuracy assessment of numerical tracing of three-dimensional magnetic field lines in tokamaks with analytical invariants, *Fusion Sci. Tech.* **68**, pp. 741–749, <https://doi.org/10.13182/FST15-127>.
- [3] Angelopoulos, V., McFadden, J. P., Larson, D., Carlson, C. W., Mende, S. B., Frey, H., Phan, T., Sibeck, D. G., Glassmeier, K-H., Auster, U., Donovan, E., Mann, I. R., Rae, J., Russell, C. T., Runov, A., Zhou, X-Z. and Kepko, L. (2008a). Tail Reconnection triggering substorm Onset, *Science* **321**, pp. 931–935, <https://doi.org/10.1126/science.1160495>.
- [4] Angelopoulos, V., Sibeck, D. G., Carlson, C. W., McFadden, J. P., Larson, D., Lin, R. P., Bonnell, J. W., Mozer, F. S., Ergun, R., Cully, C., Glassmeier, K-H., Auster, U., Roux, A., LeContel, O., Frey, S., Phan, T., Mende, Frey, H., Donovan, E., Russell, C. T., Strangeway, R., Liu, J., Mann, I. R., Rae, J., Raeder, J., Li, X., Liu, W., Singer, H. J., Sergeev, V. A., Apatenkov, S., Parks, G. Fillingim, M., Sigwarth, J. (2008b). First Results from the THEMIS Mission, *Space Sci. Rev.* **141**, pp. 453–476, <https://doi.org/10.1007/s11214-008-9378-4>.
- [5] Antipov, S. V., Nezlin, M. V., Snezhkin, E. N. and Trubnikov, A. S. (1982). Rossby soliton in the laboratory, *Sov. Phys. JETP* **55**, p. 85, <https://ui.adsabs.harvard.edu/#abs/1982ZhETF..82..145A/abstract>.
- [6] Antipov, S. V. Nezlin, M. V., Snezhkin, E. N. and Trubnikov, A. S. (1985). Rossby autosoliton and laboratory model of Jupiter's Great Red Spot, *Soviet Physics JETP* **62**, p. 1097, .
- [7] Antonova, R. A. (1983). Drift solitons in a shallow rotating fluid, *JETP Lett.* **37**, p. 651, <https://ui.adsabs.harvard.edu/abs/1983ZhPmR..37..545A/abstract>.
- [8] Ayachit, U., Whitlock, B., Wolf, M., Loring, B., Geveci, B., Lonie, D. and Bethel, E. Wes (2016). The SENSEI generic in situ interface, 2016 Second Workshop on In Situ Infrastructures for Enabling Extreme-Scale Analysis and Visualization (ISAV), 13 Nov. 2016, Salt Lake City, UT, USA, <https://doi.org/10.1109/ISAV.2016.013>.
- [9] Balay, S., Brown, J., Buschelman, K., Eijkhout, V. *et al.* (2013). PETSc Users Manual.

- [10] Balescu, R. (1988). *Transport Processes in Plasmas* (North–Holland–Amsterdam), Vols. 1–2.
- [11] Barnes, D. C. and Milroy, R. D. (1991). Stabilization of the field-reversed configuration (FRC) tilt instability with energetic ion beams, *Phys. Fluids B: Plasma Phys.* **3**, p. 2609, <https://doi.org/10.1063/1.859973>.
- [12] Baylor, L. R., Commaux, N., Jernigan, T. C., Brooks, N. H., Combs, S. K., Evans, T. E., Fenstermacher, M. E., Isler, R. C., Lasnier, C. J., Meitner, S. J., Moyer, R. A., Osborne, T. H., Parks, P. B., Snyder, P. B., Strait, E. J., Unterberg, E. A. and Loarte, A. (2013). Reduction of edge-localized mode intensity using high-repetition rate-pellet injection in tokamak H-mode plasmas, *Phys. Rev. Lett.* **110**, p. 245001, <https://doi.org/10.1103/PhysRevLett.110.245001>.
- [13] Belova, E. V., Jardin, S., Ji, H., Yamada, M. and Kulsrud, R. (2001). Numerical study of global stability of oblate field-reversed configurations, *Phys. Plasmas* **8**, p. 1267, <https://doi.org/10.1063/1.1355027>.
- [14] Belova, E. V., Davidson, R. C., Ji, H. and Yamada, M. (2003). Kinetic effects on the stability properties of field-reversed configurations. I. Linear Stability, *Phys. Plasmas* **10**, p. 2361, <https://doi.org/10.1063/1.1568118>.
- [15] Belova, E. V., Davidson, R. C., Ji, H. and Yamada, M. (2004). Kinetic effects on the stability properties of field-reversed configurations. II. Nonlinear evolution, *Phys. Plasmas* **11**, pp. 2523–2531, <https://doi.org/10.1063/1.1666293>.
- [16] Belova, E. V., (2015). Beam ion effects on FRC stability, 57th Annual Meeting of the APS Division of Plasma Physics, November 16–20, 2015, Savannah, Georgia, <http://meetings.aps.org/link/BAPS.2015.DPP.BP12.9>.
- [17] Binderbauer, M. W., Tajima, T., Steinhauer, L. C., Garate, E., Tuszewski, M., Schmitz, L., Guo, H. Y., Smirnov, A., Gota, H., Barnes, D., Deng, B. H., Thompson, M. C., Trask, E., Yang, X., Putvinski, S., Rostoker, N., Andow, R., Aefsky, S., Bolte, N., Bui, D. Q., Ceccherini, F., Clary, R., Cheung, A. H., Conroy, K. D., Detrick, S. A., Douglass, J. D., Feng, P., Galeotti, L., Giannanco, F., Granstedt, E., Gupta, D., Gupta, S., Ivanov, A. A., Kinley, J. S., Knapp, K., Korepanov, S., Hollins, M., Magee, R., Mendoza, R., Mok, Y., Necas, A., Primavera, S., Onofri, M., Osin, D., Rath, N., Roche, T., Romero, J., Schroeder, H., Sevier, L., Sibley, A., Song, Y., Van Drie, A. D., Walters, J. K., Waggoner, W., Yushmanov, P., Zhai, K., and the TAE Team (2015). A high-performance field-reversed configuration, *Phys. Plasmas* **22**, p. 056110, <http://dx.doi.org/10.1063/1.4920950>.
- [18] Birdsall, C. K. and Langdon, A. B. (2004). *Series in Plasma Physics* (Taylor and Francis Group), ISBN:9780750310253.
- [19] Biskamp, D., Camaargo, S. J. and Scott, B. D. (1994). Spectral properties and statistics of resistive drift-wave turbulence, *Phys. Lett. A*, **186**, p. 239, [https://doi.org/10.1016/0375-9601\(94\)90346-8](https://doi.org/10.1016/0375-9601(94)90346-8).

- [20] Biskamp, D., Schwarz, E. and Drake, J. F. (1997). Two-fluid theory of collisionless magnetic reconnection, *Phys. Plasmas* **4**, p. 1002, <https://doi.org/10.1063/1.872211>.
- [21] Bowers, K. J. (2001). Accelerating a particle-in-cell simulation using a hybrid counting sort, *J. Comput. Phys.* **173**, pp. 393–411, <https://doi.org/10.1006/jcph.2001.6851>.
- [22] Burlaga, L. F., Ness, N. F., Berdichevsky, D. B., Park, J., Jian, L. K., Szabo, A., Stone, E. D. and Richardson, J. D. (2019). Magnetic field and particle measurements made by Voyager 2 at and near the heliopause, *Nature Astron.* **3**, pp. 1007–1012, <https://doi.org/10.1038/s41550-019-0920-y>.
- [23] Burch, J. L. and Angelopoulos, V. (2008). The THEMIS mission, *Space Sci. Rev.* **141**, pp. 1–583, <https://doi.org/10.1007/s11214-008-9474-5>.
- [24] Burrell, K. H. (1997). Effects of  $\mathbf{E} \times \mathbf{B}$  velocity shear and magnetic shear on turbulence and transport in magnetic confinement devices *Phys. Plasmas* **4**, p. 1499, <http://dx.doi.org/10.1063/1.872367>.
- [25] Caldas, I. L., Marcus, F. A., Batista, A. M., Viana, R. L., Lopes, S. R., Heller, M. V. A. P., Guimarães–Filho, Morrison, P. J. and Horton, W. (2006). Turbulence induced transport in tokamaks, *AIP Conf. Proceedings* **875**, p. 341, <https://doi.org/10.1063/1.2405962>.
- [26] Carreras, B. A., Garcia, L. and Diamond, P. H. (1987). Theory of resistive pressure-gradient–driven turbulence, *Phys. Fluids* **30**, p. 1388, <http://dx.doi.org/10.1063/1.866518>.
- [27] Ceccherini, F., Detrick, S., Barnes, D., Galeotti, L. and TAE Team (2016). FPIC Study of the  $n = 1$  Toroidal Mode in FRC Plasmas, 58th Annual Meeting of the APS Division of Plasma Physics, Vol. 61, Number 18, October 31–November 4 2016; San Jose, California, <http://meetings.aps.org/link/BAPS.2016.DPP.CP10.87>.
- [28] Chang, C. S. and Ku, S. (2008). Spontaneous rotation sources in a quiescent tokamak edge plasma, *Phys. Plasmas* **15**, p. 062510, <https://doi.org/10.1063/1.2937116>.
- [29] Chen, F. F. (1965a). Resistive over-stabilities and anomalous diffusion, *Phys. Fluids* **8**, p. 912, <http://dx.doi.org/10.1063/1.1761335>.
- [30] Chen, F. F. (1965b). Excitation of drift instabilities in thermionic plasmas, *J. Nucl. Energy Pt. C*, **7**, p. 399, <https://doi.org/10.1088/0368-3281/7/4/305>.
- [31] Chen, F. F. (1965c). Effects of sheaths on drift instabilities in thermionic plasmas, *Phys. Fluids* **8**, p. 752, <https://doi.org/10.1063/1.1761294>.
- [32] Chen, L. and Cheng, C. Z. (1980). Drift-wave eigenmodes in toroidal plasmas, *Phys. Fluids* **23**, p. 2242, <https://doi.org/10.1063/1.862907>.

- [33] Chen, J. and Sen, A. K. (1995). Experimental study of a mixed slab and toroidal ion-temperature-gradient mode, *Phys. Plasmas* **2**, p. 3063, <https://doi.org/10.1063/1.871204>.
- [34] Chen, L. and Zonca, F. (2019). Self-consistent kinetic theory with nonlinear wave-particle resonances, *Plasma Sci. Technol.* **21**, p. 125101, <https://doi.org/10.1088/2058-6272/ab3dce>.
- [35] Chen, J., Yuan, C., Sun, X. and Huo, L. (2019). Transmissivity of electromagnetic wave propagating in magnetized plasma sheath using variational method, *Plasma Sci. Technol.* **21**, p. 125001, <https://doi.org/10.1088/2058-6272/ab4199>.
- [36] Childs, H., Brugger, E., Whitlock, B. Meredith, J., Ahern, S., Pugmire, D., Biagas, K., Miller, M., Harrison, C., Weber, G. H., Krishnan, H., Fogal, T., Sanderson, A., Garth, C., Bethel, E. W., Camp, D., Rübel, O., Durant, M., Favre, J. and Navratil, P. (2012). VisIt: An End-User Tool for Visualizing and Analyzing Very Large Data, Lawrence Berkeley National Laboratory, <https://escholarship.org/uc/item/69r5m58v>.
- [37] Colas, L., Zou, X. L., Paume, M., Chareau, J., Guiziou, L., Hoang, G. T., Michelot, Y. and Grésillon, D. (1998). Internal magnetic fluctuations and electron heat transport in the Tora Supra Tokamak: Observation by cross-polarization scattering, *Nuclear Fusion* **38**, pp. 903–918, <http://dx.doi.org/10.1088/0029-5515/38/6/308>.
- [38] Connor, J. W. (1993). Pressure gradient turbulent transport and collisionless reconnection, *Plasma Phys. Control. Fusion* **35**, pp. 757–763, <http://dx.doi.org/10.1088/0741-3335/35/6/009>.
- [39] Coppi, B., Laval, G. and Pellat, R. (1966). Dynamics of the geomagnetic tail, *Phys. Rev. Lett.* **16**, p. 1207, <https://doi.org/10.1103/PhysRevLett.16.1207>.
- [40] De Zeeuw, D. L., Sazykin, S., Wolf, R. A., Gombosi, T. I., Ridley, A. J. and Toth, G. (2004). Coupling of a global MHD code and an inner magnetospheric model: Initial results. *J. Geophys. Res.* p. 109, <https://doi.org/10.1029/2003JA010366>.
- [41] Derr, J., Horton, W. and Wolf, R. (2019). Shear flow-interchange instability in nightside magnetotail causes auroral beads as a signature of substorm onset, *Plasma Phys.: Space Phys.*, <https://arxiv.org/abs/1904.11056v1>.
- [42] Dessler, A. J. (1983). *Physics of the Jovian Magnetosphere* (Cambridge Planetary Science Old). (Cambridge and New York, Cambridge University Press, 1983), pp. 498–504 , <https://doi.org/10.1017/CBO9780511564574>
- [43] Devynck, P., Garbet, X., Laron, C., Payan, J., Saha, S. K., Gervais, F., Hennequin, P., Quemeneur, A. and Truc, A. (1993). Localized measurements of turbulence in the TORE SUPRA tokamak *Plasma Phys. Control. Fusion* **35**, p. 63, <https://doi.org/10.1088/0741-3335/35/1/005>.

- [44] Dey, S. and Mittra, R. (1997). locally conformal finite-difference time-domain (FDTD) algorithm for modeling three-dimensional perfectly conducting objects, *IEEE Microwave and Guided Wave Lett.* **7**, pp. 273–275, <https://doi.org/10.1109/75.622536>.
- [45] Detrick, S., Barnes, D., Ceccherini, F., Galeotti, L., Guerrero, V., Hendrix, D., Hubbard, K., Milroy, R., Necas, A. and TAE Team (2015). FPIC: A Key Next Step for Stability Studies of Advanced Beam Driven FRCs, 57th Annual Meeting of the APS Division of Plasma Physics. Vol. 60, Number 19, November 16–20, 2015, Savannah, Georgia, <http://meetings.aps.org/link/BAPS.2015.DPP.BP12.31>.
- [46] Dimits, A. M., Bateman, G., Beer, M. A., Cohen, B. I., Dorland, W., Hammett, G. W., Kim, C., Kinsey, J. E., Kotschenreuther, M., Kritz, A. H., Lao, L. L. Andrekas, J. M., Nevins, W. M., Parker, S. E., Redd, A. J., Shumaker, D. E., Sydora, R., and Weiland, J. (2000). Comparisons and physics basis of tokamak transport models and turbulence simulations *Phys. Plasmas* **7**, pp. 969–983, <https://doi.org/10.1063/1.873896>.
- [47] Dong, J-Q., Mahajan, S. M. and Horton, W. (1997) Coupling of  $\eta_i$  and trapped electron modes in plasmas with negative magnetic shear, *Phys. Plasmas* **4** 755, <https://doi.org/10.1063/1.872169>.
- [48] Dong, J-Q., Horton, W., Bengtson, Roger D. and Li, G. X. (1998). Momentum-energy transport from turbulence driven by parallel flow shear, *Phys. Plasmas* **1**, p. 3250, <https://doi.org/10.1063/1.870477>.
- [49] Dong, J-Q., Sanuki, H., Itoh, K. and Chen, L. (2002). Electron temperature gradient instability in toroidal plasmas, *Phys. Plasmas* **9**, p. 4699, <https://doi.org/10.1063/1.1515275>.
- [50] Dong, J-Q., Jian, G. D., Wang, A. K., Sanuki, H. and Itoh, K. (2002b). Instability and Transport Driven by Electron Temperature Gradient Close to Critical, 19th IAEA Fusion Energy Conference, (Lyon, France, October 2002), IAEA-CN-94/TH/1–6.
- [51] Dongarra, J. (2013). International HPC Forum (IHPCF), Changsha, China, May 28–29, 2013.
- [52] Donovan, E., Liu, W., Liang, J., Spanswick, E., Voronkov, I., Connors, M., Syrjäsuo, M., Baker, G., Jackel, B., Trondsen, T., Greffen, M., Angelopoulos, V., Russell, C. T., Mende, S. B., Frey, H. U., Keiling, A., Carlson, C. W., McFadden, J. P., Glassmeier, K-H., Auster, U., Hayashi, K., Sakaguchi, K., Shiokawa, K., Wild, J. A. and Rae, I. J. (2008). Simultaneous THEMIS in situ and auroral observations of a small substorm. *Geophys. Res. Lett.* **35**, p. L17S18, <https://doi.org/10.1029/2008GL033794>.
- [53] Dorland, W., Jenko F., Kotschenreuther, M. and Rogers, B. N. (2000) .*Phys. Rev. Lett.* **85** p. 5579, <https://doi.org/10.1103/PhysRevLett.85.5579>.

- [54] Doyle, E. J., Groebner, R. J., Burrell, K. H., Gohil, P., Lehecka, T., Luhmann, Jr., N. C., Matsumoto, H., Osborne, T. H., Peebles, W. A. and Philipona, R. (1991). Modifications in turbulence and edge electric fields at the L–H transition in the DIII–D tokamak, *Phys. Fluids B* **3**, pp 2300–2307, <https://doi.org/10.1063/1.859597>.
- [55] Durst, R. D., Fonck, R. J., Kim, J. S., Paul, S. F., Bretz, N., Bush, C., Chang, Z. and Hulse, R., (1993). Observation of a localized transition from edge to core density turbulence in the TFTR tokamak, *Phys. Rev. Lett.* **71**, pp. 3135–3138, <https://doi.org/10.1103/PhysRevLett.71.3135>.
- [56] Erba, M., Parail, V., Springmann, E. and Taroni, A. (1995). Extension of a Bohm model for L-mode electron heat transport to ion heat transport and to the ohmic regime, *Plasma Phys. Control. Fusion* **37**, p. 1249, <https://doi.org/10.1088/0741-3335/37/11/005>.
- [57] Erba, M., Aniel, T., Basiuk, V., Becoulet, A. and Litaudon, X. (1998). Validation of a new mixed Bohm/gyroBohm model for electron and ion heat transport against the ITER, Tore Supra and START database discharges, *Nucl. Fusion* **38**, p. 1013, <http://dx.doi.org/10.1088/0029-5515/38/7/305>.
- [58] Erba, M., Horton, W. and Ottaviani, M. (1999). Predictive tests of ITG based models of tokamak heat transport on ITER database discharges, *Nucl. Fusion* **39**, p. 495, <http://dx.doi.org/10.1088/0029-5515/39/4/307>.
- [59] Esirkepov, T. Zh. (2001). Exact charge conservation scheme for particle-in-cell simulation with an arbitrary form-factor, *Comp. Phys. Comm.* **135**, pp. 144–153, [https://doi.org/10.1016/S0010-4655\(00\)00228-9](https://doi.org/10.1016/S0010-4655(00)00228-9).
- [60] Forsyth, C., Watt, C. E. J., Rae, I. J., Fazakerley, A. N., Kalmoni, N. M. E., Freeman, M. P., Boakes, P. D., Nakamura, R., Dandouras, I., Kistler, L. M., Jackman, C. M., Coxon, J. C. and Carr, C. M. (2014). Increases in plasma sheet temperature with solar wind driving during substorm growth phases, *Geophys. Res. Lett.* **41**, pp. 8713–8721, <https://doi.org/10.1002/2014GL062400>.
- [61] Friedrich, E., Samson, J. C. and Voronkov, I. (2001). Ground-based observations and plasma instabilities in auroral substorms. *Phys. Plasmas* **8**, pp. 1104–1110, <https://doi.org/10.1063/1.1355678>.
- [62] Fu, X. R., Horton, W., Xiao, Y., Lin, Z., Sen, A. K. and Sokolov, V. (2012). Validation of electron temperature gradient turbulence in the Columbia Linear Machine, *Phys. Plasmas* **19**, p. 032303, <https://doi.org/10.1063/1.3686148>.
- [63] Fukuyama, K., Itoh, S-I., Itoh, M., Yagi, M. and Azumi, M. (1994). Theory of improved confinement in high- $\beta_p$  tokamaks, *Plasma Phys. Control. Fusion* **36**, p. 1385, <https://doi.org/10.1088/0741-3335/36/9/001>.

- [64] Fujita, T., Kamada, Y., Ishida, S., Neyatani, Y., Oikawa, T., Ide, S., Takeji, S., Koide, Y., Isayama, A., Fukuda, T., Hatae, T., Ishii, Y., Ozeki, T., Shirai, H. and JT-60 Team. (1999). High performance experiments in JT-60U reversed shear discharges, *Nucl. Fusion* **39**, p. 1627, <http://iopscience.iop.org/0029-5515/39/11Y/302>.
- [65] Fulton, D. P., Lau, C. K., Schmitz, L., Holod, I., Lin, Z., Tajima, T., Binderbauer, M.W. and TAE Team. (2016). Gyrokinetic simulation of drift wave instability in field-reversed configuration, *Phys. Plasmas* **23**, p. 056111, <https://doi.org/10.1063/1.4948285>.
- [66] Furnish, G., Horton, W., Kishimoto, Y., LeBrun, M. J. and Tajima, T. (1999) Global gyrokinetic simulation of tokamak transport *Phys. Plasmas* **6**, p. 1227, <https://doi.org/10.1063/1.873366>.
- [67] Futatani, S., Horton, W., Benkadda, S., Bespamyatnov, I. O. and Rowan, W. L. (2010). Fluid models of impurity transport via drift wave turbulence, *Phys. Plasmas* **17**, p. 072512, <http://dx.doi.org/10.1063/1.3459062>.
- [68] Futatani, S., Huijsmans, G., Loarte, A., Baylor, L. R., Commaux, N., Jernigan, T. C., Fenstermacher, M. E., Lasnier, C., Osborne, T. H. and Pegourié, B. (2014). Nonlinear MHD modeling of ELM triggering by pellet injection in DIII-D and implications for ITER, *Nucl. Fusion* **54**, p. 073008, <https://doi.org/10.1088/0029-5515/54/7/073008>.
- [69] Futatani, S., Huijsmans, G. T. A., Loarte, A., Mantsinen, M., Pamela, S., Garzotti, L., Hoelzl, M., Lang, P. T. and Orain, F. (2017). Nonlinear MHD Simulations of Pellet-Triggered ELM for ITER Plasma Scenarios. In 44th EPS Conference on Plasma Physics. Geneva: European Physical Society, <http://hdl.handle.net/21.11116/0000-0000-B2B2-D>.
- [70] Gal, K., Belonohy, E., Kocsis, G., Lang, P. T., Veres, G. and the ASDEX Upgrade Team. (2008). Role of shielding in modeling cryogenic deuterium pellet ablation, *Nucl. Fusion* **48**, p. 085005, <https://doi.org/10.1088/0029-5515/48/8/085005>.
- [71] Galeotti, L., Barnes, D., Ceccherini, F. and Pegoraro, F. (2011). Plasma equilibria with multiple ion species: Equations and algorithm, *Phys. Plasmas* **18**, p. 082509, <https://doi.org/10.1063/1.3625275>.
- [72] Gallardo-Lacourt, B., Nishimura, Y., Lyons, L. R., Ruohoniemi, J. M., Donovan, E., Angelopoulos, V., McWilliams, K. A. and Nishitani, N. (2014). Ionospheric flow structures associated with auroral beading at substorm auroral onset, *J. Geophys. Res.: Space Physics* **119**, pp. 9150–9159, <https://doi.org/10.1002/2014JA020298>.
- [73] Gang, F. Y., Diamond, P. H. and Rosenbluth, M. N. (1991). A kinetic theory of trapped-electron-driven drift wave turbulence in a sheared magnetic field, *Phys. Fluids B* **3**, p. 68, <https://doi.org/10.1063/1.859957>.
- [74] Garbet, X. and Waltz, R. E. (1996). Action at distance and Bohm scaling of turbulence in tokamaks, *Phys. Plasmas* **3**, pp. 1898–1907, <https://doi.org/10.1063/1.871985>.

- [75] Gurnett, D. and Kurth, W. S. (2019). Plasma densities near and beyond the heliopause from the Voyager 1 and 2 plasma wave instruments, *Nature Astron.* **3**, pp. 1024–1028, <https://doi.org/10.1038/s41550-019-0918-5>.
- [76] Hahm, T. S. (2002). Physics behind transport barrier theory and simulations, *Plasma Phys. Control. Fusion* **44**, p. A87, <https://doi.org/10.1088/0741-3335/44/5A/305>.
- [77] Halfmoon, M., Hatch, D., Kotschenreuther, M., Mahajan, S., Hassan, E., Nelson, O., Lagner, F., Diallo, A. and Groebner, R. (2019). Application of gyrokinetic “Fingerprints: in identifying microinstabilities in DIII-D pedestals, 61st Annual Meeting of the APS Division of Plasma Physics, October 21–25, 2019, Fort Lauderdale, Florida.
- [78] Hallatschek, K. and Biskamp, D. (2001). Transport control by coherent zonal flows in the core/edge transitional regime, *Phys. Rev. Lett.* **86**, p. 1223, <https://doi.org/10.1103/PhysRevLett.86.1223>.
- [79] Hasegawa, A. and Mima, K. (1977). Stationary spectrum of strong turbulence in magnetized nonuniform plasma, *Phys. Rev. Lett.* **39**, p. 205, <https://doi.org/10.1103/PhysRevLett.39.205>.
- [80] Hasegawa, A. and Mima, K. (1978). Pseudo-three-dimensional turbulence in magnetized nonuniform plasma, *Phys. Fluids* **21**, pp. 87–92, <https://doi.org/10.1063/1.862083>.
- [81] Hasegawa, A. MacLennan, C. G. and Kodama, Y. (1979). Nonlinear behavior and turbulence spectra of drift waves and Rossby waves, *Phys. Fluids*, **22**, pp. 2122–2129, <https://doi.org/10.1063/1.862504>.
- [82] Hasegawa, A. and Wakatani, M. (1983). Plasma edge turbulence, *Phys. Rev. Lett.* **50**, p. 682, <https://doi.org/10.1103/PhysRevLett.50.682>.
- [83] Hazeltine, R. (2009). Research needs for magnetic fusion energy sciences, Report of the Research Needs Workshop (ReNeW), U. S. Department of Energy (Washington, DC).
- [84] Hendel, H. W., Chu, T. K. and Politzer, P. A. (1968). Collisional Drift Waves—Identification, Stabilization, and Enhanced Plasma Transport, *Phys. Fluids* **11**, p. 2426, <http://dx.doi.org/10.1063/1.1691833>.
- [85] Hill, D. (2008). Report of the FESAC Toroidal Alternates Panel, USDOE, Washington, D.C.
- [86] Hinton, F. L. and Horton, W. (1971). Amplitude limitation of a collisional drift wave instability, *Phys. Fluids* **14**, pp. 116–123, <https://doi.org/10.1063/1.1693260>.
- [87] Hirose, A., Elia, M. and Smolyakov, A. I. (2002). Short wavelength temperature gradient driven modes in tokamaks, *Phys. Plasmas* **9**, p. 1659, <https://doi.org/10.1063/1.1469025>.

- [88] Hirose, A. and Elia, M. (2002). Short wavelength temperature gradient driven modes in tokamaks. II. Electron mode, *Phys. Plasmas* **9**, p. 4664, <https://doi.org/10.1063/1.1513470>.
- [89] Hoang, G. T., Saoutic, B., Guiziou, L., Basiuk, V., Becoulet, A., Budny, R. V., Clairet, F., Colas, L., Devynck, P., Gil, C., Joffrin, E., Litaudon, X., Segui, J.-L., Voitsekhovitch, I. and Zou, X. L. (1998). *Nucl. Fusion* **38**, p. 117, <https://doi.org/10.1088/0029-5515/38/1/311>.
- [90] Hoang, G. T., Bourdelle, C., Garbet, X., Giruzzi, G., Aniel, T. and Ottaviani, M., Horton, W., Zhu, P. and Budny, R. V. (2001). Experimental determination of critical threshold in electron transport on tore supra, *Phys. Rev. Lett.* **87**, p. 125001, <http://dx.doi.org/10.1103/PhysRevLett.87.125001>.
- [91] Holod, I., Zhang, W. L., Xiao, Y., and Lin, Z. H. (2009). Electromagnetic formulation of global gyrokinetic particle simulation in toroidal geometry, *Phys. Plasmas* **16**, p. 122307, <https://dx.doi.org/10.1063/1.3273070>.
- [92] Holland, C. and Diamond, P. H. (2002). Electromagnetic secondary instabilities in electron temperature gradient turbulence, *Phys. Plasmas* **9**, p. 3857, <http://dx.doi.org/10.1063/1.1496761>.
- [93] Hong, B.-G., Horton, W., Hamaguchi, S., Wakatani, M., Yagi, M., and Sugama, H. (1991). Transition from resistive- $G$  to  $\eta_i$  driven turbulence in stellarator systems, *Phys. Fluids B: Plasma Phys.* **3**, p. 1638, <https://doi.org/10.1063/1.859683>
- [94] Horton, W. (1976). Spectral distribution of drift-wave fluctuations in tokamaks, *Phys. Rev. Lett.* **37**, p. 1269, <http://dx.doi.org/10.1103/PhysRevLett.37.1269>.
- [95] Horton, W., Hong, B.-G. and Tang, W. M. (1988). Toroidal electron temperature gradient driven drift modes, *Phys. Fluids* **31**, p. 2971–2983, <http://dx.doi.org/10.1063/1.866954>.
- [96] Horton, W. (1989). Drift wave vortices and anomalous transport, *Phys. Fluids B* **1**, p. 524, <https://doi.org/10.1063/1.859168>.
- [97] Horton, W. (1990). Nonlinear drift waves and transport in magnetized plasma, *Phys. Rep.* **192**, pp. 1–177, [https://doi.org/10.1016/0370-1573\(90\)90148-U](https://doi.org/10.1016/0370-1573(90)90148-U).
- [98] Horton, W. and Hasegawa, A. (1994). Quasi-two-dimensional dynamics of plasmas and fluids, *Chaos* **4**, p. 227, <https://doi.org/10.1063/1.166049>.
- [99] Horton, W. and Rowan, W. (1994). Impurity transport studies in the Texas Experimental Tokamak (TEXT), *Phys. Plasmas* **1**, p. 901, <https://doi.org/10.1063/1.870749>.
- [100] Horton, W. and Ichikawa, Y. (1996). *Chaos and Structures in Nonlinear Plasmas* (World Scientific) ISBN:8177642340.

- [101] Horton, W., Tajima, T., Dong, J-Q., Kim, J-Y., and Kishimoto, Y. (1997). Ion transport analysis of a high-beta poloidal JT60-U discharge, *Plasma Phys. Control. Fusion* **39**, pp. 83–104.
- [102] Horton, W., Park, H-B., Kwon, J-M., Strozzi, D., Morrison, P. J. and Choi, D-I. (1998). Drift wave test particle transport in reversed shear profile, *Phys. Plasmas* **5**, p. 3910, <https://doi.org/10.1063/1.873110>.
- [103] Horton, W., Zhu, P., Hoang, G. T., Aniel, T., Ottaviani, M. and Garbet, X. (2000). Electron transport in tore supra with fast wave electron heating, *Phys. Plasmas* **7**, pp. 1494–1511, <http://dx.doi.org/10.1063/1.873969>.
- [104] Horton, W., Hu, B., Dong, J-Q. and Zhu, P. (2003). Turbulent electron thermal transport in tokamaks, *New J. Phys.* **5**, p. 14, <http://dx.doi.org/10.1088/1367-2630/5/1/314>.
- [105] Horton, W., Wong, H. V., Morrison, P. J., Wurm, A., Kim, J. A., Perez, J. C., Pratt, J., Hoang, G. T., LeBlanc, B. P. and Ball, R. (2005). Temperature gradient driven electron transport in NSTX and Tore Supra, *Nucl. Fusion* **45**, p. 976, <https://doi.org/10.1088/0029-5515/45/8/025>.
- [106] Horton, W., Fu, X. R. and Beklemishev, A. (2010). Parameter optimization studies for a tandem mirror neutron source, *J. Fusion Energy* **29**, pp. 521–526, <https://doi.org/10.1007/s10894-010-9332-9>.
- [107] Hu, G. and Krommes, J. A. (1994). Generalized weighting scheme for  $\delta f$  particle–simulation method, *Phys. Plasmas* **1**, p. 863, <https://doi.org/10.1063/1.870745>.
- [108] Hu, G. and Horton, W. (1997). Minimal model for transport barrier dynamics based on ion–temperature–gradient turbulence, *Phys. Plasmas* **4**, pp. 3262–3272, <https://doi.org/10.1063/1.872467>.
- [109] Huang, Q., Hu, B., Zhong, W., Chen, L. and Shi, Y. (2019). Effects of background pressure on the arc characteristics of gas spark gap, *Plasma Sci. Technol.* **21**, p. 125401, <https://doi.org/10.1088/2058-6272/ab3058>.
- [110] Huijsmans, G. T. A. and Czarny, O. (2007). MHD stability in X-point geometry: simulation of ELMs, *Nucl. Fusion* **47**, pp. 659–666, <https://doi.org/10.1088/0029-5515/47/7/016>.
- [111] Idomura, Y., Wakatani, M. and Tokuda, S. (2000). Gyrokinetic theory of slab electron temperature gradient mode in negative shear tokamaks *Phys. Plasmas* **7** p. 2456, <https://doi.org/10.1063/1.874085>.
- [112] Ishida, S., Fujita, T., Akasaka, H., Akino, N., Annou, K., Aoyagi, T., Arai, T., Arakawa, K., Asakura, N., Azumi, M., Budny, R., Chiba, S., Da Costa, O., Ebisawa, N., Fujii, T., Fukuda, T., Funahashi, A., Grisham, L., Gunji, S., Hamamatsu, K., Hiratsuka, H., Hirauchi, S., Hirayama, T., Honda, A., Honda, M., Hosogane, N., Ichige, H., Ide, S., Ikeda, Y., Isaka,

- M., Isayama, A., Isei, N., Ishii, Y., Isozaki, N., Itami, K., Itoh, T., Iwahashi, T., Kamada, Y., Kaminaga, A., Kashiwabara, T., Kawai, M., Kawamata, Y., Kawano, Y., Kazama, D., Kazawa, M., Kikuchi, M., Kimura, H., Kimura, T., Kishimoto, H., Kishimoto, Y., Kitamura, S., Kiyono, K., Kodama, K., Koide, Y., Kokusen, S., Kondoh, T., Konoshima, S., Koog, J., Kramer, G. J., Kubo, H., Kurihara, K., Kurita, G., Kuriyama, M., Kusama, Y., Masaki, K., Matsuda, T., Matsumoto, T., Matukawa, M., Miura, T., Miya, N., Miyachi, K., Miyata, H., Miyo, Y., Mogaki, K., Mori, M., Morimoto, M., Morioka, S., Moriyama, S., Nagami, M., Nagashima, A., Nagashima, K., Nagaya, S., Naito, O., Nakamura, Y., Nemoto, M., Neyatani, Y., Nishitani, T., Ogiwara, N., Ohga, T., Ohsawa, M., Ohshima, T., Oikawa, T., Okabe, T., Okano, J., Omori, K., Omori, S., Omori, Y., Onose, Y., Oohara, H., Ozeki, T., Saidoh, M., Saigusa, M., Saito, N., Sakasai, A., Sakata, S., Sakurai, S., Sasajima, T., Sato, M., Scott, S. D., Seimiya, M., Seiki, H., Seki, M., Shimada, M., Shimizu, K., Shimizu, M., Shimojo, M., Shinozaki, S., Shirai, H., Shitomi, M., Siganuma, K., Sugie, T., Sunaoshi, H., Takahashi, M., Takahashi, S., Takeji, S., Takenaga, H., Takizuka, T., Tamai, H., Terakado, M., Terakado, T., Tobita, K., Tokuda, S., Totsuka, T., Toyokawa, Y., Toyoshima, N., Tsuchiya, K., Tsugita, T., Tsukahara, Y., Tuda, T., Uramoto, Y., Ushigusa, K., Usui, K., Yagyu, J., Yamagiwa, M., Yamamoto, M., Yamamoto, T., Yamashita, O., Yokokura, K., Yoshida, H., Yoshida, M. and Yoshino, R. (1997). Achievement of high-fusion performance in JT60-U reversed shear discharges, *Phys. Rev. Lett.* **79**, p. 3917, <https://doi.org/10.1103/PhysRevLett.79.3917>.
- [113] Ivanov, A. A. and Prikhodko, V. V. (2013). Gas-dynamic trap: an overview of the concept and experimental results, *Plasma Phys. Control. Fusion* **55**, p. 63001, <https://doi.org/10.1088/0741-3335/55/6/063001>.
- [114] Jenko F, Dorland, W., Kotschenreuther, M. and Rogers B. N. (2000). Electron temperature gradient driven turbulence, *Phys. Plasmas* **7** p. 1904, <https://doi.org/10.1063/1.874014>.
- [115] Jenko, F., Dorland, W. and Hammett, G. W. (2001). Critical gradient formula for toroidal electron temperature gradient modes, *Phys. Plasmas* **8**, p. 4096, <https://doi.org/10.1063/1.1391261>.
- [116] Jokipii, J. R. and Kóta, J. (2014). Interpretation of the disturbance in galactic cosmic rays observed on Voyager 1 beyond the heliopause, *Astrophys. J. Lett.* **794 L4**, <https://doi.org/10.1088/2041-8205/794/1/L4>.
- [117] Kadomtsev, B. B. and Pogutse, O. P. (1979). Electron heat conductivity of the plasma across a ‘braided’ magnetic field, *Nucl. Fusion, Suppl.* **1**, pp. 649–662, <https://ui.adsabs.harvard.edu/abs/1979ppcf....1..649K/abstract>.
- [118] Kadomtsev, B. B. (1992). *Tokamak Plasma: A Complex Physical System* (Institute of Physics Pub., Bristol, UK and Philadelphia) p. 153, ISBN:0750302348.

- [119] Kalmoni, N. M. E., Rae, I. J., Watt, C. E. J., Murphy, K. R., Forsyth, C. and Owen, C. J. (2015). Statistical characterization of the growth and spatial scales of the substorm onset arc, *J. Geophys. Res.: Space Phys.* **120**, pp. 8503–8516, <https://doi.org/10.1002/2015JA021470>.
- [120] Kaye, S. M., Greenwald, M., Stroth, U., Kardaun, O., Kus, A., Schissel, D., DeBoo, J., Bracco, G., Thomsen, K., Cordey, J., Miura, Y., Matsuda, T., Tamai, H., Takizuda, T., Hirayama, T., Kikuchi, H., Naito, O., Chudnovskij, A., Ongena, J., and Hoang, G. T. (1997). *Nucl. Fusion* **37**, pp. 1303–1328, <https://doi.org/10.1088/0029-5515/37/9/I10>.
- [121] Kaye, S. M., Levinton, F. M., Stutman, D., Tritz, K., Yuh, H., Bell, M. G., Bell, R. E., Domier, C. W., Gates, D., Horton, W., Kim, J-Y. LeBlanc, B. P., Luhman, Jr., N. C., Maingi, R., Mazzucato, E., Menard, J. E., Mikkelsen, D., Mueller, D., Park, H., Rewoldt, G., Sabbagh, S. A., Smith, D. R. and Wang, W. (2007). Confinement and local transport in the National Spherical Torus Experiment (NSTX), *Nucl. Fusion* **47**, p. 499, <http://dx.doi.org/10.1088/0029-5515/47/7/001>.
- [122] Kaye, S. M., Gerhardt, S., Guttenfelder, W., Maingi, R., Bell, R. E., Diallo, A., LeBlanc, B. P. and Podesta, M. (2013). The dependence of H-mode energy confinement and transport on collisionality in NSTX, *Nucl. Fusion* **53**, p. 063005, <https://doi.org/10.1088/0029-5515/53/6/063005>.
- [123] Kim, D. E., Choi, D.-I., Horton, W., Yushmanov, P. N. and Parail, V. V. (1990). Transition from neoclassical to turbulent electron diffusion, *Phys. Fluids B* **2**, p. 547, <https://doi.org/10.1063/1.859291>.
- [124] Kishimoto, Y., T. Tajima, Horton, W., M. J. LeBrun and J-Y. Kim. (1996). Theory of self-organized critical transport in tokamak plasmas, *Phys. Plasmas* **3**, pp. 1289–1307, <http://dx.doi.org/10.1063/1.871754>.
- [125] Kivelson, M. G. and Russell, C. T. (1995). *Introduction to Space Physics* (Cambridge Univ. Press) ISBN:0-521-45714-9.
- [126] Koide, Y., Kikuchi, M., Mori, M., Tsuji, S., Ishida, S., Asakura, N., Kamada, Y., Nishitani, T., Kawano, Y., Hatae, T., Fujita, T., Fukuda, T., Sakasai, A., Kondoh, T., Yoshino, R. and Neyatani, Y. (1994). Internal transport barrier on  $q = 3$  surface and poloidal plasma spin-up in JT-60U high- $\beta_p$  discharges, *Phys. Rev. Lett.* **72**, pp. 3662–3665, <http://dx.doi.org/10.1103/PhysRevLett.72.3662>.
- [127] Koniges, A. E., Crottinger, J. A. and Diamond, P.H. (1992). Structure formation and transport in dissipative drift-wave turbulence, *Phys. Fluids B: Plasma Phys.* **4**, p. 2785, <https://doi.org/10.1063/1.860151>.
- [128] Krimigis, S. M., Decker, R. B., Roelof, E. C., Hill, M. E., Bostrom, C. O., Dialynas, K., Gloeckler, G., Hamilton, D. C., Keath, E. P., and Lanzerotti, L. J. (2019). Energetic charged

- particle measurements from Voyager 2 at the heliopause and beyond, *Nature Astron.* **3**, pp. 997–1006, <https://doi.org/10.1038/s41550-019-0927-4>.
- [129] Krommes, J. A. and Hu, G. (1994). The role of dissipation in the theory and simulation of homogeneous plasma turbulence, and resolution of entropy paradox *Phys. Plasmas* **1**, p. 3211, <https://doi.org/10.1063/1.870475>.
- [130] Lang, P., Conway, G. D., Eich, T., Fattorini, L., Gruber, O., G unter, S., Horton, L. D., Kalvin, S., Kallenbach, A., Kaufmann, M., Kocsis, G., Lorenz, A., Manso, M. E., Maraschek, M., Mertens, V., Neuhauser, J., Nunes, I., Schneider, W., Suttrop, W., Urano, H. and the ASDEX Upgrade Team. (2004). ELM pace making and mitigation by pellet injection in ASDEX Upgrade, *Nucl. Fusion* **44**, p. 665, <https://doi.org/10.1088/0029-5515/44/5/010>.
- [131] Lang, P., Frigione, D., Geraud, Alarcon, T., Bennett, P., Cseh, G., Garnier, D., Garzotti, L., Köchl, F., Kocsis, G., Lennholm, M., Neu, R., Mooney, R., Saarelma, S., Sieglin, B. and JET–EFDA Contributors. (2013). ELM pacing and trigger investigations at JET with the new ITER–like wall, *Nucl. Fusion* **53**, p. 073010, <https://doi.org/10.1088/0029-5515/53/7/073010>.
- [132] Lau, C. K., Fulton, D. P., Holod, I., Lin, Z., Binderbauer, M., Tajima, T. and Schmitz, L. (2017). Drift–wave stability in the field–reversed configuration, *Phys. Plasmas* **24**, p. 082512, <https://doi.org/10.1063/1.4993630>.
- [133] LeBlanc, B. P., Bell, R. E., Kaye, S. M., stutman, D., Bell, M. G., Bitter, M. L., Bourdelle, C., Gates, D. A., Maingi, R., Medley, S. S., Menard, J. E., Mueller, D., Paul, S. F., Roquemore, A. L., Rosenberg, A., Sabbagh, S. A., Soukhanovskii, V. A., Synakowski, E. J., Wilson, J. R. and the NSTX Research Team, Confinement studies of auxiliary heated NSTX plasmas, *Nucl. Fusion* **44**, p. 513, <https://doi.org/10.1088/0029-5515/44/4/005>.
- [134] Lee, Y. C., Dong, J.-Q. Gudzar, P. N. and Liu, C. S. (1987). Collisionless electron temperature gradient instability, *Phys. Fluids* **30**, p. 1331, <https://doi.org/10.1063/1.866248>.
- [135] Levinton, F. M., Zarnstorff, M. C., Batha, S. H., Bell, M., Bell, R. E., Budny, R. V., Bush, C., Chang, Z., Fredrickson, E., Janos, A., Manickam, J., Ramsey, A., Sabbagh, S. A., Schmidt, G. L., Synakowski, E. J. and Taylor, G. (1995). Improved confinement with reversed magnetic shear in TFTR, *Phys. Rev. Lett.* **75**, pp. 4417–4420, <http://dx.doi.org/10.1103/PhysRevLett.75.4417>.
- [136] Li, J. and Kishimoto, Y. (2002). Interaction between small–scale zonal flows and large–scale turbulence: A theory for ion transport intermittency in tokamak plasmas, *Phys. Rev. Lett.* **89**, pp. 115002–1, <https://doi.org/10.1103/PhysRevLett.89.115002>.
- [137] Lin, Z., Hahm, T. S., Lee, W. W., W. M. Tang and R. B. White. (1998). Turbulent transport reduction by zonal flows: massively parallel simulations, *Science* **281**, pp. 1835–1837, <http://dx.doi.org/10.1126/science.281.5384.1835>.

- [138] Lin, Z., Ethier, S., Hahm, T. S. and Tang, W. M. (2002). Size scaling of turbulent transport in magnetically-confined plasmas, *Phys. Rev. Lett.* **88**, p. 195004, <https://doi.org/10.1103/PhysRevLett.88.195004>.
- [139] Liu, Xing (2018). Gyrokinetic simulation of pedestal turbulence using GENE, Dissertation, The University of Texas at Austin, <http://hdl.handle.net/2152/69104>.
- [140] Mazzucato, E. (1976). Small-scale density fluctuations in the adiabatic toroidal compressor, *Phys. Rev.* **36**, p. 792, <http://dx.doi.org/10.1103/PhysRevLett.36.792>.
- [141] Mazzucato, E. and Nazikian, R. (1993). Radial scale length of turbulent fluctuations in the main core of TFTR plasmas, *Phys. Rev. Lett.* **71**, p. 1840–1843, <https://doi.org/10.1103/PhysRevLett.71.1840>.
- [142] Mazzucato, E., Smith, D. R., Bell, R. E., Kaye, S. M., Hosea, J. C., LeBlanc, B. P., Wilson, J. R., Ryan, P. M., Domier, C. W., Luhmann, Jr., N. C., Yuh, H., Lee, W., and Park, H. (2008). *Phys. Rev. Lett.* **101**, p. 075001, <https://doi.org/10.1103/PhysRevLett.101.075001>.
- [143] Mazzucato, E., Bell, R. E., Ethier, S., Hosea, J. C., Kaye, S. M., LeBlanc, B. P., Lee, W. W., Ryan, P. M., Smith, D. R., Wang, W. X., Wilson, J. R., and Yuh, H. (2009). Study of turbulent fluctuations driven by the electron temperature gradient in the National Spherical Torus Experiment, *Nucl. Fusion* **49**, p. 055001, <https://doi.org/10.1088/0029-5515/49/5/055001>.
- [144] McPherron, R. L., Hsu, T.-S., Kissinger, J., Chu, X. and Angelopoulos, V. (2011). Characteristics of plasma flows at the inner edge of the plasma sheet, *J. Geophys. Res.* **116**, p. A00I33, <https://doi.org/10.1029/2010JA015923>.
- [145] McWilliams, J. C., Weiss, J. B. and Yavneh, I. (1999). The vortices of homogeneous geostrophic turbulence, *J. Fluid Mech.* **401**, pp. 1–26, <https://doi.org/10.1017/S0022112099006382>.
- [146] Mende, S. B., Harris, S. E., Frey, H. U., Angelopoulos, V., Russell, C. T., Donovan, E., Jackel, B., Greffen, M. and Peticolas, L. M. (2008). The THEMIS Array of ground-based observatories for the study of auroral substorms, *Space Sci. Rev.* **141**, pp. 357–387, <https://dx.doi.org/10.1007/s11214-008-9380-x>.
- [147] Meng, X., Zhu, X., Wang, P., Zhao, Y., Liu, X., Zhang, B., Xiao, Y., Zhang, W. and Lin, Z. (2013). Heterogeneous programming and optimization of gyrokinetic toroidal code and large-scale performance test on TH-1A, in International Supercomputing Conference, 2013, pp. 81–96, [https://doi.org/10.1007/978-3-642-38750-0\\_7](https://doi.org/10.1007/978-3-642-38750-0_7).
- [148] Milroy, R. D., Barnes, D. C., Bishop, R. C. and Webster, R. B. (1989). Nonlinear magneto-hydrodynamic studies of the tilt mode in field configurations, *Phys. Fluids B: Plasma Phys.* **1**, p. 1225, <https://doi.org/10.1063/1.858998>.

- [149] Milroy, R. D., Macnab, A. I. D., Kim, C. C. and Sovinec, C. R. (2008). FRC Simulations using the NIMROD Code, *J. Fusion Energy* **27**, pp. 73–76, <https://doi.org/10.1007/s10894-007-9089-y>.
- [150] Motoba, T., Hosokawa, K., Kadokura, A. and Sato, N. (2012). Magnetic conjugacy of northern and southern auroral beads, *Geophys. Res. Lett.* **39**, p. L08108, <https://doi.org/10.1029/2012GL051599>.
- [151] Nelson, A., Kolemen, E., Laggner, F., Izacard, O., Groebner, R., Eldon, D., Shafer, M., Leonard, A., Shiraki, D. and Sontag, A. (2018). Pedestal fueling variation in a closed divertor configuration at DIII-D, APS Division of Plasma Physics Meeting 2018, abstract id.PP11.030, <https://ui.adsabs.harvard.edu/abs/2018APS..DPPP11030N>.
- [152] Nishimura, Y., Lyons, L. R., Nicolls, M. J., Hampton, D. L., Michell, R. G., Samara, M., Bristow, W. A., Donovan, E. F., Spanswick, E., Angelopoulos, V. and Mende, S. B. (2014). Coordinated ionospheric observations indicating coupling between preonset flow bursts and waves that lead to substorm onset, *J. Geophys. Res.: Space Phys.* **119**, p. 3333–3344, <https://doi.org/10.1002/2014JA019773>.
- [153] Nishimura, Y., Yang, J., Pritchett, P. L., Coroniti, F. V., Donovan, E. F., Lyons, L. R., Wolf, R. A., Angelopoulos, V. and Mende, S. B. (2016). Statistical properties of substorm auroral onset beads/rays, *J. Geophys. Res.: Space Phys.* **121**, pp. 866–8676, <https://doi.org/10.1002/2016JA022801>.
- [154] Ohkawa, T. and Yoshikawa, M. (1967). Experimental observation and theoretical interpretation of low-frequency interchange instability in “average minimum- $B$ ” configurations, *Phys. Rev. Lett.* **19**, p. 1374, <https://doi.org/10.1103/PhysRevLett.19.1374>.
- [155] Ohkawa, T. (1978). A transport model for alcator scaling in tokamaks, *Phys. Lett. A* **67**, p. 35, [https://doi.org/10.1016/0375-9601\(78\)90560-1](https://doi.org/10.1016/0375-9601(78)90560-1).
- [156] Okabayashi, M. and Arunasalam, V. (1977). Study of drift-wave turbulence by microwave scattering in a toroidal plasma, *Nuclear Fusion*, **17**, pp. 497–513, <https://doi.org/10.1088/0029-5515/17/3/010>.
- [157] Omelchenko, A. and Karimabadi, H. (2014). Parallel asynchronous hybrid simulations of strongly inhomogeneous plasmas, Proceedings of the Winter Simulation Conference, pp. 3435–3446, <http://dx.doi.org/10.1109/WSC.2014.7020176>.
- [158] Ottaviani, M., Horton, W. and Erba, M. (1997). The long wavelength behaviour of ion-temperature-gradient-driven turbulence and the radial dependence of the turbulent ion conductivity, *Plasma Phys. Control. Fusion* **39**, pp. 121–146, [https://doi.org/10.1016/S0370-1573\(96\)00056-7](https://doi.org/10.1016/S0370-1573(96)00056-7).

- [159] Ottaviani, M. and Manfredi, G. (1999). The gyroradius scaling of ion thermal transport from global numerical simulations of ion temperature gradient driven turbulence, *Phys. Plasmas* **6** pp. 3267–3275, <https://doi.org/10.1063/1.873567>.
- [160] Parks, P. B. and Schaffer, M. J. (2003). Analytical equilibrium and interchange stability of single- and double-axis field-reversed configurations inside a cylindrical cavity, *Phys. Plasmas* **10**, p. 1411, <https://doi.org/10.1063/1.1566025>.
- [161] Pécseli, H. L., Rasmussen, J. Juul, and Thomsen, K. (1984). Nonlinear interaction of convective cells in plasmas, *Phys. Rev. Lett.* **52** pp. 2148–2151, <https://doi.org/10.1103/PhysRevLett.52.2148>.
- [162] Pécseli, H. L., Rasmussen, J. Juul and Thomsen, K. (1985). Nonlinear interaction of convective cells in plasmas, *Plasma Phys. Control. Fusion* **27** pp. 837–846, <https://doi.org/10.1088/0741-3335/27/8/002>.
- [163] Perkins, F. W., Barnes, Cris W., Johnson, D. W., Scott, S. D., Zarnstorff, M. C., Bell, M. G., Bell, R. E., Bush, C. E., Grek, B., Hill, K. W., Mansfield, D. K., Park, H., Ramsey, A. T., Schivell, Stratton, B. C. and Synakowski, E. (1993). Nondimensional transport scaling in the tokamak fusion test reactor: Is tokamak transport Bohm or gyro–Bohm? *Phys. Fluids B* **5**, pp. 477–498, <https://doi.org/10.1063/1.860534>.
- [164] Petty, C. C., Luce, T. C., Burrell, K. H., Chiu, S. C., deGrassie, J. S., Forest C. B., Gohil, P., Greenfield, C. M., Groebner, R. J., Harvey, R. W., Pinsker, R. I., Prater, R. and Waltz, R. E. (1995). Nondimensional transport scaling in DIII-D: Bohm versus gyroBohm resolved, *Phys. Plasmas* **2**, pp. 2342–2348, <https://doi.org/10.1063/1.871259>.
- [165] Petviashvili, V. I. (1977). Self-focusing of an electrostatic drift wave, *Sov. J. Plasma Phys.* **3**, p. 150, <https://ui.adsabs.harvard.edu/abs/1977FizPl...3..270P/abstract>.
- [166] Prager, S. C., Sen, A. K. and Marshall, T. C. (1974). Dissipative trapped-electron instability in cylindrical geometry, *Phys. Rev. Lett.* **33** pp. 692–695, <https://doi.org/10.1103/PhysRevLett.33.692>.
- [167] Rae, I. J., Watt, C. E. J., Mann, I. R., Murphy, K. R., Samson, J. C., Kabin, K. and Angelopoulos, V. (2010). Optical characterization of the growth and spatial structure of a substorm onset arc, *J. Geophys. Res.* **115**, p. A10222, <https://doi.org/10.1029/2010JA015376>.
- [168] Rebut, P. H., Watkins, M. L., Gambier, D. J. and Boucher, D. (1991). A program towards a fusion reactor, *Phys. Fluids B* **3**, p. 2209, <https://doi.org/10.1063/1.859638>.
- [169] Redd, A. J., Kritz, A. H., Bateman, G. and Kinsey, J. E. (1997). Sensitivity of predictive tokamak plasma transport simulations *Phys. Plasmas* **4**, pp. 2207–2214, <https://doi.org/10.1063/1.872384>.

- [170] Rewoldt, G. and Tang, W. M. (1990). Toroidal microinstability studies of high-temperature tokamaks, *Phys. Fluids B: Phys. Plasmas* **2** p. 318, <https://doi.org/10.1063/1.859320>.
- [171] Richardson, J. D., Belcher, J. W., Garcia-Galindo, P. and Burlaga, L. F. (2019). Voyager 2 plasma observations of the heliopause and interstellar medium, *Nature Astron.* **3**, pp. 1019–1023, <https://doi.org/10.1038/s41550-019-0929-2>.
- [172] Robinson, P. A. (1997). Nonlinear wave collapse and strong turbulence, *Rev. Mod. Phys.* **69**, pp. 507–574, <https://doi.org/10.1103/RevModPhys.69.507>.
- [173] Rogers, B. N., Drake, J. F. and Zeiler, A. (1998). Phase space of tokamak edge turbulence, the L–H transition, and the formation of the edge pedestal *Phys. Rev. Lett.* **81**, p. 4396, <https://doi.org/10.1103/PhysRevLett.81.4396>.
- [174] Rosenbluth, M. N., Krall, N. A., and Rostoker, N. (1962). Finite Larmor radius stabilization of “weakly” unstable confined plasmas, *Nucl. Fusion Suppl.* **143**, OSTI ID:4808729.
- [175] Ross, D. W., Tang, W. M. and Adam, J.C. (1977). Study of trapped electron instabilities driven by magnetic curvature drifts, *Phys. Fluids* **20** p. 613, <https://doi.org/10.1063/1.861920>.
- [176] Rowan, W. L., Bespamyatnov, Igor O. and Fiore, C. L. (2008). Light impurity transport at an internal transport barrier in Alcator C–Mod, *Nucl. Fusion* **48**, p. 105005, <https://doi.org/10.1088/0029-5515/48/10/105005>.
- [177] Ryter, F., Imbeaux, F., Leuterer, F., Fahrbach, H.–U., Suttrop, W. and ASDEX Upgrade Team. (2001a). Experimental characterization of the electron heat transport in low-density ASDEX Upgrade Plasmas, *Phys. Rev. Lett.* **86**, pp. 5498–5501, <http://dx.doi.org/10.1103/PhysRevLett.86.5498>.
- [178] Ryter, F., Leuterer, F., Pereverzev, G., Fahrbach, H.–U., Stober, J., Suttrop, W. and ASDEX Upgrade Team. (2001b). Experimental evidence for gradient length–driven electron transport in tokamaks, *Phys. Rev. Lett.* **86**, pp. 2325–2328, <http://dx.doi.org/10.1103/PhysRevLett.86.2325>.
- [179] Ryutov, D. D. (1990). Mirror type neutron source, *Plasma Phys. Control. Fusion* **32**, p. 999, <https://doi.org/10.1088/0741-3335/32/11/012>.
- [180] Scarmozzino, R., Sen, A. K. and Navratil, G. A. (1986). Production and identification of a collisionless, curvature–driven, trapped–particle instability, *Phys. Rev. Lett.* **57**, pp. 1729–1732, <https://doi.org/10.1103/PhysRevLett.57.1729>.
- [181] Schmitz, L., Fulton, D. P., Ruskov, E., Lau, C., Deng, B. H., Tajima, T., Binderbauer, M. W., Holod, I., Lin, Z., Gota, H., Tuszewski, M., Detrick, S. A. and Steinhauer, L. C. (2016). Suppressed ion–scale turbulence in a hot high– $\beta$  plasma, *Nature Comm.* **7**, p. 13860, <https://doi.org/10.1038/ncomms13860>.

- [182] Schmitz, L., Ruskov, E., Deng, B. H., Binderbauer, M., Tajima, T., Gota, H., Tuszewski, M. and the TAE Team (2016). Control of ion gyroscale fluctuations via electrostatic biasing and sheared  $\mathbf{E} \times \mathbf{B}$  flow in the C–2 field reversed configuration, *AIP Conference Proceedings* **1721**, <http://dx.doi.org/10.1063/1.4944018>.
- [183] SciDAC Project, Whole Device Modeling of Compact Tori. submitted (Funding Opportunity Announcement DE–FOA–0001670 , Tracking Number GRANT12349965) (2017).
- [184] Scott, B. (1989). Global consistency for thin flux tube treatment of toroidal geometry, *Phys. Plasmas* **5**, p. 2334, <https://doi.org/10.1063/1.872907>.
- [185] Sen, A. K., Chen, J. and Mauel, M. (1991). Production and identification of the ion–temperature–gradient instability, *Phys. Rev. Lett.* **66**, pp. 429–432, <http://dx.doi.org/10.1103/PhysRevLett.66.429>.
- [186] Sergeev, V., Angelopoulos, V., Kubyshkina, M., Donovan, E., Zhou, X.–Z., Runov, A. and Nakamura, R. (2011). Substorm growth and expansion onset as observed with ideal ground–spacecraft THEMIS coverage, *J. Geophys. Res.: Space Phys.* **116**, p. A00I26, <https://doi.org/10.1029/2010JA015689>.
- [187] Shaing, K. C. (1988). Neoclassical quasilinear transport theory of fluctuations in toroidal plasmas, *Phys. Fluids* **31**, p. 2249, <http://dx.doi.org/10.1063/1.866626>.
- [188] Slough, J., Navratil, G. A. and Sen, A. K. (1981). Production and observation of the dissipative trapped–ion instability, *Phys. Rev. Lett.* **47**, p. 1057, <https://doi.org/10.1103/PhysRevLett.47.1057>.
- [189] Slusher, R. E. and Surko, C. M. (1978). Study of density fluctuations in the absorption of oxygen on silicon, *Phys. Rev. Lett.* **40**, p. 400, <https://doi.org/10.1103/PhysRevLett.40.400>, Erratum *Phys. Rev. Lett.* **40**, p. 593.
- [190] Smolyakov, A. I., Yagi, M. and Kishimoto, Y. (2002). Short wavelength temperature gradient driven modes in tokamak plasmas, *Phys. Rev. Lett.* **89**, p. 125005, <https://doi.org/10.1103/PhysRevLett.89.125005>.
- [191] Steinhauer, Loren C. (2011). Review of field–reversed configurations, *Phys. Plasmas* **18**, p. 070501, <http://dx.doi.org/10.1063/1.3613680>.
- [192] Stenzel, R. L. (1978). Experiments on current–driven three–dimensional ion sound turbulence. Part I: Return–current limited electron beam injection, *Phys. Fluids* **21**, p. 99, <http://dx.doi.org/10.1063/1.862085>.
- [193] Stone, E., Cummings, A. C., Heikkila, B. C. and Lal, N. (2019). Cosmic ray measurements from Voyager 2 as it crossed into interstellar space, *Nature Astron.* **3**, pp. 1013–1018, <https://doi.org/10.1038/s41550-019-0928-3>.

- [194] Sugama, H., Wakatani, M. and Hasegawa, A. (1988). Study of resistive drift and resistive interchange modes in a cylindrical plasma with magnetic shear, *Phys. Fluids* **31** p. 1601, <https://doi.org/10.1063/1.866699>
- [195] Sugama, H., Okamoto, M., Horton, W. and Wakatani, M. (1996). Transport processes and entropy production in toroidal plasmas with gyrokinetic electromagnetic turbulence, *Phys. Plasmas* **3**, pp. 2379–2394, <http://dx.doi.org/10.1063/1.871922>.
- [196] Surko, C. M. and Slusher, R. E. (1976). Study of the density fluctuations in the adiabatic toroidal compressor scattering tokamak using CO<sub>2</sub> laser, *Phys. Rev. Lett.* **37**, pp. 1747–1750, , Erratum *Phys. Rev. Lett.* **38**, p. 258 (1977).
- [197] Synakowski, E. J., Batha, S. H., Beer, M. A., Bell, M. G., Bell, R. E., Budny, R. V., Bush, C. E., Efthimion, P. C., Hahm, T. S., Hammett, G. W., LeBlanc, B., Levinton, F., Mazzucato, E., Park, H., Ramsey, A. T., Schmidt, G., Rewoldt, G., Scott, S. E., Taylor, G. and Zarnstorff, M. C. (1997). Local transport barrier formation and relaxation in reverse-shear plasmas on the tokamak fusion test reactor, *Phys. Plasmas* **4**, pp. 1736–1744, <https://doi.org/10.1063/1.872275>.
- [198] Strait, E. J., Lao, L. L., Mauel, M. E., Rice, B. W., Taylor, T. S., Burrell, K. H., Chu, M. S., Lazarus, E. A., Osborne, T. H., Thompson, S. J., and Turnbull A. D. (1995). Enhanced confinement and stability in DIII-D discharges with reversed magnetic shear, *Phys. Rev. Lett.* **75**, pp. 4421–4424, <https://doi.org/10.1103/PhysRevLett.75.4421>.
- [199] Sudo, S., Tamura, N., Suzuki, C., Muto, S., Funaba, H. and LHD Group (2012). Multiple-tracer TESPEL injection for studying impurity behavior in a magnetically-confined plasma, *Nucl. Fusion* **52**, p. 063012, <http://dx.doi.org/10.1088/0029-5515/52/6/063012>.
- [200] Horton, W., Wootton, A. and Wakatani, M. (Eds.) (1994). In U.S.–Japan Workshop on Ion Temperature Gradient Driven Turbulent Transport, *AIP Conference Proceedings*, Vol. 284, p. 255 (10 pp.).
- [201] Tajima, T. and Asai, T. (2016). US–Japan Workshop on Compact Torus.
- [202] Taroni, A., Erba, M., Tibone, F. and Springmann, E. (1994). Global and local energy confinement properties of simple transport coefficients of the Bohm type, *Plasma Phys. Control. Fusion* **36**, p. 1629, <http://dx.doi.org/10.1088/0741-3335/36/10/003>.
- [203] Tsyganenko, N. A. (1995). Modeling the Earth's magnetospheric magnetic field confined within a realistic magnetopause, *J. Geophys. Res.* **100**, pp. 5599–5612, <https://doi.org/10.1029/94JA03193>.
- [204] Tsyganenko, N. A. (1996). Effects of the solar wind conditions in the global magnetospheric configurations as deduced from databased field models (Invited), International Conference on Substorms, Proceedings of the 3rd International Conference held in Versailles, 12–17 May

1996. (Edited by E. J. Rolfe and B. Kaldeich). ESA SP-389. Paris: European Space Agency, 1996., p. 181.
- [205] van Milligen, B. Ph., Nicolau J. H., Garcia, L., Carreras, B. A., Hidalgo, C. and the TJ-II Team. (2017). The impact of rational surfaces on radial heat transport in TJ-II, *Nucl. Fusion* **57**, p. 056028, <https://doi.org/10.1088/1741-4326/aa611f>.
  - [206] Voronkov, I., Rankin, R., Frycz, P., Tikhonchuk, V. T. and Samson, J. C. (1997). Coupling of shear flow and pressure gradient instabilities, *J. Geophys. Res.* **102**, pp. 9639–9650, <https://doi.org/10.1029/97JA00386>.
  - [207] Wakatani, M. and Hasegawa, A. (1984). A collisional drift wave description of plasma edge turbulence, *Phys. Fluids* **27**, p. 611, <https://doi.org/10.1063/1.864660>.
  - [208] Wakatani, M., Watanabe, K., Sugama, H. and Hasegawa, A. (1992). Resistive drift wave and interchange turbulence in a cylindrical plasma with magnetic and velocity shear, *Phys. Fluids B: Plasma Phys.* **4**, pp. 1754–1765, <https://doi.org/10.1063/1.860031>.
  - [209] Waltz, R. E., DeBoo, J. C. and Rosenbluth, M. N. (1990). Magnetic-field scaling of dimensionally similar tokamak discharges, *Phys. Rev. Lett.* **65**, p. 2390, <https://doi.org/10.1103/PhysRevLett.65.2390>.
  - [210] Wenninger, R. P., Eich, T. H., Huijsmans, G. T. A., Lang, P. T., Devaux, S., Jachmich, S., Köchl, F. and JET EFDA Contributors. (2011). Scrape-off layer heat transport and divertor power deposition of pellet-induced edge localized modes, *Plasma Phys. Control. Fusion* **53**, p. 105002, <https://doi.org/10.1088/0741-3335/53/10/105002>.
  - [211] Wolf, R. A. (1995). Physics of the magnetosphere (course notes).
  - [212] Wolf, R. A., Toffoletto, F. R., Schutza, A. M. and Yang, J. (2018). Buoyancy waves in earth's magnetosphere: Calculations for a 2D wedge magnetosphere, *J. Geophys. Res.: Space Phys.* **123**, pp. 3548–3564, <https://doi.org/10.1029/2017JA025006>.
  - [213] Wong, K. L., Bretz, N. L., Hahm, T. S. and Synakowski, E. (1997). Short wavelength fluctuations and electron heat conductivity in enhanced reversed shear plasmas, *Phys. Lett. A* **236** p. 339–344, [https://doi.org/10.1016/S0375-9601\(97\)00806-2](https://doi.org/10.1016/S0375-9601(97)00806-2).
  - [214] Xiao, Y. and Lin, Z. (2009). Turbulent transport of trapped-electron modes in collisionless plasmas, *Phys. Rev. Lett.* **103**, p. 085004, <https://doi.org/10.1103/PhysRevLett.103.085004>.
  - [215] Yagi, M. and Horton, W. (1994). Reduced Braginskii equations, *Phys. Plasmas* **1**, p. 2135, <https://doi.org/10.1063/1.870611>.
  - [216] Yamada, M., Ji, H., Gerhardt, S. P., Belova, E. V., Davidson, R. C. and Mikkelsen, D. R. (2007). A self-organized plasma with induction, reconnection, and injection techniques:

- the SPIRIT concept for field reversed configuration research, *Plasma Fusion Res.* **2**, p. 4, <https://doi.org/10.1585/pfr.2.004>.
- [217] Yamamoto, T. (2008). A linear analysis of the hybrid Kelvin–Helmholtz/Rayleigh–Taylor instability in an electrostatic magnetosphere–ionosphere coupling system, *J. Geophys. Res.* **113**, p. A06206, <https://doi.org/10.1029/2007JA012850>.
- [218] Yamamoto, T. (2009). Hybrid Kelvin–Helmholtz/Rayleigh–Taylor instability in the plasma sheet, *J. Geophys. Res.* **114**, p. A06207, <https://doi.org/10.1029/2008JA013760>.
- [219] Yoshinuma, M., Ida, K., Yokoyama, M., Osakabe, M. and Nagaoka, K. (2010). Charge–exchange spectroscopy with pitch–controlled double–slit fiber bundle on LHD, *Fusion Sci. Tech.* **58**, pp. 375–382, <https://doi.org/10.13182/FST10-A10823>.
- [220] Zakharov, V. E. (1972). Collapse of Langmuir waves, *Zh. Eksp. Teor. Fiz.* **62**, pp. 1745–1759.
- [221] Zakharov, V. E., L'vov, V. S. and Falkovich, G. (1992). Kolmogorov spectra of turbulence 1. Wave turbulence, (Springer–Verlag, Germany), p. 275, ISBN:3–540–54533–6.
- [222] Zhong, W. L., Shen, Y., Zou, X. L., Gao, J. M., Shi, Z. B., Dong, J–Q., Duan, X. R., Xu, M., Cui, Z. Y., Li, Y. G., Ji, X. Q., Yu, D. L., Cheng, J., Xiao, G. L., Jiang, M., Yang, Z. D. C., Zhang, B. Y., Shi, P. W., Liu, Z. T., Song, X. M., Ding, X. T. and Liu, Y. (HL–2A Team). (2016). Observation of double impurity critical gradients for electromagnetic turbulence excitation in tokamak plasmas, *Phys. Rev. Lett.* **117**, p. 045001, <https://doi.org/10.1103/PhysRevLett.117.045001>.
- [223] Zou, X. L., Colas, L., Paume, M., Chareau, J. M., Laurent, L., Devynck, P. and Gresillon, D. (1995). Internal magnetic turbulence measurement in plasma by cross polarization scattering, *Phys. Rev. Lett.* **75**, p. 1090, <https://doi.org/10.1103/PhysRevLett.75.1090>.
- [224] Zou, S., Moldwin, M. B., Lyons, L. R., Nishimura, Y., Hirahara, M., Sakanoi, T., Asamura, K., Nicolls, M. J., Miyashita, Y., Mende, S. B. and Heinselman, C. J. (2010). Identification of substorm onset location and the preonset sequence using REIMEI, THEMIS BGO, PFISR, and Geotail, *J. Geophys. Res.* **115**, <https://doi.org/10.1029/2010JA015520>.